

Insights Into Stellar Explosions From Infrared Light

Thesis by
Samaporn Tinyanont

In Partial Fulfillment of the Requirements for the
Degree of
Doctor of Philosophy

The logo for the California Institute of Technology (Caltech), featuring the word "Caltech" in a bold, orange, sans-serif font.

CALIFORNIA INSTITUTE OF TECHNOLOGY
Pasadena, California

2020
Defended May 25, 2020

© 2020

Samaporn Tinyanont
ORCID: 0000-0002-1481-4676

All rights reserved except where otherwise noted

The Sky is the Limit — Infrared Astronomer's Proverb

To Mom and Dad

ACKNOWLEDGEMENTS

Five years is a long period of time to stay resolute to a task that is the completion of this thesis. Along the way, before and throughout my graduate school career, I have found love, friendship, and support from numerous people.

First and foremost, to my advisors Dimitri Mawet and Mansi Kasliwal: I have learned innumerable lessons and received supports from both of you every step of the way. Dimitri allowed me to work on a novel instrumentation project as a first year graduate student and a total engineering novice, an experience not many graduate students get to enjoy. The journey with WIRC+Pol from its conception, building, initial commissioning, upgrading, and recommissioning to finally producing scientific result was truly fulfilling. I am also glad to report that my engineering skills are now non-zero. Mansi taught me most everything one needs to know about time-domain astronomy. My first venture into research was an undergraduate summer project with her at Carnegie Observatories, working on the Census of the Local Universe project where I learned how to find uncatalogued galaxies using two $H\alpha$ filters, and also how *not* to cross-match two million-entry catalogs using nested for loops. In January 2014, she invited me to join a little survey called SPitzer InfraRed Intensive Transients Survey, SPIRITS, which paved way for my graduate career at Caltech. Both of you have given me a solid foundation for my scientific career, one that I seek to build into something of which you can be proud.

I would like to thank my thesis committee members: Lynne Hillenbrand, Jim Fuller, and Chuck Steidel for advice throughout my time at Caltech. I also thank Nathan Smith (University of Arizona) for our fruitful collaborations on dust and all things interacting supernova, and also for writing me recommendation letters for my applications to postdoctoral positions.

I learned innumerable lessons from working with extremely talented postdoctoral scholars in both groups. To Max Millar-Blanchaer, thank you for teaching me the science of polarimetry and the art of resolving its numerous associated headaches. Without your guidance and expertise, much of the work presented in this thesis would not have been possible, especially the first measurement of infrared spectropolarimetry of supernovae. To Ricky Nilsson, I cherish our time during the planning of WIRC+Pol and throughout the first tumultuous years of commissioning getting the instrument to work. To Ryan Lau, thank you for enlightening me

on the coolness of dust and the difficulties of observing them, especially in the mid-infrared, and more especially from the ground. When people ask me what is the most exciting moment in your graduate career, my answer is always seeing SN 2014C from the ground at $10\ \mu\text{m}$ from the data that you took. I also thank you and for hosting me for more than two weeks in Japan, during which I learned a great deal about working in a non-US setting.

I am lucky to be a part of two energetic and enthusiastic groups of world-class researchers at Caltech and JPL. I thank members of Dimitri's Exoplanet Technology Laboratory for sharing with me the exciting world of directly imaging exoplanets, and for not ostracizing me for not working on them. I thank members of the time-domain astronomy group, whose expertise sets a standard for me to reach. Special thanks are due to Jacob Jencson, Anna Ho, Kishalay De, and Yuhan Yao for helping me solving numerous research problems and listening to me complain about everything under the sun. Discussions with you have guided me through my graduate career, and I hope to continue our collaboration.

I owe a depth of gratitude to all staff members of Palomar Observatory, whose assistance allows me to complete the instrumentation and most observational work in my thesis. In particular, I would like to thank the Assistant Astronomers and Telescope Operators John Baker, Carolyn Heffner, Paul Nied, Joel Pearman, Kajsa Peffer, and Kevin Rykoski. I also would like to thank the Palomar Monastery staff who make sure I am comfortable and well fed. While the period of my frequent visits to the Observatory, whether in person or remotely, is sadly coming to an end, I will always remember your kindness and professionalism that make Palomar a place like nowhere else. In addition, I also thank Jennifer Milburn for your work on the instrument software control for WIRC and for supporting us countless of times, many at ungodly hours.

My experience at Caltech would not be the same if it were not for the amazing cohort of graduate students in Cahill. I thank you all for embarking on the arduous journey that is graduate school together, enjoying the exploration of the universe while making our voices heard to improve the program along the way. Thank you Anna, Bhawna, Ivanna, and Yuguang for navigating graduate school together from the first year.

Administrative officers of Cahill, especially Gita Patel and Judy McClain, have supported me greatly over my five years working here. Thank you Judy for helping me plan (and pay for) all of the memorable trips to visit and to attend conferences all

over the US and beyond. Thank you Gita for ensuring the department continues to run smoothly and dealing with literally everything from hunting down a cockroach to fixing a broken elevator. In addition, I have to thank our IT staff, Anu Mahabal, Patrick Shopbell, and Carl Smay, for your continued patience with us. Despite our knowledge about the Universe, we have proven time after time that we have little clue how computers work (let alone networking and printers). Your work truly enables research in this building.

I sing with the Caltech Glee Club and the Chamber Singers throughout my time here. To our choral director, Nancy Sulahian, thank you very much for the love of music you share with us. I have had an excellent time singing with you and the group.

To Billy Scanlon, you have been with me every step of the way throughout these five adventurous years. It is inspiring to see you build your career with competence and dedication as cornerstones. I admire your contagious passion on music, car, photography, design, and all cool things in general. Despite living in Los Angeles area throughout my undergraduate years, I never felt like LA is home until I met you. Thank you for your friendship and companionship, and I look forward to our years to come. The last few months of graduate career were spent on lockdown due to the novel coronavirus pandemic of 2019–2020 (one instance where novel is really bad). I am grateful to Billy and Greg Rezek for allowing me to share your living space with me. Lastly, the trio of felines Calvin, Lewis, and Clark gave us both joy when playing with them and purpose of giving them food.

Harvey Mudd College provided me with an undergraduate education and experience I cannot expect from anywhere else. The rigorous suite of required classes provided me with tools I use in research every day. I would like to thank Ann Esin and Phil Choi (of Pomona College) for a fantastic introduction to academic astronomy and astronomical research. Without your advice and supports, I would not have been able to pursue and finish my graduate career. I am also indebted to Vatche Sahakian, with whom I had a pleasure of taking five physics classes from the wonder of special relativity to the terror of general relativity.

My life as an astronomer did not start when I arrived in the US, so I cannot conclude this acknowledgement without recognizing a number of amazing astronomers in Thailand, especially the tight-knitted amateur astronomy community at the Thai Astronomical Society. I spent a large amount of time during my formative years in high school participating and eventually helping to organize numbers of public

events, lectures, stargazing under the harsh light pollution of Bangkok, and trips to the countryside where I got introduced to the dark sky. To Prapee Viraporn, thank you for your guidance throughout my Astronomy Olympiad years, and I would not be where I am today without your support from almost 15 years ago. To Pop Pornchai Amornsrijiratorn, thank you for introducing me to the wonderful world of astronomical optics and astrophotography, something my younger self would not believe will become his career. Thanks are also due to the rest of the Thai Astronomical Society team: Ari Sawasdee, Sukanya Phungpholngam, Pornchai Rangsitanapaisal, Wittaya Srichai, Niti Suibvises, Chalermchai Maklam, and many others. Further, I would like to thank my high school physics teacher Pom Pongsakorn Thammabut, whose instructions really made me appreciate the subject.

Finally, to my family: I dedicate this thesis to you. I cannot express how grateful I am to have you by my side always. It is a privilege have a family who loves and supports me unconditionally every step of the way.

ABSTRACT

Massive stars are the workhorse of the Universe. While accounting for a minute fraction of baryonic mass, their influence on the cosmos is profound. Their lives and deaths lead to nucleosynthesis of all elements heavier than helium, including those essential to life. They produce some of the most energetic eruptions and explosions, core-collapse (CC) supernovae (SNe) at the end of their life. These explosions are common, about once per century per galaxy, and are one of the primary drivers of the gas dynamics of their host galaxies. Despite their importance, many facets of the massive stars' evolution and their eventual death in CCSNe are still uncertain. In this thesis, I use a variety of observations in the infrared (IR) part of the electromagnetic spectrum to probe aspects of these stellar explosions elusive to visible light.

IR observations of SNe remain sparse compared to the optical, even for the most nearby events. I present the first systematic study of CCSNe light curves from the *Spitzer Space Telescope* showing trends in IR properties of CCSNe and identifying outliers that exhibit signs of interactions between the SN shock and the circumstellar medium (CSM) ejected from the star. I also present in-depth explorations of nearby SN 2017eaw, a typical and common hydrogen-rich explosion; and SN 2014C, a hydrogen-poor explosion whose shock wave crashes into the CSM containing material lost from the star. IR observations provide insights into the chemical evolution and circumstellar environment in these SNe.

In the second part of this thesis, I present the development and commissioning of a near-IR spectropolarimeter WIRC+Pol at Palomar Observatory. WIRC+Pol utilizes a novel, highly efficient polarization grating as its polarimetric beam splitter and spectral disperser. The resulting high sensitivity allows WIRC+Pol to observe sources as faint as $J = 14.5$ to 0.1% polarimetric accuracy in 2 hours. I also present the first scientific results from the instrument: the spectropolarimetric measurements of four nearby SNe, which are the first such observations in the IR. We detected polarization from SN 2018hna, which allowed us to constrain that its explosion geometry looks similar to the very well-studied SN 1987A observed from a different angle, suggesting the same underlying geometry.

PUBLISHED CONTENT AND CONTRIBUTIONS

- Tinyanont, S. et al. (2020). “The First Infrared Spectropolarimetric Detection of Intrinsic Polarization from a Core-Collapse Supernova”. Submitted.
Submitted for Publication, S.T. led some of the proposals to obtain the data; contributed to data acquisition, reduction, and analysis; and wrote the manuscript.
- Tinyanont, S. et al. (Sept. 2019a). “Achieving a spectropolarimetric precision better than 0.1% in the near-infrared with WIRC+Pol”. In: *Proc. SPIE*. Vol. 11132. Society of Photo-Optical Instrumentation Engineers (SPIE) Conference Series. DOI: 10.1117/12.2529863. arXiv: 1908.10409 [astro-ph.IM].
S.T. contributed in developing the WIRC+Pol data reduction pipeline; designed and characterized slit mask in laboratory; contributed to the half-wave plate installation at Palomar and the subsequent data acquisition and analysis for the commissioning; and wrote the manuscript.
- Tinyanont, S. et al. (Dec. 2019b). “Supernova 2014C: Ongoing Interaction with Extended Circumstellar Material with Silicate Dust”. In: *ApJ* 887.1, 75. DOI: 10.3847/1538-4357/ab521b. arXiv: 1909.06403 [astro-ph.SR].
S.T. led some of the proposals to obtain the data; contributed to data acquisition, reduction, and analysis; and wrote the manuscript.
- Tinyanont, S. et al. (Mar. 2019c). “Supernova 2017eaw: Molecule and Dust Formation from Infrared Observations”. In: *ApJ* 873.2, 127. DOI: 10.3847/1538-4357/ab0897. arXiv: 1901.01940 [astro-ph.HE].
S.T. led some of the proposals to obtain the data and contributed to data acquisition, reduction, and analysis; and wrote the manuscript.
- Tinyanont, S. et al. (Feb. 2019d). “WIRC+Pol: A Low-resolution Near-infrared Spectropolarimeter”. In: *PASP* 131.996. DOI: 10.1088/1538-3873/aaef0f. arXiv: 1811.03138 [astro-ph.IM].
S.T. contributed in developing the WIRC+Pol data reduction pipeline; characterized the detector installed in WIRC+Pol; contributed in the data acquisition and analysis for the commissioning; and wrote the manuscript.
- Tinyanont, S. et al. (Dec. 2016). “A Systematic Study of Mid-infrared Emission from Core-collapse Supernovae with SPIRITS”. In: *ApJ* 833.2, 231. DOI: 10.3847/1538-4357/833/2/231. arXiv: 1601.03440 [astro-ph.SR].
S.T. contributed to data acquisition and analysis, and wrote the manuscript.

TABLE OF CONTENTS

Acknowledgements	v
Abstract	ix
Published Content and Contributions	x
Table of Contents	x
List of Illustrations	xiii
List of Tables	xvi
Chapter I: Introduction	1
1.1 Different Flavors of Core-Collapse Supernovae	3
1.2 Binary Interaction and Mass Loss in Massive Stars	6
1.3 Asymmetric Explosion Mechanism and the Shape of the Ejecta	7
1.4 Polarimetry: How to Measure the Shape of Unresolvable Sources	8
1.5 Infrared Observations of Supernovae	11
1.6 Challenges to Infrared Observations	13
1.7 Thesis Outline	17
Chapter II: A Systematic Study of Mid-Infrared Emission from Core-Collapse Supernovae with SPIRITS	20
2.1 Introduction	21
2.2 Observations	24
2.3 Results	28
2.4 Case Studies	40
2.5 Conclusion	48
Chapter III: Supernova 2017eaw: Molecule and Dust Formation from Infrared Observations	53
3.1 Introduction	54
3.2 Observations	58
3.3 Analysis and Discussion	65
3.4 Summary and Conclusions	81
Chapter IV: Supernova 2014C: Ongoing Interaction with Extended Circum- stellar Material with Silicate Dust	85
4.1 Introduction	86
4.2 Observations	90
4.3 Analysis	97
4.4 Discussion and Conclusions	108
Chapter V: WIRC+Pol: a Low-Resolution Near-Infrared Spectropolarimeter	114
5.1 Introduction	115
5.2 The Instrument	117
5.3 Data Reduction Pipeline	123
5.4 Instrument Commissioning	133
5.5 Future Instrument Upgrades	142

5.6 Conclusion	144
Chapter VI: Achieving a Spectropolarimetric Precision Better than 0.1% in the Near-Infrared with WIRC+Pol	146
6.1 Introduction	147
6.2 Half-Wave Plate and Linear Polarizer Upgrades	149
6.3 New Focal Plane Mask with Slit	152
6.4 Observational Technique	155
6.5 Calibrating Instrumental Polarization	156
6.6 Future Characterizations	158
6.7 Conclusion	160
Chapter VII: The First Infrared Spectropolarimetric Detection of Intrinsic Polarization from a Core-Collapse Supernova	162
7.1 Introduction	163
7.2 Observations and Data Reduction	164
7.3 Results and Discussions	171
7.4 Conclusion	174
Chapter VIII: The Future is Infrared Bright	178
8.1 Landscape of Science Cases Enabled by WIRC+Pol	178
8.2 Future of Supernova Spectropolarimetry	179
8.3 Large-Sample Survey of Supernovae in the Infrared	180
8.4 Next Decades with a Sensitive Mid-Infrared Observatory	181
Bibliography	183
Appendix A: MCMC Fitting of the SED and Light Curve of SN 2014C	212
A.1 SED Fitting with Dust Models	212
A.2 Light-Curve Fitting with CSM Models	212
Appendix B: WIRC+Pol Calibration and Data Verification	216
B.1 Verification of WIRC+Pol Results against Background Subtraction	216
B.2 Polarimetric Efficiency and Angle of Polarization Calibration from Observations of Polarized Standard Stars	217

LIST OF ILLUSTRATIONS

<i>Number</i>	<i>Page</i>
1.1 Representative optical and near-infrared spectra near peak light of supernovae of different subtypes	4
1.2 Schematics showing how scattering can cause polarization and how non-zero polarization indicates departure from symmetry in the scattering region.	9
1.3 Schematics comparing traditional surface relief grating and polarization grating	16
2.1 Histograms of supernova detections and non-detections in <i>Spitzer</i> data	30
2.2 <i>Spitzer</i> light curves of Type Ib/c supernovae	31
2.3 <i>Spitzer</i> light curves of Type II supernovae	33
2.4 Time evolution of dust luminosity, temperature, and mass inferred from <i>Spitzer</i> infrared observations	39
2.5 Light curves of the interacting Type II-P SN 2011ja compared to other interacting Type II-P supernovae	42
2.6 Evolution of the spectral density distribution of SN 2014C	46
2.7 Light curves of SNe 1979C and 1993J showing continued decline 20–30 years post-explosion	49
2.8 Galaxy background-subtracted images of five Type II supernovae detected more than 20 years post-explosion	50
3.1 Infrared images of NGC 6946 with SN 2017eaw	60
3.2 Images, light curve, and spectral energy distribution of the progenitor star of SN 2017eaw	61
3.3 Near-infrared photometry of SN 2017eaw compared to other Type II-P supernovae	64
3.4 Near-infrared spectra of SN 2017eaw with line identifications	66
3.5 Evolution of the spectral energy distribution of SN 2017eaw	73
3.6 High-velocity helium 1.083 μm absorption feature in SN 2017eaw	75
3.7 Evolution of carbon monoxide emissions in SN 2017eaw	79
3.8 Dust mass evolution of SN 2017eaw compared to other Type II-P and SN 1987A-like supernovae	82
4.1 False-color infrared image of NGC 7331 with SN 2014C	93

4.2	Mid-infrared images at 3.8, 4.6, and 9.7 μm of SN 2014C	94
4.3	Infrared photometry of SN 2014C	94
4.4	Near-infrared spectra of SN 2014C	98
4.5	Spectral energy distribution of SN 2014C from 1–10 μm	101
4.6	Spectral energy distribution of SN 2014C compared with all other H-rich interacting SNe with mid-IR ($> 10 \mu\text{m}$) data in the literature .	103
4.7	Dust luminosity, temperature, and mass of SN 2014C from <i>Spitzer</i> photometry fitting	104
4.8	Helium 1.083 μm line profile	108
5.1	The polarization grating inside WIRC+Pol and the schematic of the focal plane	120
5.2	Raw image from WIRC+Pol in the imaging mode, with the focal plane mask, and with the focal plane mask and the polarization grating	121
5.3	The schematic of the data reduction pipeline	125
5.4	Comparison between different flat fielding techniques	126
5.5	WIRC+Pol's transmission in the <i>J</i> and <i>J</i> bands	137
5.6	Degree and angle of polarization measured from three unpolarized standard stars showing time-varying instrumental polarization	138
5.7	Stokes parameters <i>q</i> and <i>u</i> of the same source measured at two po- sitions on the focal plane showing spatial dependence of the instru- mental polarization	140
5.8	Temporal variation of the broadband instrumental polarization over three hours	141
5.9	Degree and angle of polarization of two polarized standard stars, Elia 2-25 and Schulte 14 compared to the literature values	143
6.1	Example of WIRC+Pol background-subtracted data	148
6.2	Schematic of angles of polarization traced by the four spectral traces of WIRC+Pol at four different half-wave plate angles	152
6.3	New slit mask of WIRC+Pol	155
6.4	Improvement in Instrumental Polarization after the half-wave plate installation	158
6.5	Stokes parameters measured from faint unpolarized sources	159
7.1	Near-IR spectropolarimetry of SNe 2018hna (87A-like), 2019ein (Ia), 2020oi (Ic), and 2020ue (Ia)	170
7.2	Optical and near-IR light curves of the SNe observed by WIRC+Pol .	171

7.3	Compilation of recent spectropolarimetric measurements of different types of SNe	175
7.4	Schematic of SN 2018hna’s ejecta in comparison to those of SN 1987A showing that SN 2018hna and SN 1987A may share the same underlying geometry but observed from a different angle.	176
A.1	Corner plot from the Markov Chain Monte Carlo fit of SN 2014C’s spectral energy distribution using a dust model with only carbonaceous dust	213
A.2	Corner plot from the Markov Chain Monte Carlo fit of SN 2014C’s spectral energy distribution using a dust model with carbonaceous and silicate dust	214
A.3	Corner plot from the Markov Chain Monte Carlo fit of SN 2014C’s light curve	215
B.1	Normalized Stokes parameters extracted from the synthetic data showing that background subtraction does not introduce systematic biases.	217
B.2	WIRC+Pol Mueller matrix terms: polarimetric efficiencies and crosstalks, obtained from observations of three polarized standard stars	219
B.3	Corrected Stokes parameters after applying the Mueller matrix correction	219

LIST OF TABLES

<i>Number</i>	<i>Page</i>
2.1 SN Sample	26
2.2 Near-IR Photometry of the SNe	28
2.3 Mid-IR Photometry and SED Fitting Results	36
2.4 Additional one-channel mid-IR photometry and upper limits	37
3.1 Near-infrared photometry	63
3.2 Properties of SNe II-P used to compare with SN 2017eaw	70
4.1 IR photometry of SN 2014C	95
4.2 Log of spectroscopic observations of SN 2014C	97
4.3 Luminosity, temperature, and mass of dust in the warm component of SN 2014C, assuming 38% silicate	105
5.1 Specifications of WIRC in different modes.	124
7.1 Supernovae observed with WIRC+Pol	165

Chapter 1

INTRODUCTION

Massive stars with mass greater than $8M_{\odot}$ are the major actors of the Universe. In life, they produce high-energy ultraviolet photons capable of ionizing gas in the surrounding medium, creating bright HII regions that can be seen millions of parsecs away. They launch strong stellar winds akin to our Sun but orders of magnitude greater in velocity and mass-loss rate, sculpting bubbles and voids into their birth nebulae. One of the most spectacular examples of a young massive-star environment is the famous Orion nebula complex wherein a cluster of massive stars called the Trapezium blows an enormous bubble into their natal cloud while illuminating the whole structure with their ionizing photons.

Massive stars live eventful albeit short lives; in death, their effects on the surroundings only multiply. Their large mass yields conditions in the core that can burn through nuclear fusion fuel quickly, turning hydrogen to helium to carbon to oxygen to neon to silicon and finally to iron. A few days after silicon burning commenced, the mass of the iron core reaches the critical mass of $1.4 M_{\odot}$, the Chandrasekhar mass. The core becomes unstable due to electron capture and photodissociation, both of which remove pressure support of the core, leading to a gravitational collapse. The exact physics of this moment is an active area of theoretical research, but from observations we know that the sudden halt of the core collapse (due to nuclear strong force when the core reaches nuclear density) launches a shock wave that, with neutrino heating, propagates outward disrupting the entire star. The total gravitational energy change in the collapse of the degenerate iron core from the initial size of one earth radius to a proto-neutron star with 10 km radius is

$$\Delta E_{\text{grav}} = \frac{G(1.4 M_{\odot})^2}{R_{\oplus}} - \frac{G(1.4 M_{\odot})^2}{10 \text{ km}} = -5 \times 10^{53} \text{ erg} \quad (1.1)$$

Most of this energy is carried away by neutrinos formed in the neutronization reaction in which proton and electron combine to produce neutron and electron neutrino. About 1% of the total energy (10^{51} erg) is imparted into the gas as kinetic energy due to the nuclear weak coupling between the neutrinos streaming out and the gas of the star. It is this kinetic energy that, in aggregate over the dynamical timescale of a galaxy, drives the gas dynamics in the host galaxy. The ejecta of

the SN return metal-rich nucleosynthetic materials, created both throughout the evolution of the progenitor star and during the final explosion, into the interstellar medium (ISM), ready to form the next generation of stars.

We would not be able to witness the spectacle of the core collapse if it were not for the 1% of the kinetic energy— 10^{-4} of the total energy—that is emitted in light. The resulting firework known as core-collapse supernova (CCSN) is among the most luminous explosions in the Universe, often at a comparable luminosity as the $\sim 10^{11}$ other stars in the host galaxy combined. It is these electromagnetic radiations, especially in the visible spectrum between $0.3\text{--}1\ \mu\text{m}$, that tell us most of what we know today about CCSNe.

The great luminosity of SNe creates a spectacular cosmic firework when one happens within our own Galaxy: a bright source visible during the day lasting for several weeks or months. A few SNe have been observed throughout human history from the SN of 1054 whose remnant is known today as the Crab Nebula to the most recent SNe 1572 and 1604 (Tycho and Kepler SNe) observed predominantly in Europe. Their origin remained elusive until Walter Baade and Fritz Zwicky proposed their connection with the death of a massive star forming a neutron star in 1934 (Baade and Zwicky, 1934). We now know that an explosion of a white dwarf can also produce a transient with 10^{51} erg of kinetic energy called Type Ia SN (Tycho's SN 1572 was Type Ia). This work pays most attention to the core-collapse variant. Since then, thousands of SNe have been discovered and observed especially with the advent of optical searches for transient events from the earlier galaxy-targeted searches such as Lick Observatory Supernova Search (Filippenko et al., 2001) and Carnegie Supernova Project (Hamuy et al., 2006) to the later wide-field all-sky searches like the Palomar Transient Factory (PTF; Law et al., 2009) and its successor Zwicky Transient Facility (ZTF; Bellm et al., 2019), the Panoramic Survey Telescope & Rapid Response System (Pan-STARRS; Chambers et al., 2016), All-Sky Automated Survey for Supernovae (ASAS-SN; Shappee et al., 2014), and SN program of the Asteroid Terrestrial-impact Last Alert System (ATLAS; Tonry et al., 2018).

As one may expect for an explosion of a $>8M_{\odot}$ star with several chemically stratified shells, there are many facets of this phenomenon that we do not understand. Decades of observations and explorations with surveys listed above have provided us with an increasingly detailed account of what happens in CCSNe, yet many more unanswered questions arise. I begin this thesis by delving into a subset of them before discussing how observations in the infrared (IR) wavebands can provide clues to resolving these

problems.

1.1 Different Flavors of Core-Collapse Supernovae

CCSNe come in several spectroscopic and photometric flavors, along with rare events that defy classification. See Filippenko (1997) for detailed discussions of SN classification and Fig. 1.1 for examples of spectra from different types in the optical and near-IR. The diversity in the photometric and spectroscopic properties of CCSNe arises from the varying amounts of hydrogen left in the envelope of the progenitor star at the time of core collapse. Stars with most of the hydrogen envelope intact explode as a Type II-P SN: Type II indicates the presence of hydrogen while P refers to the characteristic 100-day plateau in the light curve arising from the extended envelope (See Fig. 3.3 for an example of SN II-P light curve showing 100-d plateau). The progenitor to SNe II-P has been identified as red supergiant (RSG) from several nearby SNe II-P for which the progenitor star is identified in pre-explosion images and confirmed to have disappeared in images taken after the SN faded (Smartt, 2009; Van Dyk et al., 2017, and references therein). In some H-rich SNe, the plateau is either shortened or absent, and they are classified as Type II-L, where L stands for the linear decline in the magnitude of the SN. It is still debated whether this is due to some degree of envelope stripping, CSM interactions, or other contributing factors (see, e.g., Moriya et al., 2016; Morozova et al., 2017, 2018). Also debated is whether there exists a smooth continuum between the II-P and II-L classification (e.g., Anderson et al., 2014), or that they come from two distinct progenitor populations (Arcavi et al., 2012).

Progenitor stars with most or all hydrogen envelope removed before core collapse produce stripped-envelope (SE) SNe. If some hydrogen remains in the envelope, hydrogen features appear in early spectra and disappear post-peak-light, and the SN is classified as the transitional Type IIb. With more envelope stripping, Type Ib SNe show no signal of hydrogen while Type Ic show no helium. The direct progenitor identifications of SESNe are rare; a handful of SNe IIb (e.g., SNe 1993J, Fox et al., 2014, and referenced therein; 2001ig, Ryder et al., 2018; 2008ax, Folatelli et al., 2015; and 2011dh, Folatelli et al., 2014; Maund et al., 2011; Van Dyk et al., 2011), one SN Ib (iPTF13bvn; Cao et al., 2013), and possibly one SN Ic (SN 2017ein; Kilpatrick et al., 2018; Van Dyk et al., 2018) have the progenitor star and/or surviving binary companion directly identified.

In addition to this sequence of SN types as a function of envelope stripping, there

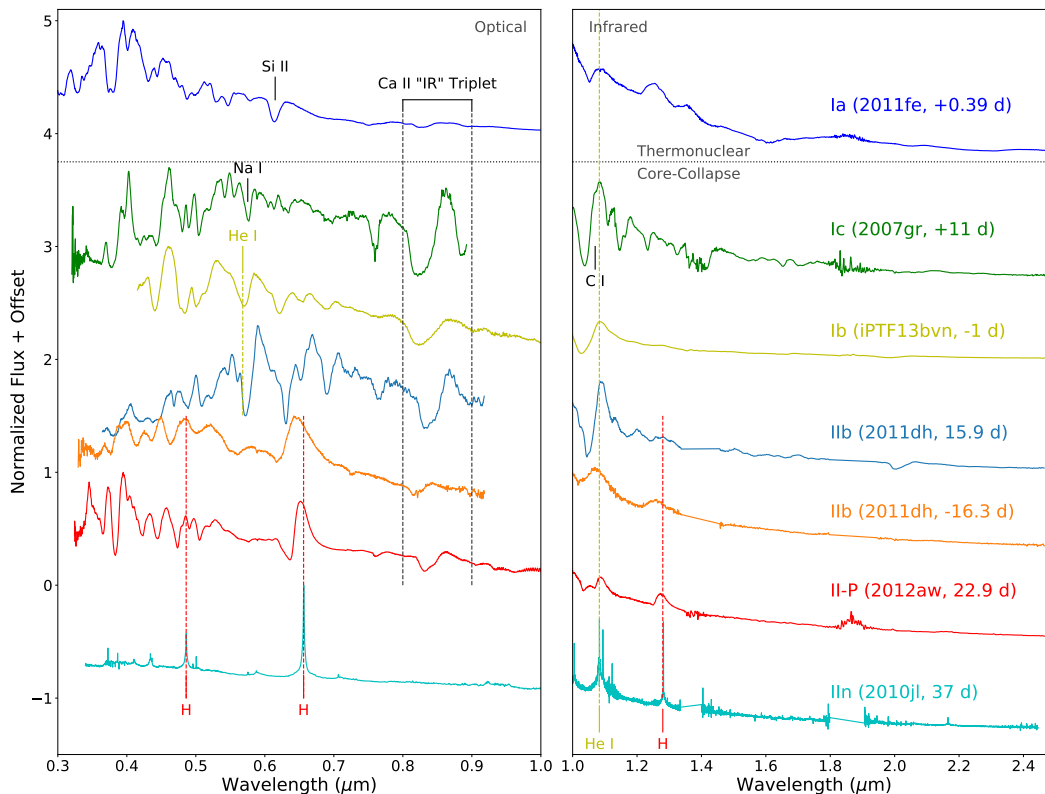


Figure 1.1: Optical (left) and near-IR (right) spectra of supernovae of different subtypes near peak light. Optical and near-IR spectra of the same SN are normalized differently, so they do not appear to match at $1 \mu\text{m}$. The spectral type, specific SN displayed here, and the epoch are shown alongside the spectrum. All epochs are with respect to the maximum light, except for SNe II-P and IIc where the epochs are since the explosion. Top part of the figure shows thermonuclear Type Ia SN 2011fe (Hsiao et al., 2013; Mazzali et al., 2014), along with the location of its characteristic Si II absorption. The bottom part of the figure shows core-collapse SNe with the decreasing degree of envelope stripping from top to bottom (excluding Type IIc). The corresponding subtypes, ordered from more stripped to less stripped, are: Type Ic (SN 2007gr; Valenti et al., 2008) shows neither hydrogen nor helium in the optical. The feature around $1.07 \mu\text{m}$ is highly disputed whether it is He I $1.083 \mu\text{m}$ or C I $1.06 \mu\text{m}$ (or both). Type Ib (iPTF13bvn; Cao et al., 2013) shows helium absorptions, but no hydrogen features. Type IIb (SN 2011dh; Ergon et al., 2015) is a transitional object from H-rich at early time to H-poor at late time. Spectra at 16.3 d before peak and 15.9 d after peak brightness are shown to demonstrate this transition. Note the disappearance of $H\alpha$. The least stripped CCSNe of Type II-P (SN 2012aw; Dall’Ora et al., 2014) shows strong hydrogen features at all epochs. Lastly, at the bottom of this figure we show a spectrum of the strongly interacting SN of Type IIc (SN 2010jl; Borish et al., 2015), with characteristic narrow hydrogen lines with pronounced electron scattering wing.

are a few rarer spectral types that complicate this picture. There are peculiar Type II explosions that come from a more compact ($R \sim 50R_\odot$) blue supergiant (BSG) instead of the typical Type II-P's RSG progenitor ($R \sim 500R_\odot$). The most nearby CCSN in modern time, SN 1987A, happens to be of this type, so we call these events SN 1987A-like explosions. Lastly, there are CCSNe that show signatures of interactions between the SN shock and the circumstellar medium (CSM) ejected from the progenitor star shortly before the explosion. In CCSNe with strong interactions, electrons in the ionized CSM get accelerated to relativistic velocities and emit strongly in the X-ray and radio wavebands. High-energy photons from the shock front propagate out and ionize the slowly moving unshocked gas in the CSM, which produces emission lines with line width of $100\text{--}1000 \text{ km s}^{-1}$, narrow compared to the typical line width of $\sim 10,000 \text{ km s}^{-1}$ from the ejecta. These events are classified as Type Ibn or II n (n for narrow), if the narrow lines are helium or hydrogen, respectively.

The observed diversity of CCSN subtypes and their rates present a challenge to the traditional single massive-star evolution paradigm as the mass-loss rates required by observations are much higher than expected in single stars. For single stars, mass loss is luminosity driven, and thus its rate is set by the mass of the star. A commonly used single star mass-loss rate prescription is that by Nieuwenhuijzen and de Jager (1990):

$$-\dot{M} = 9.63 \times 10^{-15} M_\odot \text{ yr}^{-1} \left(\frac{L}{L_\odot} \right)^{1.42} \left(\frac{M}{M_\odot} \right)^{0.16} \left(\frac{R}{R_\odot} \right)^{0.81} \quad (1.2)$$

giving a mass-loss rate of about $10^{-5} M_\odot \text{ yr}^{-1}$ for a typical RSG ($15 M_\odot$, $10^5 L_\odot$, $1000 R_\odot$). In order for the mass-loss rate to be large enough to remove a significant portion of the hydrogen envelope and create progenitors to SESNe, the initial mass has to be greater than about $30M_\odot$ (Smith, 2014, and references therein). In this picture, SESNe with larger degree of envelope stripping must come from more massive stars, and are consequently rarer. If we assume a Salpeter initial mass function (IMF), $\xi \propto m^{-\alpha}$ with $\alpha = 2.35$, and that the minimum mass over which stars are stripped by their own wind and explode as SESNe is $M_{\text{SESNe}} = 30M_\odot$ (Woosley et al., 2002), we get that SESNe should account for

$$\frac{\int_{M_{\text{SESNe}}}^{\infty} m^{-2.35} dm}{\int_{8M_\odot}^{\infty} m^{-2.35} dm} = \left(\frac{30}{8} \right)^{-2.35+1} = 0.17 \quad (1.3)$$

of all CCSNe. In reality, SESNe are quite common, making up to 1/3 of all CCSNe, requiring an alternative formation channel (Smith et al., 2011b). Light-

curve modeling of SESNe also shows that the ejecta mass of these events is typically $2 M_{\odot}$, much too small for a star with $>30 M_{\odot}$ initial mass (Drout et al., 2011; Lyman et al., 2016). In addition to the failure to explain the observed fraction and the ejecta mass of SESNe, the single star scenario cannot explain the existence of dense CSM around SNe IIn, which requires extreme mass-loss events, nor can it explain how BSGs, which are supposed to still be on the main sequence burning hydrogen in their core, explode as SN 1987A-like events. All these problems require a paradigm shift in the understanding of massive star evolution.

1.2 Binary Interaction and Mass Loss in Massive Stars

A significant fraction of massive stars that produce CCSNe live in binary or multiple star system (Sana et al., 2012). The degree of interactions between the two binary companions is determined by the mass fraction between the two components and the separation between them. Sana et al. (2012) demonstrate from high-resolution spectroscopy of massive stars in open clusters that only 29% of massive binary systems have wide enough separation such that the two components live effectively like single stars. In the rest of the binary star systems, the binary components exchange mass and angular momentum, fundamentally altering their evolutionary path. This finding has profound effects on everything assuming single stellar evolution from population synthesis (Eldridge et al., 2017) to the subtypes of CCSNe (e.g., Eldridge et al., 2018; Smith, 2014; Smith et al., 2011b; Zapartas et al., 2019).

We now know with an increasing degree of certainty that binary mass transfer affects outcome of stellar evolution for massive stars (see review by Smith, 2014). In this picture, SESNe progenitor systems are formed when the primary component evolves out of the main sequence and overflows its Roche lobe, transferring its hydrogen envelope to the secondary star. In contrast to the single star evolution picture, the star does not need to have a high mass to be able to shed its hydrogen envelope. This explains well the frequency of SESNe in comparison to all CCSNe, and the fact that most of them have low ejecta mass. Further, the surviving binary companions of a few SNe I Ib have been identified (Folatelli et al., 2014; Fox et al., 2014). Rarer subtypes like SN 1987A-like events are likely products of binary mergers, a scenario that explains both the BSG progenitor (McCray, 1997) and the iconic triple-ring system seen in *HST* images of the SN (Morris and Podsiadlowski, 2007, and references therein).

Yet, there are still many unanswered questions. For instance, we do not know how

conservative the mass transfer process is and how much mass is not accreted to the secondary component and lost into the CSM. We do not know if there are typical timescales at which mass transfer happens before core collapse. Still, provided with a well-observed massive stellar system, we do not know how the binary components will exchange mass and what kind of SN they will produce. Theoretical modeling of binary mass transfer is difficult because it happens on a long timescale compared with the dynamical time of each star. As a result, an accurate model of the mass transfer process will be computationally very expensive. Therefore, more observations are needed to answer these questions, especially at a year or more after the explosion as the SN shock propagates out and interacts with material shed long before core collapse.

1.3 Asymmetric Explosion Mechanism and the Shape of the Ejecta

A major missing piece in the understanding of CCSNe is the exact physics of the core-collapse process itself. It has been a longstanding issue that 1D hydrodynamical models cannot produce SN explosions. When core collapse is halted by the strong nuclear force, the initial bounce creates a shock propagating outward against infalling materials. In 1D simulations, this shock stagnates and fails to grow into an explosion of the star, even after accounting for the energy deposition from escaping neutrinos from the newly formed proto-neutron star.

The breakthrough came when multi-dimensional effects like turbulence are possible to model in modern 2D and 3D simulations, enabled by the increasing computing power in the past decades. See a recent review by Janka (2017) on the current progress in core-collapse simulations. See also, e.g., Burrows et al. (2019) for recent results from low mass (9–13 M_{\odot}) progenitor models. All current 3D models show that CCSNe are a fundamentally asymmetric phenomenon; spherical symmetry should not be assumed.

The asymmetry in the core-collapse mechanism creates several observable effects. The turbulent shock mixes radioactive nickel from where it is synthesized out to the outer ejecta, producing early heating and high-energy emission detected in SN 1987A (Arnett et al., 1989). One piece of geometric evidence for asymmetry in core collapse is the asymmetric shape of Galactic CCSNe remnants like the Crab Nebula and Cassiopeia A; however, their shape is affected by interactions with the ISM after thousands of years post-explosion. Since SN remnants do not last long before they disperse, there are a limited number of nearby objects for which resolved

imaging is possible. Until the next CCSN in the Milky Way or in the Magellanic Clouds (like SN 1987A), the best way to constrain the ejecta shape in a large number of SNe is by spectropolarimetry.

1.4 Polarimetry: How to Measure the Shape of Unresolvable Sources

Polarization is a fundamental property of light, along with energy and intensity. For a classical electromagnetic wave, energy corresponds to wavelength, intensity to amplitude, and polarization to the plane of oscillation of the electric field vector. Incoherent emission processes, like thermal emission, produce randomly polarized light that lacks a common plane of polarization. Unpolarized light can become partially or fully polarized when it changes the direction of propagation due to reflection or scattering. See Fig. 1.2 (top) for a schematic of how light gets polarized in a scattering event. Polarization in SN ejecta (and many other astrophysical sources) arises in this manner: unpolarized emission from a photosphere gets polarized by electron (or gas and dust) scattering in a surrounding envelope. If the scattering envelope is symmetric from observer's view, polarization vectors sum to zero, leaving no net polarization from the source if it is observed unresolved (Fig. 1.2, bottom). Hence, net polarization from an unresolved source indicates an underlying departure from symmetry. The angle of polarization can indicate the dominant orientation of the scattering atmosphere. As such, polarimetry *coupled with adequate modeling* is a powerful tool to discern the shape of point sources that are not spatially resolved.

Polarization is a powerful but underutilized tool in the astronomers' toolkit. It has a wide range of applications from identifying the composition of the Venusian atmosphere (Hansen and Hovenier, 1974), to providing a framework for the unified model of active galactic nuclei (Antonucci and Miller, 1985), and to probe exoplanets atmosphere in polarized reflected light (Wiktorowicz et al., 2015). However, polarization can be a difficult tool to master. Astrophysical sources are often polarized to only 1% level or less, requiring a large number of photons to conduct precise measurements, and extensive characterization of instrumental systematics for accuracy. The signal-to-noise ratio (S/N) of a polarimetric measurement is $S/N_{\text{pol}} = p \times S/N_{\text{flux}}$. To measure a source to 0.1%, 1σ , precision in polarization, one needs $S/N_{\text{flux}} = 1000$, which requires 10^6 photons to achieve for bright, photon noise-limited sources. For spectropolarimetry, one needs 10^6 photons *per spectral channel*; a tall order especially for faint sources.

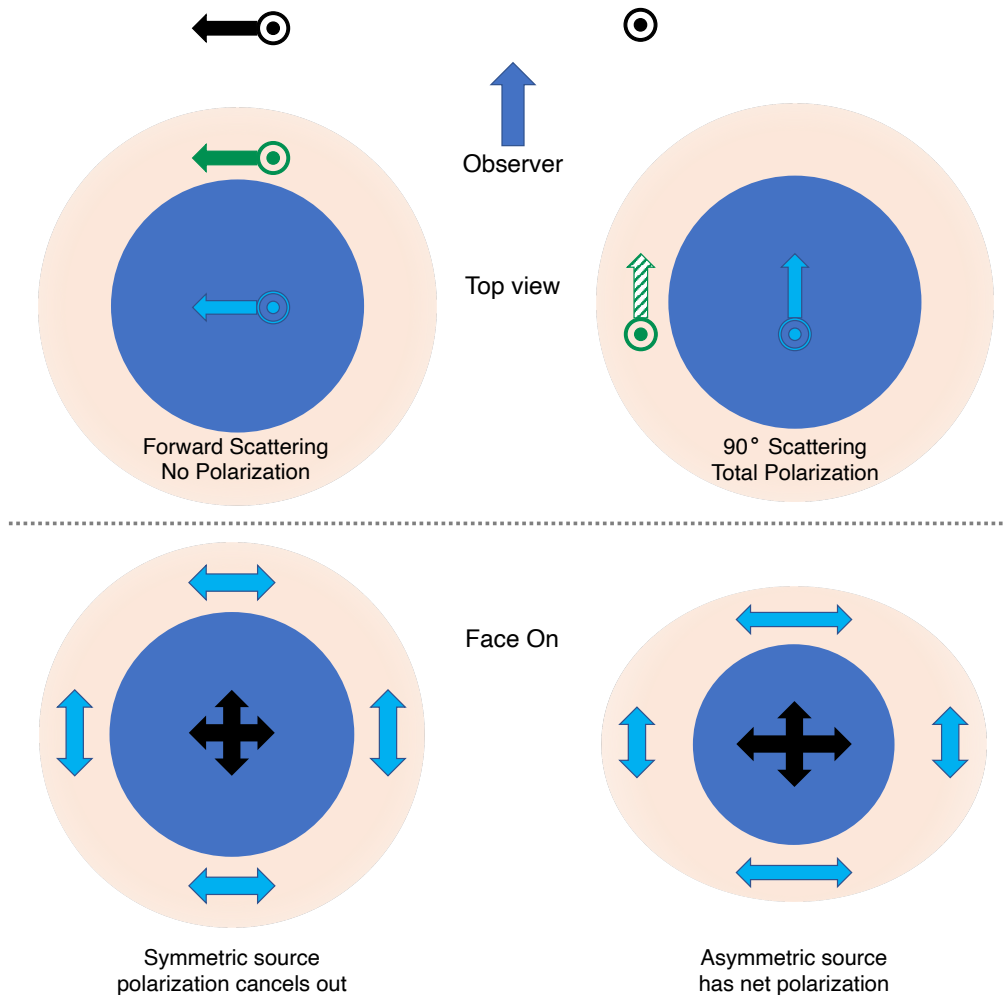


Figure 1.2: Top: top-down view of two schematics of an emitting photosphere embedded in a scattering envelope. The left (right) panel shows forward scattering (90° scattering). The three arrows in each panel notate the electric field orientation of the photon. The photon is emitted unpolarized with electric field components orthogonal to the direction of propagation (blue). In the forward scattering case, the photon travels upward, getting forward scattered in the atmosphere with no direction change (green). Both electric field components survive and the photon travels to the observer unpolarized (black). In the 90° scattering, the photon travels to the left of the figure and get scattered towards the observer. The electric field component along the new direction of propagation is removed (shaded green), and the photon propagates to the observer polarized in the plane orthogonal to the scattering. Scattering at smaller angle imparts partial polarization. Bottom: face-on view, but now the left panel shows a symmetric source while the right shows an asymmetric one. The blue arrows indicate the plane of polarization of the photon scattered from that part of the atmosphere. The black arrows in the middle indicate the net polarization observed by a faraway observer who cannot spatially resolve the source. For the symmetric source, all polarization vectors cancel out and light is unpolarized. However, a departure from symmetry will result in an incomplete cancellation of the polarization vector, leaving some net polarization from the unresolved source.

Supernova Spectropolarimetry

Despite its difficulties, the power of spectropolarimetry to measure the shape of SN ejecta has been recognized early by Shapiro and Sutherland (1982). The first SN for which extensive and reliable optical (spectro)polarimetry is SN 1987A (e.g., Jeffery, 1991). These observations show significant ($\sim 1\%$) polarization at a persistent angle of polarization throughout its evolution, indicative of a common axisymmetry all the way from the exploding core to the outer layer of the star. The polarimetry indicates that the ejecta of SN 1987A are either a prolate spheroid with the axis of symmetry pointing at 14° on-sky or an oblate spheroid pointing at 104° . Late time imaging with the *Hubble Space Telescope* shows that indeed the ejecta are distributed in a prolate spheroid pointing at about 14° on sky, very close to the expectation from early-time polarimetry (Wang et al., 2002).

In the majority of SNe, there is no hope to obtain a spatially resolved image of the ejecta due to their distance and low flux; polarimetry is the only way to provide a measurement of their shape and orientation on-sky. Wang and Wheeler (2008) summarize the results of SN optical spectropolarimetry up until 2008. In brief, CCSNe of all subtypes have been observed spectropolarimetrically and they all show varying degree of polarization. The most common SNe II-P show small ($\sim 0.1\%$) polarization during the plateau phase as the ejecta are optically thick and the asymmetric interior is not yet visible (but see Dessart and Hillier, 2011 on how radiative transfer at early time can yield no polarization even for asymmetric outer part of the ejecta.) The polarization peaks at ($\sim 1\%$) at the end of the plateau phase as the asymmetric core becomes visible, then decays as $p \propto t^{-2}$ due to the decreasing electron scattering in the expanding ejecta (e.g., Leonard et al., 2006; Nagao et al., 2019). In SESNe, the degree of polarization can be higher and the polarization peaks much sooner after the peak light due to the lack of an extensive hydrogen envelope obscuring the asymmetric core (e.g., Tanaka et al., 2008, 2009). In interacting SNe IIn, polarization measurements probe the combination of scattering in the SN ejecta and the interaction-ionized CSM. In this scenario, the interpretation is complicated and requires careful modeling (e.g., Bilinski et al., 2018; Mauerhan et al., 2014; Reilly et al., 2017).

Thus far, all spectropolarimetric observations of SNe—and almost all broadband polarimetry except for a few measurements of SN 1987A in the near-IR—are performed in the optical. In the optical, the sky background is dark and the instrumentation is more advanced, making the titan task of collecting 10^6 photons more

manageable. There are also several prominent spectral lines in the optical, allowing optical spectropolarimetry to probe the inhomogeneous distribution of nucleosynthetic products in SN ejecta. However, optical polarimetry has difficulty providing an accurate measure of the continuum polarization that probes the global shape of the ejecta. First, the plenitude of spectral lines leaves little room in wavelength space to see the continuum directly—commonly a small window redward of the $H\alpha$ line is used for this purpose. Second and more importantly, optical polarization can be severely contaminated by dust, both in the CSM around the SN and in the ISM in the host galaxy and in the Milky Way along the line of sight (interstellar polarization; ISP). The ISP is difficult to measure and remove, and can affect the polarimetric analysis significantly (see, e.g., Reilly et al., 2017, vs. Mauerhan et al., 2014). The effects of CSM dust are even more difficult to characterize because it cannot be estimated by observing other sources in similar line of sight. CSM dust polarization can affect not just continuum polarization (Nagao et al., 2017), but also the line polarization because of its proximity to the SN (Wang and Wheeler, 1996). I will review how IR spectropolarimetry can resolve these issues in a subsection below and discuss why it has not been done until this work.

1.5 Infrared Observations of Supernovae

The IR portion of the electromagnetic continuum refers to the wavelength range of 1–700 μm ; works presented in this thesis focus on the near-IR regime between 1–5 μm along with some mid-IR observations around 10 μm . IR observations are much more difficult to perform than optical observations due to the much (orders of magnitude) brighter background emission and the more limited detector technology. Despite the challenges, IR observations present two major benefits in contrast with optical observations: less contamination from interstellar dust and a direct probe of molecule and dust formation in the SN ejecta.

Less Contamination from Dust Scattering

IR observations are less affected by dust grains in the CSM around the SN and in the ISM of the host galaxy and the Milky Way. Dust grains, especially local to the SN, can produce significant amount of extinction. Indeed, the SN rate is thought to be a lower limit as a significant number of SNe are not observable in the optical due to extinction. The interstellar dust grains have a typical size of $a \sim 0.1 \mu\text{m}$; hence, they act as Rayleigh scatterers ($a \ll \lambda$) in the optical and near-IR and the scattering cross-section varies as λ^{-4} . As a result, the dust scattering cross-section, and thus

the extinction, at $4.5\mu\text{m}$ is a factor of 6000 smaller than that in the optical V band ($0.5\mu\text{m}$).

The only large galaxy-targeted time domain survey in the IR is the SPitzer InfraRed Intensive Transients Survey (SPIRITS), which uses the InfraRed Array Camera (IRAC; Fazio et al., 2004) on board the *Spitzer Space Telescope* (Gehrz et al., 2007; Werner et al., 2004) to image 190 nearby galaxies within 20 Mpc with weeks to months cadences to detect new transient events (Kasliwal et al., 2017). Operating at 3.6 and $4.5\mu\text{m}$ SPIRITS peers through dust and gas in these galaxies, seeing a range of transient phenomena ranging from the classical novae and SNe to a class of eSPecially Red Intermediate-luminosity Transient Events (SPRITEs). Using SPIRITS, Jencson et al. (2019) show that about 40% of CCSNe in typical star-forming galaxies may be missed by optical surveys due to dust extinction. I will discuss SPIRITS and its results on nearby optically-discovered SNe in Chapter 2.

In addition to extinction, ISM dust grains have an oblong shape and are aligned to the large-scale galactic magnetic field. Collectively, they linearly polarize light from background sources, including extragalactic SNe. The empirical relation describing interstellar polarization is derived by Serkowski et al. (1975)

$$p_{\text{ISP}}(\lambda) = p_{\text{max}} \exp \left[-K \ln^2 \left(\frac{\lambda_{\text{max}}}{\lambda} \right) \right] \quad (1.4)$$

where the typical Galactic values are $K = 1.15$, $p_{\text{max}} = 9\% \times E(B - V)$, and $\lambda_{\text{max}} = 0.55\mu\text{m}$ (Voshchinnikov, 2012). This equation shows that the ISP is reduced by 60% in the J band, and 80% in the H band (compared to the optical V band). For CSM dust Nagao et al. (2018) show a similar reduction in its polarization effects in the IR compared to the optical.

Probing Molecule and Dust Evolution in Supernova Ejecta

IR observations are sensitive to several emission processes not present in the optical. Spectral features from ro-vibrational transitions of common molecules such as carbon monoxide (CO) and silicon monoxide (SiO) are all in the IR. CO has the fundamental ($\nu = 1 - 0$) and first overtone ($\nu = 2 - 0$) vibrational transitions at around 4.7 and $2.3\mu\text{m}$, respectively, while the SiO fundamental transitions are around $8\mu\text{m}$. These molecules play crucial roles in the chemical evolution of the SN ejecta. Molecular line emission is a major radiative coolant in the SN ejecta because, similarly to the forbidden lines emission, the optical depth to these photons is low compared to that of recombination photons. Further, the formation of CO

affects the chemical evolution of SN ejecta by depleting the gas of carbon and oxygen in equal amount, leaving the remaining species available to form larger molecules and dust when the temperature drops lower. If the gas has C/O ratio slightly greater than unity, the gas after CO formation is C-rich and will form carbonaceous dust. Conversely, if the C/O ratio is less than one, the gas after CO formation is O-rich and will form SiO and other O-rich molecules, which are precursor species to silicate dust.

Dust grains start to condense out of the gas in the SN ejecta at temperatures around 1000 K, putting their thermal emission peak squarely in the near-IR at $3\ \mu\text{m}$. Further, observations at $10\ \mu\text{m}$ allow us to distinguish silicate dust with strong emission bands around that wavelength from the featureless carbonaceous dust. The dust formation in SNe has been proposed as a major contributor to the observed dust content at high redshift since the universe's age at that epoch is too young for the primary contributor to the dust content in the local universe—*asymptotic giant branch (AGB) stars*—to exist (Gall et al., 2011, and references therein). However, there are still lively debates on whether CCSNe produce more dust than they destroy, or whether dust in CCSNe observed at early time survive long enough to be dispersed into the ISM (e.g., Martínez-González et al., 2019, and references therein). Even though optical observations can reveal evolving effects from the forming dust (increasing reddening of the optical light curve and attenuation in the red wing of optical spectral lines), IR observations directly probe the emission from the dust providing constraints on its mass and composition. These observations of both molecule and dust formations are needed to constrain chemical evolution models in SN ejecta (e.g., Sluder et al., 2018), to understand how SNe chemically contribute to the dust content of the universe. I will discuss the issues of molecule and dust production directly, first in the population of CCSNe in SPIRITS galaxies (Chapters 2) and specifically in the nearby SN 2017eaw (Chapter 3). I then discuss how IR observations of dust can be used to probe the composition and density distribution of CSM around a strongly interacting SN 2014C, including the first evidence for silicate dust feature in an interacting SN (Chapter 4).

1.6 Challenges to Infrared Observations

Bright Sky Emission

Despite their unique utilities in complementing optical observations of SNe, the use of IR observations has been largely limited when I started this thesis work in 2015. The reason for this is that IR observations are generally more challenging and more

telescope time-intensive to perform. The first challenge is that sky background in the IR from the ground is bright, and the longer wavelength you attempt to observe, the brighter it gets. These sky photons flood the detector, forcing us to use shorter exposure time, making the observations less efficient against detector read-out overhead. From 1–2.5 μm (*JHK* bands), the sky background is largely dominated by emission lines from the OH molecules in our atmosphere. This emission is bright and highly variable, both spatially and temporally. For imaging in these wavelengths, it is necessary to take several images with large telescope offset (few arcmin) between them in order to construct a sky background frame to subtract from the data. In spectroscopy, at a modest resolving power of about 2000, the sky lines are resolved and the wavelengths between those lines have relatively low background up to about 2.2 μm , where thermal emission from the sky and the telescope starts to dominate. A challenge in near-IR spectroscopy is that in addition to the sky emission lines, water vapor and molecules in the atmosphere produce significant opacity to IR photons. In fact, the photometric bands in the IR are defined to fall between bands of heavy absorption from molecular water. To correct for the telluric absorption, one must observe a standard star with a known spectral type to measure the telluric absorption spectrum and correct the science observation accordingly. Because of the quickly evolving nature of the sky background, these observations have to be performed as close to the science observations as possible, both in time and in telescope pointing. Telluric standard observations present a large overhead for near-IR spectroscopic observations.

Beyond 2.5 μm , sensitive observations from the ground are almost impossible due to the severe sky background emission, whose thermal component rises exponentially and peaks at around 10 μm . I did obtain such observations for one of the SNe presented in this thesis, and it was challenging. At 4.5 μm , a 100-second exposure image from the 0.85-meter *Spitzer Space Telescope* has 40 times better signal-to-noise ratio than a 1600-second exposure image from the 8.2-meter Gemini Telescope on the ground. As a result, the only aforementioned dust and molecule features accessible from the ground is the CO first overtone feature in the *K* band. Photometry in the same band as the CO fundamental modes (4.7 μm), the SiO fundamental modes (8 μm), and the silicate features (10 μm) are possible for bright sources with a significant telescope time investment; spectroscopy to directly detect the spectral features is impossible in these bands from the ground.

Technological Limitations

In addition to the physical limitations imposed by our atmosphere, IR photons have low energy per photon, requiring different semiconductor technology for their detection. The band gap of silicon semiconductor at 100 K is 1.16 eV, corresponding to a wavelength of $1.07 \mu\text{m}$; thus, IR photons cannot benefit from the silicon semiconductor technology that has advanced greatly in the past few decades due to its commercial applications. IR detectors, instead, are “hybridized” meaning that they use two semiconductors to perform photons detection and read-out. Most commonly, mercury cadmium telluride (HgCdTe) is used to convert IR photons into photoelectrons. The detection layer is connected to a read-out chip made from silicon via indium bumps. This architecture is similar to the Complementary Metal–Oxide–Semiconductor (CMOS) optical detector common in consumer digital camera. IR detectors typically have higher dark currents and read-out noise compared to research-grade optical detectors. Lastly, IR detectors cost orders of magnitude more per pixel compared with science-grade optical detectors, a factor that can impede instrumentation development.

Enabling Technology for Infrared Spectropolarimetry: Polarization Grating

For IR spectropolarimetry presented in the last three chapters of this thesis, there was simply no suitable instrumentation prior to 2017. A classical polarimeter utilizes a birefringent medium like Wollaston prisms to split the two polarization components of the incoming light into two outgoing beams (“ordinary” and “extraordinary”). The light is then passed through a traditional spectral disperser like a grating or a grism to obtain spectral information. This setup needs at least two optical devices and can have low throughput due to the nature of surface relief grating.

A breakthrough came with an optical device called a polarization grating (PG), which allows for a very high throughput spectropolarimeter to be constructed using a single piece of optics to perform both spectral dispersion and polarization beam splitting with an efficiency of $>90\%$. While I will describe the WIRC+Pol instrument that utilizes this technology in details in Chapters 5 and 6, I explain here the basic principle of how a PG works.

In a typical surface relief grating (Fig. 1.3, left), incoming light is transmitted through or reflected off of a surface with pattern at a regular separation d . Light passing through (or reflecting off of) two adjacent slits deflecting by some angle θ picks up a phase difference of $\Delta\phi = (2\pi d \sin \theta)/\lambda$. For these two outgoing beams

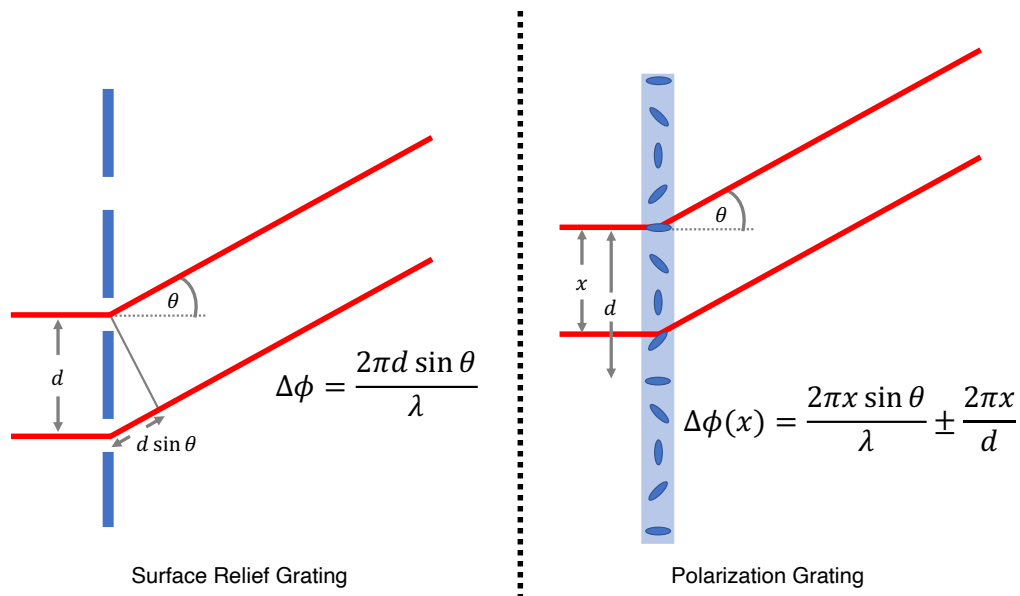


Figure 1.3: Schematics of surface relief grating (left) and PG (right). The grating period for both is d . The phase shift introduced to the two beams separated by d is written as $\Delta\phi$ for both gratings. For the PG, the orientation of the liquid crystals is shown. Over one grating period, the liquid crystals rotate by 180° (π), introducing an extra phase shift of 360° (2π)

to interfere constructively, we need $\Delta\phi = 2\pi m$ where m is an integer. Solving this yields the grating equation

$$\sin \theta = \frac{md}{\lambda} \quad (1.5)$$

where different wavelengths interfere constructively at different angle θ , dispersing a point of light into a spectrum. A major caveat to this design is the efficiency. First, a surface relief grating relies on a regular pattern of transmission (or reflection) and obstruction of light; some incoming light is lost. Second, m from the equation above can be any integer, meaning that a simple grating subdivides the incoming light into several spectra, or “orders”. Typically there is only enough detector real estate to detect a few orders, and others are lost. There are some design improvements that can alleviate the second problem, by using a reflective grating blazed at a specific angle to enhance reflection to a particular order. However, the grating efficiency is only optimized at one wavelength, and falls off quickly away from it.

A PG can solve both of these problems: light gets diffracted only to the three central orders $m = 0, \pm 1$ with no leaks to higher order, and the dispersion efficiency into the $m = \pm 1$ orders can remain $>90\%$ over a wide wavelength range. To demonstrate the fact that PG loses no light to higher order, consider two rays separated by some

distance x smaller than a grating period d diffracting to some angle θ in Fig. 1.3 (right). The phase difference between the two outgoing rays consists of two terms: one from the path length difference like in the case of surface relief grating, but an additional term from liquid crystals in the PG. This additional term in the phase difference is called geometric phase or Pancharatnam's phase (Pancharatnam, 1956), and its sign is positive (negative) for right (left) circular polarization. Thus, the phase shift as a function of x is

$$\Delta\phi(x) = \frac{2\pi x \sin \theta}{\lambda} \pm \frac{2\pi x}{d} \quad (1.6)$$

Because of the continuity in the PG, an angle θ that has constructive interference requires that all rays are in phase regardless of x . The in-phase condition can be written as

$$\phi(x) = \frac{2\pi x \sin \theta}{\lambda} \pm \frac{2\pi x}{d} = 2\pi k \quad (1.7)$$

$$\sin \theta = \frac{k\lambda}{x} \mp \frac{\lambda}{d} \quad (1.8)$$

where k can be any integer. However, if $k \neq 0$, θ is x dependent. Hence, we get that PG creates constructive interference only at

$$\sin \theta = \mp \frac{\lambda}{d} \quad (1.9)$$

or the $m = \pm 1$ orders of an equivalent surface relief grating. Further, the $m = 1$ order is purely left circular polarization and $m = -1$ is right circular polarization. For a more general calculation showing that the $m = 0$ order leak is possible, but there is no leak to $|m| > 1$ orders, see Tervo and Turunen (2000). For a multi-layer construction that produces achromatic PG that operates at near unity efficiency over the entire optical bandpass, see Oh and Escuti (2008). A quarter-wave plate (QWP) can be installed upstream from the PG to make it operate on linear polarization. In summary, PG is an optical device that utilizes liquid-crystal polymer to perform both polarimetric beamsplitting and spectral dispersion with near perfect efficiency over a broad bandpass. Its use in astronomy has been pioneered by Packham et al. (2010) and Millar-Blanchaer et al. (2014). PG is the key technology that enables WIRC+Pol (Chapters 5, 6) and the first spectropolarimetry of SNe in the IR (Chapter 7).

1.7 Thesis Outline

This thesis can be divided into two parts. I start by presenting ground- and space-based IR observations of nearby SNe to probe different aspects of their evolution.

In Chapter 2, I present the systematic study of SNe light curves in the 3.6 and 4.5 μm channels of *Spitzer* as part of SPIRITS. SPIRITS observed sites of 141 SNe of all types in 190 galaxies; for which we detected 8 SNe Ia and 36 CCSNe. Of which, 12 have pre-explosion *Spitzer* images, which allow for accurate photometry. I discuss general properties of light curves of these 12 SNe and identify some outliers with unique IR properties, likely due to CSM interactions. In Chapter 3, I discuss the nearby, typical Type II SN 2017eaw in NGC 6946, showing dust and molecule formation in its ejecta. I show a remarkable similarity in the evolution of the CO line profile in SN 2017eaw to that in SN 1987A at 1 year post-explosion, even though they come from very different progenitor stars (RSG vs BSG), suggesting a common chemical evolution in the ejecta. In Chapter 4, I report results from a five-year long observation campaign of SN 2014C, a peculiar Type Ib SN that interacts strongly with its extended CSM. The interaction was still ongoing by the time that *Spitzer* ceased operation in January 2020, six years after the explosion. SN 2014C is the first SN since SN 1987A to be detected in the mid-IR from the ground at 10 μm , providing a strong evidence for silicate dust, never seen before in an interacting SN. The long-term light curves from *Spitzer* also allow me to fit a CSM interaction light-curve model to show that the outer CSM around SN 2014C has a wind-driven $\rho \propto r^{-2}$ profile with a mass-loss rate and wind velocity comparable to the binary Roche-lobe overflow mass-loss scenario.

The second part of the thesis is dedicated to WIRC+Pol, a low-resolution near-IR spectropolarimeter at Palomar Observatory and its first science results. WIRC+Pol is the first instrument of its kind, employing PG discussed earlier, which allows it to observe sources as faint as $J = 14.5$ to a polarimetric precision of 0.1% in less than two hours, a capability unprecedented in the near-IR. It opens up the possibility of near-IR spectropolarimetry of faint objects like extragalactic SNe. In Chapter 5, I provide a detailed description of WIRC+Pol and its performance in its first iteration as a single-shot spectropolarimeter. I also describe the data reduction pipeline of WIRC+Pol that I developed with Max Millar-Blanchaer. Chapter 6 provides an update to WIRC+Pol's performance after the installation of a half-wave plate (HWP) modulator in March 2019, along with the updated data reduction process for data taken with the HWP. I show that the instrumental polarization can be measured and removed down to better than 0.03%. In Chapter 7, I present the first scientific results from WIRC+Pol: observations of four nearby SNe, two core collapse and two Type Ia.

Finally I conclude in Chapter 8 and briefly summarize the bright outlook of SNe observations in the IR, both with large-sample IR photometric/spectroscopic surveys and a polarimetric survey of a number of nearby CCSNe with contemporaneous optical and IR coverage in several epochs. The thesis closes with an outlook to what may be possible in the era of *James Webb Space Telescope* where mid-IR spectroscopy of a statistically significant number of nearby SNe can be obtained.

Chapter 2

A SYSTEMATIC STUDY OF MID-INFRARED EMISSION FROM
CORE-COLLAPSE SUPERNOVAE WITH SPIRITS

Tinyanont, S. et al. (Dec. 2016). “A Systematic Study of Mid-infrared Emission from Core-collapse Supernovae with SPIRITS”. In: *ApJ* 833.2, 231. DOI: 10.3847/1538-4357/833/2/231. arXiv: 1601.03440 [astro-ph.SR].

Samaporn Tinyanont¹ Mansi M. Kasliwal¹ Ori D. Fox² Ryan Lau^{1,3} Nathan Smith⁴
Robert Williams² Jacob Jencson¹ Daniel Perley⁵ Devin Dykhoff⁶ Robert Gehrz⁶
Joel Johansson⁷ Schuyler D. Van Dyk⁸ Frank Masci⁸ Ann Marie Cody⁹ Thomas
Prince¹

¹Division of Physics, Mathematics and Astronomy, California Institute of Technology, Pasadena, CA 91125, USA

²Space Telescope Science Institute, 3700 San Martin Drive, Baltimore, MD 21218, USA

³Jet Propulsion Laboratory, California Institute of Technology, 4800 Oak Grove Dr., Pasadena, CA 91109, USA

⁴Steward Observatory, University of Arizona, Tucson, AZ 85721, USA

⁵Dark Cosmology Centre, Niels Bohr Institute, University of Copenhagen, Juliane Maries Vej 30, 2100 København Ø, Denmark

⁶Minnesota Institute for Astrophysics, School of Physics and Astronomy, University of Minnesota, 116 Church Street, S. E., Minneapolis, MN 55455, USA

⁷Benozio Center for Astrophysics, Weizmann Institute of Science, 76100 Rehovot, Israel

⁸Infrared Processing and Analysis Center, California Institute of Technology, M/S 100-22, Pasadena, CA 91125, USA

⁹NASA Ames Research Center, Moffett Field, CA 94035, USA

Abstract

We present a systematic study of mid-infrared emission from 141 nearby supernovae observed with *Spitzer*/IRAC as part of the ongoing SPIRITS survey. We detect 8 Type Ia and 36 core-collapse SNe. All Type Ia/Ibc SNe become undetectable within 3 years of explosion whereas $22 \pm 11\%$ of Type II SNe continue to be detected. Five Type II SNe are detected even two decades after discovery (SN 1974E, 1979C, 1980K, 1986J, and 1993J). Warm dust luminosity, temperature, and a lower limit on mass are obtained by fitting the two IRAC bands, assuming an optically thin dust shell. We derive warm dust masses between 10^{-6} and $10^{-2} M_{\odot}$ and dust color temperatures between 200 and 1280 K. This observed warm dust could be pre-existing or newly created, but in either case represents a lower limit to the

dust mass because cooler dust may be present. We present three case studies of extreme SNe. SN 2011ja (II-P) was over-luminous ($[4.5] = -15.6$ mag) at 900 days post-explosion with increasing hot dust mass, suggesting either an episode of dust formation or intensifying CSM interactions heating up pre-existing dust. SN 2014bi (II-P) showed a factor of 10 decrease in dust mass over one month suggesting either dust destruction or reduced dust heating. The IR luminosity of SN 2014C (Ib) stays constant over 800 days, possibly due to strong CSM interaction with H-rich shell, which is rare among stripped-envelope SNe. The observations suggest that this CSM shell originated from an LBV-like eruption roughly 100 years pre-explosion. The observed diversity demonstrates the power of mid-IR observations of a large sample of SNe.

2.1 Introduction

The mid-infrared (mid-IR) evolution of core-collapse supernovae (CCSNe) has been studied in some events, but studies of a large sample containing multiple different SN subtypes have only become possible recently with multi-year observations by the *Spitzer* Space Telescope. A comprehensive and systematic study of a large sample of CCSNe across all types is essential to delineate the temporal evolution of a massive star after its explosive death. Mid-IR studies complement and expand on the body of knowledge obtained from extensive studies in optical and near-IR (see, e.g., Bianco et al., 2014; Gerardy et al., 2002; Wheeler et al., 2015). One of the advantages of the mid-IR is that it is virtually free of dust extinction. Jencson et al. (2017) recently demonstrated that *Spitzer* can detect a SN entirely missed by optical surveys due to heavy host galaxy extinction. The mid-IR also traces emission from warm dust in the ejecta of a CCSN or in the circumstellar material (CSM) that is related to the progenitor star. CCSNe have long been proposed as major possible sources of dust production, especially in high-redshift galaxies where other possible dust factories (e.g., stellar winds of AGB stars) could not be in operation either because those galaxies were too young to form AGB stars or the stellar metallicity in that epoch was inadequate to form dust particles (Cherchneff, 2014; Gall et al., 2011, and references therein). Theoretical models predict the mass of dust produced in CCSNe to be around 0.1 to 1 M_{\odot} , which is adequate for CCSNe to contribute significantly to the observed dust content in the early universe (Nozawa et al., 2003, 2008). Dust characteristics of SNe, such as grain size, mass, and temperature can be quantified by analyzing the Spectral Energy Distribution (SED) and the light curve of a SN (see, for example, Fox et al., 2010, 2011, 2013; Szalai and Vinkó, 2013).

Gehrz and Ney (1990) described three distinct signatures of dust formation that were observed in SN 1987A and that are expected to be generally observable in other SNe that form dust. (1) Optical spectral lines are asymmetrically blueshifted because the newly formed dust absorbs light coming from the receding side of the ejecta. (2) The decline rate of the optical light curves increases because the new dust causes more extinction in the UBV wavebands. (3) The emission in the mid-IR brightens due to thermal emission from warm dust, making it a more dominant component than the optical and near-IR.

A number of SNe have been identified as dust producers through observations in the mid-IR. For example, Helou et al. (2013) and Ergon et al. (2015) conducted mid-IR studies of the Type IIb SN 2011dh in Messier 51 (see Filippenko, 1997 for more information on supernova classification.) The time evolution of its SED showed that the mid-IR emission became relatively brighter than optical emission at late times. The light curve also showed excess mid-IR emission that could not be explained by an IR echo alone, indicating an additional dust heating mechanism or the formation of new dust. Meikle et al. (2011) and Szalai et al. (2011) analyzed the Type II-P SN 2004dj and found a significant rebrightening ~ 400 days post-explosion. Similarly, Fabbri et al. (2011) studied the Type II-P SN 2004et and observed rebrightening at 1000 days after the explosion. In both cases, they inferred new dust formation by observing red-wing attenuation in optical spectral lines and the sharp rate of decline in the optical light curves. A mid-IR population study of 12 Type II-P SNe by Szalai and Vinkó (2013) found warm dust emission with an inferred dust mass of $\sim 10^{-3} M_{\odot}$. Fox et al. (2011, 2013) conducted a survey on all known 68 Type IIn events. These are CCSNe with narrow emission lines that are indicators of circumstellar interactions that either produce new dust or heat up pre-existing dust. They detected late-time emission from 10 targets with an inferred dust mass of up to $10^{-2} M_{\odot}$. They concluded that most of the warm emitting dust was pre-existing. In addition to Type IIn SNe whose CSM interactions were discovered early on, recent late-time observations reveal that many SNe interact with the CSM later in their evolution, providing additional channels for dust production. Andrews et al. (2016) presented spectroscopic evidence for CSM interactions in the Type II-P SN 2011ja at 64–84 days post-explosion accompanied by an episode of dust production between the forward and the reverse shocks. These interactions with dust production have also been observed in a small number of Type Ibc SNe, such as SN 2006jc (see, e.g., Foley et al., 2007; Mattila et al., 2008; Sakon et al., 2009; Smith et al., 2008, and references therein.)

The mass of newly formed dust observed in a number of CCSNe is significantly lower than dust masses predicted by theoretical models, falling between 10^{-3} and $10^{-4} M_{\odot}$ per event instead of 0.1 and $1 M_{\odot}$ (see, in addition, Andrews et al., 2010; Gall et al., 2014). It has been shown, however, that the large amount of dust associated with CCSNe is too cold to be detected in the mid-IR. Recent studies of SN 1987A and other supernova remnants (SNRs) reveal a large amount of dust emitting in the far-IR and submillimeter wavelengths. Matsuura et al. (2015) used the *Herschel Space Observatory* (Pilbratt, 2003) to observe SN 1987A and deduced, depending on dust composition, 0.5–0.8 M_{\odot} of cold dust in the remnant. Indebetouw et al. (2014) used the Atacama Large Millimeter/Submillimeter Array (ALMA; Brown et al., 2004) to observe SN 1987A at high spatial resolution and confirmed that $> 0.2 M_{\odot}$ of dust was formed in the inner ejecta and was neither heated by CSM interactions as suggested by some authors (e.g., Bouchet and Danziger, 2014) nor pre-existing. This dust mass is consistent, but orders of magnitude higher than the $\sim 10^{-4} M_{\odot}$ lower limit derived by Wooden et al. (1993) two years post-explosion. This suggests that bulk of the dust condensed late in the evolution of this particular SN. Alternatively, Dwek and Arendt (2015) suggested that the dust was hidden in the optically thick part of the ejecta at early times ($< 1000d$), and hence, not observed until later. The presence of about 0.1 M_{\odot} of cold dust was also suggested by far-infrared and submillimeter observations of nearby SNRs, Cassiopeia A (Barlow et al., 2010) and the Crab Nebula (Gomez et al., 2012). Recently, Lau et al. (2015) have reported that 0.02 M_{\odot} of ejecta-formed dust has survived in the 10,000 yr-old SNR Sgr A East. These results demonstrate that a large fraction of the dust formed in the inner core of a SN can survive the reverse shocks and later be dispersed into the ISM. A large fraction of the newly formed dust appears to emit at longer wavelengths, however, observations in two IRAC bands of warm *Spitzer* are sensitive to only a small, relatively hot fraction of that dust. Nevertheless, these observations are still powerful tools for identifying SNe with dust formation or CSM interactions, which heat pre-existing dust to high temperatures.

This work seeks to study a comprehensive sample of different types of CCSNe observed with *Spitzer* at a variety of epochs after explosion in order to construct an overview of the mid-IR time evolution of these events. This work complements the mid-IR light-curve templates that have already been compiled for Type Ia SNe (Johansson et al., 2017). The collage of light curves from a number of well-observed SNe Ia shows that these events are homogeneous in their time evolution. In this paper, we compile a light-curve collage for core-collapse supernovae in order to

identify the typical time evolution of these events and to potentially uncover some unusual SNe. A simple one-component, graphite dust model is fitted to the SED to extract the luminosity, temperature, and mass of warm dust emitting in the mid-IR. We emphasize here that our observations are only sensitive to warm dust with a temperature of more than a few hundred Kelvin. Many SNe are observed at several epochs, allowing us to trace the time evolution of dust parameters. In §2.2, we discuss the SPIRITS survey in more detail along with the SNe sample in galaxies covered by SPIRITS. We present the demographics of the SNe and light-curve collages for Type Ib/c and II SNe and identify and discuss events which are outliers in §2.3. We extract and present dust parameters for each observation in this section. In §2.4 we present four intriguing case studies: the over-luminous Type II SN 2011ja, the rebrightening Type Ib SN 2014C, the under-luminous and extremely red Type II-P SN 2014bi, and a sample of senior SNe with mid-IR emission detected more than 20 years after their explosions.

2.2 Observations

The Supernova Sample and *Spitzer*/IRAC Photometry

The *Spitzer* InfraRed Intensive Transients Survey (SPIRITS; Kasliwal et al., 2017) targets 190 nearby galaxies within 20 Mpc to a depth of 20 mag. The observations are performed in the 3.6 μm and 4.5 μm bands of the InfraRed Array Camera (IRAC, Fazio et al., 2004) on board the warm *Spitzer* Space Telescope (Gehrz et al., 2007; Werner et al., 2004). Magnitudes in both bands are denoted [3.6] and [4.5] hereafter. All magnitudes are in the Vega system and the conversion $m_{\text{AB}} - m_{\text{Vega}}$ is +2.78 for [3.6] and +3.26 for [4.5] computed from the zeropoints given in the IRAC Instrument Handbook. The SPIRITS galaxy sample has hosted 141 SNe in total since the year 1901 and these SNe have been observed with *Spitzer* in at least one epoch.¹ With the combination of archival data and new SPIRITS observations, 44 SNe are detected: 8 are Type Ia, 9 are Type Ib/c, and the remaining 27 are Type II. Seven new SNe exploded in this galaxy sample during 2014. All of them are observed and 6 are detected. The non-detection, SN 2014bc, is inside its host's nucleus and all observations of it are saturated. Two Type Ia events, SN 2014J and SN 2014dt, are discussed in detail in Johansson et al. (2017) and Fox et al. (2016), respectively.

We used a combination of data from new SPIRITS observations and from other

¹The SNe list is obtained from the IAU Central Bureau for Astronomical Telegram at <http://www.cbat.eps.harvard.edu/lists/Supernovae.html>.

programs, both publicly available from the *Spitzer* Heritage Archive, to study mid-IR emission from the SNe of Type Ib/c and different subtypes of Type II. We used Post-Basic Calibrated Data (pbcd) which had been coadded and calibrated by the standard pipeline. The SPIRITS pipeline performs PSF matching image subtraction using stacks of archival *Spitzer* data, generally ranging from 2004 to 2008, as references. The actual range of epochs used as reference depends on the availability of the data for each host galaxy.

For 34 out of 44 SNe that exploded after this range of epochs, there is no SN light present in the reference frames. In this case the aperture photometry is performed on the subtracted image to eliminate the flux contribution from the galaxy background, which is bright and spatially varying. This methodology is applied to every epoch of each SN for which a pre-explosion reference image exists. We checked our photometry against IRAC photometry of SN 2011dh presented by Ergon et al. (2015) between 18 and 1061 days post-explosion. The results agree to within 5%. 12 SNe of Type Ib/c and II that are detected and have reliable photometry (i.e., not too close to the host's nucleus) are shown in boldface in Table 2.1 and are used further in our analysis in §2.3 and §2.3. In some epochs of SN 2011ja, the SN location is near the edge of the frame and the pipeline fails to produce good subtraction images. We instead use aperture photometry on all frames, then subtract the average baseline flux in pre-explosion images from each epoch in which the SN appears. This method provides good agreement with the image-subtraction method in other epochs where we have high quality subtractions.

For SNe whose reference frames were contaminated with SN light, we searched for a distinct point source at the location of a SN directly in the science frame to judge whether or not we had a detection. In cases judged to be detections, forced aperture photometry with sky background subtraction was performed on the science frames. The aperture corrections from the IRAC Instrument Handbook were then applied. Because the galaxy background could not be completely eliminated in these cases, the photometric data had larger uncertainties, especially at late times when the SNe light was comparable in brightness to the background. In order to ascertain the detection, the thumbnails of every observation of every SN were visually vetted. We excluded SN impostors SN 1997bs and SN 2008S (Adams and Kochanek, 2015; Kochanek et al., 2012). We also excluded SNe that were located near their host's nucleus as all observations were saturated (e.g., SN 2004am, 2008iz, and 2014bc). By doing image subtraction, we were able to identify mid-IR light from old and

slowly evolving SNe that had escaped notice in previous works because they were very dim in comparison to the background (see, e.g., Table 1 in Fox et al., 2011). All SNe with at least one detection by *Spitzer*, either with the new data from SPIRITS or from other programs, are presented in Table 2.1.

Table 2.1: SN Sample

Name	Type	Discovery	RA (J2000)	Dec (J2000)	Host	d (Mpc)	Reference
1974E	II	1974-03-21	180.475	-18.866667	NGC 4038	20.04	—
1979C	II-L	1979-04-19	185.744292	15.797694	NGC 4321	17.95	Dwek (1983)
1980K	II-L	1980-10-28	308.875292	60.106611	NGC 6946	6.67	Dwek (1983) and Dwek et al. (1983)
1986J	II	1986-08-21	35.630417	42.3325	NGC 891	8.36	Cappellaro and Turatto (1986) and Milisavljevic et al. (2008)
1993J	I Ib	1993-03-28	148.854167	69.020278	NGC 3031	3.63	Filippenko et al. (1993)
1999bw	I In	1999-04-20	154.945042	45.526389	NGC 3198	11.64	Sugerman et al. (2004)
2003gd	II-P	2003-06-12	24.177708	15.739139	NGC 628	8.59	Meikle et al. (2007) and Sugerman et al. (2006)
2003hn	II-P	2003-08-25	56.150417	-44.630278	NGC 1448	13.43	Salvo et al. (2003) and Szalai and Vinkó (2013)
2003J	II-P	2003-01-11	182.7405	50.4755	NGC 4157	14.32	Ayani et al. (2003) and Szalai and Vinkó (2013)
2004cc	Ic	2004-06-10	189.143333	11.242444	NGC 4568	33.73	Foley et al. (2004)
2004dj	II-P	2004-07-31	114.320917	65.599389	NGC 2403	3.18	Meikle et al. (2011) and Szalai et al. (2011)
2004et	II	2004-09-27	308.855542	60.121583	NGC 6946	6.67	Fabbri et al. (2011) and Kotak et al. (2009)
2004gn	Ib/c	2004-12-01	188.550417	2.659556	NGC 4527	9.6 8	Pugh and Li (2004)
2005ae	I Ib?	2005-02-01	119.566	-49.855528	ESO 209-9	12.30	Filippenko and Foley (2005)
2005af	II-P	2005-02-08	196.183583	-49.566611	NGC 4945	3.80	Kotak et al. (2006) and Szalai and Vinkó (2013)
2005at	Ic	2005-03-15	287.473208	-63.823	NGC 6744	7.69	Kankare et al. (2014)
2005cs	II-P	2005-06-28	202.469917	47.176583	NGC 5194	7.66	Szalai and Vinkó (2013)
2005df	Ia	2005-08-04	64.407708	-62.769306	NGC 1559	10.76	Diamond et al. (2015) and Salvo et al. (2005)
2006mq	Ia	2006-10-22	121.551625	-27.562611	ESO 494-G26	11.12	Duszanowicz et al. (2006)
2006gov	II-P	2006-11-24	185.480417	4.487972	NGC 4303	18.45	Szalai and Vinkó (2013)
2006X	Ia	2006-02-04	185.724958	15.809194	NGC 4321	17.95	Lauroesch et al. (2006) and Wang and Wheeler (2008)
2007it	II	2007-09-13	214.606792	-43.381611	NGC 5530	12.94	Andrews et al. (2011)
2007sr	Ia	2007-12-18	180.47	-18.972694	NGC 4038	20.04	Pojmanski et al. (2008)
2009hd	II-L	2009-07-02	170.070667	12.979611	NGC 3627	10.81	Elias-Rosa et al. (2011)
2010br	Ib/c	2010-04-10	180.795625	44.528639	NGC 4051	22.39	Maxwell et al. (2010)
2011dh	I Ib	2011-06-01	202.521333	47.169667	NGC 5194	7.66	Ergon et al. (2015) and Helou et al. (2013)
2011fe	Ia	2011-08-24	210.774208	54.273722	Messier 101	7.38	McClelland et al. (2013)
2011ja	II-P	2011-12-10	196.296333	-49.524167	NGC 4945	3.80	Andrews et al. (2016)
2012aw	II-P	2012-03-16	160.974	11.671639	NGC 3351	8.79	Siviero et al. (2012)
2012cc	II	2012-04-29	186.736708	15.045972	NGC 4419	13.49	Marion et al. (2012a)
2012cg	Ia	2012-05-17	186.803458	9.420333	NGC 4424	7.31	Marion et al. (2012b)

Table 2.1 – *Continued*

Name	Type	Discovery	RA (J2000)	Dec (J2000)	Host	d (Mpc)	Reference
2012fh	Ib/c	2012-10-18	160.891875	24.891389	NGC 3344	19.05	Nakano et al. (2012)
2013ai	II	2013-03-01	94.076458	-21.375806	NGC 2207	14.26	Conseil et al. (2013)
2013am	II	2013-03-21	169.737292	13.063722	NGC 3623	18.54	Nakano et al. (2013)
2013bu	II	2013-04-21	339.259042	34.401444	NGC 7331	13.12	Itagaki et al. (2013)
2013df	I Ib	2013-06-07	186.622208	31.227306	NGC 4414	20.51	Morales-Garoffolo et al. (2014) and Szalai et al. (2016)
2013dk	Ic	2013-06-22	180.469667	-18.87175	NGC 4038	20.04	Elias-Rosa et al. (2013)
2013ee	II	2013-07-13	150.486792	55.695556	NGC 3079	14.86	Cortini et al. (2013)
2013ej	II-P	2013-07-25	24.200667	15.758611	NGC 628	8.59	Bose et al. (2015)
2014bi	II-P	2014-05-31	181.512458	47.492639	NGC 4096	11.27	Kumar et al. (2014)
2014C	Ib	2014-01-05	339.273333	34.408861	NGC 7331	13.12	Kim et al. (2014) and Milisavljevic et al. (2015)
2014df	Ib	2014-06-03	56.099958	-44.668917	NGC 1448	13.43	Monard et al. (2014)
2014dt	Ia-p	2014-10-29	185.489875	4.471806	NGC 4303	18.45	Fox et al. (2016)
2014J	Ia	2014-01-21	148.925583	69.673889	NGC 3034	3.52	Johansson et al. (2017)
2014L	Ic	2014-01-26	184.702833	14.412083	NGC 4254	16.83	Yamaoka et al. (2014)

SNe in this sample that are detected by *Spitzer* for at least one epoch.

Bold are CCSNe with pre-explosion images for image subtraction.

Near-Infrared Photometry

As part of the follow-up campaign accompanying SPIRITS, some of the recent SNe listed in Table 2.1 were observed in near-IR from multiple observatories. SN 2013bu, SN 2013df, SN 2014C, and SN 2014bi were observed in the J , H , and K_s bands using the Two Micron All-Sky Survey spectrometer (2MASS; Milligan et al., 1996) on the 60-inch telescope at the University of Minnesota’s Mount Lemmon Observing Facility (MLOF; Low et al., 2007). The science frame and the surrounding sky are observed alternately for sky subtraction. No SNe were detected, so the limiting magnitudes (5σ) are given in Table 2.2. SN 2014C was observed in the J , H , and K_s bands using the $4' \times 4'$ Nordic Optical Telescope near-infrared Camera and spectrograph (NOTCam; Abbott et al., 2000) at the Nordic Optical Telescope under the programme 51-032 (PI: Johansson). We used the wide-field imaging mode and beam-switching to guarantee successful sky subtraction. Data reduction was performed with the NOTCam Quick-Look reduction package based on IRAF. PSF fitting photometry was performed on the sky-subtracted frames, which were then calibrated using 2MASS stars in the field. SN 2014C was also observed in the K_s band using the Wide-field InfraRed Camera (WIRC; Wilson et al., 2003) on the 200-inch Hale Telescope at Palomar Observatory. The data were sky subtracted and calibrated using 2MASS stars in the field. The resulting photometry is listed in Table 2.2.

Table 2.2: Near-IR Photometry of the SNe

MJD	Epoch days	J	H	K_s	Instrument
SN 2013bu (II)					
56809	405.5	>16.1	>15.5	>15.1	MLOF/2MASS
56901	497.5	>16.2	>15.5	>15.3	MLOF/2MASS
56931	527.5	>16.1	>15.3	>14.9	MLOF/2MASS
56950	546.5	—	—	>19.0	P200/WIRC
56962	558.5	>16.1	>15.1	>14.5	MLOF/2MASS
SN 2013df (IIb)					
56717	266.5	>15.9	>14.9	>14.9	MLOF/2MASS
57023	572.5	>14.5	>13.7	>13.9	MLOF/2MASS
SN 2014C (Ib)					
56809	146.5	>13.4	>12.7	>12.1	MLOF/2MASS
56901	238.5	>13.9	>13.0	>12.6	MLOF/2MASS
56931	268.5	>13.5	>12.8	>12.3	MLOF/2MASS
56950	287.5	—	—	14.38(0.06)	P200/WIRC
56962	299.5	>13.5	>12.5	>12.3	MLOF/2MASS
57292	630.5	18.0 (0.1)	16.6 (0.1)	14.9 (0.1)	NOT/NOTCam
SN 2014bi (II-P)					
57113	304.5	—	>14.8	>15.3	MLOF/2MASS

This table summarizes all near-infrared photometry of the SNe in Table 2.1. Magnitudes listed are Vega, calibrated using 2MASS stars.

2.3 Results

Demographics

The detection statistics for each type of SNe are presented in Fig. 2.1. We consider separately three time bins after discovery: less than one year, one to three years, and more than three years. In each bin, if a SN is observed with at least one detection, it is marked as detected even though it might fade to non-detection later in the same bin. Otherwise, if all observations of a SN in that bin result in non-detections, then that SN is marked as a non-detection. The number of detections and non-detections of each type of SNe in each bin is then tallied up. The error estimates for small number statistics are done using the method described in Cameron (2011) based on Bayesian statistics.

The distance to a SN affects our sensitivity to detect the event. When one considers a given type of SNe, events further away tend to fall off the detection limit first. However, across different types, the distance distributions in our sample are similar. As a result, the different detection statistics we find for each type of SNe are not only on account of the Malmquist bias (the preferential detection of intrinsically bright

objects). In other words, the relative fraction of detected Type II SNe versus Type Ia at late time is not due to the distance distribution. The results reflect the intrinsic difference in mid-IR evolution between CCSNe and Type Ia SNe.

The results show that almost all SNe across all types are detected within 1 year after discovery. The only two exceptions are Type Ia SN 2004W and SN 2011B. Both SNe were undetected in both IRAC channels, six and ten months, respectively, after their discovery dates. Overall, the mid-IR emission from most Type Ia SNe in our sample is shorter lived compared to CCSNe. We note that our sample does not include Type Ia events with CSM interactions (Ia-CSM), in which case mid-IR emission lasts longer (see, e.g., SN 2005gj and SN 2002ic, Fox and Filippenko, 2013; SN 2014dt Fox et al., 2016).

Between 1 and 3 years after discovery, the fractions of Type Ia and Ib/c detected dropped dramatically, to $22\pm 24\%$ and $55\pm 28\%$, respectively. However, most of Type II SNe ($82\pm 18\%$) continued to be detected. As discussed above, this is not a result of the distance bias in the sample. In fact, 3 out of 4 detected Type Ib/c events in this bin are further away than all 4 non-detected ones.

Finally, after 3 years, none of the Type Ia or Ib/c was detected. However, $22\pm 11\%$ of the Type II events remained detected, mostly in the $4.5\ \mu\text{m}$ band. These long-lived events are SN 1974E (II), SN 1979C (II-L), SN 1986J (II_n), SN 1993J (II_b), SN 1999bw (II_n; Filippenko et al., 1999; Kochanek et al., 2012), SN 2004dj (II-P), SN 2004et (II-P), SN 2007it (II-P), SN 2009hd (II-L), and 2011ja (II-P; Andrews et al., 2016). Additional discussion of a well-sampled subset of these old SNe follows in §2.4. It is worth noting that the SN impostors, SN 1997bs and SN 2008S, were detected in our observations more than 3 years post-discovery, outlasting many other real Type II events even though they are not particularly nearby. Because late-time mid-IR emission comes mostly from warm dust, this data set allows us to probe evolution of warm dust properties in these CCSNe.

Light Curves

Type Ib/c Supernovae

The light curves of all four Type Ib/c SNe for which we have image-subtracted photometry are shown in Figure 2.2. The data coverage spans epochs from 40 to 800 days after discovery, with multi-epoch data for SN 2013dk (Ic), SN 2014L (Ic), and SN 2014C (Ib). The projected peak brightness ranges from $[4.5] = -18.3$ and $[3.6] = -18.3$ mags for SN 2014L to $[4.5] = -19.7$ and $[3.6] = -19.0$ for SN 2014C.

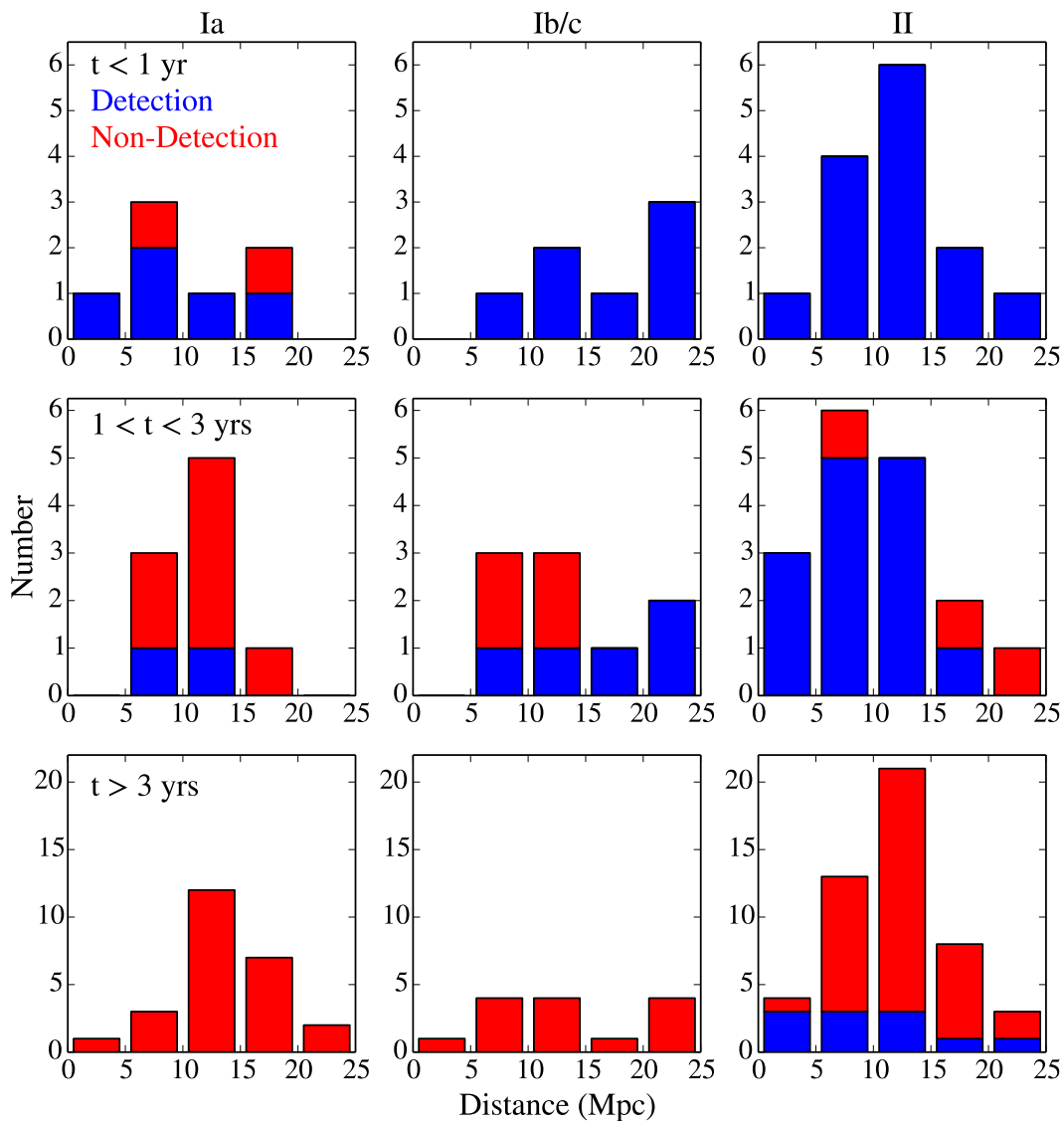


Figure 2.1: Stacked histograms showing detection statistics in our SN sample. Each column represents one type of SN and each row represents one bin of time after first discovery. Due to the small number of counts in our sample, we follow the procedure described by Cameron (2011) based on a Bayesian approach to estimating uncertainties.

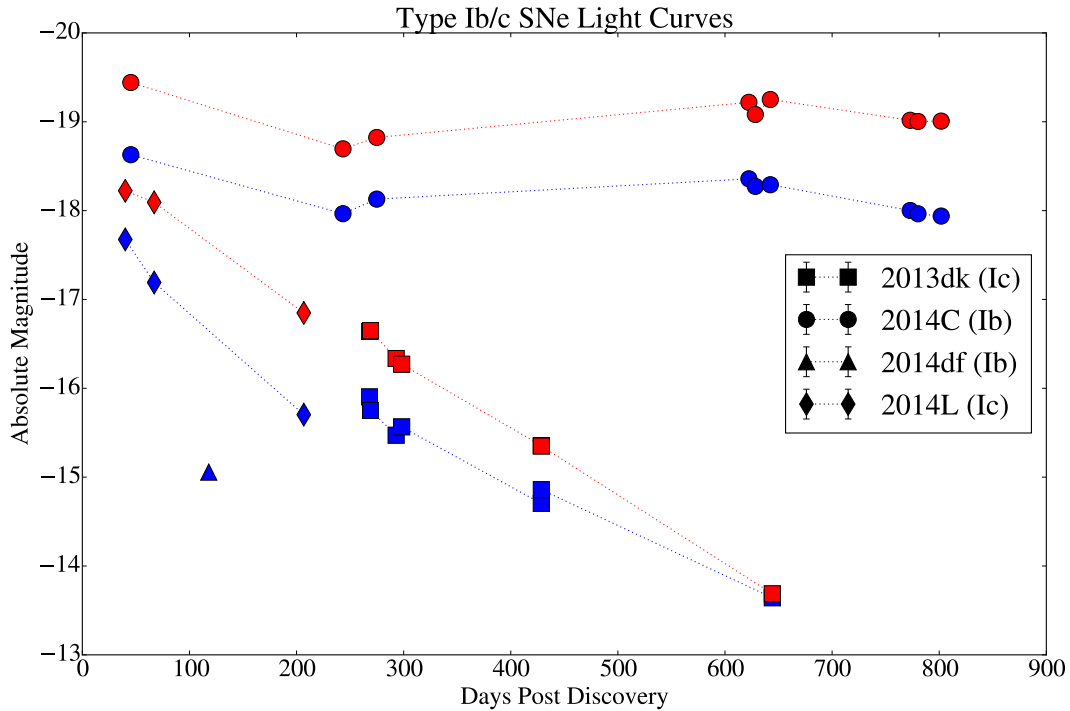


Figure 2.2: A collage of light curves of Type Ib/c SNe with photometry based on image subtraction. Red and blue markers represent [4.5] and [3.6], respectively. The error bars are smaller than the plotting symbols.

The decline rate for SN 2014C is 0.5 mags/100 days in both channels within 200 days after the explosion. The two Type Ic events decay at roughly the same rates in [4.5]: about 0.8 mags/100 d within 450 d. However, the [3.6] decline rates for these events are quite different. SN 2014L decays for 1 mag/100 d out to 200 days, while SN 2013dk only decays at the rate of 0.68/100 d between 250 and 430d. SN 2014df (Ib) is about 3.5 mags dimmer than SN 2014C, another Ib event, at the same epoch, but the lack of concurrent photometry yields no color information. No further observations of this galaxy have been made since 2015. The most interesting Type Ib/c SN observed in our sample is SN 2014C, which rebrightens by 0.15 mags in 4.5 μm and 0.24 mags in 3.6 μm around 250d. It was observed again more than a year later at 620 d to be even brighter in both bands then maintained nearly constant luminosity out to 800d. This peculiar time evolution in the mid-IR sets this event apart from other SNe in this sample. Further discussions of this SN are presented in §2.4. We also note that, apart from the peculiar Type Ib SN 2006jc with strong CSM interaction (see Smith et al., 2008; Mattila et al., 2008), dust emission has not been detected for any other Type Ib/c events.

Type II Supernovae

The light curves of all 8 Type II SNe for which we have image-subtraction photometry are presented in Figure 2.3. SN 2011dh has the most well-sampled light curves covering epochs from pre-maximum to 1200 days after the detection, providing a template with which other SNe can be compared. Helou et al. (2013) interpolated [4.5] data to fill in the visibility gap between 90 and 250 days and found that SN 2011dh left its initial plateau into a decay at 150 ± 25 days post-explosion. Between 200 and 400 days, SN 2011dh has steep decline rates of 1.96 and 1.57 mags/100 d at $3.6 \mu\text{m}$ and $4.5 \mu\text{m}$, respectively. After 400 days, the light curves in both bands plateau to decline rates of 0.57 and 0.75 mags/100 d at $3.6 \mu\text{m}$ and $4.5 \mu\text{m}$, respectively. After 600 days, the decline rates decrease to only 0.02 mags/100 d in both channels. In these epochs after 100 days, Helou et al. (2013) reported that an IR echo alone cannot account for the flux and that dust formation, additional heating mechanisms, a nearby interstellar cloud, or line or band emission must contribute. Ergon et al. (2015) reported the fractional increase of $3.6 \mu\text{m}$, $4.5 \mu\text{m}$, and K bands luminosity compared to optical in conjunction with an increase in the decline rate of the optical pseudo-bolometric light curve. They also observed small blueshifts in the [OI] and [MgI] lines at 415 days. These results suggest that new dust is being created inside the expanding shell of ejecta attenuating optical light coming from the receding side of the shell.

The collage in Fig. 2.3 shows heterogeneity in the Type II light curves in comparison with SN 2011dh. Some SNe—such as SN 2013bu (II), SN 2013df (IIb), and SN 2013ej (II-P)—have similar temporal evolution as that of SN 2011dh in terms of the absolute magnitudes, which are within 1 mag of SN 2011dh, and the decline rates. SN 2013ai shows similar plateauing after 400 days at $4.5 \mu\text{m}$ to a decline rate of 0.23 mags/100 d, but there is insufficient coverage in the $3.6 \mu\text{m}$ band. For a detailed discussion of SN 2013df, see Szalai et al. (2016).

SN 2013am and SN 2011ja (Andrews et al., 2016) rebrighten in different epochs. SN 2013am rebrightens slightly in the $4.5 \mu\text{m}$ band at around 370 days post-discovery, but not in the $3.6 \mu\text{m}$ band. SN 2011ja stays luminous from 100 to 400 d with higher fluxes at 400d. It is possible for the SN to have rebrightened between 100 and 400d. The secondary peak in the mid-IR has been observed in other Type II events, but at later times. Meikle et al. (2011) and Szalai et al. (2011) observed a rebrightening of SN 2004dj (II-P) in all IRAC bands, except the $4.5 \mu\text{m}$, in the $16 \mu\text{m}$ and $22 \mu\text{m}$ bands of IRS Peak-Up Imaging (IRS-PUI) and $24 \mu\text{m}$

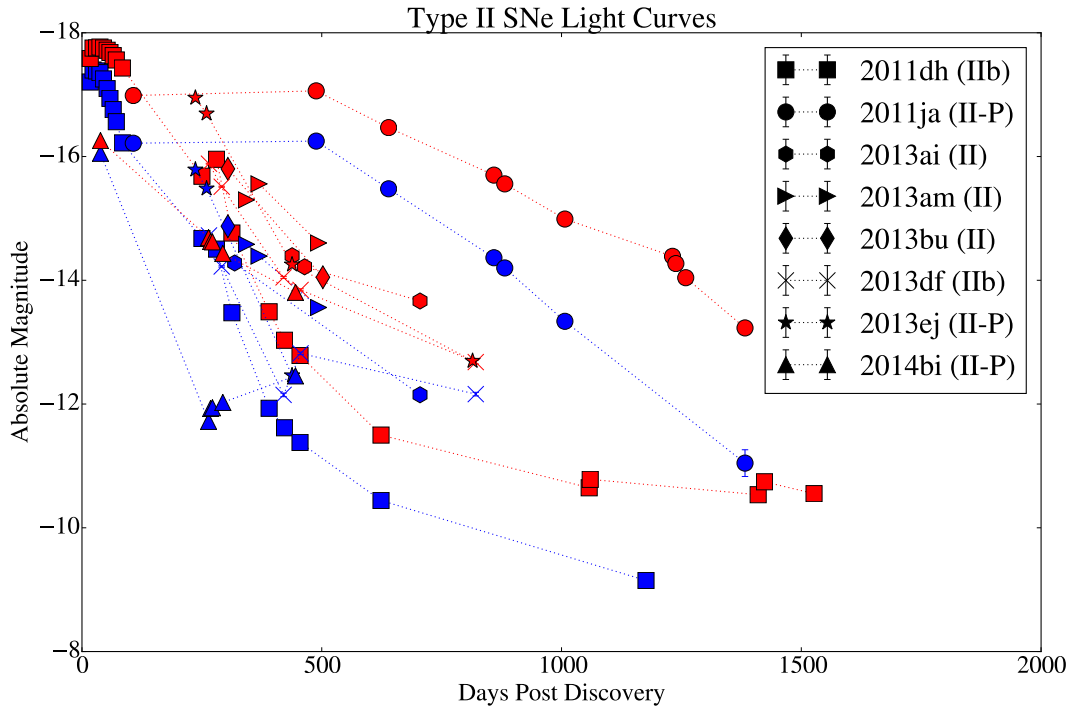


Figure 2.3: A collage of light curves of Type II SNe with photometry based on image subtraction. Red and blue markers represent [4.5] and [3.6], respectively. The error bars are smaller than the plotting symbols.

MIPS at 450–800 days post-explosion with the shorter wavelengths peaking first. The absence of a secondary peak in the 4.5 μm band was attributed to a strong contribution from CO 1-0 vibrational band at 4.65 μm before 500d. Fabbri et al. (2011) reported a secondary mid-IR peak for SN 2004et (II-P) in all IRAC bands, 16 μm IRS-PUI, and 24 μm MIPS at 1000d. For both II-P events, attenuation in the red-wing of spectral lines and an increase in optical light-curve decline rates were observed as the mid-IR light curves started to rise again. This strongly suggested that the rebrightening was due to dust production in the ejecta of these SNe. However, in the case of SN 2013am, where we do not have spectroscopic data, other sources of mid-IR flux such as additional heating mechanisms and CSM interactions cannot be ruled out. We also note that the amplitude of SN 2013am’s rebrightening is very small compared to that observed in SN 2004dj and SN 2004et. The interesting case of SN 2011ja will be discussed in §2.4.

In addition to the rebrightening events, another outlier is evident in the light curves collage shown in Fig. 2.3. SN 2014bi (II-P) is under-luminous, especially in the 3.6 μm band in which it is 3–4 mags dimmer than other SNe. The color [3.6]-[4.5] is as much as 2.95 mags at 264 days. This event will also be discussed in detail in §2.4.

The Spectral Energy Distribution and Dust Parameter Fitting

The Spectral Energy Distribution (SED) for each SN is fitted with an elementary one-component homogeneous dust model. A more sophisticated model fitting would require additional data from other bands. The analysis follows the procedure described by Fox et al. (2010, 2011). The flux density coming from warm dust at one equilibrium temperature is given by the Planck function modified with the dust mass absorption coefficient, which is frequency dependent. Assuming an optically thin dust shell with $\Delta r/r \sim 1/10$, the flux is given by

$$F_\nu = \frac{M_d B_\nu(T_d) \kappa_\nu(a)}{d^2} \quad (2.1)$$

where $B_\nu(T_d)$ is the Planck function, $\kappa_\nu(a)$ is the dust mass absorption coefficient as a function of the grain size a , M_d is the dust mass and d is the distance of the source from the observer. The dust mass absorption coefficient is given by

$$\kappa_\nu(a) = \left(\frac{3}{4\pi\rho a^3} \right) \left(\pi a^2 Q_\nu(a) \right) \quad (2.2)$$

where ρ is the volume density of the dust and $Q_\nu(a)$ is the frequency dependent emission efficiency of the dust. $Q_\nu(a)$ is given in Fig. 4 of Fox et al. (2010) and it is computed numerically. Because we only have two data points for each SN at each epoch, we are limited to using one temperature component and one dust composition. Fox et al. (2011) found that assuming a pure graphite dust population with $a = 0.1 \mu\text{m}$ gives the best fitting coefficients. The distinction between a graphite and a silicate dust population is a spectral feature around $9 \mu\text{m}$, which is not captured by our data. They also found that a silicate dust model resulted in higher temperatures, masses, and luminosities. In many cases, silicate grains require an improbably high luminosity from the SN to heat them up to the observed temperature. Thus, we assume a graphite dust population with a grain radius of $0.1 \mu\text{m}$. We note here that at early time ($\lesssim 200\text{d}$), the SN light still dominates dust emission in mid-IR and the results from SED fitting in those epochs might not reflect dust properties accurately. We also note that the $3.6 \mu\text{m}$ band can be contaminated by the PAH emission while the $4.5 \mu\text{m}$ band can be contaminated by CO emission at $4.65 \mu\text{m}$.

We fit equation (2.1) to our data using the method `curve_fit` in SciPy package, which varies fitting parameters to find the best fit to the data using the method of least squares (Jones et al., 2001). The standard deviations of the fitting parameters are also computed by `curve_fit`. Table 2.3 shows best-fit temperatures and dust masses with corresponding uncertainties for all SNe for which data in both IRAC

bands at the same epoch exist. Other epochs of observations where only one band is observed are presented in Table 2.4. We note that these uncertainties are small because they are derived solely from the photometric uncertainties. They do not reflect the errors due to our assumption that the dust emission is optically thin and the spectrum is a modified blackbody. The dust luminosity is computed by integrating equation (2.1) at all frequencies using the fitted warm dust mass and temperature. We note that due to the lack of spectral information, we cannot rule out pre-existing dust and the best-fit dust masses reported here should be taken as an upper limit to the amount of newly formed dust. We also reiterate here that our observations are only sensitive to warm dust and there could be a large fraction of dust mass hiding at colder temperatures. We find that dust masses are between 10^{-6} and $10^{-2} M_{\odot}$, in agreement with previous works concluding that warm dust alone cannot account for all the dust predicted to be produced in a CCSN. Fig. 2.4 shows the time evolution of dust luminosity, temperature and mass along with data on Type II-P SNe from Szalai and Vinkó (2013) and Type IIn SNe from Fox et al. (2011). The Type II-P events in Szalai and Vinkó (2013) and SNe in our sample have dust luminosity, temperatures, and mass estimates in the same range. In comparison with Type IIn events with confirmed early CSM interactions that can heat pre-existing dusts to high temperatures, SNe in our sample have less luminous dust emission, and at roughly the same temperature, less inferred dust mass.

In the plot showing warm dust mass (Fig. 2.4), two dotted lines represent the predicted dust mass that has been processed by the forward shock from the SN, which is given by Eq. 6 in Fox et al. (2011). Assuming a dust-to-gas ratio of 0.01, we get

$$M_d(M_{\odot}) \approx 0.0028 \left(\frac{v_s}{15,000 \text{ km s}^{-1}} \right)^3 \left(\frac{t}{\text{yr}} \right)^2 \left(\frac{a}{\mu\text{m}} \right) \quad (2.3)$$

where v_s is the shock velocity, t is the time post-explosion, and a is the grain size, (assumed in this work to be $0.1 \mu\text{m}$). The last panel in Fig. 2.4 shows that, for almost all cases, the predicted shocked dust mass is much lower than the mass derived from our observations. As a result, shock heating of pre-existing dust is likely ruled out for all events within a year following the explosion. Even for later times, to invoke shock heating we must assume a high shock velocity of $15,000 \text{ km s}^{-1}$.

The temporal evolution of the observed mass seems to show two different trends at about a year post-explosion. Some of the events such as SN 2011dh, SN 2013dk, and especially SN 2014bi, show a large decrease in the dust mass at this epoch. This could be a signature of either dust destruction or reduced CSM/shock interactions.

Another group of SNe, especially SN 2011ja and SN 2014C show an increase in the dust mass, which could be due to either the formation of new dust or an intensifying dust heating source. For SN 2011ja, both the dust luminosity and dust temperature are dropping while the warm dust mass is growing. This disfavors the fading dust heating source scenario. Next we discuss case studies of some extreme SNe in our sample.

Table 2.3: Mid-IR Photometry and SED Fitting Results

MJD	Epochs days	$F_{[3.6]}$ mJy	$F_{[4.5]}$ mJy	r_s 10^{15} cm	r_{bb} 10^{15} cm	L_d $10^6 L_\odot$	M_d $10^{-5} M_\odot$	T_d K
SN 2011dh (IIb)								
55730*	17	5.309(0.004)	4.87(0.01)	0.744	8.45(0.15)	6.47(0.22)	7.10(0.11)	836(2)
55736*	23	6.344(0.006)	5.69(0.01)	0.996	8.88(0.15)	7.93(0.26)	7.51(0.11)	858(2)
55743*	30	6.261(0.006)	5.71(0.01)	1.31	9.07(0.16)	7.69(0.25)	8.08(0.12)	842(2)
55750*	37	6.104(0.006)	5.78(0.02)	1.62	9.54(0.16)	7.25(0.23)	9.60(0.14)	809(2)
55758*	44	5.556(0.006)	5.70(0.01)	1.93	10.4(0.2)	6.32(0.19)	13.2(0.2)	747(2)
55765*	52	4.808(0.005)	5.51(0.01)	2.27	11.8(0.2)	5.43(0.16)	20.3(0.3)	676(1)
55771*	58	4.16(0.01)	5.33(0.01)	2.52	13.5(0.2)	4.92(0.17)	31.0(0.6)	618(1)
55778*	65	3.52(0.01)	5.09(0.01)	2.81	15.5(0.3)	4.58(0.16)	48.2(0.9)	565(1)
55785*	71	2.94(0.01)	4.77(0.01)	3.09	17.7(0.3)	4.35(0.16)	71.8(1.4)	523(1)
55797*	84	2.145(0.008)	4.23(0.01)	3.64	22.2(0.4)	4.25(0.16)	140(3.0)	464(1)
55963*	250	0.517(0.003)	0.845(0.004)	10.8	7.52(0.22)	0.773(0.042)	13.1(0.4)	521(2)
55993*	280	0.441(0.004)	1.087(0.005)	12.1	15.8(0.6)	1.33(0.10)	87.6(4.0)	412(2)
56026*	312	0.171(0.002)	0.363(0.002)	13.5	7.24(0.32)	0.385(0.032)	16.0(0.8)	446(2)
56103*	390	0.0413(0.0008)	0.112(0.001)	16.9	5.92(0.47)	0.154(0.024)	13.5(1.3)	392(4)
56135*	422	0.0309(0.0007)	0.074(0.001)	18.2	3.89(0.38)	0.0868(0.163)	5.17(5.7)	419(5)
56168*	454	0.0248(0.0006)	0.0586(0.0009)	19.6	3.43(0.38)	0.0686(0.145)	3.98(4.9)	421(6)
56337*	623	0.0105(0.0004)	0.0179(0.0005)	26.9	1.17(0.23)	0.0167(0.063)	0.336(0.07)	505(14)
SN 2011ja (II-P)								
56012*	106	5.88(0.02)	7.73(0.01)	4.62	10.1(0.2)	2.57(0.08)	18.2(0.3)	606(1)
56393*	488	6.07(0.01)	8.29(0.02)	21.1	11.0(0.1)	2.72(0.07)	22.7(0.3)	589(1)
56544*	639	2.98(0.01)	4.80(0.01)	27.6	10.6(0.2)	1.59(0.05)	25.4(0.5)	526(1)
56764	859	1.07(0.02)	2.365(0.009)	37.1	11.9(0.9)	0.945(0.135)	45.1(3.6)	435(4)
56787	881	0.92(0.02)	2.076(0.008)	38.1	11.5(1.0)	0.846(0.137)	43.1(4.0)	430(5)
56912	1007	0.42(0.01)	1.23(0.01)	43.5	13.5(1.3)	0.681(0.129)	75.5(8.7)	376(4)
57288	1382	0.05(0.01)	0.24(0.02)	59.7	13.3(9.5)	0.291(0.406)	106(90)	306(24)
SN 2013ai (II)								
57057	704	0.0099(0.0002)	0.0258(0.0003)	30.5	6.02(0.51)	0.172(0.028)	134(1.3)	400(4)
SN 2013am (II)								
56715	342	0.0550(0.0004)	0.0688(0.0005)	14.8	4.36(0.24)	0.553(0.057)	3.14(0.16)	629(5)
56741	369	0.0461(0.0004)	0.0873(0.0006)	15.9	8.83(0.40)	0.738(0.064)	21.3(1.1)	475(3)
56865	493	0.0215(0.0003)	0.0362(0.0004)	21.3	4.80(0.34)	0.289(0.039)	5.56(0.42)	510(5)
SN 2013bu (II)								
56707	304	0.1435(0.0007)	0.218(0.001)	13.1	7.17(0.21)	0.850(0.047)	10.9(0.3)	546(2)
SN 2013df (IIb)								
56715	264	0.0512(0.0004)	0.0963(0.0006)	11.4	10.2(0.4)	0.993(0.082)	28.0(1.3)	477(2)
56741	291	0.0322(0.0003)	0.0684(0.0005)	12.6	10.2(0.5)	0.767(0.076)	31.9(1.8)	446(3)

Table 2.3 – *Continued*

MJD	Epochs days	$F_{[3.6]}$ mJy	$F_{[4.5]}$ mJy	r_s 10^{15} cm	r_{bb} 10^{15} cm	L_d $10^6 L_\odot$	M_d $10^{-5} M_\odot$	T_d K
56870	420	0.0048(0.0001)	0.0177(0.0003)	18.2	12.6(1.4)	0.396(0.083)	78.3(10.4)	340(4)
56906*	455	0.0088(0.0002)	0.0147(0.0002)	19.7	3.31(0.37)	0.143(0.031)	2.60(0.30)	515(8)
57271	821	0.0048(0.0001)	0.0050(0.0001)	35.5	1.03(0.22)	0.0577(0.234)	0.132(0.025)	736(27)
SN 2013dk (Ic)								
56733	268	0.1588(0.0007)	0.2021(0.0009)	11.6	8.26(0.26)	1.89(0.11)	11.6(0.3)	621(3)
56734	269	0.1378(0.0007)	0.2040(0.0009)	11.6	10.2(0.3)	1.85(0.11)	21.5(0.7)	556(2)
56758	292	0.1067(0.0006)	0.1528(0.0008)	12.7	8.44(0.30)	1.39(0.09)	14.1(0.5)	569(3)
56763	298	0.1164(0.0006)	0.1440(0.0008)	12.9	6.72(0.25)	1.36(0.10)	7.35(0.26)	635(3)
56894	428	0.0526(0.0004)	0.0620(0.0005)	18.5	4.13(0.24)	0.603(0.066)	2.59(0.14)	660(6)
57109	644	0.0198(0.0003)	0.0133(0.0002)	27.8	1.02(0.20)	0.511(0.184)	0.0484(0.006)	1277(51)
SN 2013ej (II-P)								
56734	236	0.778(0.002)	1.465(0.002)	10.2	16.6(0.2)	2.65(0.06)	75.0(0.9)	477(1)
56758	259	0.587(0.001)	1.158(0.002)	11.2	15.8(0.2)	2.16(0.05)	71.5(1.0)	464(1)
56936	438	0.0363(0.0004)	0.1224(0.0007)	18.9	11.8(0.5)	0.413(0.032)	63.9(3.1)	355(1)
SN 2014C (Ib)								
56707	45	4.560(0.004)	6.236(0.005)	1.96	33.1(0.2)	24.4(0.3)	204(1)	588(1)
56905	243	2.474(0.003)	3.134(0.004)	10.5	21.2(0.2)	12.6(0.2)	75.2(0.6)	623(1)
56937	274	2.878(0.003)	3.527(0.004)	11.9	21.5(0.2)	14.4(0.2)	74.0(0.5)	640(1)
57284	622	3.551(0.004)	5.076(0.005)	26.9	31.8(0.2)	19.8(0.2)	199(1)	570(1)
57290	628	3.284(0.003)	4.476(0.004)	27.1	27.9(0.2)	17.5(0.2)	145(1)	590(1)
57304	642	3.340(0.003)	5.227(0.005)	27.7	36.6(0.2)	20.5(0.2)	295(2)	535(1)
57435	772	2.558(0.003)	4.214(0.004)	33.4	35.4(0.2)	16.7(0.2)	293(2)	518(1)
57442	780	2.471(0.003)	4.165(0.004)	33.7	36.3(0.2)	16.7(0.2)	317(2)	510(1)
57464	801	2.414(0.003)	4.179(0.004)	34.6	37.8(0.3)	16.9(0.2)	355(2)	502(1)
SN 2014L (Ic)								
56723	40	1.152(0.002)	1.234(0.002)	1.73	13.7(0.2)	9.23(0.23)	24.4(0.3)	718(1)
56750	67	0.738(0.002)	1.095(0.002)	2.90	19.9(0.3)	7.01(0.17)	82.3(1.1)	555(1)
56890	206	0.1874(0.0008)	0.348(0.001)	8.93	15.5(0.4)	2.39(0.11)	64.3(1.6)	481(1)
SN 2014bi (II-P)								
56847*	38	0.576(0.001)	0.450(0.001)	1.67	3.83(0.11)	2.90(0.15)	1.04(0.02)	1015(5)
57072	264	0.0106(0.0002)	0.1060(0.0007)	11.4	88.9(5.1)	4.94(0.55)	7240(570)	241(1)
57076	268	0.0129(0.0002)	0.1003(0.0007)	11.6	56.4(3.1)	2.70(0.29)	2540(190)	260(1)
57080	272	0.0130(0.0002)	0.0996(0.0006)	11.8	54.5(3.0)	2.59(0.27)	2360(170)	261(1)
57102	293	0.0141(0.0002)	0.0840(0.0006)	12.7	32.7(1.8)	1.30(0.14)	731(53)	284(1)
57253	445	0.0210(0.0003)	0.0470(0.0004)	19.2	5.07(0.32)	0.167(0.02)	8.32(0.58)	432(3)

Table 2.4: Additional one-channel mid-IR photometry and upper limits

Name	MJD	$F_{[3.6]}$ (mJy)	$F_{[4.5]}$ (mJy)
2011dh	56771.17	–	0.0082(0.0002)
2011dh	56773.34	–	0.0093(0.0002)
2011dh	56889.65	0.0032(0.0001)	<0.018
2011dh	57123.57	–	0.0074(0.0002)
2011dh	57136.77	–	0.0089(0.0002)
2011dh	57240.05	–	0.0075(0.0002)

2011dh	57493.52	–	<0.0066
2011ja	57136.92	–	0.706(0.008)
2011ja	57143.95	–	0.634(0.007)
2011ja	57164.49	–	0.514(0.008)
2013ai	56670.92	0.0703(0.0005)	–
2013ai	56790.67	<0.021	0.0507(0.0005)
2013ai	56816.68	–	0.0430(0.0004)
2013ai	57168.89	<0.016	<0.013
2013am	57253.44	<0.020	<0.013
2013bu	56905.83	–	0.043(0.004)
2013bu	57284.82	<0.016	<0.013
2013df	57459.83	<0.022	<0.021
2013dk	57115.25	<0.025	<0.025
2013ej	57312.98	<0.0059	0.029(0.001)
2014L	57280.41	<0.027	<0.027
2014df	56929.54	0.162(0.001)	–
2014df	57331.12	<0.008	<0.007

A table of additional photometry points from epochs with only one channel detection. An upper limit in another channel is provided when the SN is observed with a non-detection. Finally, for each SN with image-subtraction photometry, we provide flux upper limits for the first epoch the SN fades to non-detection. All limits are 9σ while error bars are 1σ . All data come from SPIRITS, PID 10136 and 11063 (PI: Kasliwal).

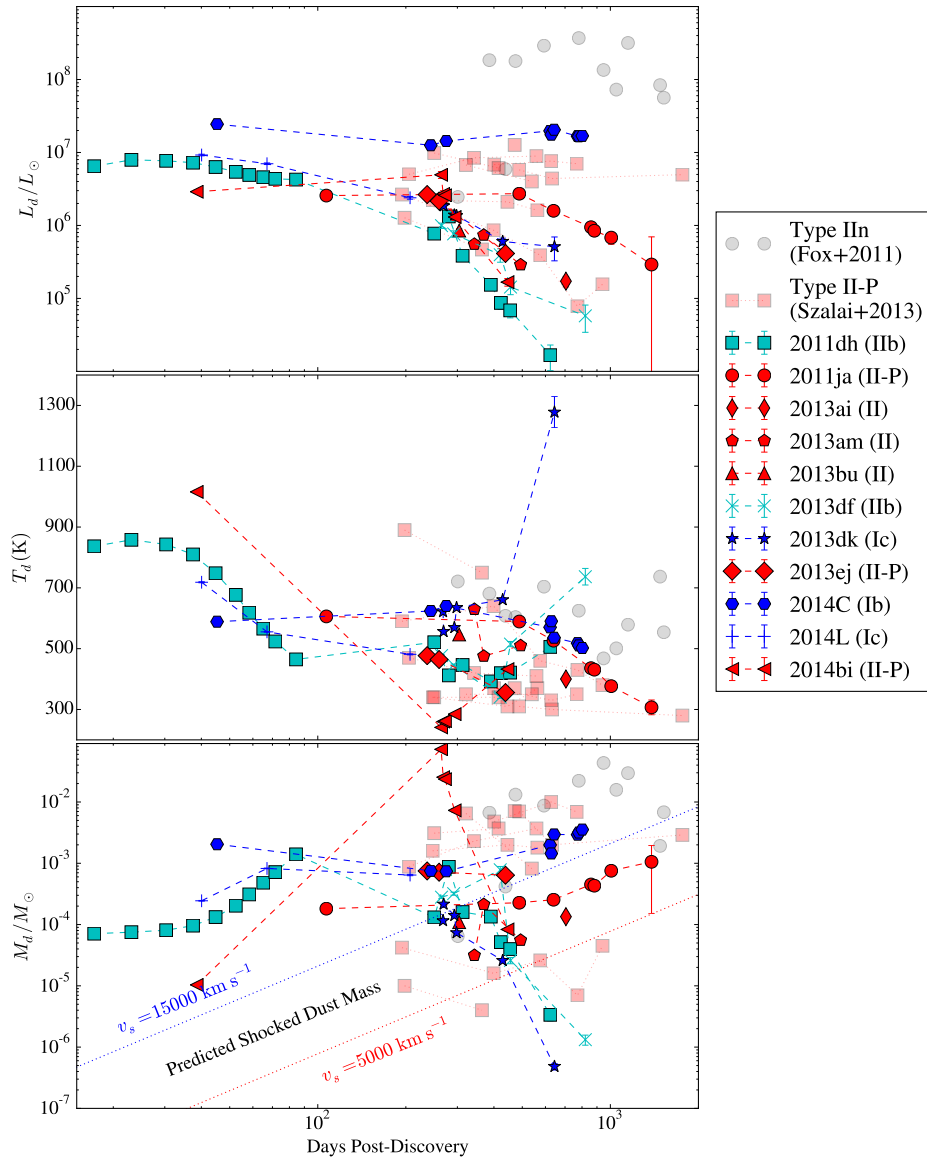


Figure 2.4: Time evolution of dust luminosity (top panel), temperature (middle panel), and mass (bottom panel) from fitting equation (2.1) assuming $0.1 \mu\text{m}$ graphite grains. Overplotted (dotted line) on the warm dust mass evolution plot is the estimated dust mass assuming a shock heating scenario. The red points are Type II SNe, cyan points are Type IIb, and blue points are Type IIc. Error bars (1σ) are plotted but are smaller than the symbol size in most cases. The transparent grey circles are data for Type IIc SNe from Fox et al. (2011). The transparent red squares are data for Type II-P from Szalai and Vinkó (2013). Data points with connecting dotted lines represent the same SN with multiple epochs of data. No uncertainties are provided for these data points. This figure shows the diversity in temporal evolution of dust properties of CCSNe in our sample.

2.4 Case Studies

SN 2011ja: A Type II-P with New Dust Formation in a Cold Dense Shell

SN 2011ja is a Type II-P SN in the nearby galaxy NGC 4945 at a distance of 3.8 Mpc (Mould and Sakai, 2008). It was discovered on 2011 December 18 by Monard et al. (2011) and the spectrum obtained a day later showed that it was a young Type II-P SN that shared similar spectral features with SN 2004et a week after maximum light (Milisavljevic et al., 2011). Chakraborti et al. (2013) obtained X-ray and radio observations in two epochs out to about 100d. They found signatures of circumstellar interaction which likely resulted from the fast moving ejecta colliding with the slower stellar wind from the progenitor before it exploded. They deduced from the observations that the progenitor was likely a red supergiant with initial mass $M \gtrsim 12 M_{\odot}$. Andrews et al. (2016) performed multi-band follow-up observations in the optical, near-IR, and mid-IR. The first 4 out of 10 epochs of the *Spitzer* observations used in this work were also presented in their paper. After 105d, they observed a decrease in the optical flux, a rise in the near-IR flux, and an attenuation in the red wing of H α emission lines. These are strong indications that SN 2011ja is producing dust early on in the cold dense shell (CDS) created when the ejecta run into the CSM. The dust could not have formed in the inner ejecta because the temperature would be too high at such an early epoch. Using a radiative transfer model to fit the SED, they inferred $\sim 10^{-5} - 10^{-4} M_{\odot}$ of dust at 100 d depending on the assumed geometry. By 857d, at least $\sim 2.0 - 6.0 \times 10^{-4} M_{\odot}$ of dust has formed. They classified SN 2011ja with a growing group of Type II-P SNe, among them SN 2004dj and SN 2007od, which exhibit unusual evolution at late times due to the CSM interactions. This indicates that their progenitors lose enough mass before the SN explosion to create a dense CSM environment that is close enough for the forward shock to encounter within a few hundred days but not so that CSM interactions commence immediately after explosion as in the case of Type IIn SNe.

SN 2011ja has been observed ten times with *Spitzer*. Seven epochs have concurrent coverage in both bands. Most notably, the light curve plateaus out to 500 d post-explosion, then declines with the increasing [3.6]-[4.5] color. This photometric evolution is consistent with a warm dust mass that increases monotonically with time from $10^{-4} M_{\odot}$ at 107 d to $10^{-3} M_{\odot}$ at 1383d. Consider the blackbody radius which serves as a lower limit for the size of the dust shell responsible for the thermal emission (e.g., Fox et al., 2011) in comparison with the shock radius. For every epoch of observations, we see that the shock radius, assuming the ejecta speed between 5,000 and 15,000 km s $^{-1}$, is a factor of a few larger than the blackbody

radius. The blackbody radius remains almost constant from 106 d to 1382 d, with $r_{\text{bb}} \approx 10^{16}$ cm while the shock radius assuming shock velocity of $v_s = 5,000 \text{ km s}^{-1}$ evolves from 4.62×10^{15} cm to 5.97×10^{16} cm. This places the size lower limit of the emitting dust shell smaller than the shock radius in most epochs, even assuming the minimum shock velocity. This is consistent with the scenario proposed by Andrews et al. (2016) in which dust grains condense in the cold dense shell (CDS) between the forward and reverse shocks with the inner and outer circumstellar radii of at 4.5×10^{15} and 4.5×10^{16} cm, respectively. Since the blackbody radius only provides a lower limit of the location of the emitting dust, we cannot reject the scenario in which the dust emission comes from beyond the shock front, from pre-existing dust being radiatively heated by the CSM interaction. We note as well that for the highest velocity shock with $v_s = 15,000 \text{ km s}^{-1}$, Fig. 2.4 suggests that the dust mass seen could be explained by collisional heating of the pre-existing dust by the shock front. However, given the spectroscopic evidence of newly formed dust presented by Andrews et al. (2016), we conclude that at least some of the observed dust must be newly formed.

In comparison with other Type II events in our sample, SN 2011ja's early luminosity is very similar to that of SN 2011dh (Iib) in both channels. However, SN 2011ja's luminosity remains mostly constant out to 500d, at which point it outshines every other SN in the sample. In comparison to the well-studied Type II-P SN 2004dj (Meikle et al., 2011; Szalai et al., 2011) and SN 2004et (Fabbri et al., 2011), SN 2011ja is more than a magnitude brighter than both of them out to about 1000 d (see Fig. 2.5). In terms of dust properties, SN 2004dj has $3.35 \times 10^{-5} M_{\odot}$ and $5.1 \times 10^{-5} M_{\odot}$ of warm dust at 859 d and 996 d, respectively (Szalai et al., 2011). For SN 2004et, Fabbri et al. (2011) used a more sophisticated clumpy dust model with an R^{-2} density distribution, a range of grain sizes from 0.1 to 1 μm , and a graphite to silicate ratio of 1:4. Their largest mass estimate is $\sim 10^{-3} M_{\odot}$ at 690d. Szalai and Vinkó (2013), using a graphite dust model, reported a maximum dust mass of $10^{-2} M_{\odot}$ for SN 2006bp at 628d. Most of the other Type II-P SNe in their sample produced around $5 \times 10^{-3} M_{\odot}$ of dust. The Type IIIn SNe with strong CSM interactions tend to show more warm dust mass as shown in Fig. 2.4. Fox et al. (2011, 2013) reported the typical dust mass, assuming graphite dust composition, of at most $2.2 \times 10^{-2} M_{\odot}$ with most of their sample having an observed dust mass of around $5 \times 10^{-3} M_{\odot}$. They conclude, as well, that most of the dust was pre-existing, and that the strong CSM interactions in Type IIIn events are able to heat up more dust than in other events with weaker or no CSM interactions. We conclude that

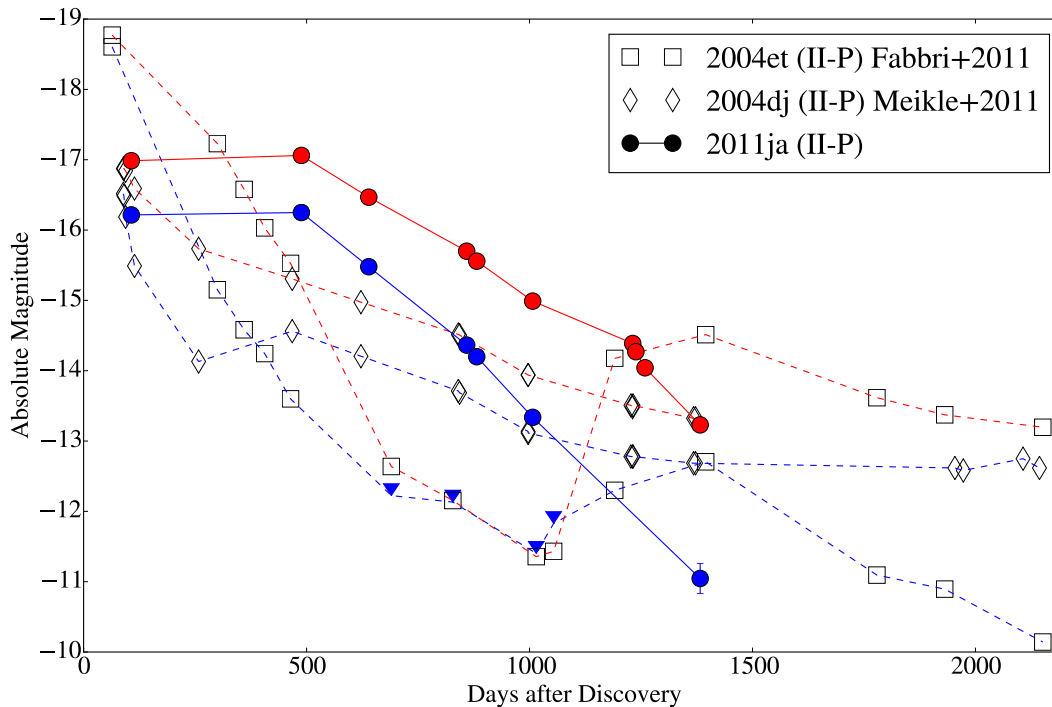


Figure 2.5: The light curve of SN 2011ja in both IRAC channels, in comparison with that of SN 2004et (Fabbri et al., 2011) and SN 2004dj (Meikle et al., 2011; Szalai et al., 2011). SN 2004et was not detected in the $3.6 \mu\text{m}$ band from around 700 d to 1100 d. The four downward arrows in the light curve of SN 2004et indicate the three sigma detection limits.

SN 2011ja stands out from other Type II events in our sample due to CSM interaction. In terms of the warm dust properties, it is not an outlier from the general population of interacting Type II-P SNe.

SN 2014C: An Interacting Stripped-Envelope Supernova with a Possible LBV Progenitor

SN 2014C is a Type Ib SN in the nearby galaxy NGC 7331, discovered on 2014 January 5. It was classified as a young Type Ib SN with a spectrum matching that of SN 1999ex at 6 days before maximum light (Kim et al., 2014). The velocities of He and Si absorption features are measured to be about $13,800 \text{ km s}^{-1}$ and $9,900 \text{ km s}^{-1}$, respectively. SN 2014C was observed with the Very Large Array (VLA) on 2014 January 11 to have a flux of $0.80 \pm 0.04 \text{ mJy}$ at 7 GHz (Kamble et al., 2014). It was detected by the Combined Array for Research in Millimeter Astronomy (CARMA; Bock et al., 2006) on 2014 January 13 at a flux level of $1.2 \pm 0.2 \text{ mJy}$ in 85 GHz waveband (Zauderer et al., 2014). Milisavljevic et al. (2015) analyzed optical spectra of SN 2014C and reported a remarkable metamorphosis of this SN

from a typical Type Ib to an interacting Type IIn. This is similar to the case of SN 2001em that underwent a similar transition from Type Ibc to Type IIn when $H\alpha$, X-ray, and radio emissions were detected ~ 2.5 years post-explosion (Chugai and Chevalier, 2006). Nonetheless, SN 2014C was the first example of this transition being caught in action with frequent observations during the transition. The onset of $H\alpha$ emission with intermediate line width along with an X-ray detection by the *Chandra Space Telescope* and the aforementioned radio emission are strong evidence of CSM interaction with a dense H-rich shell. The observations placed the shell radius at $\gtrsim 3 \times 10^{16}$ cm. Milisavljevic et al. (2015) constrained the density of the unshocked CSM by the relative strength of the narrow lines in the spectra. The absence of a [O II] line in the presence of [O III] lines set a lower limit on the density of 10^4 cm^{-3} . The relative strengths of the [Fe VII] lines sets the upper limit of the density at 10^7 cm^{-3} . Furthermore, the width of the unresolved [O III] line indicates that the CSM velocity is less than 100 km s^{-1} . Optical spectra presented by Milisavljevic et al. (2015) do not show a blueshifted line profile, as may be expected in case of new dust being formed in the ejecta behind the shock front (assuming spherical symmetry). If the geometry of the CSM is disk-like and not being viewed edge-on, CSM dust will not produce a blueshifted line profile. The earliest signature of CSM interactions observed from the ground came 113 d post-explosion when the SN emerged from behind the Sun. The only observation carried out before this gap was on 2014 January 9, four days before maximum in V band. The gap in ground-based observations is filled in with *Spitzer* observations presented here.

SN 2014C was observed in 9 epochs with *Spitzer*, with the first epoch at 45 d while the SN was behind the Sun for ground-based observers. The light curves in both channels were rising from ~ 250 days until the latest epoch at 801d. Fig. 2.6 shows the time evolution of the SED of SN 2014C along with concurrent NIR follow-up photometry at 274 d and 628 d post-explosion. The NIR fluxes indicate that the hot component of the SN has already faded, especially at 628d, and the SED is dominated by warm dust emissions in the mid-IR. Fluxes in both IRAC bands rise between 243 d and 622 d. The SEDs from the last three epochs from 772 to 801 d are almost identical. While this rebrightening in mid-IR has been observed in a number of other events, even in some Type Ia with CSM interactions (see SN 2005gj and SN 2002ic; Fox et al., 2013), it has rarely been observed directly in a stripped-envelope CCSN. (One such case was Type Ibn SN 2006jc (Smith et al., 2008) where dust formed in the post-shock gas at 50–100 days after discovery.) Multiple mechanisms could cause an SN to rebrighten in mid-IR at late times. In

Type II SNe such as SN 2004dj and SN 2004et discussed earlier, the rebrightening can also be attributed to new dust being formed in either the SN ejecta or the CDS behind the shock. However, due to the lack of dust attenuation in optical spectral lines, this scenario is unlikely. In the cases of Type Ia-CSM events where dust production is not expected, Fox et al. (2013) showed that the rebrightening can be attributed to a pre-existing dust shell being radiatively heated by optical and X-Ray photons from CSM interactions. Another possible scenario is the collisional heating of pre-existing dust by the forward shock. Next we consider these last two shock heating mechanisms.

Assuming a gas-to-dust mass ratio of 100 and that the dust sputtering timescales are significantly shorter than the cooling timescale of the shocked CSM, Fig. 2.4 shows that the observed dust mass of SN 2014C is consistently higher than the predicted CSM mass heated by a $15,000 \text{ km s}^{-1}$ shock. Notably, the blackbody radius, which gives the lower limit for the dust shell size (e.g., Fox et al. 2011), is a factor of 5 larger than the shock radius assuming a shock velocity of $v_s = 15,000 \text{ km s}^{-1}$ at +45 d. This is an indication that, at least for this earliest epoch, the observed mid-IR flux is likely due to pre-existing dust radiatively heated by CSM interactions. This requires that SN 2014C starts to interact with the environment as early as 45 days post-explosion. However, there are no X-Ray observations at that epoch to confirm the CSM interactions. Milisavljevic et al. (2015) report an X-Ray luminosity of $1.3 \times 10^7 L_\odot$ at 373 d, which can provide the dust luminosity observed around the same epochs.

We can estimate the CSM density by making a simple assumption about the geometry for this scenario. At the 45 d epoch, the site of interaction is at the shock radius $r_s = (2 - 6) \times 10^{15} \text{ cm}$ assuming shock velocities of $v_s = 5,000 - 15,000 \text{ km s}^{-1}$. The number density of hydrogen in the CSM can be approximated by

$$n_{\text{H}} = \frac{3M_{\text{d}}}{4\pi((r_s + r_d)^3 - r_s^3)} \frac{\chi}{m_{\text{H}}}, \quad (2.4)$$

where r_d is the radial thickness of the mid-IR-emitting dust and χ is the gas-to-dust mass ratio for which we adopt a value of 100. The thickness r_d can be approximated assuming the dust in the CSM is in thermal equilibrium with the incident radiation from the shock at a temperature of 550 K (the mean inferred dust temperature over all epochs). We assume the CSM is optically thin and composed of a uniform distribution of $0.1 \mu\text{m}$ -sized amorphous carbon-type grains, where $0.1 \mu\text{m}$ is representative of the peak of the (Mathis et al., 1977) grain size distribution.

The approximate distance at which $0.1 \mu\text{m}$ carbonaceous grains are in thermal equilibrium with optical and UV photons of luminosity $\sim 10^7 L_\odot$ (Milisavljevic et al., 2015; this work) is $r_d \sim 6 \times 10^{16}$ cm, consistent within a factor of 2 of the blackbody radius. From equation (2.4), we therefore derive a gas number density of $n_{\text{H}} \sim 3 \times 10^5 \text{ cm}^{-3}$. This is consistent with the limits of $10^4 - 10^7 \text{ cm}^{-3}$ independently derived by Milisavljevic et al. (2015). We note that the range of assumed shock velocities does not significantly affect n_{H} since $r_d \gg r_s$ at 45 d. Furthermore, taking the velocity of the CSM of 100 km s^{-1} to be constant, and the blackbody radius as an approximate size of the CSM shell, this material must have been ejected from the progenitor of SN 2014C at least 100 years before the explosion.

Milisavljevic et al. (2015) propose three possible origins for the CSM shell around SN 2014C: a short-lived Wolf–Rayet (WR) phase that swept up a slower red supergiant (RSG) wind, a single eruptive ejection from a luminous blue variable (LBV) or binary interaction, or externally influenced CSM confinement. All of these scenarios require a brief (10^3 yr) phase after the hydrogen envelope has been stripped. Although a thorough analysis of each scenario is beyond the scope of this paper, we present brief discussions on the implications of our results on the binary interaction and LBV eruption scenarios.

A possible origin for the dense dusty CSM of SN 2014C is an outflow from a massive binary formed as the result of non-conservative mass transfer during a brief Roche-lobe overflow phase (Vanbeveren et al., 1998). Such an event is thought to produce stripped-envelope WRs and is claimed to be occurring in the interacting binary system such as NaSt1 (e.g., Crowther and Smith, 1999; Mauerhan et al., 2015) and RY Scuti (Smith et al., 2011a). Both systems host a WR-like star surrounded by a dusty, hydrogen-rich shell and may therefore be an example of a possible SN 2014C progenitor. The dust-formation efficiency and mass-loss properties from massive binaries during non-conservative mass transfer are, however, unclear due to the paucity of observations of these systems.

We now consider the LBV eruption scenario. LBV nebulae exhibit outflow velocities of $\sim 100 \text{ km/s}$ (Smith, 2014), which are consistent with the observational constraints on the CSM velocity ($\lesssim 100 \text{ km/s}$; Milisavljevic et al., 2015) and imply a dynamical timescale of $\lesssim 100$ yr given the inferred CSM blackbody radius. This timescale agrees with the observed $\sim 1-10$ yr eruptive phases of LBVs. Given the inferred dust mass of the CSM ($2 \times 10^{-3} M_\odot$) and assuming a gas-to-dust mass ratio of 100, the implied mass-loss rate during the formation of the CSM is therefore $\gtrsim 2 \times 10^{-2} M_\odot$.

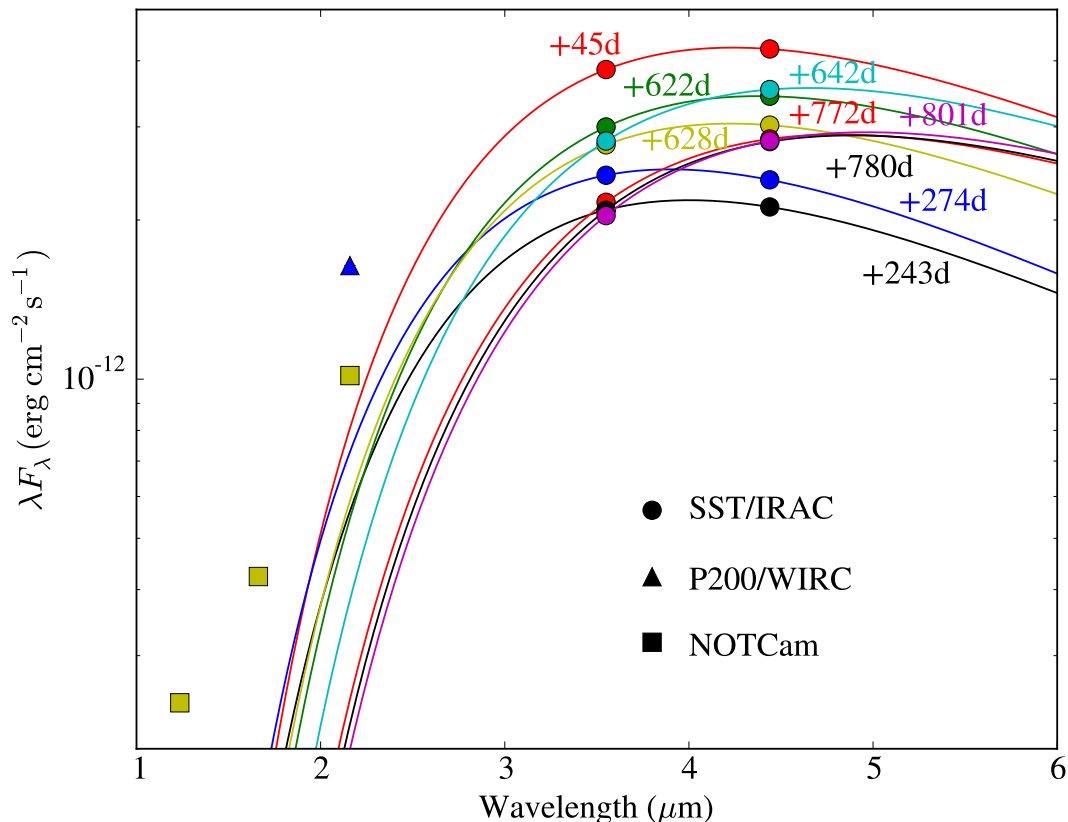


Figure 2.6: An SED of SN 2014C ranging from 45 d to 642 d post-explosion. *Spitzer*/IRAC data are plotted in circles. Near-IR follow-up observations obtained at the Nordic Optical Telescope near-infrared Camera and spectrograph (NOTCam) are plotted in squares, and the data obtained using the Wide-field InfraRed Camera (WIRC) on the 200-inch Telescope at Palomar Observatory are plotted in triangles. The overplotted lines are the best fit of equation (2.1) using only mid-IR data.

yr^{-1} and consistent with observed and predicted LBV mass-loss rates (Kochanek, 2011; Smith, 2006). Observations of dusty LBV nebulae typically reveal $\gtrsim 0.01 M_{\odot}$ (Smith, 2006) of dust; however, we note that several LBV nebulae such as G24.73+0.69, HD 168625, and Hen 3-519 exhibit dust masses similar to that of the CSM ($0.003 - 0.007 M_{\odot}$; O’Hara et al., 2003, Clark et al., 2003, Smith et al., 1994). The consistency between mass loss properties of an LBV outburst and the measured dust mass and radius of the CSM point to a single LBV-like eruption roughly 100 years pre-explosion as a plausible origin of the CSM shell around SN 2014C.

We conclude that the *Spitzer* observations of SN 2014C are consistent with dust being heated by optical/X-Ray photons from an ongoing interaction between the SN shock and a CSM that originated from a LBV-like eruption.

SN 2014bi: The Extremely Low Color Temperature

SN 2014bi is a low-luminosity Type II-P SN detected in the galaxy NGC 4096, 11.3 Mpc away, on 2014 May 31 (Kumar et al., 2014). At the first epoch, 39 d post-explosion, the SED is still dominated by the SN light. SN 2014bi is about 1.5 mags dimmer than SN 2011dh at the same epoch in both channels with a smaller [3.6]-[4.5] color of 0.2 mag. However, 200 days later, SN 2014bi becomes a very red source with [3.6]-[4.5] = 2.97 mag. This color temperature is associated with a low blackbody temperature of around 200 K. The warm dust mass calculated for this event is about $7.24 \times 10^{-2} M_{\odot}$ at 264d, which is relatively high in comparison to dust masses for other CCSNe. However, the dust mass drops sharply to $2.54 \times 10^{-2} M_{\odot}$ only 4 days later. And by 293d, the dust mass drops further to $7.31 \times 10^{-3} M_{\odot}$, an order of magnitude lower than that in the second epoch. At 445d, the warm dust is almost gone, with a residual value of only $8.32 \times 10^{-5} M_{\odot}$. During this period, the apparent color temperature also increases to 423 K.

There are a number of possible causes for this drop in warm dust mass. Firstly, this could be a signature of the SN shock that overtakes and destroys the dust shell. If the existing dust was being destroyed by a shock, then it would need to heat up before being destroyed, consistent with the observed small increase in color temperature. If we assume this scenario we can calculate the density of the dust shell. To get an upper limit of the density, we assume a slow shock velocity of $v_s = 5,000 \text{ km s}^{-1}$. Assuming a grain size of $0.1 \mu\text{m}$ as before and a grain density of 2 g cm^{-3} , the number density of dust particles needed to account for the observed decline in mass is only $3 \times 10^{-2} \text{ cm}^{-3}$ which is very low considering the typical density of a dust shell $\sim 10^5 \text{ cm}^{-3}$. Second, another possible explanation is that the radiative heating source, e.g., emission from CSM interactions, is fading; thus the amount of heated dust decreases. Finally, due to the lack of data at shorter wavelengths, it is also possible that a hotter component of the SN has cooled down and started to emit more significantly in the $3.6 \mu\text{m}$ band. In this case, the SED fit will underestimate the dust mass. We emphasize again that the $3.6 \mu\text{m}$ band can be contaminated by the PAH emission while the $4.5 \mu\text{m}$ band can be contaminated by CO emission at $4.65 \mu\text{m}$. If *Spitzer* has still been cold, the IRS spectroscopy could have elucidated the nature of this SN.

Supernovae with Long-lived Infrared Emission Decades After Explosion

We detect IR emission from SN 1974E (II), SN 1979C (II-L), SN 1980K (II-L), SN 1986J (IIIn), and SN 1993J (IIb), more than 20 years after explosion. The ex-

tended light curves for SN 1993J and SN 1979C in Fig. 2.7 show that the luminosity for both events is still declining. This indicates that we are still detecting the light associated with the SN and not just a constant background source, the remnant, or the companions of the progenitors of those SNe. The notable features of these old SNe are that they have a color of $[3.6]-[4.5] \approx 1$ mag, and that the evolution is very slow. SN 1993J faded by ≈ 1 mag over the course of a decade while the older SN 1979C evolved even more slowly, fading only by ≈ 0.2 mag over a decade. For other events without enough epochs of data to construct good light curves, we present the image-subtraction thumbnails which show that the SN has at least decayed from the reference epoch in Fig. 2.8. From the thumbnails, one can appreciate the importance of image subtraction. In most cases, it is not possible to determine from the science frames alone whether or not we have a detection. Even in cases where there is an obvious source at the location of the SN, it is still difficult to differentiate between the SN light and the surrounding contribution. Image subtraction using a baseline of almost a decade as used in this work uncovers a number of old SNe which have never been reported to have late-time mid-IR emission previously (see Table 1 in Fox et al., 2011).

2.5 Conclusion

We have presented a systematic study of the general population of nearby supernovae that are hosted by galaxies in the SPitzer InfraRed Intensive Transient Survey (SPIRITS). The main results are threefold: (1) the detection statistics for the whole SNe sample; (2) light curves for CCSNe and time evolution of dust parameters associated with each event; and (3) detailed case studies of several unusual events.

The detection statistics were obtained by visually vetting all observations of all SNe in the SPIRITS footprint. The results show that Type Ia SNe fade away much more quickly than Type Ib/c and Type II core-collapse SNe, with none of the Type Ia living past 3 years, unless they have CSM interactions. Type II SNe, on the other hand, tend to live for a very long time, with 10 events living longer than 3 years. Five of those events, SN 1974E (II), SN 1979C (II-L), SN 1980K (II-L), SN 1986J (II_n), and SN 1993J (II_b), are detected decades after the explosion, providing the first sample of mid-IR observation of CCSNe at such late epochs. Other earlier surveys of SNe in the *Spitzer* archive missed these events because image subtraction was not done to reveal the subtle time evolution underneath the bright galaxy background.

We have created light curves collages for Type Ib/c and Type II SNe that have pre-

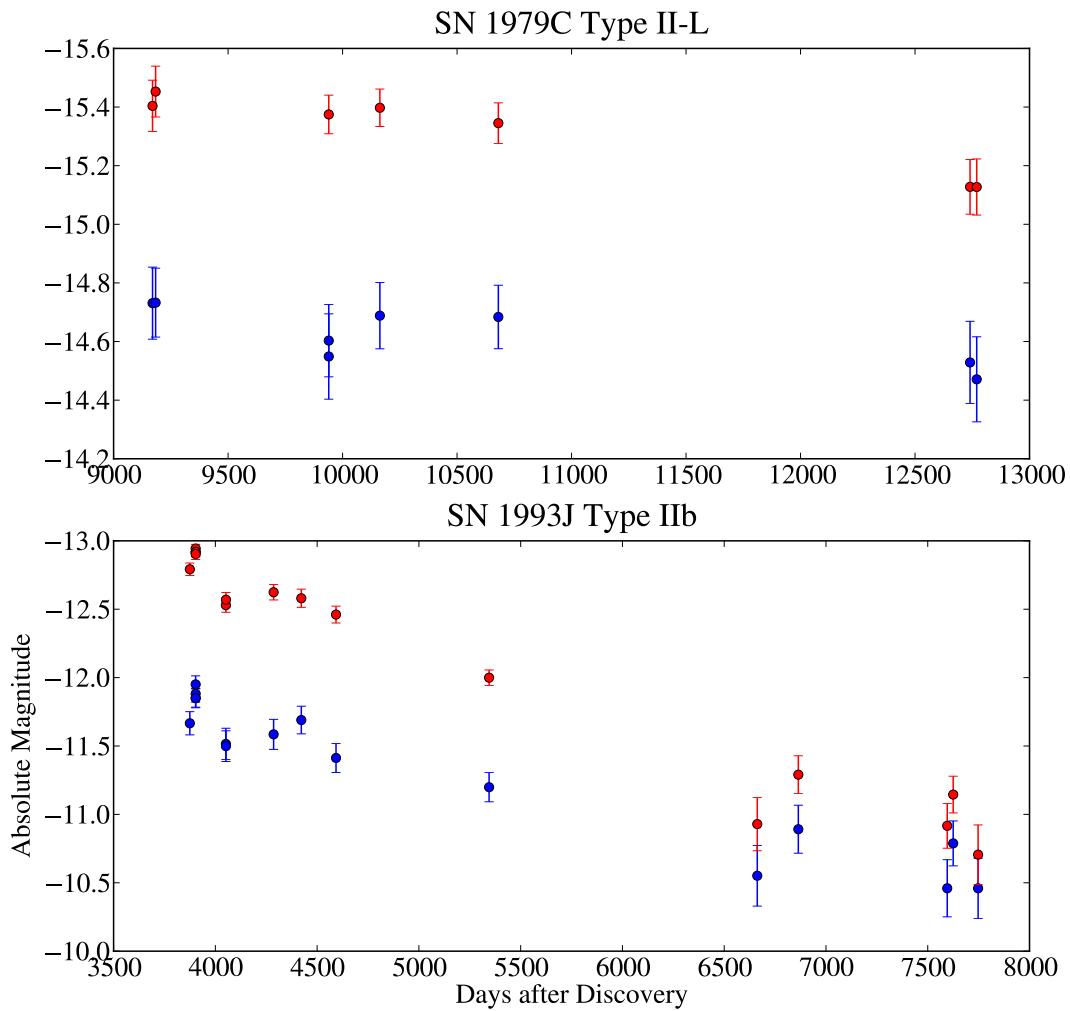


Figure 2.7: Two light curves show the very late-time evolution of SN 1979C (top) and SN 1993J (bottom). The data are aperture photometry from the science frames, so the background contribution has not been fully subtracted out. For SN 1993J, the background emission is minimal. For SN 1979C, the photometry is affected by association with a cluster. The SN light alone indeed was not as bright as [4.5] \sim -15 mag at such late epochs.

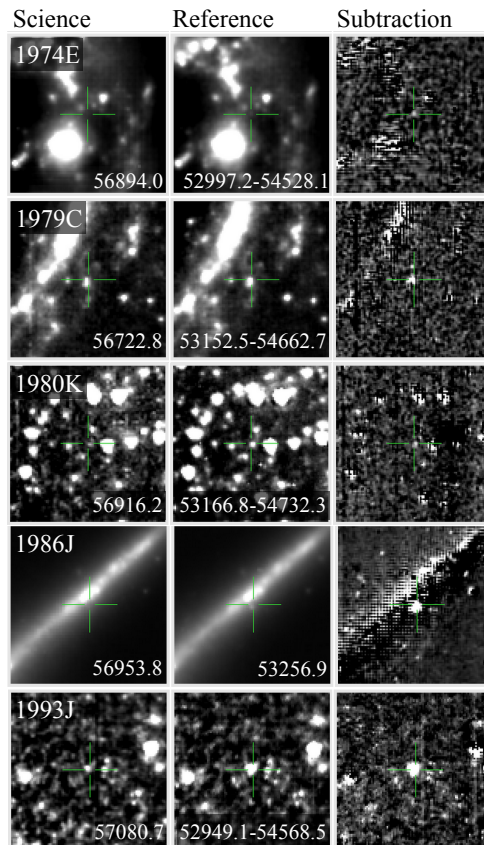


Figure 2.8: Image subtractions of five old Type II SNe showing the decrease in flux in the science frames taken at the later epochs compared to the references. From top to bottom, SN 1974E (II), SN 1979C (II-L), SN 1980K (II-L), SN 1986J (II_n), and SN 1993J (II_b). The MJD of each observation is shown on top of the image. In most cases, the references are stacks of *Spitzer* observations over the MJD ranges shown.

explosion reference images using image-subtraction-based photometry. The light curves are heterogeneous compared to the light curves of Type Ia events. The SEDs of the events with image-subtraction-based photometry of both IRAC channels at the same epoch have been fitted with an elementary dust model with graphite grains of radius $0.1 \mu\text{m}$ at a single temperature. Luminosity, temperature, and warm dust mass were obtained from the fit. Our observations are only sensitive to warm dust and there could be more cold dust in these SNe that we could not detect. The light curves and temporal evolution of the dust parameters reveal some outliers from the general norm. An outlier among the Type Ib/c SNe is SN 2014C, which rebrightens around 260 d post-explosion with increasing observed dust mass. The lack of signatures for dust formation in the optical spectra (Milisavljevic et al., 2015)

suggests that the emission in this SN comes from pre-existing dust. The blackbody radius at the first epoch suggests that the dust shell is heated by emission from CSM interaction. From the dust mass and blackbody radius, we obtain an estimate for the gas density of $\sim 10^6 \text{ cm}^{-3}$, which is consistent with an LBV origin.

The majority of the hydrogen-rich Type II SNe's light curves loosely follow that of SN 2011dh, a well-observed Type IIb SN. We identify two interesting outliers. SN 2011ja (II-P) is over-luminous at 1000 days post-discovery. The temporal evolution of its dust parameters seems to suggest either an episode of dust production near the shock front or radiative heating of pre-existing dust by CSM interactions. The location of the emission at $\sim 10^{16} \text{ cm}$ agrees with the location of new dust formation in the CDS model proposed by (Andrews et al., 2016). SN 2014bi (II-P), on the other hand, is under-luminous and has a very low color temperature. The evolution of its dust parameters is opposite of that of other events, suggesting either dust destruction or dust heating with fading source. The dust mass determined for all events agree with the consensus that core-collapse SNe only produce 10^{-6} to $10^{-2} M_{\odot}$ of dust at early times. Few studies of late-time emission from cold dust ($\sim 10 \text{ K}$) show promising signs that the amount of dust required for CCSNe to contribute significantly to the cosmic dust content could be formed later on in their evolution (e.g., Barlow et al., 2010; Gomez et al., 2012; Indebetouw et al., 2014; Lau et al., 2015).

This work demonstrates the power of multi-epoch mid-IR observations as a tool for studying the diversity in evolution of CCSNe. Future wide-field IR surveys that have no biases in pre-selecting SNe types could capture more events with shorter cadence, allowing for an even better statistical sample for a systematic study. This, accompanied by IR spectroscopic follow-up observations enabled by the *James Webb Space Telescope*, would further our understanding of physics of CCSNe.

Acknowledgement

This work made use of observations from the *Spitzer Space Telescope* operated by the Jet Propulsion Laboratory, California Institute of Technology, under a contract with NASA. We acknowledge the use of some data from PIDs 70207 (PI: Helou); 80239 and 90178 (PI: Andrews); 10139 (PI: Fox); and 10046 (PI: Sanders). Ground-based observations presented were obtained at the Palomar Observatory, operated by California Institute of Technology. The Mount Lemmon Observing Facility is operated by the University of Minnesota. The Nordic Optical Telescope is operated

by the Nordic Optical Telescope Scientific Association at the Observatorio del Roque de los Muchachos, La Palma, Spain, of the Instituto de Astrofísica de Canarias. We are grateful for support from the NASA Spitzer mission grants to the SPIRITS program (PIDs 10136 & 11063). This research made use of Astropy, a community-developed core Python package for Astronomy Astropy Collaboration et al. (2013). We thank the anonymous referee for comments and suggestions. ST thanks Bill Scanlon for a close read of the manuscript. ST was supported by the Royal Thai Scholarship and a portion of this work was done while under the Claremont-Carnegie Astrophysics Research Program. RDG was supported by NASA and the United States Air Force.

Chapter 3

SUPERNOVA 2017eaw: MOLECULE AND DUST FORMATION
FROM INFRARED OBSERVATIONS

Tinyanont, S. et al. (Mar. 2019). “Supernova 2017eaw: Molecule and Dust Formation from Infrared Observations”. In: *ApJ* 873.2, 127. DOI: 10.3847/1538-4357/ab0897. arXiv: 1901.01940 [astro-ph.HE].

Samaporn Tinyanont¹ Mansi M. Kasliwal¹ Kelsie Krafton² Ryan M. Lau³
Jeonghee Rho^{4,5} Douglas C. Leonard⁶ Kishalay De¹ Jacob Jencson¹ Dimitri
Mawet^{1,7} Maxwell Millar-Blanchaer^{7,8} Ricky Nilsson^{1,7} Lin Yan¹ Robert D.
Gehrz⁹ George Helou¹⁰ Schuyler D. Van Dyk¹⁰ Eugene Serabyn⁷ Ori D. Fox¹¹
Geoffrey Clayton²

¹Division of Physics, Mathematics and Astronomy, California Institute of Technology, 1200 E. California Blvd., Pasadena, CA 91125, USA

²Department of Physics and Astronomy, Louisiana State University, Baton Rouge, LA 70803, USA

³Institute of Space & Astronautical Science, Japan Aerospace Exploration Agency, 3-1-1 Yoshinodai, Chuo-ku, Sagami-hara, Kanagawa 252-5210, Japan

⁴SETI Institute, 189 N. Bernardo Ave, Suite 200, Mountain View, CA 94043, USA

⁵SOFIA Science Center, NASA Ames Research Center, MS 232, Moffett Field, CA 94035, USA

⁶Department of Astronomy, San Diego State University, San Diego, CA 92182, USA

⁷Jet Propulsion Laboratory, California Institute of Technology, Pasadena, CA 91109, USA

⁸NASA Hubble Fellow

⁹Minnesota Institute for Astrophysics, School of Physics and Astronomy, University of Minnesota, 116 Church Street, S. E., Minneapolis, MN 55455, USA

¹⁰Caltech/IPAC, Mailcode 100-22, Pasadena, CA 91125, USA

¹¹Space Telescope Science Institute, 3700 San Martin Dr, Baltimore, MD 21218, USA

Abstract

We present infrared (IR) photometry and spectroscopy of the Type II-P SN 2017eaw and its progenitor in the nearby galaxy NGC 6946. Progenitor observations in the *Ks* band in four epochs from 1 yr to 1 day before the explosion reveal no significant variability in the progenitor star greater than 6% that lasts longer than 200 days. SN 2017eaw is a typical SN II-P with near-IR and mid-IR photometric evolution similar to those of SNe 2002hh and 2004et, other normal SNe II-P in the same galaxy. Spectroscopic monitoring during the plateau phase reveals a possible high-velocity He I 1.083 μm absorption line, indicative of a shock interaction with the circumstellar medium. Spectra between 389 and 480 days post-explosion reveal a strong CO first

overtone emission at 389 days, with a line profile matching that of SN 1987A from the same epoch, indicating $\sim 10^{-3} M_{\odot}$ of CO at 1800 K. From the 389 days epoch until the most recent observation at 566 days, the first overtone feature fades while the $4.5 \mu\text{m}$ excess, likely from the CO fundamental band, remains. This behavior indicates that the CO has not been destroyed, but that the gas has cooled enough that the levels responsible for first overtone emissions are no longer populated. Finally, the evolution of *Spitzer* $3.6 \mu\text{m}$ photometry shows evidence for dust formation in SN 2017eaw, with a dust mass of 10^{-6} or $10^{-4} M_{\odot}$ assuming carbonaceous or silicate grains, respectively.

3.1 Introduction

Massive stars ($M \gtrsim 8 M_{\odot}$) conclude their evolution in a core-collapse supernova (CCSN) when the nuclear fuel in their core is exhausted. The most common CCSNe are of Type II-P, whose defining features are a plateau in their light curves where the bolometric luminosity remains constant for ~ 100 days and strong hydrogen features in all phases of their spectral evolution (see, e.g., Filippenko, 1997 for SN types). The persisting presence of hydrogen points to progenitor stars with hydrogen remaining in the stellar envelope at the time of core collapse. Archival pre-explosion observations of a number of nearby SNe II-P have indeed revealed hydrogen-rich red supergiant (RSG) progenitor stars (Smartt, 2009 and references therein). While SNe II-P are the most common—and most well understood—among subtypes of CCSNe, there are several aspects of the explosion that remain to be understood, both theoretically and observationally. Examples of unanswered questions regarding SNe II-P include the landscape of the circumstellar medium (CSM) around their RSG progenitors and the chemical evolution and dust formation in their ejecta. Some SNe II-P show signatures of shock interaction with a CSM, even though the typical RSG progenitors are expected to have steady wind-driven mass loss with no dense CSM at the time of core collapse. These signs of shock interaction include weak X-ray and radio emission from the shocked material and infrared (IR) emission from dust, which is either pre-existing or newly formed. Another aspect of SNe II-P that is not yet well understood is the chemical evolution of their ejecta. CCSNe are a promising source of dust in the early universe, making it crucial to understand how molecules and dust grains evolve in their ejecta. While chemical evolution models of the ejecta of SNe II-P have existed for decades, the observational data (mostly IR) required to test them remain sparse due to the limited number of nearby normal SNe II-P that can be observed in great detail out to late times.

While we expect SNe II-P in a pristine environment in comparison to SNe with stripped-envelope progenitors, recent observations, especially in the IR, show several SNe II-P with weaker signs of interactions with a CSM likely ejected within decades to centuries before the SN. In the strongest case of interaction with a dense CSM, one can observe narrow recombination lines from the CSM gas photoionized by high-energy photons from the interaction region (spectral Type IIn; Schlegel, 1990). For SNe II-P, however, the narrow lines are not present, and the main signatures of the interaction are X-ray and radio emissions coming from the shocked CSM gas, with lower luminosity indicating a less dense CSM in comparison to that of SNe IIn (e.g., SNe 2013ej, Chakraborti et al., 2013; 2011ja, Chakraborti et al., 2016). CSM interactions also leave spectroscopic imprints, such as a high-velocity absorption feature of $H\alpha$ and He I $1.083 \mu\text{m}$ (Chugai et al., 2007) and asymmetric and multi-peaked hydrogen lines associated with a toroidal CSM (e.g., SNe 2007od, Andrews et al., 2010; 2011ja, Andrews et al., 2016). Finally, the CSM interaction can trigger new dust formation and heat pre-existing dust, both of which emit in the thermal IR.

The CSM interaction can trigger dust formation by generating a reverse shock propagating back into the ejecta, creating a cold dense shell (CDS) between the forward and reverse shocks. Conditions in the CDS are suitable for dust formation. In some SNe, CDS dust formation can happen early ($\lesssim 300$ d), before the outer ejecta have cooled enough for dust formation (although recently Sarangi et al., 2018a have argued that before 380 d, high-energy photons from the shock interaction region inhibit dust formation in the CDS). Early dust formation, likely in the CDS, has been observed in many interacting SNe, for example, SNe 2005ip, (IIn; Fox et al., 2009; Smith et al., 2009a); 2006od, (II-P; Andrews et al., 2010); 2010jl, (IIn Gall et al., 2014); 2011ja (II-P Andrews et al., 2016; Tinyanont et al., 2016). Nearby SNe 2004dj and 2004et both showed rebrightening in their IR light curves attributable to dust formation (Fabbri et al., 2011; Kotak et al., 2009; Meikle et al., 2011; Szalai et al., 2011). In SN 2004et, the dust formation at $\sim 1,000$ days post-explosion likely occurred in the CDS between the SN forward shock and the reverse shock generated by a delayed CSM interaction. Kotak et al. (2009) showed that the spectral energy distribution (SED) from 200 to 500 d post-explosion exhibited strong signatures of carbon monoxide (CO) and silicon monoxide (SiO) at 4.67 and $8 \mu\text{m}$ along with a broad silicate grain feature around $9.7 \mu\text{m}$, suggesting a mixture of carbonaceous and silicate grains formation. Most of these observations were enabled by *Spitzer Space Telescope* (Gehrz et al., 2007; Werner et al., 2004)/Infrared Array Camera (IRAC; Fazio et al., 2004) observations and, for a limited number of CCSNe, by

the cold mission instruments Infrared Spectrograph (IRS; Houck et al., 2004) and the Multiband Imaging Photometer for *Spitzer* (MIPS; Rieke et al., 2004). These observations are sensitive to the thermal emission from dust with temperature of 200–1000 K. We note here that the CSM dust can create an IR light echo from the peak SN light without any CSM–shock interaction. However, observations have shown that IR light echoes cannot explain the large amount of IR radiation seen at late times, even in SN 2011dh where the IR light curve faded quickly in comparison to other CCSNe (Helou et al., 2013).

In addition to observations of a handful of SNe during its cold mission, *Spitzer* observed multiple SNe during the warm mission when only the IRAC 3.6 and 4.5 μm imaging channels were available. While the full spectral coverage, especially around the 9.7 μm silicate feature, is not available, warm *Spitzer* studies have shown a diversity in the IR light-curve evolution among SNe II-P. Our previous work (Tinyanont et al., 2016) presented a *Spitzer* survey of 36 CCSNe in nearby galaxies out to 20 Mpc showing that IR emission later than 100 d is common among CCSNe, with some SNe II-P showing signs of CSM interactions (see Szalai et al., 2019 for a more recent compilation of *Spitzer* observations of SNe). The most unique among our sample were SN 2011ja with bright and almost constant IR luminosity out to ~ 1000 d and SN 2013ej with IR rebrightening. Both SNe showed signs of CSM interactions from X-ray observations (Chakraborti et al., 2013, 2016), optical spectroscopy (Andrews et al., 2016; Mauerhan et al., 2017), and, for SN 2013ej, spectropolarimetry (Mauerhan et al., 2017). SN 2011ja likely formed dust very early at 105 d post-explosion (Andrews et al., 2016). These observations demonstrate the range of epochs at which the CSM interactions and/or dust formation begin around SNe II-P.

Dust grains can form not only in the CDS created by the CSM interaction, but also in the ejecta of the SN itself after they have sufficient time to cool. This is arguably the more important channel of dust formation because it can operate whether or not the SN has a CSM interaction. To understand dust formation in the ejecta, it is crucial to have a realistic chemical evolution model. Several models in the past have relied on simplistic classical nucleation theory (CNT) or kinetic nucleation theory (KNT) in which dust formation is parameterized in some way to simplify the calculation (see Sarangi et al., 2018b; Sluder et al., 2018 for a summary of different classes of chemical evolution models). In the past decade, modelers have started to employ molecular nucleation theory (MNT), which simulates molecule and dust

formation in the SN ejecta only using a realistic network of chemical reactions. The MNT models are the only ones that explicitly simulate molecule and dust evolution simultaneously. Molecules are crucial for dust formation because they are effective at cooling the ejecta to temperatures suitable for dust condensation and can act as seed nuclei. Some molecules are direct precursor species to dust grains. For example, SiO is a building block for silicate grains. The summary of observational data on CO and SiO mass evolution in a few SNe in comparison to a $15 M_{\odot}$ model can be found in Figures 3 and 4 in Sarangi and Cherchneff (2013), respectively. The same comparison for observed dust mass in 12 SNe and four different progenitor models can be found in Figure 10 from Sarangi and Cherchneff (2015). The observations required to measure molecule and dust mass are difficult and are sparse as a result. For molecule formation in SN ejecta, only ~ 10 observations have been reported (see the summaries by Gerardy et al., 2002 and Sarangi et al., 2018b, and references therein). Additional observations are required to bridge the gap between the small dust masses of $10^{-4} - 10^{-3} M_{\odot}$ inferred at a few hundred days post-explosion from near to mid-IR observations (e.g., Szalai and Vinkó, 2013; Tinyanont et al., 2016) and the larger dust masses of $0.01-0.1 M_{\odot}$ inferred in supernova remnants Cas A (Barlow et al., 2010; Rho et al., 2008), Crab Nebula (Gomez et al., 2012), Sgr A East (Lau et al., 2015), and in SN 1987A (Indebetouw et al., 2014; Matsuura et al., 2015) inferred from far-IR and submillimeter observations.

SN 2017eaw is the most recent nearby event for which detailed late-time IR observations, required to investigate the issues described above, were possible. SN 2017eaw was discovered on 2017 May 14 in NGC 6946 as its 10th SN in the past century (Wiggins, 2017). Early spectroscopic observations showed that it was a typical young SN II-P with a spectrum similar to that of SN 1999gi at 3.8 days post-explosion (Tomasella et al., 2017). Early radio observations immediately after detection resulted in non-detections at 1.39, 5.1, and 15 GHz by the Giant Metrewave Radio Telescope (GMRT), the electronic Multi-Element Remotely-Linked Interferometer Network (e-MERLIN), and the Arcminute Microkelvin Imager Large Array (AMI-LA), respectively. At 1.39 GHz, Nayana and Chandra (2017b) reported an early non-detection on 2017 May 18 with an upper limit of $114 \mu\text{Jy}$. Thirty-six days later on 2017 June 23, the SN was detected at $230 \pm 68 \mu\text{Jy}$ (Nayana and Chandra, 2017a). At 5.1 GHz, Argo et al. (2017a) reported an early non detection on 2018 May 20 with an upper limit of $65 \mu\text{Jy}/\text{beam}$. Subsequent observations on May 29.55, 30.81, and June 1.71 detected a rising flux of 280 ± 25 , 350 ± 51 , $427 \pm 23 \mu\text{Jy}$, respectively (Argo et al., 2017b). Lastly, AMI-LA observations at 15 GHz on May 15, 17, and 20 did

not yield any detections with upper limits of 0.5–1 mJy (Bright et al., 2017; Mooley et al., 2017). No AMI-LA observations have been reported during the epochs in which the SN was detected at 1.39 and 5 GHz. This increasing radio flux may be a sign of the SN shock running into the denser part of the CSM. X-ray observations by *Swift* on May 14 (Kong and Li, 2017) and the *Nuclear Spectroscopic Telescope Array* (*NuStar*; Harrison et al., 2013) on May 21 (Grefenstette et al., 2017) revealed a rising X-ray flux, also indicative of CSM interactions. The *NuStar* observations showed a hard spectrum with photons detected up to 30 keV and also revealed a shock-heated ionized Fe line at 6.65 keV. SN 2017eaw has also been observed with *Spitzer*/IRAC in the 3.6 and 4.5 μm bands as part of the ongoing SPitzer InfraRed Intensive Transients Survey (SPIRITS; Kasliwal et al., 2017). In addition to these potential signs of CSM interactions, optical and near-IR observations of this SN are consistent with those of other SNe with early dust formation. Tsvetkov et al. (2018) published optical photometry of the SN until 200 d post-explosion along with a preliminary comparison to different light-curve models. They noted the photometric similarity between this SN and SN 2004et, an aforementioned SN II-P in the same galaxy. Rho et al. (2018) reported Gemini near-IR spectroscopic follow-up from 22 to 205 d post discovery showing an emerging CO first overtone emission at $\sim 2.3 \mu\text{m}$, a clear signature of CO formation. They also reported a rising red continuum in the *K* band that could be coming from hot dust.

Here we present and discuss results from IR observations of SN 2017eaw and its progenitor. §3.2 summarizes archival near-IR imaging of the progenitor star and IR photometry and spectroscopy of the SN with both ground-based telescopes and *Spitzer*. In §3.2, we report near-IR photometry of the progenitor star of SN 2017eaw detected in ground-based imaging, including one epoch by the Keck/Multi-Object Spectrometer For Infra-Red Exploration (MOSFIRE) on 2017 May 9, five days before the discovery of the SN. We present IR light curves and spectroscopy of the SN in §3.2. We analyze the data in §3.3 and discuss the progenitor nonvariability in the *K* band, the IR photometry in comparison to other SNe II-P, and the SED and CO line profile and its evolution. A summary and conclusions are in §3.4.

3.2 Observations

Progenitor Infrared Photometry

NGC 6946 is a nearby galaxy ($d = 7.72$ Mpc; Anand et al., 2018), extremely prolific at producing SNe. Numerous pre-explosion observations of SN 2017eaw’s site, both from the ground and space, are available partly as a result of efforts to follow

the temporal evolution of SNe 2002hh, 2004et, and 2008S. The progenitor star has been detected in archival *Hubble* and *Spitzer* images, with an SED consistent with that of a dusty RSG star (Khan, 2017; Kilpatrick and Foley, 2018; Van Dyk et al., 2017). As part of the follow-up campaign for SPIRITS, we have imaged the SN site with the Wide field InfraRed Camera (WIRC; Wilson et al., 2003) on the 200 inch telescope at Palomar Observatory (P200 hereafter) in the J , H , and Ks bands on 2016 October 11, 7 months before the explosion, and in the Ks band on 2017 May 3, 11 days before the SN was first detected. We also imaged the SN site in the Ks band using MOSFIRE (McLean et al., 2012) at the Keck Observatory on 2016 May 30 and 2017 May 9. The second epoch was only 5 days before the SN was first detected. In both cases, data were taken with dithering patterns that send the galaxy in and out of the field of view to measure and subtract the sky background. Science images were dark subtracted and flattened using a flat-field image obtained from median-combining dithered sky images with sources masked out.

First, to identify the progenitor star, we compare pre-explosion images to an image of SN 2017eaw a year post-explosion. Fig. 3.1 (left) shows NGC 6946 in near-IR false color with the SN site annotated. The upper right panel shows the SN site (imaged by Keck/MOSFIRE in the Ks band) before and after the explosion to demonstrate that we have identified the progenitor star that is spatially coincident with the SN. We also note from these images that the galaxy light at the SN location is low in these bands, and we did not attempt any galaxy light subtraction. Moreover, the lower right panel of Fig. 3.1 shows a $24\ \mu\text{m}$ *Spitzer*/MIPS image showing that the dust emission from the SN location is also minimal. As such, we assume only Galactic extinction for SN 2017eaw ($E(B - V) = 0.305$; Schlafly and Finkbeiner, 2011) with no host extinction (consistent with Tomasella et al., 2017).

A point source is detected at the location of the SN in all observations, as shown in Fig. 3.2 top left. Aperture photometry with sky annulus subtraction was obtained with the zero point determined using ~ 100 stars in the field of view with magnitudes from the Two Micron All-Sky Survey (2MASS; Milligan et al., 1996, Skrutskie et al., 2006). The results are listed in Table 3.1 and plotted in Fig. 3.2 bottom left. We did not detect any significant variability, with a timescale greater than 200 days, of the progenitor star in the Ks band.

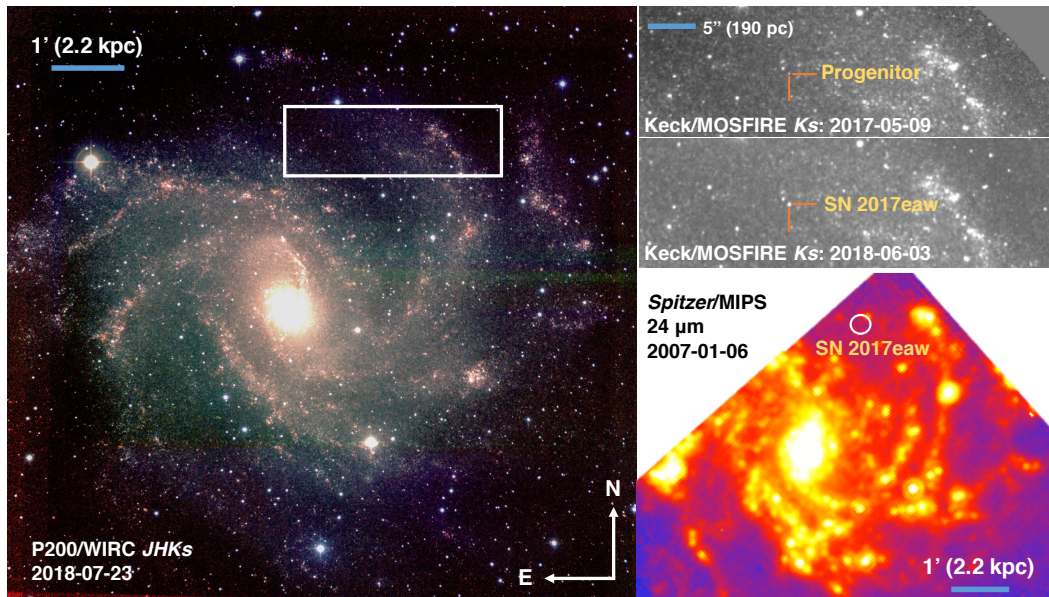


Figure 3.1: Left: color composite image of NGC 6946 taken with WIRC on 2018 July 23 with red, green, and blue corresponding to the J , H , and K_s bands. Top right: two images from the area marked by the white box in the left panel showing the location of the SN. Both images were taken with MOSFIRE on Keck. The top image shows the progenitor star on 2017 May 9 and the bottom image the SN on 2018 June 3. Bottom right: MIPS $24\ \mu\text{m}$ image of NGC 6946 taken pre-explosion on 2007 January 6 (PID 30494; PI: Sugerman). The distance scales are provided in all 3 images with the projected distances assuming the distance of 7.72 Mpc to NGC 6946. The orientation are all north up and east to the left.

Explosion Epoch

Tsvetkov et al. (2018) published optical photometry in the $UBVRI$ bands with data spanning from discovery (2018 May 14) until 208 days after discovery. They fitted a suite of light-curve models to the data and derived an explosion date of 2017 May 4, 10 days before the first detection. We note that this is inconsistent with our progenitor observation on 2017 May 9, which showed no increase in flux from the progenitor at that epoch. We instead fitted a low-order polynomial to their R and I bands light curves, which best capture the rise. We constrain the explosion date to 2017 May 10, consistent with our progenitor observation and also with the spectroscopic age constraint (+3.8 d on May 14; Tomasella et al., 2017). This simple polynomial fitting neglects the shock break-out phase, which typically only lasts ~ 1 day. We take 2017 May 10 as the explosion date of SN 2017eaw throughout this paper.

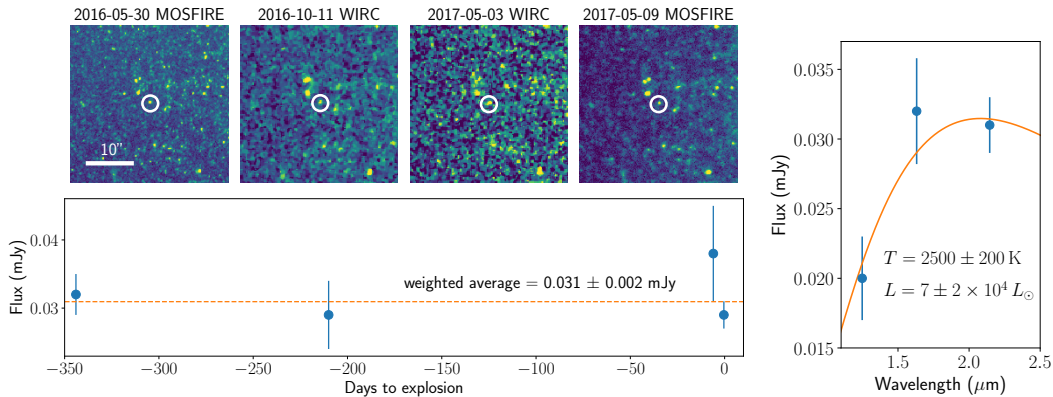


Figure 3.2: Left: images of the progenitor of SN 2017eaw from a year to ~ 1 day before explosion (5 days before first detection) taken in the Ks band with Keck/MOSFIRE and P200/WIRC. The progenitor is encircled in each image. WIRC images have been smoothed using a median filter for visualization. Photometry from these images (shown below the images) revealed no significant variability of the progenitor at a 6% level. Right: the near-IR SED of the progenitor star corrected for foreground extinction (Schlafly and Finkbeiner, 2011). Data in the J and H bands are from 2016 October 11 while the Ks band is the weighted average over all 4 epochs shown on the left. Assuming $d = 7.72$ Mpc, the best blackbody parameters fitted to the SED are $T = 2500 \pm 200$ K and $L = 7 \pm 2 \times 10^4 L_{\odot}$. These parameters are consistent with a RSG progenitor.

Supernova Photometry

We obtained photometry of SN 2017eaw in the near-IR J , H , and Ks bands using P200/WIRC and Keck/MOSFIRE in nine epochs, spanning 31–490 days post-explosion, with seven epochs during the nebular phase. The process for data reduction and aperture photometry was the same as in the last section. All near-IR photometry results are presented in Table 3.1, including those reported in Arkharov et al. (2017) and Rho et al. (2018). The 2MASS magnitudes were converted to flux densities using zero-magnitude flux densities of 1594, 1024, and 666.7 Jy for the J , H , and Ks bands, respectively (Cohen et al., 2003).

SN 2017eaw was observed with the *Spitzer* IRAC (Fazio et al., 2004) at $3.6 \mu\text{m}$ and $4.5 \mu\text{m}$ in six epochs: 126, 197, 246, 295, 315, 498, and 566 days post-explosion (PID 13053, PI: Kasliwal; PID 13239, PI: Krafton). We used a stack of archival pre-explosion *Spitzer* images to estimate and remove the galaxy background and nearby source contamination.¹ Archival images were rotated and aligned based

¹Archival *Spitzer* images used for background-subtraction came from the following PIDs and PIs: 60071, 70008, 80131, 90178, PI: Andrews; 80015, 10081, 11084, PI: Kochanek; 10136, 11063, 80196, 13053, PI: Kasliwal; 10002, PI: Sugerman.

on the sky coordinates supplied in *Spitzer* data, then median combined. In IRAC images in both channels of the 126 d epoch and the 3.6 μm channel of the 215 d epoch, columns of low counts due to a saturating star in the field of view crossed the SN. To remove these low count columns, we fitted a Gaussian profile across each column and added the missing flux back in. We conducted aperture photometry on the background-subtracted images and applied appropriate aperture corrections as given by the IRAC instrument handbook. *Spitzer* photometry results are listed in Table 3.1. *Spitzer* fluxes were converted to magnitudes for plotting purposes (Fig. 3.3) using the zero-magnitude fluxes of 280.9 and 179.7 Jy for the 3.6 and 4.5 μm channels, respectively. Fig. 3.3 shows the near-IR light curves of SN 2017eaw in comparison with those of other well-studied SNe II-P. The top panel shows light curves of the *J*, *H*, *Ks*, 3.6, and 4.5 μm bands of SN 2017eaw in comparison to those of SNe II-P 2002hh and 2004et in the same galaxy. The bottom panel shows only *Spitzer* data points compared with all SNe II-P observed with *Spitzer* (photometry taken from Szalai et al., 2019). Throughout the paper, we assume the distance to NGC 6946 of 7.72 Mpc based on the “tip of the red giant branch” (TRGB) technique (Anand et al., 2018; also used by Rho et al., 2018).

Spectroscopy

We obtained medium-resolution ($R \sim 2500$) near-IR (1–2.5 μm ; *YJHK*) spectroscopy with P200/TripleSpec (Herter et al., 2008) on 2017 August 9 (91 d), 2017 September 3 (116 d), 2018 June 22 (408 d), and 2018 July 23 (439 d). TripleSpec is a long-slit (1" \times 30") spectrograph, and we observed the SN using an ABBA dither pattern for sky subtraction. Type A0V standard stars HIP 94140 and HIP 75230 were observed either immediately before or after the SN observations to provide telluric correction and flux calibration. Standard and SN observations were taken on different parts of the slit when the SN was observed after the standard to avoid persistence on the detector. The reduction for TripleSpec data was done using a version of *Spextool* modified for TripleSpec (Cushing et al., 2004). It applies field flattening, retrieves a wavelength solution from sky lines present in science observations, subtracts each AB pair to remove most of the sky emission, and then fits a low-order polynomial to the different orders of spectral traces in the images. Simple spectral extraction is performed on the subtracted images (the optimal extraction algorithm (Horne, 1986) is not available in this version of the software). Telluric and flux calibrations were performed using *xtellcor* (Vacca et al., 2003), which derives the instrument’s efficiency by comparing the observed standard star spectrum with an A0V spectrum

Table 3.1: Near-infrared photometry

Date	MJD	Epoch (day)	F_J (mJy)	σ_{F_J} (mJy)	F_H (mJy)	σ_{F_H} (mJy)	F_{K_s} (mJy)	$\sigma_{F_{K_s}}$ (mJy)	$F_{[3.6]}$ (mJy)	$\sigma_{F_{[3.6]}}$ (mJy)	$F_{[4.5]}$ (mJy)	$\sigma_{F_{[4.5]}}$ (mJy)	Telescope
2016-05-30	57538.5	-345	—	—	—	—	0.030	0.003	—	—	—	—	Keck/MOSFIRE
2016-10-11	57672.1	-211	0.016	0.002	0.028	0.003	0.028	0.005	—	—	—	—	P200/WIRC
2017-05-03	57876.5	-7	—	—	—	—	0.04	0.01	—	—	—	—	P200/WIRC
2017-05-09	57882.6	-1	—	—	—	—	0.03	0.01	—	—	—	—	Keck/MOSFIRE
2017-05-17	57890.0	7	28.92	0.53	21.93	0.40	14.80	0.27	—	—	—	—	AZT/SWIRCAM ^a
2017-06-10	57914.5	31	33.82	4.67	22.34	1.65	17.95	1.65	—	—	—	—	P200/WIRC
2017-06-16	57920.0	37	36.07	1.33	28.38	1.31	21.99	0.81	—	—	—	—	MIRO ^b
2017-09-13	58009.7	126	—	—	—	—	—	—	4.441	0.003	6.132	0.006	Spitzer/IRAC
2017-10-03	58029.1	146	—	—	—	—	4.81	0.44	—	—	—	—	P200/WIRC
2017-10-10	58036.2	153	—	—	—	—	—	—	—	—	—	—	P200/WIRC
2017-10-30	58056.0	173	4.80	0.27	3.67	0.27	2.30	0.21	—	—	—	—	MIRO ^b
2017-11-23	58080.8	197	—	—	—	—	—	—	1.493	0.002	4.133	0.001	Spitzer/IRAC
2017-11-25	58082.1	199	—	—	2.66	0.17	2.08	0.15	—	—	—	—	P200/WIRC
2017-12-05	58092.0	209	3.71	0.24	2.52	0.23	1.64	0.18	—	—	—	—	MIRO ^b
2018-01-11	58129.4	246	—	—	—	—	—	—	0.715	0.001	2.860	0.002	Spitzer/IRAC
2018-02-25	58174.5	291	0.63	0.05	—	—	0.50	0.05	—	—	—	—	P200/WIRC
2018-03-01	58178.2	295	—	—	—	—	—	—	0.418	0.001	1.796	0.001	Spitzer/IRAC
2018-03-21	58198.1	315	—	—	—	—	—	—	0.336	0.002	1.521	0.001	Spitzer/IRAC
2018-06-03	58272.6	389	0.29	0.03	0.30	0.05	0.18	0.01	—	—	—	—	Keck/MOSFIRE
2018-06-23	58292.3	409	0.24	0.01	—	—	0.13	0.01	—	—	—	—	P200/WIRC
2018-07-23	58322.3	439	0.18	0.01	0.19	0.01	0.08	0.01	—	—	—	—	P200/WIRC
2018-09-12	58373.3	490	0.10	0.01	0.12	0.01	0.064	0.007	—	—	—	—	P200/WIRC
2018-09-20	58381.9	498	—	—	—	—	—	—	0.095	0.001	0.316	0.001	Spitzer/IRAC
2018-10-26	58417.3	534	0.057	0.005	0.071	0.006	0.046	0.005	—	—	—	—	P200/WIRC
2018-11-27	58449.3	566	—	—	—	—	—	—	0.074	0.001	0.196	0.001	Spitzer/IRAC

^aArkharov et al. (2017) using the Short-Wave Infrared Camera (SWIRCAM) on the AZT-24 telescope at Campo Imperatore Observatory. ^bRho et al., 2018 using Mount Abu Infrared Observatory (MIRO)

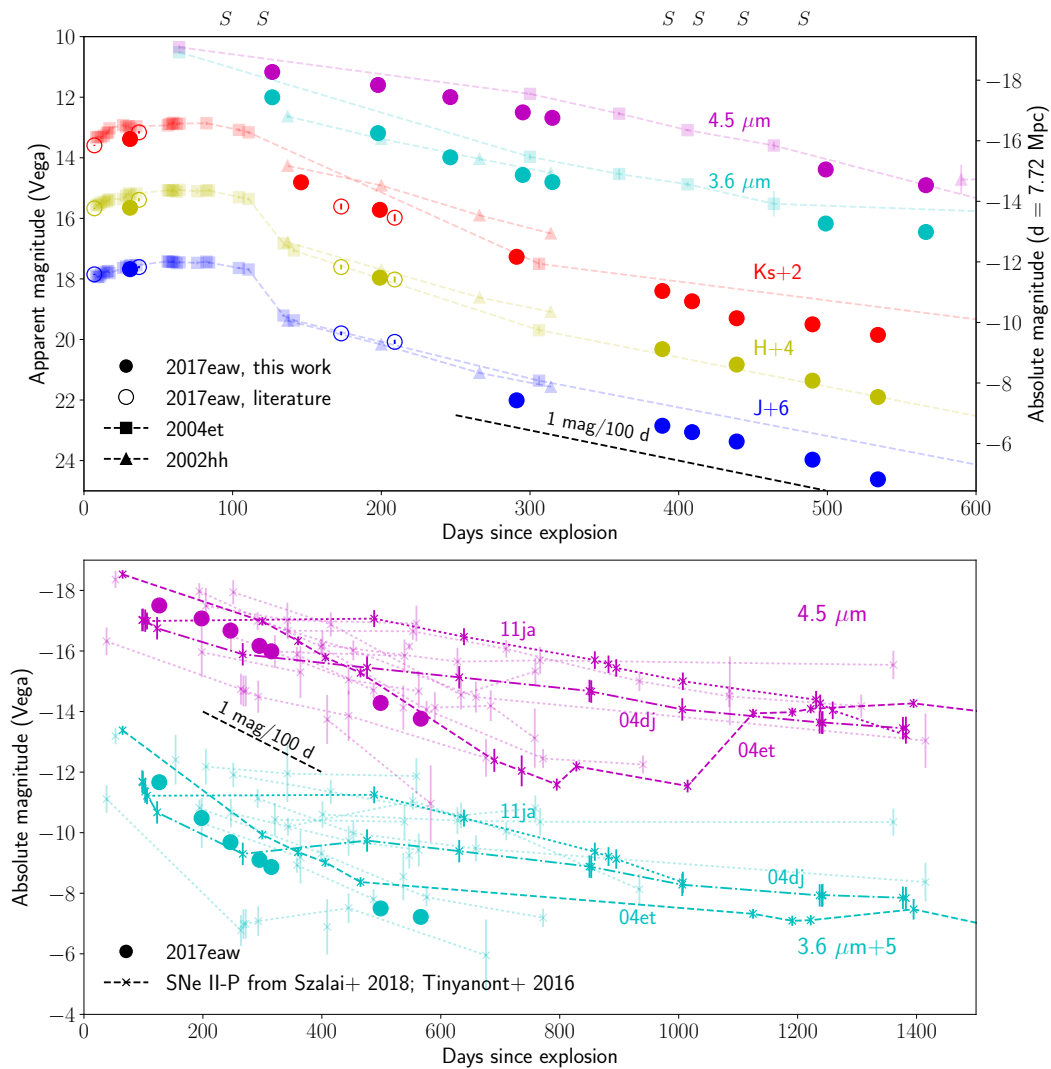


Figure 3.3: Top: near-IR photometry of SN 2017eaw in the J , H , and Ks bands and the IRAC 3.6 and 4.5 μm bands compared with photometry of SN 2004et and SN 2002hh. Filled symbols for SN 2017eaw are our data, while open symbols are from Arkharov et al. (2017) and Rho et al. (2018). The $JHKs$ photometry results for SN 2004et are from Maguire et al. (2010). *Spitzer* photometry are from Fabbri et al. (2011). SN 2002hh data are from Pozzo et al. (2006). Note that the 3.6 μm data for this SN is from L' -band ground-based observations. The “S” marks above the axis indicate epochs for which we obtained spectroscopy. Bottom: SN 2017eaw *Spitzer* photometry compared to all other SNe II-P photometry as aggregated by Szalai et al. (2019). No offsets between SNe are applied here, but all 3.6 μm magnitudes are shifted by 5 mags for visualization. SNe 2004dj, 2004et, and 2011ja are highlighted for comparison. All magnitudes here are in the Vega system. The 1 mag/100 d decline rate expected from light curves powered by radioactive decay of ^{56}Co is plotted in both subplots.

model from a high-resolution spectrum of Vega. We obtained J - and K -band spectra with Keck/MOSFIRE on 2018 June 3 (389 d). Data reduction and spectral extraction were performed using MOSFIRE’s data reduction pipeline,² and telluric and flux calibrations were performed using `xtellcor`. Finally, we obtained a 1–2.5 μm spectrum using the Near-Infrared Echellette Spectrometer (NIRES)³ on the Keck telescope on 2018 September 2 (480 d). The instrument is very similar to TripleSpec, except with a narrower 0.5 slit to take advantage of the better seeing from Maunakea. The observation strategy was similar. The data were reduced using a version of `Spextool` modified for NIRES, and the telluric and flux calibrations were performed using `xtellcor`. The standard spectra used for this calibration were from HIP 94140, observed before the SN. Fig. 3.4 displays our near-IR spectra for SN 2017eaw from 91 to 480 d post-explosion with identifications of strong lines. The identifications were guided by Rho et al. (2018) and Meikle et al. (1993). Each epoch is multiplied by a factor listed on the right of the figure for visualization. TripleSpec spectra at 408 and 439 d are smoothed by a running median with a seven-pixel window, and the NIRES spectrum at 480 d is smoothed in the same way with a three-pixel window. The unsmoothed versions of the spectra are plotted as translucent lines.

3.3 Analysis and Discussion

Progenitor Nonvariability and SED

Some SNe II-P have shown stronger signs of CSM interaction than that of a typical SN II-P. This is indicative of a denser CSM in comparison to what expected from steady-state RSG wind-driven mass loss. The required enhanced mass loss would result in a variability in the progenitor’s light curve, which may be a gradual brightening over timescales of years, or short-term variability in the case of eruptive mass loss. Such nearby and recently ejected CSM has been inferred in a variety of ways for a number of SNe II-P. Some SNe show signs of early dust formation and intermediate-velocity ($\text{few} \times 10^3 \text{ km s}^{-1}$) hydrogen emission lines or X-rays from the shocked CSM gas, for example, SNe 2007od (Andrews et al., 2010), 2011ja (Andrews et al., 2016; Chakraborti et al., 2013), and 2013ej (Chakraborti et al., 2016; Mauerhan et al., 2017). Some, like SN 2009kf, show early, strong ultraviolet emissions that require either a very energetic explosion or some degree of CSM interaction (Botticella et al., 2010; Moriya et al., 2011). Lastly, an emerging

²<https://keck-datareductionpipelines.github.io/MosfireDRP/>

³<https://www2.keck.hawaii.edu/inst/nires/>

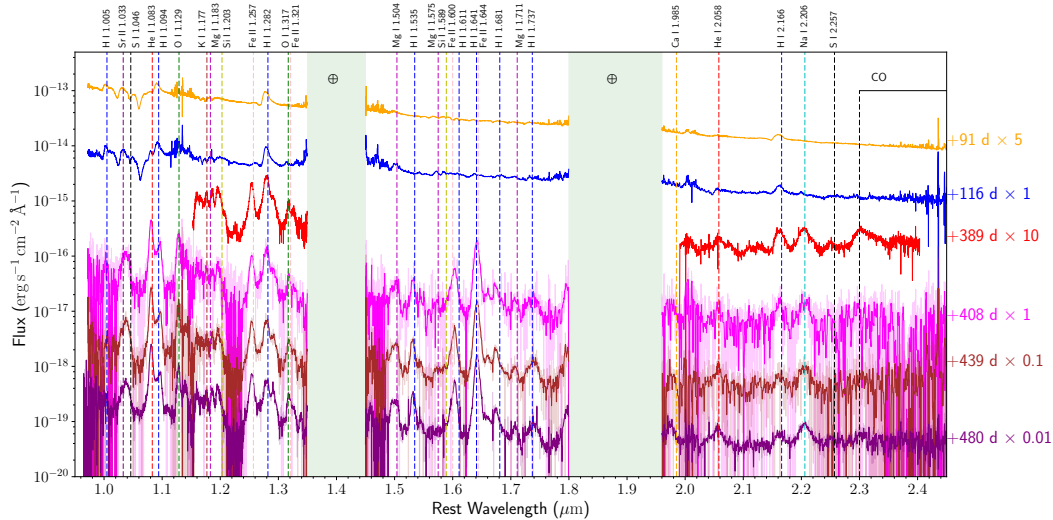


Figure 3.4: Near-IR spectra of SN 2017eaw taken at 91, 116, 389, 408, 439, and 480 days post-explosion. The wavelength plotted is corrected for the host galaxy’s redshift of $z_{\text{host}} = 0.00013$ (Epinat et al., 2008). Rest wavelengths of common strong atomic lines are overplotted along with the CO vibrational first overtone band beyond $2.3 \mu\text{m}$. The spectrum on +389 d was taken with Keck/MOSFIRE in the *J* and *K* bands only. Strong telluric bands around 1.4 and $1.85 \mu\text{m}$ are marked with \oplus symbols. The flux at each epoch is multiplied by a factor indicated on the right for visualization. Spectra on 408, 439, and 480 d are smoothed by a running median with seven-, seven-, and three-pixel window, respectively. Unsmoothed spectra are shown as translucent lines.

class of SNe II-P with very early spectra show narrow emission lines coming from the nearby CSM being ionized by the ultraviolet flash of the shock breakout, for example, SNe 2013fs (Yaron et al., 2017) and 2016bkv (Hosseinzadeh et al., 2018). These narrow lines disappear quickly (as opposed to SNe II_n with narrow emission lines near peak).

There are multiple proposed mechanisms for ejecting mass from a RSG within a decade pre-explosion, such as wave-driven mass loss (Fuller, 2017; Fuller and Ro, 2018) and heavy element nuclear-burning instability ($9\text{-}11 M_{\odot}$ RSG, Woosley and Heger, 2015). In the wave-driven scenario for RSGs, the predicted variability for the smallest eruption case is of order 20%, ejecting $\sim 0.1 M_{\odot}$ the lowest heating efficiency ($\eta = 1/3$) case in Fuller, 2017. For the heavy element burning instability scenario, Smith and Arnett (2014) argued that a $9\text{-}11 M_{\odot}$ RSG can exhibit a detectable flash when the silicon burning commences. Nevertheless, the variability of the RSG progenitor star itself, which accompanies the mass-loss event, has yet to be directly

observed for progenitors to SNe II-P.⁴ In addition, and there are other mechanisms proposed to explain the early-time observations that do not involve any dense CSM surrounding the progenitor (e.g., Kochanek, 2019).

Indeed, our progenitor photometry in the near-IR (Fig. 3.2 bottom left) shows that SN 2017eaw’s progenitor is not variable in the Ks band from one year to one day pre-explosion on a timescale greater than 200 days. To put an upper limit on the variability of the progenitor, we compute the uncertainty of the weighted-mean flux from the progenitor’s Ks -band photometry presented in Table 3.1. The uncertainty of the mean is $0.25\sqrt{\Delta F_{Ks} = \Sigma_i(\sigma_{F_{Ks},i}^2)}$ where i ’s are four epochs at 345, 211, 7, and 1 days pre-explosion. The weighted-mean flux with the uncertainty is $\bar{F}_{Ks} = 0.031 \pm 0.002$ mJy. Assuming the distance of 7.72 Mpc to the SN, we obtain the variability limit of $\Delta \nu L_\nu \lesssim 6 \times 10^3 L_\odot$. The total luminosity is $\nu L_\nu = 8 \times 10^4 L_\odot$, typical of a RSG. This is consistent with the luminosity derived from fitting the SED, discussed later in this section. This corresponds to the variability upper limit of 6% over a year. In comparison, the weakest variability presented in Fuller (2017) is of order of 20%. Further, short-term variability immediately before core collapse is ruled out by our last two epochs of observations within a few days before the explosion. We note that our finding of Ks -band nonvariability does not conflict with that of Kilpatrick and Foley (2018), who presented a 20% increase in the $4.5 \mu\text{m}$ flux over 3 yr pre-explosion, but no variability in the $3.6 \mu\text{m}$ band.

The near-IR SED of the progenitor star in the near-IR is shown in Fig. 3.2 (right). The photometry has been corrected for Galactic extinction ($E(B - V) = 0.304$; Schlafly and Finkbeiner, 2011) with no additional host extinction. We fitted a blackbody curve to the SED and found the best-fit parameters to be $T = 2500 \pm 200$ K and $L = 7 \pm 2 \times 10^4 L_\odot$. We note that the blackbody luminosity is consistent with νL_ν obtained from Ks -band observations presented above. These parameters are consistent with the progenitor star of SN 2017eaw being a RSG.

The progenitor star of SN 2017eaw has also been observed by the Large Binocular Telescope (LBT) search for failed SNe in the optical ($UBVR$ bands) in 35 epochs from 9 yr to a few months before the explosion (Johnson et al., 2018). They found no significant stochastic variability in the luminosity down to $\Delta \nu L_\nu \lesssim 700 L_\odot$ in the V and R bands. Johnson et al. (2018) also reported nonvariability in three other

⁴Pre-SN eruption has been documented in some SNe Ibn/IIn, which have denser CSMs. The most well studied cases are SNe 2006jc (e.g., Foley et al., 2007; Pastorello et al., 2008) and 2009ip (e.g., Mauerhan et al., 2013). The definitive class of progenitors to those strongly interacting SNe has yet to be identified.

progenitor stars to SNe 2013am, SN 2013ej, and ASASSN-2016fq. One of these SNe, SN 2013ej, has a nearby dense CSM inferred from X-ray (Chakraborti et al., 2016) and optical spectropolarimetry (Mauerhan et al., 2017) despite its progenitor having exhibited no variability in the last 5 yr before the explosion. They argued that while outbursts may happen on a timescale shorter than their observing cadence, it is unlikely that the decline from these outbursts is fast enough to escape a detection because the dynamical and thermal timescales for these RSGs are much longer (years) than the observational cadence (months).

Our observations, along with those of Johnson et al. (2018), do not find major eruptive mass-loss events around SN 2017eaw’s progenitor in the last 10 yr of its life. The CSM around SN 2017eaw, inferred from radio and X-ray observations (Grefenstette et al., 2017; Kong and Li, 2017; Nayana and Chandra, 2017a), may be ejected in minor mass-loss events that cause variability smaller than 6% or last shorter than our observational cadence. Alternatively, the CSM around the RSG progenitor may be more akin to the compact CSM shell observed around Betelgeuse (Le Bertre et al., 2012). Mackey et al. (2014) presented a scenario in which such a compact CSM shell is constructed by a progenitor wind being trapped by ionizing photons in the star’s environment. The CSM shell will eventually interact with the SN shock, and as shown by Smith et al. (2009b), this interaction will not be strong enough to produce typical Type II_n narrow lines. However, weak signs of CSM interactions may be detected in the X-ray and radio. For comparison, Pooley et al. (2002) derived from 0.2 to 10 keV X-ray observations that SN 1999em (typical II-P) has a progenitor mass-loss rate of $\dot{M} \sim 2 \times 10^{-6} M_{\odot} \text{ yr}^{-1}$, similar to that of Betelgeuse. From the literature, the 0.3-10 keV X-ray luminosity of SN 2017eaw is $1.1 \times 10^{39} \text{ erg s}^{-1}$ at 11 d post-explosion (Grefenstette et al., 2017). In comparison, SN 1999em’s X-ray luminosity is $2 \times 10^{38} \text{ erg s}^{-1}$ at 4 d post-explosion, (Pooley et al., 2002). Since the X-ray luminosity scales with \dot{M}^2 (see Equation (3.10) from Fransson et al., 1996), SN 2017eaw’s progenitor would have a mass-loss rate of $\dot{M} \sim 5 \times 10^{-6} M_{\odot} \text{ yr}^{-1}$, which is in the typical range for a RSG. This mass-loss rate is consistent with the figure of $9 \times 10^{-7} M_{\odot} \text{ yr}^{-1}$ derived by Kilpatrick and Foley (2018) using *Hubble* and *Spitzer* photometry. Hence, it is possible that the CSM for SN 2017eaw is created by a trapped wind like that seen around Betelgeuse, and not by eruptive mass loss in the last decade of the progenitor’s life.

Photometric Evolution and Comparison

In order to assess SN 2017eaw’s place in the Type II-P population, we compare its IR photometric evolution to those of other well-studied SNe II-P (Table 3.2). We first caution that SN evolution in the near-IR remains poorly sampled in the nebular phase, making direct comparison to other individual SNe difficult. In the optical, Tsvetkov et al. (2018) has shown that SN 2017eaw bears photometric similarities to SN 2004et both in terms of flux and color evolution. Fig. 3.3 (top) shows SN 2017eaw’s 1-5 μm light curves in comparison to those of SN 2004et (Fabbri et al., 2011; Kotak et al., 2009; Maguire et al., 2010) and SN 2002hh (Pozzo et al., 2006), two normal SNe II-P in NGC 6946. SN 2017eaw is fainter than SN 2004et by about 0.5 mag in all bands, including the optical (Tsvetkov et al., 2018), without a strong wavelength dependence, which indicates that SN 2017eaw is intrinsically less energetic and not that it suffers more extinction and reddening. In *Spitzer* 3.6 and 4.5 μm bands, the evolutions of SNe 2017eaw and 2004et are very similar. Except for the 4.5 μm band, other near-IR bands show a similar linear decline of ~ 1.5 mag/100 d after 120 d. The 4.5 μm band, however, declines at a slower rate of 0.80 mag/100 d. For SN 2004et, Kotak et al. (2009) showed, using a series of SEDs with all *Spitzer* bands from 3.6 to 24 μm , that this different decline rate in the 4.5 μm band is due to the CO fundamental vibrational emission at 4.65 μm . From this comparison alone, we can infer that CO is forming in SN 2017eaw. This is consistent with the emerging CO first overtone emission band starting around 120 d reported by Rho et al. (2018). Our spectra, presented above in §3.2 and discussed in §3.3, also confirm the presence of CO. After 250 d, the decline rate in the *J*, *H*, and *Ks* bands are 1 mag/100 d, the canonical decline rate for a light curve powered by ^{56}Co decay.

Fig. 3.3 (bottom) shows SN 2017eaw’s *Spitzer* light curves in comparison to all other SNe II-P light curves observed by *Spitzer*, aggregated by Szalai et al. (2019). Data here include photometry from Tinyanont et al. (2016). SN 2017eaw falls in the middle of the distribution of SNe II-P absolute magnitudes in both the 3.6 and 4.5 μm bands, suggesting that it is a typical SN II-P. That SN 2017eaw is typical implies that the results we derive for SN 2017eaw in this paper may be more generally applicable to other SNe II-P that are fainter and more difficult to observe. More specifically, SN 2017eaw’s (and SN 2004et’s) decline rates of 1.5 and 0.8 mag/100d in the 3.6 and 4.5 μm bands are typical among other SNe II-P with observations between 100 and 300 d. This suggests that strong CO emission in the 4.5 μm band may be ubiquitous among SNe II-P. The implication here is that previous studies of SN dust based

Table 3.2: Properties of SNe II-P used to compare with SN 2017eaw

Name	Host	Comparison Points	References
2017eaw	NGC 6946		Rho et al. (2018) and Tsvetkov et al. (2018)
1987A (II-pec)	LMC	CO evolution and line profile	e.g., Liu et al. (1992), Meikle et al. (1989, 1993), and Spyromilio et al. (1988)
1999em	NGC 1637	Typical SN II-P X-ray luminosity	Pooley et al. (2002)
2002hh	NGC 6946	Photometric similarities in optical and IR	Pozzo et al. (2006)
2004et	NGC 6946	Photometric similarities in optical and IR	Maguire et al. (2010)
2004dj	NGC 2403	Silicate dust detection <i>Spitzer</i> light curves for SNe II-P with early CSM interactions	Kotak et al. (2009) Kotak et al. (2005) and Meikle et al. (2011)
2011ja	NGC 4945	<i>Spitzer</i> light curves for SNe II-P with early CSM interactions	Andrews et al. (2016) and Tinyanont et al. (2016)

on warm *Spitzer* data with only 3.6 and 4.5 μm data may provide unreliable dust estimates because the 4.5 μm band is dominated not by thermal emission from dust, but CO line emission. The result is that the dust luminosity—and, consequently, dust mass—is overestimated.

While SN 2017eaw’s early temporal evolution is similar to that of most other SNe II-P, we note that it is markedly different from SNe 2004dj (Kotak et al., 2005) and 2011ja (Andrews et al., 2016; Tinyanont et al., 2016). Both of these SNe show signs of CSM interaction and dust formation at much earlier epochs: 65–165 d for SN 2004dj (Meikle et al., 2011) and 105 d for SN 2011ja (Andrews et al., 2016). Lastly, SN 2017eaw’s resemblance to SN 2004et’s *Spitzer* light curve presents an intriguing possibility that SN 2017eaw will rebrighten just like SN 2004et at ~ 1000 d because of shock interaction with a distant CSM shell (see Fig. 3.3 bottom and Kotak et al., 2009). This possibility warrants continued monitoring of this SN, and other nearby CCSNe in the future, in the IR by either *Spitzer* or ground-based instruments. More generally, future IR observations of nearby CCSNe will reveal a range of epochs when CSM interactions and/or dust formation commence, from ~ 100 to $\sim 1,000$ d post-explosion. Such observations will provide clues to the physical processes in the last stage of RSG evolution that are responsible for the distant CSM shell seen in, for example, SN 2004et.

SED Modeling

We performed radiative transfer (RT) modeling of the SEDs for SN 2017eaw to estimate the mass of dust associated with the SN. We used MOnTe CARlo SimulationS of Ionized Nebulae (MOCASSIN; version 2.02.72), which is a fully self-consistent

3D Cartesian dust RT code (Ercolano et al., 2005, 2003, 2008). The models accept multiple user inputs, but due to the limited wavelength coverage in our SED data, we limited the number of parameters we fitted, in order to avoid overfitting. While MOCASSIN takes a series of user inputs, such as number of dimensions, grid size, dust density, composition, and distribution, the only parameters we varied to fit the SED were the inner and outer radii of the dust shell, and the density at the inner edge of the shell. We discuss the other parameters, which are held constant, later in this section. The luminosity and temperature of the photon source (the SN) were measured or extrapolated from the optical data. Any interactions, whether absorption or scattering, between photons and dust grains are governed by Mie scattering theory. MOCASSIN returns the temperature, mass, and opacity of the dust shells.

We used MOCASSIN to calculate the mass of dust at 126, 197, 295, and 498 d, epochs for which we had *Spitzer* coverage. The optical data for 126 and 197 d are from Tsvetkov et al. (2018), while the 295 d epoch is extrapolated (plotted as open symbols). We checked that the extrapolated photometry did not differ significantly from SN 2004et photometry at the same epoch. We did not extrapolate to 498 d, and simply used the same blackbody input for the 295 and 498 d epochs. The near-IR data for 126 d are from the flux-calibrated TripleSpec spectrum. Optical through near-IR photometry has been corrected for Galactic extinction ($E(B - V) = 0.304$; Schlafly and Finkbeiner, 2011), assuming that the host galaxy extinction is negligible.

We chose to model this system as a central point source surrounded by a gas-free dust shell. The shell was further assumed to be “smooth,” which means that there are no inhomogeneities (“clumps”), with the dust density profile falling by r^{-2} from the inner radius (R_{in}) to the outer radius (R_{out}). We used the standard Mathis Rumpl Nordsieck (MRN; Mathis et al., 1977) power-law distribution, $a^{-3.5}$, to specify the size distribution of the dust grains. We tested two compositions for the dust grains: 100% amorphous carbon (amC) and 100% silicate grains (Hanner, 1988; Ossenkopf et al., 1992; respectively). We were unable to constrain the composition because of a lack of data beyond $4.5 \mu\text{m}$. We do not fit the R , I , and $4.5 \mu\text{m}$ bands in our SEDs because they are contaminated by strong emission from $H\alpha$, the IR Ca II triplet, and CO bands, respectively. Our fits are not unique. We used the shape of the SED to set our input parameters. We used an inner radius R_{in} of 10^{16} cm and an outer radius R_{out} of 10^{17} cm as initial inputs, based on the optical and IR contributions to the SED. The input optical luminosity and temperature were based on the optical

continuum.

At 126 days, the input SED was our best fit, indicating no dust was detected. Starting from 197 but more clearly at 295 and 498 d, a small amount of dust ($\sim 7 \times 10^{-6} M_{\odot}$ for carbon grains and $\sim 10^{-4} M_{\odot}$ for silicate grains) was required to fit the SED. The peak temperature of the dust is ~ 500 K. Fig. 3.5 shows the SED evolution of SN 2017eaw, compared with SN 2004et (Fabbri et al., 2011; Maguire et al., 2010), with the best-fit models from MOCASSIN overplotted for each epoch. Solid and dashed lines represent amorphous carbon and silicate grains, respectively. Dotted lines are a blackbody provided for comparison. The excess flux in the $4.5 \mu\text{m}$ band is similar in both SNe. For SN 2004et, it was shown to be due to emission from the CO fundamental band (Kotak et al., 2009). Our data cannot distinguish between carbonaceous and silicate dust, due to the lack of data around $10 \mu\text{m}$. However, we note that in the case of SN 2004et, a broad silicate and SiO feature around $10 \mu\text{m}$ was detected, pointing to some silicate grains (Kotak et al., 2009). Furthermore, dust condensation models predict that for SNe II-P, carbonaceous dust does not form until ~ 1000 d post-explosion (discussed above), while silicate dust (like forsterite) can start to form as early as 200 d (Fig. 5 in Sarangi and Cherchneff, 2015). The comparison with SN 2004et and models suggests that dust responsible for SN 2017eaw's $3.6 \mu\text{m}$ excess at 295 d may be $\sim 10^{-4} M_{\odot}$ of silicates. In summary, the SED evolution of SN 2017eaw is similar to that of SN 2004et. A single-component blackbody can fit the SED reasonably well for the 126 and 197 d epochs, while a small amount of dust, likely $\sim 10^{-4} M_{\odot}$ of silicate dust is required to fit the 295 and 498 d epochs. Finally we note that the rising IR excess is in agreement with Rho et al. (2018)'s report of rising flux in the red part of their K -band spectra starting at ~ 120 d.

Spectroscopic Evolution and High-velocity Absorption Features

Spectra of SN 2017eaw shown in Fig. 3.4 evolved from the photospheric phase to the nebular phase after the 116 d epoch. The photospheric spectra at 91 and 116 d were dominated by strong continuum with hydrogen lines with P-Cygni profiles. Metal lines started to emerge from 116 d to 389 d as the SN transitioned into the nebular phase. The helium line at $1.083 \mu\text{m}$ emerged at 116 d and became strong in the nebular phase, blended with Pa- γ . Numerous metal species were also present in the nebular spectra, notably [Fe II] at 1.257, 1.600, and $1.644 \mu\text{m}$. The latter two were blended with hydrogen. Na I at $2.206 \mu\text{m}$ emerged at 116 d and became as strong as Br- γ in the last four epochs. Modeling these spectra to obtain physical

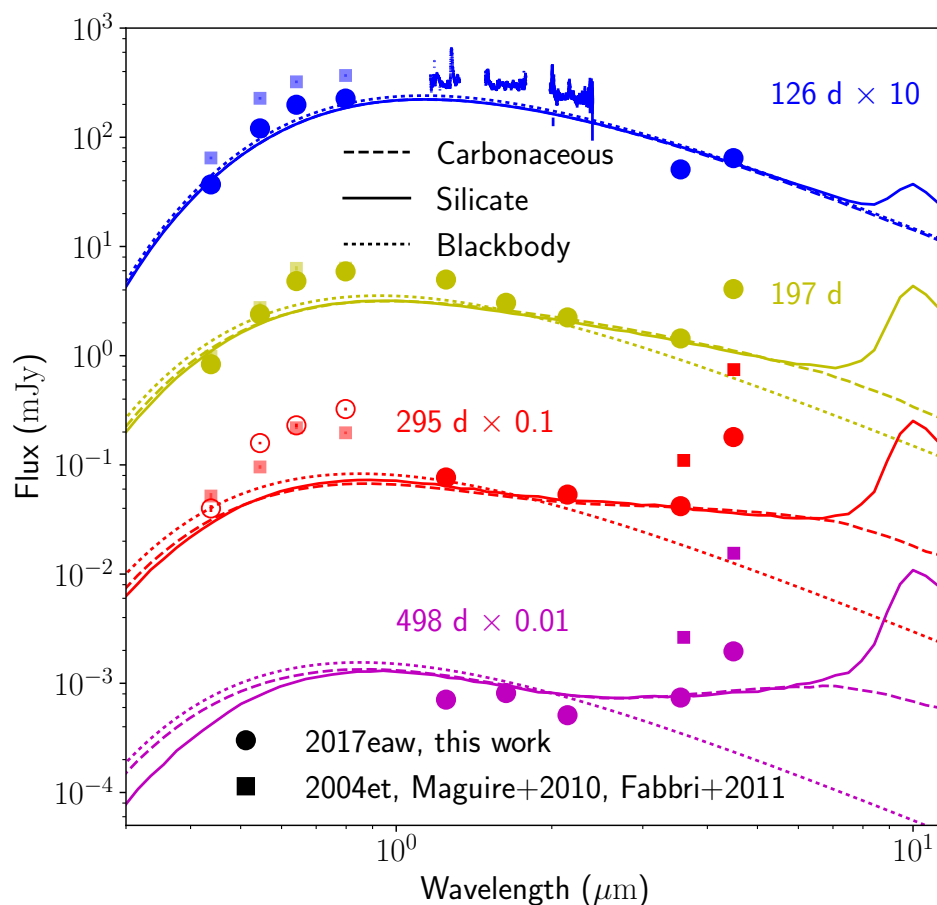


Figure 3.5: Evolution of the SED of SN 2017eaw (circle points, optical data from Tsvetkov et al., 2018) in comparison to SN 2004et (square points, from Maguire et al., 2010) at 126, 197, 295, and 498 d. Optical data for the 295 d epoch are extrapolated, and are shown with open symbols. SED models of blackbody with dust grain emission from MOCASSIN are overplotted. Dashed lines represent model with purely carbonaceous dust grains while solid lines represent those with purely silicate grains. Dotted lines are blackbody fits, provided for comparison. The fits ignore optical R, I bands, and *Spitzer* 4.5 μm band due to contaminations from $\text{H}\alpha$, Ca triplet, and CO fundamental band, respectively.

parameters for the ejecta is outside the scope of this paper.

Fig. 3.6 shows a series of continuum-normalized near-IR spectra of SN 2017eaw during the plateau phase from 26 to 116 days post-explosion. Data for days 91 and 116 are from this work, and the rest are from Rho et al. (2018). The hydrogen Paschen- γ line at $1.094 \mu\text{m}$ with a P-Cygni profile is present throughout the plateau phase with decreasing photospheric velocity, as expected in a normal SN II-P. Another P-Cygni absorption trough, likely from He I $1.083 \mu\text{m}$, is present. It also has a decreasing velocity from $\sim 10^4 \text{ km s}^{-1}$ at 26 d to $\sim 5000 \text{ km s}^{-1}$ at 116 d. The spectra show an absorption feature at $1.045 \mu\text{m}$, corresponding to the He I $1.083 \mu\text{m}$ line at $v = 10,000 \text{ km s}^{-1}$. While there is a Si I $1.046 \mu\text{m}$ line nearby, it is not expected to be present during the photospheric phase as the metal-rich ejecta have not yet been exposed. The velocity of this feature, unlike that of the P-Cygni absorption trough, remains constant throughout the photospheric phase. We identify this feature as the high-velocity He I $1.083 \mu\text{m}$ absorption line, predicted by Chugai et al. (2007) in the case of CSM interactions. Chugai et al. (2007) argued that the high-velocity absorption features for $\text{H}\alpha$ and He I $1.083 \mu\text{m}$ are formed by the recombined gas in the outer ejecta excited by high-energy photons from the CSM interaction. The presence of this line provides an evidence that there is CSM interaction going on in SN 2017eaw. We note here, however, that the high-velocity He I $1.083 \mu\text{m}$ absorption during the plateau is predicted as a result of time-dependent ionization effect in the expanding ejecta (Dessart and Hillier, 2008).

Temporal Evolution of the CO First Overtone Feature

Our series of near-IR spectra capture the evolution of the $2.3\text{--}2.5 \mu\text{m}$ band of the CO vibrational first overtone ($\Delta v = 2$) transition. Rho et al. (2018) reported that the feature emerged at 124 d and strengthened until their last epoch at 205 d. Assuming an LTE level population, they inferred a growing CO mass from $(0.6\text{--}1.6)\times 10^{-4} M_{\odot}$ at 124 d to $(1.9\text{--}2.2)\times 10^{-4} M_{\odot}$ at 205 d, with the temperature declining in their last three epochs, reaching 2700 K at 205 d. Our spectrum at 389 d showed that the CO feature continued to strengthen and had become as prominent as hydrogen by this epoch. Spectra from 408, 439, and 480 d subsequently showed that the CO feature started to fade. The series of these last four spectra are shown in Fig. 3.7 (left) in the linear scale to demonstrate the fading CO feature. Wavelengths for CO band heads of the $\Delta v = 2$ transitions are overplotted, both for ^{12}CO and ^{13}CO with $v = -500 \text{ km s}^{-1}$.

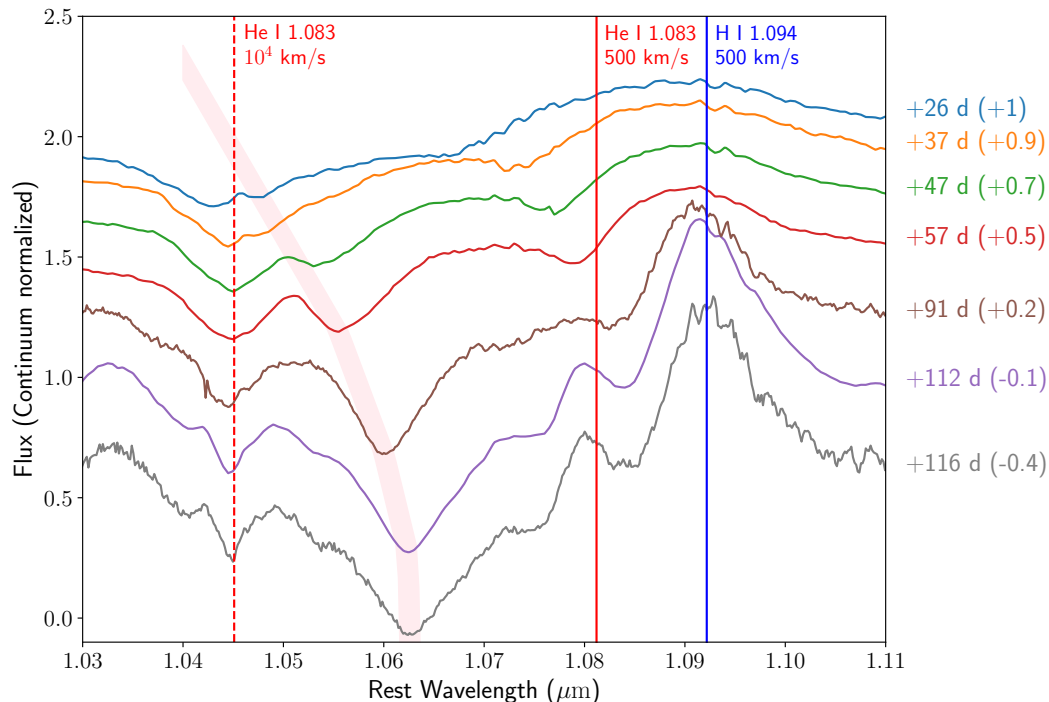


Figure 3.6: Series of spectra of SN 2017eaw between 1.03 and 1.11 μm during the plateau phase from 26 to 116 days post-explosion. Spectra from days 91 and 116 are from this work; other epochs are from Rho et al. (2018). The spectra are normalized by the continuum and offset for visualization. The epoch and offset for each spectrum are noted to the right of the plot. Wavelengths of the He I 1.083 μm and H I 1.094 μm at 500 km s^{-1} and the He I 1.083 μm at 10,000 km s^{-1} are marked. The shaded band indicates the absorption trough, likely from the He I 1.083 μm P-Cygni profile.

The fading of the CO first overtone feature may indicate either that CO molecules have been destroyed or that the gas has cooled down enough that the $\nu \geq 2$ vibrational levels are no longer excited. Some authors argued that CO can be easily destroyed by high-energy electrons from ^{56}Co decay and that most atomic carbon condenses into amorphous carbonaceous dust grains starting at 200–300 d post-explosion (Todini and Ferrara, 2001). However, in this scenario, the CO formation would have been inhibited in the first place (not formed and destroyed later), and their model predicted the CO mass for SN 1987A to be a factor of three smaller than what was observed. They did not address how dust grains could survive the same energetic electrons from ^{56}Co decay that destroyed the CO molecules.

Alternatively, the fading of the first overtone feature may indicate that the ejecta where CO formed have cooled enough that the $\nu \geq 2$ vibrational levels corresponding to the first overtone emission are no longer excited. The scenario is further supported

by the fact that the $4.5 \mu\text{m}$ excess in the SED (see §3.3), likely due to the CO fundamental emission, did not disappear. This is because the fundamental transition can happen as long as the $\nu = 1$ level, which is less energetic, remains populated. Another line of evidence that CO did not get destroyed in SN 2017eaw’s ejecta is the similarity between its CO line evolution and that of SN 1987A. Recall that in SN 2017eaw, the first overtone bands emerged at ~ 200 d and started to disappear at ~ 400 d while the fundamental bands ($4.5 \mu\text{m}$ band) remained detected at 566 d. This behavior is consistent with what was observed in SN 1987A, where the CO first overtone emerged as early as 100 d and faded by 574 d while the CO fundamental band remained strong until 600–700 d (e.g., Liu et al., 1992; Meikle et al., 1989, 1993; Spyromilio et al., 1988). The survival of CO in SN ejecta was shown for SN 1987A by late-time observations with ALMA, more than 25 yr post-explosion, that detected CO (along with SiO) rotational emission (Abellán et al., 2017; Kamenetzky et al., 2013). In summary, the fading CO first overtone feature indicates that the ejecta have cooled, and not that CO molecules are destroyed.

The survival of CO is favored by more recent MNT chemical evolution models that treat chemical reactions in SN ejecta more realistically (e.g., Sarangi and Cherchneff, 2013, 2015; Sluder et al., 2018). Specifically, the chemical evolution of the SN ejecta is modeled using a realistic network of chemical reactions to track molecules and dust formation together. Sarangi and Cherchneff (2013, 2015), assuming stratified ejecta, found that in the ejecta layers where carbon is abundant (zones 4 and 5 in their papers), CO forms in the oxygen-rich layer (zone 4) and carbonaceous dust can only form in the oxygen-poor part (zone 5). This is because CO is more easily formed and is not destroyed once formed, so that all carbon atoms in zone 4 end up in CO. Sluder et al. (2018) used a realistic ejecta model that has some radioactive species mixed into the ejecta to model molecule and dust dissociation due to the high-energy electrons from radioactive decays. They concluded that, while high-energy electrons keep the ejecta gas from becoming fully molecular, they do not destroy all CO, and that up to $0.06 M_{\odot}$ of CO survives to 10,000 d (see their Figure 14). The implication of this result is that CO is not easily destroyed to form carbonaceous dust, as was concluded by Todini and Ferrara (2001).

Line Profile of the CO First Overtone Feature

The CO emission from SN 2017eaw is similar to that from SN 1987A, not only in its temporal evolution, but also in the line profile. In this subsection, we consider our 389 d epoch, which has the strongest detection of the CO feature. To isolate

SN 2017eaw’s CO line profile, we first estimated and subtracted the underlying continuum by fitting a blackbody curve to parts of the K -band spectrum at 389 d without strong lines. The blackbody temperature and radius are $T = 809$ K and $r_{\text{BB}} = 4 \times 10^{15}$ cm, respectively. The model is shown in Fig. 3.7 (left). This warm continuum is likely coming from the same component that Rho et al. (2018) reported in their spectra. By 480 d, this continuum has substantially decreased. The continuum-subtracted CO profile is shown in Fig. 3.7 (right).

The CO line profile of SN 2017eaw observed on day 389 is very similar to that of SN 1987A at 377 d (Spyromilio et al., 1988). On top of the continuum-subtracted CO line profile shown in Fig. 3.7 (right), we plotted the non-LTE model by Liu et al. (1992), which was fitted to SN 1987A’s spectrum at 377 d. We shifted the wavelength with $v = -500$ km s⁻¹ (blueshift), a line peak velocity estimated from the Br- γ line from the same epoch. We only scaled the flux of the model by the squared ratio of the distances to SNe 1987A (51.4 kpc, Panagia, 2005) and 2017eaw. The result assuming $d = 7.72$ Mpc fitted our data reasonably well. We next describe the Liu et al. (1992) model and how we can use it to explain SN 2017eaw.

The Liu et al. (1992) model predicts the CO emission features while accounting for non-LTE effects by assuming that the CO vibrational-level populations are determined by collisional excitation and radiative de-excitation. This is a reasonable assumption because, at low temperature and density at this epoch, the collisional timescale is an order of magnitude longer than the radiative timescale, rendering collisional de-excitation ineffective. Liu et al. (1992) contrasted their non-LTE results with the LTE results from Spyromilio et al. (1988) to demonstrate that the level population at this epoch is clearly non-LTE as their model provided a superior fit to the data (see their figures 1 and 2 for LTE and non-LTE results, respectively). Further, the non-LTE models implied an order of magnitude higher CO mass for SN 1987A in comparison to LTE models. For the particular model of SN 1987A we use for comparison to our SN 2017eaw data, the CO mass is $9.1 \times 10^{-4} M_{\odot}$, the temperature is 1800 K, and the ejecta velocity is 2000 km s⁻¹.

The fact that the model fitted to SN 1987A data at 377 d explains our SN 2017eaw data well suggests that the CO properties (mass, temperature, and velocity) between the two SNe are similar. This implied CO mass of $\sim 10^{-3} M_{\odot}$ for SN 2017eaw is a factor of a few higher than the values determined by Rho et al. (2018); however, we note earlier that this discrepancy is expected from comparing non-LTE to LTE models. The line ratios between different transitions in this band are determined by

the relative population in different vibrational excitation states. This is determined by the electron temperature since CO is excited by collisions with free electrons in this model (Liu et al., 1992). Comparing SN 2017eaw’s CO profile to different models at $T = 1800\text{--}4000$ K from Liu et al. (1992), it is clear that the plotted model at 1800 K fits our data best. Finally, the width of the profile is determined by the ejecta velocity, and again, this model with $v = 2000 \text{ km s}^{-1}$ explains our data well. In summary, we are able to estimate electron temperature, CO mass, and velocity for SN 2017eaw at 389 d by comparing its observed CO first overtone line profile with a non-LTE model for SN 1987A’s CO at 377 d. The similarity in line profiles indicates that the two SNe have similar CO mass, temperature, and velocity at this epoch, which is surprising since SN 1987A is a very different kind of explosion coming from a different type of progenitor (blue supergiant, instead of RSG). Future work fitting the entire sequence of SN 2017eaw spectra with non-LTE models is required to get a complete picture of its CO mass evolution.

Molecule and Dust Formation in Comparison to Chemical Evolution Models

Near-IR spectroscopy, along with cadenced *Spitzer* observations, provided a detailed monitoring of the chemical evolution of SN 2017eaw’s ejecta, which can be compared to different chemical evolution models. The series of near-IR spectra presented by Rho et al. (2018) and this work are the best nebular-phase near-IR spectra of any SNe since SN 1987A. From previous subsections, we have presented the following. (1) CO formed in SN 2017eaw’s ejecta by ~ 200 d (observed by Rho et al., 2018) and cooled such that the first overtone transitions were no longer excited by ~ 400 d. The $4.5 \mu\text{m}$ band excess, likely due to the less energetic fundamental transitions, was still detected at 566 d, showing that the CO molecules were not destroyed. (2) A contribution of hot dust emission to the $3.6 \mu\text{m}$ channel has been detected starting at 300 d post-explosion, indicating the presence of warm dust (which may be newly formed or pre-existing). We estimated the dust mass of $7 \times 10^{-6} M_{\odot}$ and $10^{-4} M_{\odot}$ assuming pure carbonaceous and silicate grains, respectively. We now compare these observations with predictions from the simpler CNT along with those from the more realistic MNT.

First, we consider the formation and survival of CO. CNT models generally consider molecule and dust formation as different processes. The only influence molecules have on dust formation is that they deplete different species in the gas phase available to form dust. For example, Todini and Ferrara (2001) show, assuming a complete mixing of radioactive species throughout the ejecta, that most carbon atoms end up

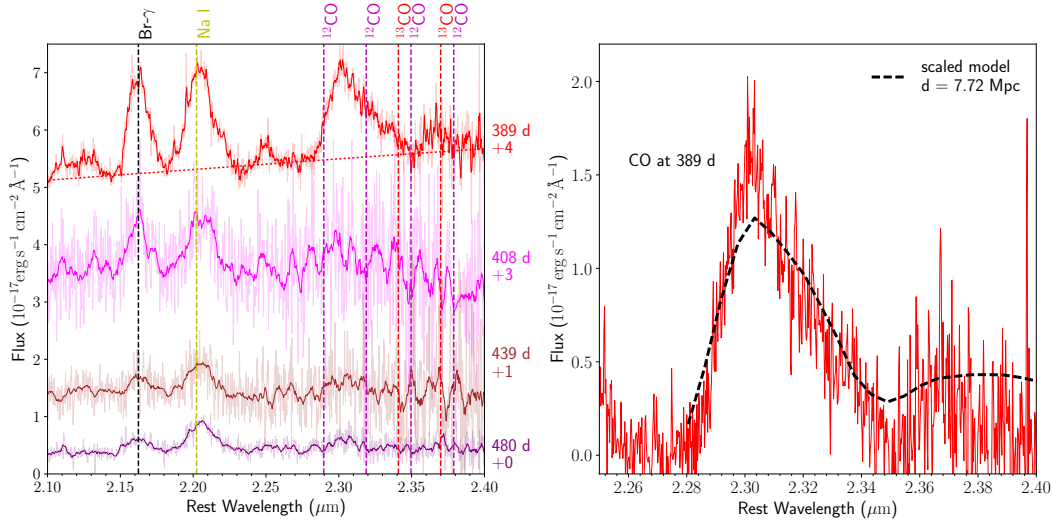


Figure 3.7: Left: The evolution of K -band spectra of SN 2017eaw from 389 to 480 d. The colors correspond to the same epochs as in Fig. 3.4. Text on the right of the spectrum from each epoch indicates the epoch and the offset applied for visualization. The window sizes for smoothing these spectra are 5, 21, 21, and 17 pixels, respectively, for visualization and the unsmoothed spectra are shown in translucent lines. Wavelengths of the Br- γ , Na I, and CO band heads, all with $v = -500 \text{ km s}^{-1}$, are plotted. The red dotted line is the blackbody fit to the continuum at 389 d with temperature and blackbody radius $T = 804 \text{ K}$ and $r_{BB} = 4 \times 10^{15} \text{ cm}$. Right: CO line profile of SN 2017eaw at 389 d with the fitted continuum shown on the left subtracted. Dashed lines are the non-LTE model fitted to the spectrum of SN 1987A at 377 d post-explosion (Liu et al., 1992). The model has been shifted with $v = -500 \text{ km s}^{-1}$, which is estimated from the Br- γ line from the same epoch.

in amorphous carbonaceous dust grains as CO molecules are destroyed by energetic electrons from ^{56}Co decays. MNT models, like Sarangi and Cherchneff (2013, 2015), show that CO is not a precursor molecule to carbonaceous dust grain formation because CO and carbon dust form via different chemical pathways, in different parts of the ejecta. In their models, Sarangi and Cherchneff (2015) assumed that the ejecta are stratified into different zones with different compositions. In the zones with abundant carbon, if oxygen is present, all carbon atoms are used up in CO. Carbonaceous grains, on the other hand, only form in the oxygen-poor part of the carbon-rich ejecta. Sluder et al. (2018) presented results from their MNT models using a more realistic ejecta model with some degree of mixing. They showed that up to $10^{-2} M_{\odot}$ of CO can form in the first 100 d post-explosion in SN 1987A-like ejecta (massive progenitor) and survive until 10,000 d where their simulation ends. The major role of CO in dust formation is that it radiatively cools the ejecta. SiO formation may as well play a role here, but we do not have direct evidence due to

the lack of observations at wavelengths longer than $5 \mu\text{m}$ (though we note that SiO was observed in SN 2004et). Our observations showing that a $\sim 10^{-3} M_{\odot}$ of CO has formed by 389 d, and that CO survives to at least 566 d agree with the scenario predicted by MNT.

Secondly, we consider the formation of dust and the evolution of its mass. Fig. 3.8 shows the dust mass measurement of SN 2017eaw in comparison to some other SNe and model predictions from Todini and Ferrara (2001), Sarangi and Cherchneff (2015), and Sluder et al. (2018). CNT models tend to predict quick precipitation of dust in the SN ejecta, with Todini and Ferrara (2001) predicting $0.1 M_{\odot}$ of amorphous carbon formed by 400 d and $0.4 M_{\odot}$ of Mg_2SiO_4 formed by 600 d. MNT, on the other hand, predicts a range of dust-formation behavior depending on the progenitor mass and ejecta composition. For example, Sarangi and Cherchneff (2015) predicted only $2 \times 10^{-2} M_{\odot}$ of Mg_2SiO_4 at 300 d with carbonaceous dust not forming until 900 d in their $15 M_{\odot}$ progenitor model with homogeneous SN ejecta and low ($0.01 M_{\odot}$) of ^{56}Ni . Their $15 M_{\odot}$ progenitor model with a normal amount ($0.075 M_{\odot}$) of ^{56}Ni predicts slower dust formation, with the total dust mass reaching $2 \times 10^{-2} M_{\odot}$ at around 800 d. For their $19 M_{\odot}$ models, they considered both homogeneous and clumpy ejecta. They found that the dust condenses gradually in the homogeneous ejecta, only reaching $10^{-2} M_{\odot}$ at 1,100 d. In contrast, clumpy ejecta form $10^{-3} M_{\odot}$ of Mg_2SiO_4 at 100 d and reach $10^{-2} M_{\odot}$ by 300 d with carbonaceous dust not forming until 700 d. In all cases, Mg_2SiO_4 dominates the total dust mass for the first 200–300 d of dust formation. In Sluder et al. (2018), another MNT model specifically for SN 1987A, which can be compared to the clumpy $19 M_{\odot}$ model of Sarangi and Cherchneff (2015), predicts $0.1 M_{\odot}$ of Mg_2SiO_4 by 300 d, with $10^{-2} M_{\odot}$ of carbonaceous dust by 500 d. We present this range of models to demonstrate that the predictions from different dust-formation models still widely disagree. Broadly, the dust mass inferred from the SED of SN 2017eaw of 10^{-4} (10^{-6}) M_{\odot} assuming silicate (carbonaceous) dust, starting at 200 d is a factor of 100 to 10,000 smaller than model predictions for a normal SN II-P.

The small amount of dust determined from the IR SED fitting at early time is in line with dust mass determined from IR observations in other II-P SNe (e.g., Szalai et al., 2011; Tinyanont et al., 2016), including SNe 2004dj and 2004et (Kotak et al., 2009; Meikle et al., 2011). While the total amount of dust found at a few hundred days post-explosion is insufficient for SNe II-P to be a major source of cosmic dust production, observations of SN 1987A and Galactic SN remnants reveal $0.1\text{--}1 M_{\odot}$

of dust. As shown by ALMA observations, SN 1987A has as much as $0.2 M_{\odot}$ of dust in its inner ejecta in 2012, 26 yr after the explosion (Indebetouw et al., 2014). Long-wavelength observations of supernova remnants also reveal similar amounts of dust surviving the passage of the reverse shock, available to be dispersed into the ISM. One explanation for this behavior is that dust continues to form in the ejecta over the course of a few years, as predicted by Sarangi and Cherchneff (2015). Another possibility is that dust is formed quickly, but is optically thick at early time. As a result, the dust mass inferred from near to mid-IR observations at these epochs only accounts for dust in the outermost layer of the ejecta, then subsequently grows as $M_{\text{obs}} \propto t^2$ (Dwek et al., 2019). From Fig. 3.8, the dust mass we measured for SN 2017eaw (assuming silicate) evolves roughly consistently with this power law; however, long-term monitoring is required. We note here that in Dwek et al. (2019), the authors compared their $M_{\text{obs}} \propto t^2$ prediction to the observed mass of SNe 1987A, 2004dj, and 2004et. In Fig. 3.8, we show that the measured dust mass from SN 2011ja (Tinyanont et al., 2016) also follows this power law. Future observations, especially at very late times, of nearby CCSNe are still needed to probe the evolution of dust from a few hundred to a few thousand days post-explosion, which will test different chemical evolution models of SN ejecta. Such observations will be greatly enabled in the era of the *James Webb Space Telescope* (JWST).

3.4 Summary and Conclusions

In this paper, we have presented the following:

1. We presented observations of SN 2017eaw’s progenitor in the *Ks* band from 344 to ~ 1 day before the explosion. We detected no photometric variability of the progenitor in this band down to $\Delta \nu L_{\nu} \lesssim 5000 L_{\odot}$, 6% of the *Ks*-band luminosity. Further, there was no evidence of short-term variability days before core collapse.
2. SN 2017eaw is similar in near-IR photometric evolution to normal SNe II-P 2002hh and 2004et, both also in NGC 6946, although SN 2017eaw is dimmer than SN 2004et by 0.5 mag in the *Spitzer*/IRAC 3.6 and 4.5 μm bands. The *Spitzer*/IRAC 3.6 and 4.5 μm band light curves of SN 2017eaw and SN 2004et are nearly identical from the time of the explosion out to our last epoch at 566 d. Long-term monitoring of SN 2017eaw in the mid-IR will reveal whether it will have a late-time CSM interaction that rebrightens the mid-IR light curve, as was observed in SN 2004et.

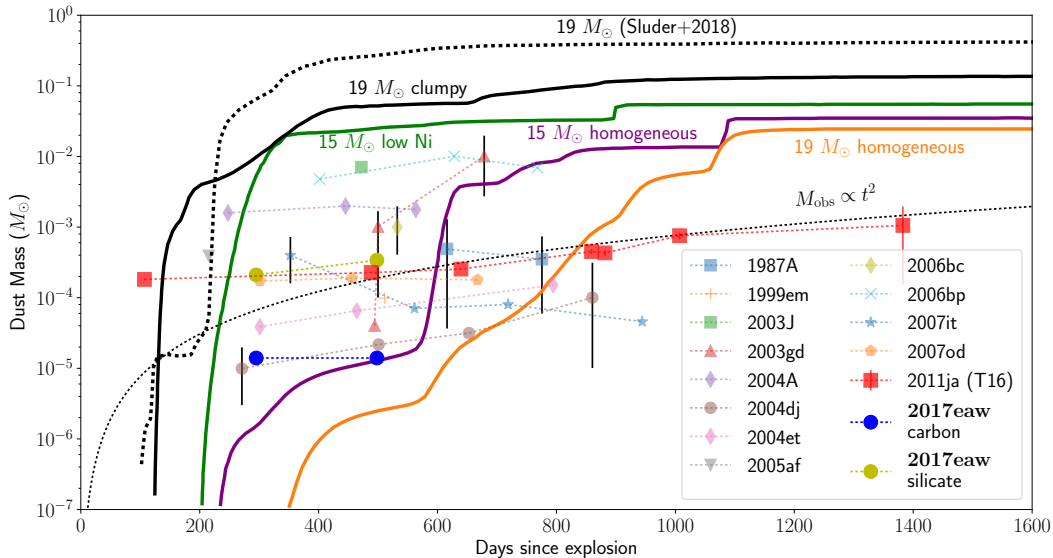


Figure 3.8: Dust mass evolution of SN 2017eaw derived from the SED fitting in comparison to other SNe II-P and II-pec (1987A). Yellow and blue circles are results for 100% silicate and 100% carbon grain cases, respectively. Other points are observed dust mass from other SNe from the literature, taken from Figure 10 of Sarangi and Cherchneff (2015) apart from those of SN 2011ja, which are from Tinyanont et al. (2016). Solid lines are dust mass predictions from different models in Sarangi and Cherchneff (2015) with progenitor mass and ejecta assumptions noted. The dashed black line is the total dust mass from the Sluder et al. (2018) model specifically for SN 1987A. They noted that their model should be compared to the $19 M_{\odot}$ with clumpy ejecta scenario from Sarangi and Cherchneff (2015). We note that these models consider only dust formation in the SN ejecta and do not consider pre-existing dust and newly formed dust in the CSM. The black dotted line denotes the observed dust mass evolution of $M_{\text{obs}} \propto t^2$ (arbitrarily scaled) expected from the evolution of the dust opacity (Dwek et al., 2019).

3. The SED evolution showed a rising warm dust emission continuum in the $3.6 \mu\text{m}$ band and an excess in the $4.5 \mu\text{m}$ band that was likely due to CO fundamental band emission. Small amounts of dust ($10^{-6} M_{\odot}$ carbonaceous or $10^{-4} M_{\odot}$ silicate) were needed to fit the SED at 197 and 295 d. While we cannot distinguish the two dust compositions from our data because of the lack of wavelength coverage around the silicate features at $\sim 10 \mu\text{m}$, we note that silicate dust was detected in SN 2004et. We note that the small observed dust mass at early time may be due to the high opacity, even in the IR (Dwek et al., 2019).
4. We identify the absorption feature at $1.045 \mu\text{m}$ as the He I $1.083 \mu\text{m}$ line at $10,000 \text{ km s}^{-1}$. The presence of a high-velocity He I $1.083 \mu\text{m}$ absorption

line at the velocity near that of the shock front indicates that gas in the outer ejecta is excited by high-energy photons, suggestive of CSM interaction.

5. The CO first overtone band at $2.3 \mu\text{m}$ continued to evolve from 205 d as reported by Rho et al. (2018). The CO feature peaked at 389 d and subsequently faded with respect to the continuum in later epochs, similar to the behavior observed in SN 1987A. We conclude that the CO feature faded because the gas had cooled enough so that CO vibrational levels required for the first overtone emission were no longer populated. The $4.5 \mu\text{m}$ excess, likely due to the CO fundamental bands, was still detected at 566 d. The formation and survival of CO are in line with predictions from the MNT chemical evolution models presented by Sarangi and Cherchneff (2013, 2015), and Sluder et al. (2018).
6. At 389 d, the CO line profile was similar to that of SN 1987A at 377 d. As a result, a non-LTE model fitted to SN 1987A (Liu et al., 1992) also fits our data. This suggests that the CO mass ($\sim 10^{-3} M_{\odot}$) and temperature (1800 K) of the two SNe are similar at this epoch.

This study underlines the need for future IR observations of CCSNe in order to study molecule and dust formation in their ejecta in greater detail. Such observations, enabled by advances in IR instruments, especially *JWST*, will allow us to put constraints on chemical models of SNe ejecta and to paint a more complete picture of the contribution of CCSNe to the molecular and dust budget of the interstellar medium.

Acknowledgement

We thank Jim Fuller and Luc Dessart for helpful discussions and input on the paper draft. We also thank the anonymous referee for reviewing the article. Some of the data presented herein were obtained at the W. M. Keck Observatory, which is operated as a scientific partnership among the California Institute of Technology, the University of California, and the National Aeronautics and Space Administration. The Observatory was made possible by the generous financial support of the W. M. Keck Foundation. The authors wish to recognize and acknowledge the very significant cultural role and reverence that the summit of Maunakea has always had within the indigenous Hawaiian community. We are most fortunate to have the opportunity to conduct observations from this mountain. Some of the data presented herein were obtained at Palomar Observatory, which is operated by a

collaboration between California Institute of Technology, Jet Propulsion Laboratory, Yale University, and National Astronomical Observatories of China. This work is based in part on observations made with the *Spitzer Space Telescope*, which is operated by the Jet Propulsion Laboratory, California Institute of Technology, under a contract with NASA. Support for this work was provided by NASA through an award issued by JPL/Caltech. This research has made use of the NASA/IPAC Extragalactic Database (NED), which is operated by the Jet Propulsion Laboratory, California Institute of Technology, under contract with the National Aeronautics and Space Administration. RDG was supported by NASA and the United States Air Force.

Chapter 4

SUPERNOVA 2014C: ONGOING INTERACTION WITH
EXTENDED CIRCUMSTELLAR MATERIAL WITH SILICATE
DUST

Tinyanont, S. et al. (Dec. 2019). “Supernova 2014C: Ongoing Interaction with Extended Circumstellar Material with Silicate Dust”. In: *ApJ* 887.1, 75. DOI: 10.3847/1538-4357/ab521b. arXiv: 1909.06403 [astro-ph.SR].

Samaporn Tinyanont¹ Ryan M. Lau² Mansi M. Kasliwal¹ Keiichi Maeda³ Nathan
Smith⁴ Ori D. Fox⁵ Robert D Gehrz⁶ Kishalay De¹ Jacob Jencson⁴ John Bally⁷
Frank Masci⁸

¹Division of Physics, Mathematics and Astronomy, California Institute of Technology, 1200 E. California Blvd., Pasadena, CA 91125, USA.

²Institute of Space & Astronautical Science, Japan Aerospace Exploration Agency, 3-1-1 Yoshinodai, Chuo-ku, Sagamihara, Kanagawa 252-5210, Japan

³Department of Astronomy, Kyoto University, Kitashirakawa-Oiwake-cho, Sakyo-ku, Kyoto 606-8502, Japan

⁴Steward Observatory, 933 North Cherry Avenue, Tucson, AZ 85721, USA.

⁵Space Telescope Science Institute, 3700 San Martin Dr, Baltimore, MD 21218, USA

⁶Minnesota Institute for Astrophysics, School of Physics and Astronomy, University of Minnesota, 116 Church Street, S. E., Minneapolis, MN 55455, USA

⁷Center for Astrophysics and Space Astronomy, Department of Astrophysical and Planetary Sciences, University of Colorado, Boulder, CO 80389, USA

⁸IPAC, California Institute of Technology, 1200 E. California Blvd., Pasadena, CA 91125, USA

Abstract

Supernova (SN) 2014C is unique: a seemingly typical hydrogen-poor SN that started to interact with a dense, hydrogen-rich circumstellar medium (CSM) ~ 100 days post-explosion. The delayed interaction suggests a detached CSM shell, unlike in a typical SN II_n where the CSM is much closer and the interaction commences earlier post-explosion; indicating a different mass-loss history. We present infrared observations of SN 2014C 1–5 years post-explosion, including uncommon $9.7 \mu\text{m}$ imaging with COMICS on the Subaru telescope. Spectroscopy shows the intermediate-width He I $1.083 \mu\text{m}$ emission from the interacting region up to the latest epoch 1639 days post-explosion. The last *Spitzer*/IRAC photometry at 1920 days confirms ongoing CSM interaction. The 1–10 μm spectral energy distributions (SEDs) can be explained by a dust model with a mixture of 62% carbonaceous and 38% silicate

dust, pointing to a chemically inhomogeneous CSM. The inference of silicate dust is the first among interacting SNe. An SED model with purely carbonaceous CSM dust, while possible, requires more than $0.22 M_{\odot}$ of dust, an order of magnitude larger than what has been observed in any SNe at this epoch. The light curve beyond 500 days is well fit by an interaction model with a wind-driven CSM and a mass-loss rate of $\sim 10^{-3} M_{\odot} \text{ yr}^{-1}$, which presents an additional CSM density component exterior to the constant-density shell reported previously in the literature. SN 2014C could originate in a binary system, similar to RY Scuti, which would explain the observed chemical and density profile inhomogeneity in the CSM.

4.1 Introduction

Massive stars significantly drive the chemical evolution of the interstellar medium (ISM), with mass loss throughout their lives leading up to the final core-collapse supernova (CCSN). However, much is unknown about the last stages of their evolution. While we understand several physical processes behind mass loss in massive stars, such as various types of stellar winds and eruptive outflows, quantitative modeling of stellar evolution to determine the endpoint remains difficult, due to uncertainties in the model assumptions. As a result, we currently do not have a definitive model that maps classes of progenitor stars with different amounts of hydrogen in their envelopes and different circumstellar media (CSM) to the resulting subtypes of CCSNe with different strengths of hydrogen features in their spectra. In recent years, binary interactions and episodic mass loss have become more preferred over the steady wind-driven outflow as the mass-loss mechanism for massive stars because the rate expected from wind-driven mass loss is insufficient, in most cases, to strip the entire hydrogen envelope to produce progenitors to SNe Ib/c e.g., De Marco and Izzard, 2017; Smith, 2014. Wind-driven mass loss also cannot explain the large amount of CSM observed in some SNe that have signatures of strong CSM interactions, those of Type IIn. Observations of the interaction between the SN shock and the CSM allow us to probe the mass-loss history, providing clues to the identity of the progenitor star.

The CSM around some Galactic massive stars have been directly observed, showing a vast diversity in terms of density and symmetry, ranging from a diffuse media around red supergiants (RSGs) like Betelgeuse (e.g., Kervella et al., 2016; Smith et al., 2009b) to the massive, dense, and asymmetric nebula around the peculiar luminous blue variable (LBV) η Car (e.g., Smith, 2006). One feature these nebulae have in common, however, is that they show strong signatures of silicate dust at

10–20 μm . Some examples include the nebula around a typical LBV, HR Car (Umana et al., 2009), and most RSG observed at these wavelengths (e.g., Woods et al., 2011). Dust grains typically form in the cooling outflow after the formation of carbon monoxide (CO), which equally depletes C and O atoms from the medium. If the outflow is oxygen rich, there are leftover O that can form precursor species to silicate dust, like SiO_2 and Mg_2SiO_4 ; otherwise, carbonaceous dust grains can form (which happens in SN ejecta as described by Sarangi and Cherchneff, 2013 and Sarangi and Cherchneff, 2015). The presence of silicates in most Galactic massive stars indicates that their outflows are oxygen rich. The Galactic massive stars with carbonaceous dust grains in their nebulae are primarily the carbon-rich variant (WC) of the H-poor Wolf–Rayet stars (WR) such as Ve-245, which produce dust when their high-velocity, carbon-rich, wind decelerates as it interacts with the wind from its companion star (e.g., Gehrz and Hackwell, 1974; Marchenko and Moffat, 2017). If these WCs were to explode as a SN, it would be of Types Ib/c with large ejected mass. As a result, both silicate and carbonaceous dust are not expected to form in the same medium with a homogeneous C/O ratio because either C or O will be depleted first in the CO formation.

The CSM around an extragalactic massive star can be probed when the star explodes as a SN, sending out a shock wave that will interact with its surroundings. The shock-CSM interaction accelerates electrons to relativistic speeds, causing them to emit at X-ray and radio wavelengths. The X-ray photons can photoionize the unshocked gas in the CSM, which then recombines. In the densest CSM, the narrow emission lines from this process can be observed, constituting the Type IIn SNe, which account for $8.8^{+3.3}_{-2.9}\%$ of CCSNe (Smith et al., 2011b). Pre-existing dust in the CSM gets radiatively or collisionally heated by the shock and emit strongly in the infrared (IR). Population studies of SNe IIn using the *Spitzer Space Telescope* (Gehrz et al., 2007; Werner et al., 2004) have shown that these SNe are luminous and long lasting in the IR (e.g., Fox et al., 2011, 2013). As a result, IR spectral energy distribution (SED) or spectra, when available, can reveal the dust composition of the CSM, allowing for a comparison with Galactic massive stars to identify the type of the progenitor star. The most distinguishing features between the carbonaceous and silicate dust are the broad mid-IR silicate features at around 10 and 18 μm .

IR observations of SNe at these long wavelengths are difficult to obtain from the ground owing to the high thermal background from the atmosphere and the telescope, and the atmospheric absorptions from water vapor. Hence, these observations are

rare: for strongly interacting SNe IIn, only four have been observed beyond $5 \mu\text{m}$. Three of which, SNe 1995N (Van Dyk, 2013), 2005ip (Fox et al., 2010), and 2006jd (Stritzinger et al., 2012) were detected by *Spitzer* and/or the *Wide-field InfraRed Explorer (WISE)*, with SN 2005ip being the only one with spectroscopy. SN 2010jl was observed with the Faint Object infraRed CAmera for the *SOFIA* Telescope (FORCAST, Herter et al., 2018) on board the Stratospheric Observatory for Infrared Astronomy (*SOFIA*; Young et al., 2012) at $11.1 \mu\text{m}$ with a deep upper limit. In all cases, the SED could be explained by purely carbonaceous grain models, which is unexpected given that all the Galactic stars that are potentially progenitors to these strongly interacting, H-rich SNe (e.g., LBVs, RSGs mentioned above) have silicate dust in their CSM. We note that these four SNe may not show silicate features because the dust is optically thick and not because there are no silicate grains. However, the opacity effect is unlikely the explanation for SN 1995N, which still did not show any obvious silicate features more than 10 yrs post-explosion (see the dust opacity evolution in Dwek et al., 2019). Given the small number of these observations due to the limited options for mid-IR observations after the *Spitzer* cryogenic mission, an addition to this sample would greatly improve our understanding of the landscape of SN emission beyond $5 \mu\text{m}$.

SN 2014C was the latest nearby interacting SN for which ground-based IR observations beyond $2.5 \mu\text{m}$ were possible. It was first detected on 2014 January 5 (UT dates are used throughout the paper) in NGC 7331 (Cepheid distance of 14.7 Mpc, Freedman et al., 2001), and was quickly identified spectroscopically as a typical, noninteracting H-poor Type Ib SN (Kim et al., 2014). The SN reached maximum light on 2014 January 13 (Milisavljevic et al., 2015), which we adopted as a reference epoch throughout this paper. The SN returned from behind the Sun and was observed on 2014 May 6, 113 days post-maximum, with an emerging $\text{H}\alpha$ emission line with an intermediate width of $\approx 1200 \text{ km s}^{-1}$, indicating that the SN shock had started to interact with a hydrogen-rich CSM, likely the progenitor’s ejected envelope (Milisavljevic et al., 2015). Such a transformation from a H-poor SN Ib/c to a H-rich interacting SN IIn had been observed before in SN 2001em (Chugai and Chevalier, 2006), and since in SN 2004dk (Mauerhan et al., 2018). However, SN 2014C was the first event for which the transition was caught in action in great detail. Margutti et al. (2017) reported early-time optical, ultraviolet (UV), and X-ray observations. From the semi-bolometric luminosity obtained from the near-UV to optical photometry at early time, they derived the explosion energy and the ejected mass of $1.8 \times 10^{51} \text{ erg}$ and $1.7 M_{\odot}$, typical for a normal SN Ib (Drout et al., 2011;

Lyman et al., 2016). The X-ray flux, indicating the interaction strength, continued to rise, peaking at ≈ 400 days, which put the location of the dense shell at 6×10^{16} cm from the star, following the shock radius evolution calculated following Chevalier (1982) and Chevalier and Liang (1989). They inferred the total mass of the ionized CSM from the observed bremsstrahlung absorption and arrived at $\approx 1 M_{\odot}$, assuming that the CSM was a shell with a thickness of 10^{16} cm. Anderson et al. (2017) reported radio observations of SN 2014C at 15.7 GHz, revealing two distinct interaction phases with the transition happening between 100 and 200 days. The two phases corresponded to the phases before and after the Type II_n transition happened in the optical. All published results pointed to the progenitor of SN 2014C being a stripped-envelope star exploding in a low-density bubble as a typical SN Ib, whose forward shock began to interact strongly with its ejected, H-rich envelope located at 6×10^{16} cm at 100–200 days post-explosion.

In addition to its peculiar early-time behavior, SN 2014C’s interaction was also long lasting. Mauerhan et al. (2018) published late-time optical spectra of SN 2014C, showing that SN 2014C’s interaction was still ongoing at day 1327, their last epoch. The shock front ($v \approx 10000 \text{ km s}^{-1}$) would already be at 10^{17} cm at that epoch, indicating that the CSM shell was more extended than previously thought. With a prolonged interaction with such dense medium, one might expect the forward shock of the SN to substantially slow down, but the radio imaging of the SN using very long baseline interferometry (VLBI) showed that the velocity of the shock barely decreased during the first 1000 days (Bietenholz et al., 2018). They also showed in the resolved VLBI image at 1057 days that the CSM was likely asymmetric. The likely explanation for these results was that the CSM was not isotropic and some parts of the shock were able to propagate freely, allowing for the interaction to continue.

The IR evolution of SN 2014C up to 800 days post-explosion was discussed in our previous work, Tinyanont et al. (2016) (T16 hereafter), where we summarized the IR properties of SNe of all types observed as part of the SPitzer InfraRed Intensive Transients Survey (SPIRITS; Kasliwal et al., 2017). SN 2014C stood out in our sample of H-poor SNe Ib/c and IIb as the most luminous event, even before the interaction was detected in the optical. The evolution of the inferred dust mass was consistent with pre-existing CSM dust being heated either radiatively or collisionally by the shock interaction with a CSM shell with constant density. This was because the dust mass grew as t^2 as the (constant velocity) shock’s interacting surface area

grew as $r^2 \propto t^2$. Based on the measured dust mass and location from fitting the *Spitzer* two-point SED, we assumed a dust-to-gas ratio of 0.01 and estimated the mass-loss rate that created the CSM shell up to that epoch to be $\gtrsim 10^{-2} M_{\odot} \text{ yr}^{-1}$ (assuming the wind velocity of 100 km s^{-1}), consistent with LBV giant eruptions and also consistent with Margutti et al. (2017). In this work, we focus on the evolution of SN 2014C in the IR since then. We describe our photometric and spectroscopic observations in §4.2. We analyze the data, focusing on the SED fitting to discern the dust composition and the light-curve fitting to measure the CSM density profile, in §4.3. We discuss the two possible dust compositions of the CSM around SN 2014C, and the additional wind-driven CSM component exterior to the constant-density shell found in previous studies. The discussions and conclusions are presented in §4.4.

4.2 Observations

Photometry

Near-IR 1–2.5 μm Photometry

We obtained five epochs of photometry of SN 2014C in the 1–2.5 μm *JHKs* bands using the Wide-field InfraRed Camera (WIRC; Wilson et al., 2003, with a detector upgrade described in Tinyanont et al., 2019c) on the 200-inch Hale Telescope at Palomar Observatory (P200 hereafter). Not every epoch had all three bands and some epochs had different bands taken a few days apart. NGC 7331 was small enough to fit into the field of view of WIRC, so the data were taken with dithering patterns that send the galaxy around the field of view to measure and subtract the sky background. Science images were dark subtracted and flattened using a flat-field image obtained from median-combined dithered sky images with sources masked out. The photometric zero point was determined using ~ 30 stars in the field of view with magnitudes from the Two Micron All-Sky Survey (2MASS; Milligan et al., 1996, Skrutskie et al., 2006). The data reduction was performed using an automated IR imaging pipeline described in De et al. (2020).

Fig. 4.1 shows a false-color image using WIRC images from 2018 June 23 where red, green, and blue correspond to the *Ks*, *H*, and *J* bands, respectively. Five images in the right of the figure are from the three near-IR bands and the two *Spitzer*/IRAC bands to visually demonstrate the red color of SN 2014C at this epoch. As shown in the image, SN 2014C was located in a spiral arm of NGC 7331 with a bright and spatially varying background, making host subtraction difficult. We did not have a

pre-explosion image of the host galaxy at a comparable resolution to conduct image subtraction. As a result, we measured the near-IR photometry as follows. First, for each band in each epoch, we created a library of point spread function (PSF) using stars in the vicinity of the SN that were not on top of the host galaxy. The PSF construction was done using the `EPSFBuilder` module in the `photutils` package (Bradley et al., 2019). We used the `DAOStarFinder` module to find the (subpixel) location of the SN. The PSF photometry was obtained by iteratively subtracting the PSF with different total flux to minimize the summed squared gradient of the image. This quantity was used as the metric to indicate the “point sourceness” of the image as the slowly varying background of the galaxy had a lower gradient than the point source. We compared the residual image of the same band from different epochs to ensure that the SN light had been consistently subtracted for all epochs. The PSF subtraction routine described above was custom-built in Python. Along with the new photometry, we also plotted near-IR photometry published in T16 in Fig. 4.3. All photometry discussed here, and in the following subsections, is listed in Table 4.1.

***Spitzer*/IRAC Photometry**

SN 2014C has been observed by the InfraRed Array Camera (IRAC; Fazio et al., 2004) on board *Spitzer* at 3.6 and 4.5 μm in 16 epochs, as part of SPIRITS (PIDs 10136, 11063, 13053, 14089; PI: Kasliwal). The photometry from the first nine epochs, up to 801 days post-discovery (794 days post-maximum), were published in T16. We had multiple pre-explosion *Spitzer*/IRAC images of NGC 7331, which we combined and used as a template for background subtraction. Fluxes were measured by performing aperture photometry on the background-subtracted frames, and the uncertainties were estimated by combining (in quadrature) the source noise with the background noise measured from a grid of apertures placed around the source. We recomputed photometry for epochs that were published in T16, and found that they agree to within the uncertainty. We note that the updated error bars in this paper better reflect the more realistic uncertainties as the noise in subtracted images is non-Gaussian (Jencson et al., 2019).

Ground-based 3–5 μm Photometry

SN 2014C’s brightness at 3–5 μm permitted L' (3.43–4.13 μm) and M' (4.55–4.79 μm) band photometry from the ground. We obtained those observations with the

Near-InfraRed Imager and spectrograph (NIRI; Hodapp et al., 2003) on the Gemini North Telescope as part of a fast turnaround program (GN-2018A-FT-108; PI: Tinyanont). In these thermal IR bands, the observations were background limited and we used the $f/32$ camera, deep-well detector bias, and fast read-out mode to maximize the observing efficiency. Raw images were dark subtracted and field flattened with our Python script. The source was observed with dithering patterns that sent the source in and out of the field of view, allowing us to subtract the bright thermal background from the sky and the telescope. The total on-source integration time for the L' and M' bands were 135.15 and 1604 s resulting in signal-to-noise ratios (S/Ns) of 13 and 8, respectively. We observed a photometric standard HD 203856 ($L' = 6.871$, $M' = 6.840$; Leggett et al., 2003) after the target for flux calibration. The observing strategy for the standard star was similar to that of the SN, except that we only dither the star within the field of view. The images in the L' and M' bands are shown in Fig. 4.2 (left and center). We obtained ground-based 3–5 μm photometry in addition to the *Spitzer*/IRAC to make sure that we have the 3–5 μm coverage concurrent with the N -band imaging described next.

***N*-band Imaging with Subaru/Cooled Mid-infrared Camera and Spectrometer (COMICS)**

SN 2014C was observed by COMICS (Kataza et al., 2000) on the Cassegrain focus of the Subaru Telescope with the N9.7 filter ($\lambda = 9.7 \mu\text{m}$, $\Delta\lambda = 0.9 \mu\text{m}$) on 2018 June 28. Individual 200 s exposures were taken in chopping-only mode with a chop amplitude of 12'' and the total integration time on SN 2014C was 1.6 hr. 5 LAC (HR 8572) was used as the photometric standard from the list of mid-IR standards in Cohen et al. (1999). The COMICS N9.7 flux from 5 LAC was derived by integrating the filter bandpass over its IR spectrum provided by Cohen et al. (1999). Assuming a box function for the filter profile ranging from $\lambda = 9.25 - 10.15 \mu\text{m}$, the COMICS N9.7 flux from 5 LAC was determined to be 44.0 Jy. We note that this is closely consistent with the calibrated flux derived with the similar VLT/VISIR B9.7 filter for the same standard (42.5 Jy¹). The measured full-width at half maximum (FWHM) of the calibrator was $\sim 0''.5$, which was slightly worse than diffraction-limited performance at 9.7 μm ($0''.25$) and likely due strong winds and poor seeing conditions during the observations. SN 2014C was detected with a 5σ significance at a flux of 16 ± 3 mJy in the N9.7 filter. Fig. 4.2 (right image) shows the calibrated

¹http://www.eso.org/sci/facilities/paranal/instruments/visir/tools/zerop_cohen_Jy.txt

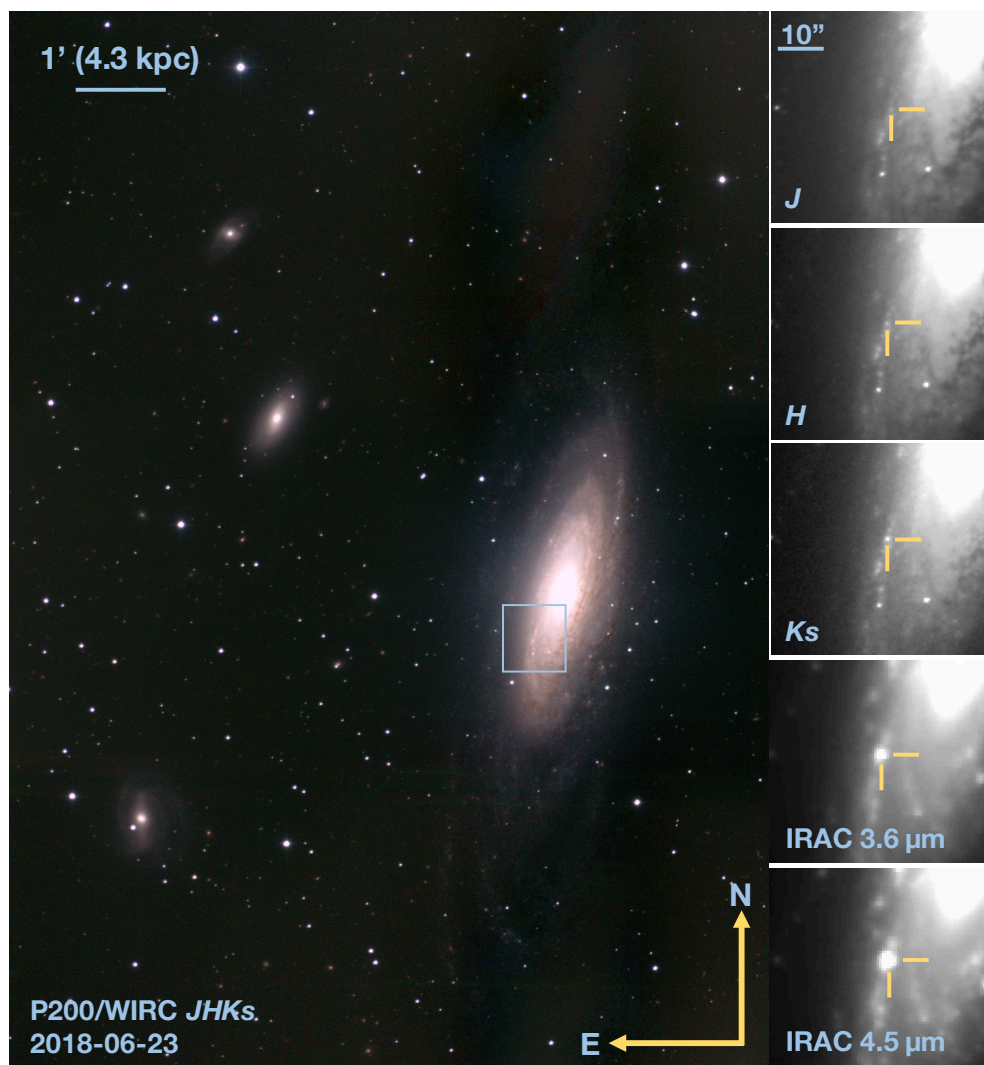


Figure 4.1: Left: a false image composite of NGC 7331 where red, green, and blue correspond to K_s , H , and J , respectively. North is up and east is to the left. The images were taken with P200/WIRC on 2018 June 23. The location of the SN in the galaxy is marked with a box. Right: five images of the boxed area in the left panel in five wavelengths: J , H , K_s from P200/WIRC and 3.6 and 4.5 μm from *Spitzer*/IRAC. The *Spitzer* observations were from 2018 February 28.

image from COMICS. The right-most plot shows the vertical profile of the flux on the source location, with a 5σ threshold indicated to illustrate the source detection significance.

Ground-based Spectroscopy

We obtained near-IR 1–2.5 μm spectra of SN 2014C in 7 epochs spanning from 1 to 5 years post-maximum. Table 4.2 summarizes all the spectra taken. We used the

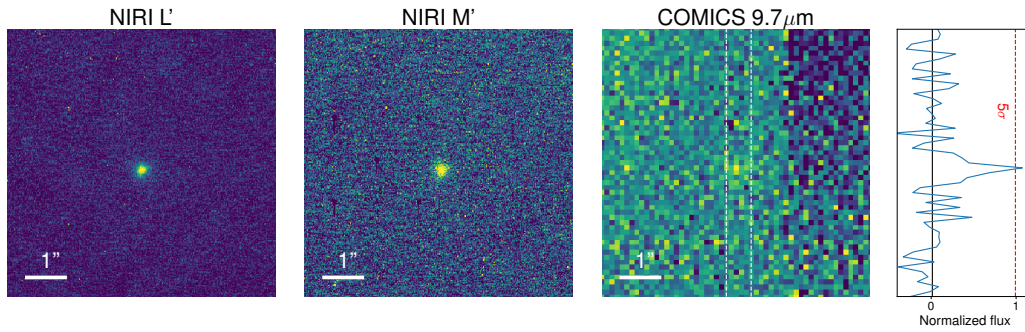


Figure 4.2: Ground-based IR images of SN 2014C from NIRI in the L' and M' bands (left and center) and COMICS in the $9.7 \mu\text{m}$ band (right). The vertical profile of the COMICS data between two dashed lines is shown in the right-most plot, with the flux normalized. The solid black line indicates the background-subtracted mean of the flux profile and the dashed red line indicates the 5σ threshold. This plot is to show that the source is detected in the COMICS image at the 5σ level.

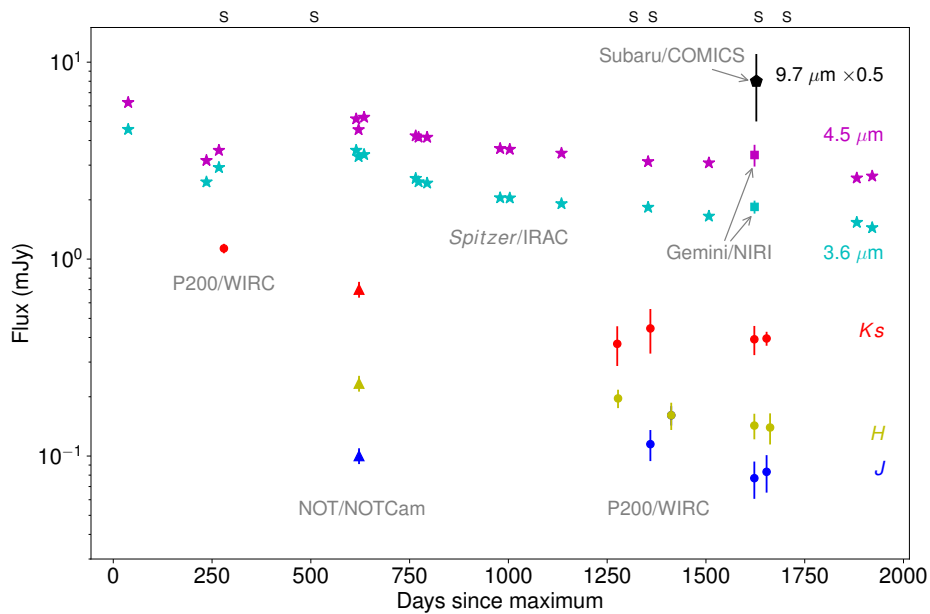


Figure 4.3: IR photometry of SN 2014C in the J , H , K_s , $3.6 \mu\text{m}$, $4.5 \mu\text{m}$, and $9.7 \mu\text{m}$ bands, plotted in colors as annotated. Different symbols correspond to different instruments. The $9.7 \mu\text{m}$ flux is divided by two for visualization. Data up to day 801 were published in T16. Letters “S” on top of the plot indicate epochs with spectroscopy.

Table 4.1: IR photometry of SN 2014C

Date (UT)	Epoch (day)	F_J	σ_{F_J}	F_H	σ_{F_H}	F_{K_s}	$\sigma_{F_{K_s}}$ (mJy)	$F_{[3,6]}$	$\sigma_{F_{[3,6]}}$	$F_{[4,5]}$	$\sigma_{F_{[4,5]}}$	Instrument
2014-02-19	37.8	—	—	—	—	—	—	4.55	0.08	6.24	0.09	Spitzer/IRAC
2014-09-05	235.8	—	—	—	—	—	—	2.46	0.10	3.17	0.06	Spitzer/IRAC
2014-10-07	267.4	—	—	—	—	—	—	2.92	0.09	3.56	0.06	Spitzer/IRAC
2015-09-19	614.8	—	—	—	—	—	—	3.57	0.09	5.15	0.07	Spitzer/IRAC
2015-09-25	620.8	—	—	—	—	—	—	3.31	0.09	4.54	0.07	Spitzer/IRAC
2015-10-09	634.8	—	—	—	—	—	—	3.39	0.09	5.25	0.06	Spitzer/IRAC
2016-02-17	765.4	—	—	—	—	—	—	2.57	0.01	4.22	0.02	Spitzer/IRAC
2016-02-24	772.7	—	—	—	—	—	—	2.47	0.01	4.16	0.02	Spitzer/IRAC
2016-03-17	794.3	—	—	—	—	—	—	2.43	0.01	4.15	0.02	Spitzer/IRAC
2016-09-18	979.2	—	—	—	—	—	—	2.05	0.02	3.64	0.02	Spitzer/IRAC
2016-10-12	1003.5	—	—	—	—	—	—	2.04	0.02	3.61	0.02	Spitzer/IRAC
2017-02-20	1134.4	—	—	—	—	—	—	1.91	0.02	3.45	0.02	Spitzer/IRAC
2017-07-11	1275.5	—	—	—	—	0.37	0.08	—	—	—	—	P200/WIRC
2017-07-13	1277.5	—	—	0.20	0.02	—	—	—	—	—	—	P200/WIRC
2017-09-27	1353.7	—	—	—	—	—	—	1.83	0.01	3.12	0.01	Spitzer/IRAC
2017-10-03	1359.4	0.11	0.02	—	—	0.44	0.11	—	—	—	—	P200/WIRC
2017-11-25	1412.2	0.16	0.02	0.16	0.03	—	—	—	—	—	—	P200/WIRC
2018-02-28	1507.5	—	—	—	—	—	—	1.65	0.02	3.08	0.01	Spitzer/IRAC
2018-06-23	1622.5	0.08	0.02	0.14	0.02	0.39	0.07	—	—	—	—	P200/WIRC
2018-06-24	1623.0	—	—	—	—	—	—	1.84	0.14	3.38	0.43	Gemini/NIRI ^a
2018-07-24	1653.5	0.08	0.02	—	—	0.40	0.03	—	—	—	—	P200/WIRC
2018-08-02	1662.3	—	—	0.14	0.03	—	—	—	—	—	—	P200/WIRC
2019-03-09	1881.8	—	—	—	—	—	—	1.54	0.02	2.58	0.02	Spitzer/IRAC
2019-04-17	1920.8	—	—	—	—	—	—	1.44	0.02	2.64	0.02	Spitzer/IRAC
2018-06-28	1627.5	—	—	—	—	—	—	$F_{[9,7]} = 16$			$\sigma_{F_{[9,7]}} = 3$	Subaru/COMICS

^aGemini/NIRI's filters are L' and M' , which are different from Spitzer/IRAC's filters.

twin medium-resolution, long-slit, echellette spectrographs: TripleSpec on P200 (Herter et al., 2008) and the Near-Infrared Echellette Spectrometer (NIRES) on the Keck telescope,² both of which provided simultaneous 1–2.5 μm spectra of a single source. The only difference between TripleSpec and NIRES was the fixed slit widths of 1" versus 0'55. The data were taken by either dithering the source along the slit or alternating between the source and the sky to enable sky subtraction. Data from both TripleSpec and NIRES were reduced using a version of `Spextool` (Cushing et al., 2004) specifically for TripleSpec and NIRES. The software applied field flattening, retrieved a wavelength solution from sky lines present in science observations, and subtracted each exposure pair to remove most of the sky emission. It located the trace of the object in the reduced 2D images, then fit a low-order polynomial across the trace to estimate host background. Finally, the spectral trace was reduced using an optimal extraction algorithm to enhance the S/N while rejecting bad pixels and cosmic ray hits (Horne, 1986). The telluric and flux calibrations were performed using `xtellcor` with the standard observations of an A0V star either before or after the SN observation (Vacca et al., 2003).

In addition, we also used the Multi-Object Spectrometer for Infra-Red Exploration (MOSFIRE; McLean et al., 2012) on the Keck telescope. MOSFIRE can obtain spectra of up to 46 sources in its field of view, one filter at a time. The filters used in each epoch are reported in Table 4.2. Exposure times for MOSFIRE observations are given for each filter. The data reduction and spectral extraction were performed using MOSFIRE's data reduction pipeline,³ and telluric and flux calibrations were performed using `xtellcor`. We caution that the accuracy of flux calibration between different epochs and different instrument can vary up to a factor of 2–3. Galaxy host contamination also varied among spectra due to the different slit widths and observing conditions. However, all subsequent analyses of the spectra will not rely on absolute flux calibration. All 1–2.5 μm spectra are shown in Fig. 4.4.

Finally, we obtained 3.0–3.9 μm spectroscopy using the Gemini Near-InfraRed Spectrograph (GNIRS) on the Gemini North telescope as part of a fast turnaround program (GN-2018A-FT-108, PI: Tinianont). Ground-based observations in this wavelength is difficult owing to the very strong thermal background from both the sky and the telescope. For these observations, we used the long red camera with the pixel scale of 0'05/pixel and the 0'15 slit with the 10 l/mm grating for the resolving power of $R \sim 1200$. The wavelength range captured in our spectra was 3.1–3.9

²<https://www2.keck.hawaii.edu/inst/nires/>

³<https://keck-datareductionpipelines.github.io/MosfireDRP/>

Table 4.2: Log of spectroscopic observations of SN 2014C

Date	Epoch (day)	Telescope/Instrument	Bands	Exposure Time (sec)
2014-10-08	268	Keck/MOSFIRE	JHK	1440, 2160, 2160
2015-05-25	497	Keck/MOSFIRE	K	1080
2017-08-09	1304	P200/TripleSpec	YJHK	5400
2017-08-11	1306	P200/TripleSpec	YJHK	9600
2017-09-28	1354	Keck/MOSFIRE	YJHK	720, 480, 480, 720
2018-06-22	1621	P200/TripleSpec	YJHK	3900
2018-08-17	1677	Gemini/GNIRS	L'	510
2018-09-02	1693	Keck/NIRES	YJHK	600

μm . To handle high background, we set the detector bias to the deep-well mode to increase the saturation threshold and the read-out mode to match the read-out noise to the sky background noise. The observations were taken on 2018 August 16–17, with the total integration time of 23 and 68 minutes on the respective nights. We found, however, that only the first 17 images from the first night contain the SN trace. Each exposure was 30 s, 2 coadds, in ABBA dithering pattern along the slit. The data were reduced using Gemini’s IRAF-based data reduction pipeline.⁴ The telluric and flux calibrations were performed using `xtellcor` with HIP 114714 (HD 219290) as a standard star. We caution that spectral features present are likely spurious, and the spectra simply probed the continuum. We overplotted the binned spectrum in Fig. 4.6, but did not use it to fit the SED.

4.3 Analysis

SED Fitting and Silicate Dust in the CSM

Thermal emission arises from dust grains at different temperatures and different locations in the SN. To roughly determine this, we first fit a simple blackbody to the IR SED of SN 2014C at 1623 days, the epoch at which we have the $10\ \mu\text{m}$ data and for which we will perform full SED fitting. We find that the near-IR ($1\text{--}2.5\ \mu\text{m}$) flux is well explained by a hot component at $T \sim 1000\ \text{K}$ located at $r \sim 10^{15}\ \text{cm}$. The $3\text{--}5\ \mu\text{m}$ flux arises from a warm component with $T \sim 500\ \text{K}$ and $r \sim 4 \times 10^{16}\ \text{cm}$. Finally, the $10\ \mu\text{m}$ flux can be explained by a cold component with $T \sim 300\ \text{K}$ and $r \sim 1.5 \times 10^{17}\ \text{cm}$. We will argue later that the $10\ \mu\text{m}$ flux is more likely from silicate dust emission feature and not a cold dust component. We note that the blackbody radii are the physical radii of optically thick dust clouds. In reality, the CSM dust is optically thin, and the blackbody radii are lower limits to the actual location of the dust grains. The shock front at this epoch, which is determined from the model that we will discuss in §4.3, is at $r_{\text{sh}} = 1.2 \times 10^{17}\ \text{cm}$, suggesting

⁴<https://www.gemini.edu/sciops/data-and-results/processing-software>

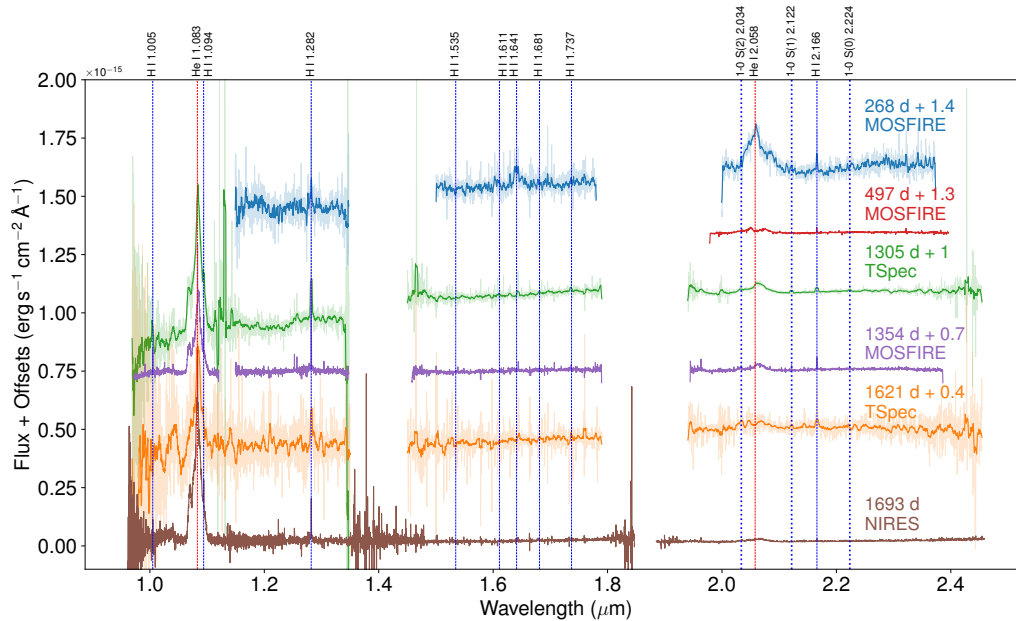


Figure 4.4: Near-IR spectra of SN 2014C from 268 to 1693 days post-maximum. Offsets applied to the spectra are indicated next to the corresponding dates. We note that TripleSpec spectra have poorer background subtraction, in comparison to MOSFIRE or NIREs spectra, due to the higher background at Palomar and also more galaxy contamination due to the wider slit. Hydrogen and helium lines, including molecular hydrogen $\nu = 1 - 0$ transitions, are marked. See text and Table 4.2 for details of the observations. Spectra in this plot are available as the data behind the figure.

that the hot component arises from likely newly formed dust inside the ejecta while the warm component is likely associated with pre-existing CSM dust heated by the shock either radiatively or collisionally.

We determine the composition of the dust in the CSM around SN 2014C by fitting its IR SED with different dust models. Following T16 and Fox et al. (2010), we fit the SED with a modified blackbody spectrum

$$F_{\nu} = \frac{M_{\text{dust}} B_{\nu}(T_{\text{dust}}) \kappa_{\nu}(a)}{d^2} \quad (4.1)$$

where M_{dust} is the total dust mass, B_{ν} is the Planck function, T_{dust} is the dust temperature, and $\kappa_{\nu}(a)$ is the dust grain opacity, which is a function of dust grain size, a . This dust SED assumes that the emitting dust is optically thin and at a single temperature. We will check the optical depth assumption after calculating the dust mass. We note that this equation poses no geometric requirements on the distribution of the dust grains. The dust emissivity (Q), and consequently opacity

(κ) for carbonaceous and silicate grains are from Draine and Lee (1984) and Laor and Draine (1993), where we only consider graphite for carbonaceous grains. We convert the tabulated emissivity into opacity using the relation $\kappa = 3Q/4\rho_{\text{bulk}}a$, where the bulk densities are $\rho_{\text{bulk}} = 2.2$ and 3 g cm^{-3} for the graphite and silicate grains, respectively. Amorphous carbon has higher emissivity, requiring less mass to explain the same IR flux, but the general shape of the SED is similar to that of graphite. We assume the grain size of $0.1 \mu\text{m}$, noting that the emissivities from different grain sizes are degenerate in the IR, unless we include the unlikely large $1 \mu\text{m}$ grains (see Figure 4, top panel from Fox et al., 2010).

Fig. 4.5 shows the SED of SN 2014C with near-IR photometry from P200/WIRC, mid-IR photometry from *Spitzer*/IRAC and Gemini/NIRI, and finally mid-IR ($9.7 \mu\text{m}$) photometry from Subaru/COMICS. All data were taken between 1622 and 1626 days post-maximum. The *Spitzer* data were interpolated from days 1515 and 1889 using a power law. The two panels of Fig. 4.5 compare two different models, which provide different explanations for the $9.7 \mu\text{m}$ flux: copious cold carbonaceous dust (left) and the silicate dust’s feature (right).

We first consider a scenario where all CSM dust around SN 2014C is carbonaceous (Fig. 4.5, left). This composition choice is based on prior observations, showing that no other interacting SNe with mid-IR observations showed silicate features. In this model, the $9.7 \mu\text{m}$ flux is dominated by cold carbonaceous dust at 276 K. We sample the parameter space with a Markov Chain Monte Carlo (MCMC) routine *emcee* (Foreman-Mackey et al., 2013) to derive the model parameters along with their robust uncertainties. More details on our MCMC sampling method are given in Appendix A.1 and the corner plot of this MCMC fitting is described in Fig. A.1. While this model fits our data well, the high mass of cold carbonaceous dust necessary to produce the observed $9.7 \mu\text{m}$ flux, $0.22 M_{\odot}$ is problematic. First, $0.22 M_{\odot}$ of carbonaceous dust at a minimum distance of $r_{\text{bb}} = 1.5 \times 10^{17} \text{ cm}$ (the blackbody radius, derived earlier in this section for a cold dust component, also consistent with the shock radius derived later in §4.3) would have maximum optical depths, $\tau_{\nu} = M_d \kappa_{\nu} / 4\pi r_{\text{bb}}^2 = 3, 2,$ and 0.6 at $3.6, 4.5,$ and $9.7 \mu\text{m}$, respectively. This means that the dust could be not optically thin, resulting in even higher total dust mass than observed. Second, this dust mass is an order of magnitude higher than that dust mass observed in any SNe at this epoch (see, e.g., Fig. 4 in Gall et al., 2014) and is an order of magnitude higher than the dust mass inferred in SN 2006jd from the 3 to $10 \mu\text{m}$ observations at a similar epoch (Stritzinger et al., 2012). We

also note that SN 2006jd had $\lambda > 5\mu\text{m}$ observations with neither signs of silicates nor cold (~ 300 K) carbonaceous dust components that appear in SN 2014C. As mentioned earlier, the dust mass inferred here is the mass of the IR-emitting dust, which is only a lower limit to the total dust mass in the CSM. Assuming the canonical gas-to-dust mass ratio of 100, the lower limit of the emitting dust mass indicates that the mass of the gas shell containing the IR-emitting dust is $\gtrsim 20 M_{\odot}$, which is large in comparison to even the most massive Galactic LBV nebulae (Smith and Owocki, 2006 and Kochanek, 2011 assumed the same gas-to-dust ratio). Furthermore, we will show in §4.3 that the total CSM mass around SN 2014C could only be about $4\text{--}9 M_{\odot}$. These are the major caveats to the purely carbonaceous dust scenario.

We now consider a second scenario, in which the $9.7\ \mu\text{m}$ flux of SN 2014C is explained by the broad silicate feature around $10\ \mu\text{m}$ (Fig. 4.5, right). In this model, we fit the SED with two dust components. The first component is a single-temperature warm dust (T_{warm}) composed of both carbonaceous and silicate grains with a total mass of M_{warm} , a fraction f_{Si} of which is silicate. The second component is hot dust at the temperature T_{hot} composed of only carbonaceous dust with the total mass of M_{hot} . We used MCMC as described previously and in Appendix A.1 to derive the model parameters along with their robust uncertainties. The composition of this hot component does not matter because the flux at $10\ \mu\text{m}$ from this component is negligible. The resulting parameters from the MCMC fits are $T_{\text{warm}} = 484^{+11}_{-13}$ K, $M_{\text{warm}} = 5.2^{+0.7}_{-0.6} \times 10^{-3} M_{\odot}$, $T_{\text{hot}} = 1165^{+140}_{-100}$ K, $M_{\text{hot}} = 4^{+4}_{-2} \times 10^{-6} M_{\odot}$, and $f_{\text{Si}} = 0.38^{+0.06}_{-0.08}$. The corner plot of the MCMC fitting is presented in Fig. A.2. The uncertainties provided here only incorporate uncertainties in the measured flux and not in the dust emissivity. The near-IR photometry is well fitted by a hot, 1165 K, carbonaceous dust component. The total warm dust mass in this scenario, $5 \times 10^{-3} M_{\odot}$, is similar to that observed in SN 2006jd (Stritzinger et al., 2012). The dust cloud of this mass could also be optically thin if dust is located around the shock radius of 1.2×10^{17} cm; the maximum optical depths are 0.01, 0.01, and 0.1 at 3.6, 4.5, and $9.7\ \mu\text{m}$, respectively. Because of the more reasonable dust mass required to fit the SED, we favor this scenario in which the $9.7\ \mu\text{m}$ is dominated by the broad silicate dust emission. Follow-up observations with more photometric bands around the $9.7\ \mu\text{m}$ band are required to robustly identify the silicate feature. The mixture of silicate and carbonaceous dust grains required to explain the SED suggests that the CSM is inhomogeneous in its composition because a homogeneous medium with $C/O \neq 1$ will form only either carbonaceous or silicate dust. We will further discuss the implication on the origin of the CSM around SN 2014C in §4.4.

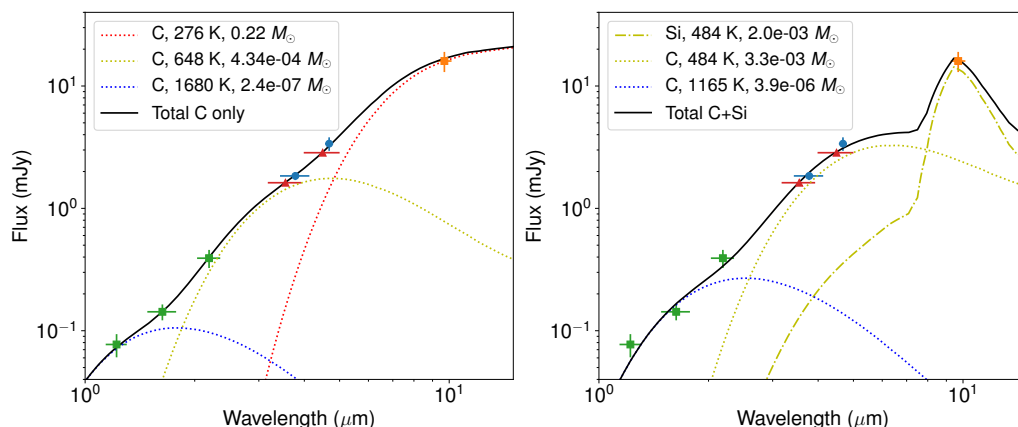


Figure 4.5: SED of SN 2014C from 1 to 10 μm observed 1622–1626 days post-maximum. The error bars in the x -direction represent the filter bandwidth. The left panel shows the SED fitted by a dust emission model with only amorphous carbonaceous dust, which required three different temperatures. The right panel shows the fit with hot carbonaceous dust and warm dust with 66% carbonaceous and 34% silicate grains (by mass). The mass ratio was obtained from fitting the data. We note that the purely carbonaceous dust model requires an order of magnitude more dust than ever observed in previous SNe at these epochs.

Comparison to Other Interacting SNe with 10 μm Observation

Fig. 4.6 compares the IR SED of SN 2014C with the SEDs of all other interacting SNe for which observations beyond 5 μm are available in the literature. Apart from SN 2014C, only four other strongly interacting SNe II_n have been observed in the mid-IR. Three of these were observed at epochs comparable to the epoch at which SN 2014C was observed in the mid-IR. SN 2005ip was observed at 936 days post-explosion during the cryogenic phase of *Spitzer*. It was the only interacting SN with an InfraRed Spectrograph (IRS; Houck et al., 2004) mid-IR spectrum from 5 to 12 μm and IRAC photometry at 5.8 and 8 μm (Fox et al., 2010). SN 2006jd was observed at 1638 days, an epoch very similar to that of SN 2014C, with *Spitzer*/IRAC and *WISE* (Stritzinger et al., 2012). SN 2010jl was observed at 1279 days with *Spitzer*/IRAC and SOFIA/FORCAST (Herter et al., 2018) at 11.1 μm , resulting in a deep upper limit after 6400 s of total integration time (Williams and Fox, 2015). In all three cases, the photometry and spectra from 1 to 10 μm are well fitted by purely carbonaceous dust models, which we overplot in Fig 4.6 using dust parameters from the literature. Lastly, SN 1995N was observed at more than ten years post-explosion by *Spitzer*/IRAC and *WISE* (Van Dyk, 2013). Its SED shape differs markedly from those of the other three SNe observed at earlier epochs. The carbonaceous dust

model that Van Dyk (2013) fitted to the data is shown in Fig. 4.6. However, we note that the shallow slope from 3–10 μm cannot be fitted with a single-temperature dust model, regardless of composition, and would require a range of dust temperatures. Given the late epoch of the observation, one might also consider a non-thermal origin for the IR emission from SN 1995N, as the SED can also be described with a broken power law ($F_\nu \propto \nu^{-3}$; also overplotted) with a knee at around 12 μm . In addition to these H-rich interacting SNe, the H-poor interacting SN 2006jc (Ibn) was also observed beyond 5 μm with *AKARI* (Sakon et al., 2009). Its SED was also best fitted with a two-temperature amorphous carbon dust model. This comparison highlights SN 2014C’s unique SED shape among other interacting SNe for which data are available beyond 5 μm at comparable epochs, showing for the first time an evidence for a silicate dust feature in the IR SED of an interacting SN. It also accentuates the need for observations of interacting SNe at late times, out to decades post-explosion, in the near- to mid-IR, which will be enabled by the upcoming *James Webb Space Telescope* (*JWST*).

Dust Parameter Evolution

To track the evolution of the dust parameters, we fit the SED at other epochs with *Spitzer*/IRAC data, assuming a fixed ratio between carbonaceous and silicate dust. We do not fit for the hot, near-IR component, due to the lack of temporal coverage and its small contribution (< 10%) to the IR luminosity. We run the MCMC fitting routine on all epochs and find that the posterior distributions of dust luminosity, temperature, and mass are Gaussian. Those parameters are shown in the top, middle, and bottom panels of Fig. 4.7, and are listed in Table 4.3. At 1620 days, the epoch for which we have the full SED, we compare the values obtained for the warm dust component by fitting the full SED to those obtained from fitting only 3–5 μm data. This is to demonstrate that the discrepancy is minimal. In the top panel, we also show the full IR luminosity including both the hot and warm dust components to demonstrate that the hot component contributes minimally to the total IR luminosity. As a result, we use the luminosity of the warm dust component as an estimate of the bolometric luminosity of the SN.

Light Curve Modeling

In this section, we fit the light curve of SN 2014C obtained in the last section with an analytic model from Moriya et al. (2013). The model assumes that the density profile in the SN ejecta follows a broken power law with $\rho_{\text{ej}} \propto r^{-\delta, -n}$ for

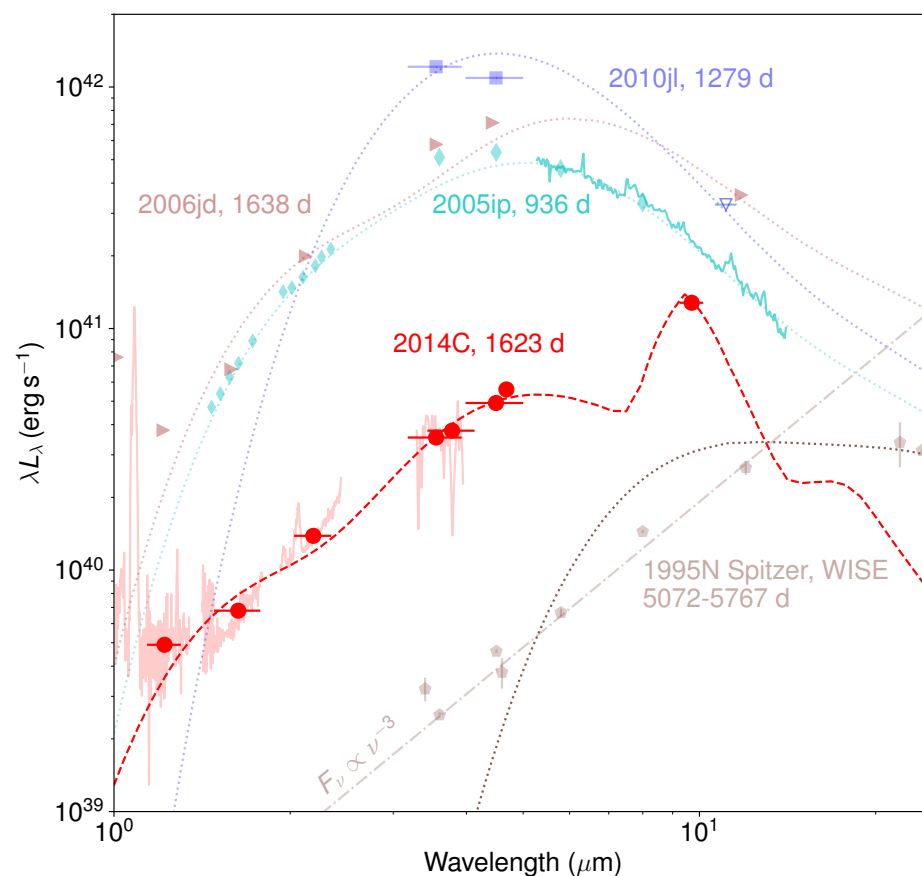


Figure 4.6: SED of SN 2014C compared with all other H-rich interacting SNe with mid-IR ($> 10 \mu\text{m}$) data in the literature, namely SNe 1995N (Van Dyk, 2013), 2005ip (Fox et al., 2010), 2006jd (Stritzinger et al., 2012), and 2010jl (Williams and Fox, 2015). The transparent red line represents the 1–2.5 μm spectra from NIRES and 3.3–3.9 μm spectrum from GNIRS taken at 1677 and 1693 d, with the flux scaled to match that from photometry. Diamond points for SN 2005ip around 1–2 μm are also taken from spectra shown in Fox et al. (2010). Apart from SN 2010jl’s 11.1 μm upper limit, all other data points are detections. We note that the SED of SNe 2005ip, 2006jd, and 2010jl could be explained with purely carbonaceous dust models, overplotted (dust parameters taken from respective papers). The SEDs of SN 1995N, taken at a much later epoch (5000–6000 days post-explosion), were ill-fitted by either carbonaceous or silicate dust.

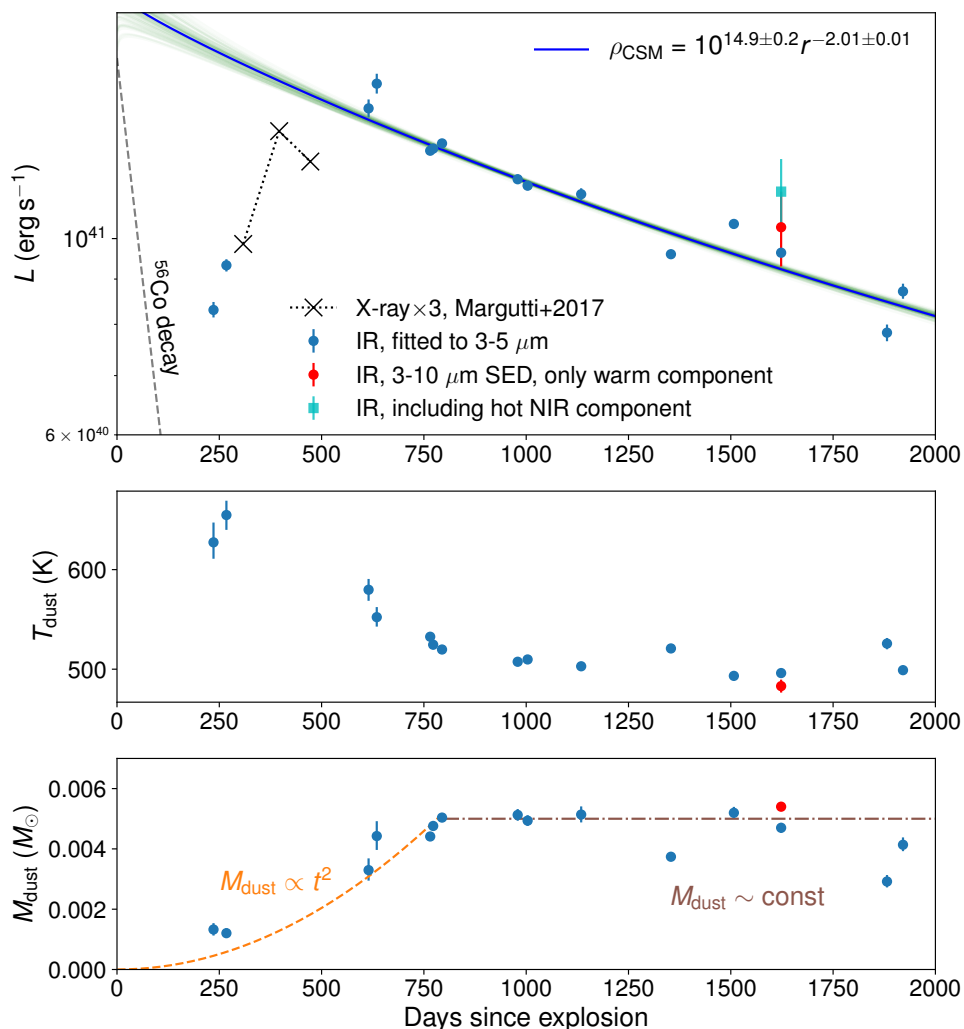


Figure 4.7: Dust luminosity (top), temperature (middle), and mass (bottom) from fitting a dust model to *Spitzer* photometry. We assume that the dust composition remains at 38% silicate, 62% carbonaceous, as derived from the 1–10 μm SED from 1620 days (see Fig. 4.5). The red points in all panels show the dust parameters of the warm component from the SED fitting including the 9.7 μm observation for comparison. The square cyan point in the top panel shows the IR luminosity from both the hot and warm components from the SED fit. The top panel includes the typical 0.01 mag/day light curve expected from radioactive decay of ^{56}Co , to demonstrate the long-lasting nature of SN 2014C. X-ray light curve from Margutti et al. (2017) (multiplied by 3) is also included to show the approximated epoch of peak interaction. The bolometric light curve model from Moriya et al. (2013), fitted to our data later than 600 days, is shown in this panel with the fitted parameters in the legend. Transparent lines in the background of the top panel are 100 individual models from the MCMC sample to representing the range of the fitted parameters. In the bottom panel, we plotted the $M_{\text{dust}} \propto t^2$ line expected for an interaction with a constant-density shell and the constant M_{dust} line expected for a wind-like CSM.

Table 4.3: Luminosity, temperature, and mass of dust in the warm component of SN 2014C, assuming 38% silicate

Epoch (day)	L (10^{40} erg s $^{-1}$)	σ_L	T (K)	σ_T	M ($10^{-3} M_{\odot}$)	σ_M
37	16.6	0.3	602	9	3.2	0.3
235	8.3	0.2	628	18	1.3	0.2
267	9.3	0.1	651	16	1.2	0.2
614	14.0	0.3	579	9	3.3	0.3
634	15.0	0.4	551	10	4.4	0.5
765	12.6	0.1	532	2	4.4	0.1
772	12.7	0.1	524	2	4.8	0.1
794	12.8	0.1	519	1	5.0	0.1
979	11.7	0.1	507	2	5.1	0.2
1003	11.5	0.1	509	2	4.9	0.2
1134	11.2	0.2	502	3	5.1	0.2
1353	9.6	0.1	520	2	3.7	0.1
1507	10.4	0.1	493	2	5.2	0.2
1623	9.6	0.1	496	2	4.7	0.2
1881	7.8	0.1	525	5	2.9	0.2
1920	8.7	0.2	499	4	4.1	0.2

the inner and outer ejecta, respectively. These ejecta interact with the CSM, whose density profile is $\rho_{\text{CSM}} = Dr^{-s}$. The interaction starts in the outer ejecta, and then transitions into the inner ejecta at time t_t post-explosion. Moriya et al. derived analytic expressions for the bolometric luminosity in the general CSM case where s and D are free parameters, for both $t < t_t$ (eq. 23) and $t > t_t$ (eq. 26). The latter scenario is applicable to our data taken after 600 days, when the flux in the *Spitzer* bands appear to dominate the SED. We fit the following equation (eq. 26 in Moriya et al., 2013) to our data:

$$L(t) = 2\pi\epsilon D r_{\text{sh}}(t)^{2-s} \left(\frac{(3-s)M_{\text{ej}} \left(\frac{2E_{\text{ej}}}{M_{\text{ej}}} \right)^{1/2}}{4\pi D r_{\text{sh}}(t)^{3-s} + (3-s)M_{\text{ej}}} \right)^3 \quad (4.2)$$

where the time dependence is in $r_{\text{sh}}(t)$, which is numerically solved using their eq. (12):

$$\frac{4\pi D}{4-s} r_{\text{sh}}(t)^{4-s} + (3-s)M_{\text{ej}} r_{\text{sh}}(t) - (3-s)M_{\text{ej}} \left(\frac{2E_{\text{ej}}}{M_{\text{ej}}} \right)^{1/2} t = 0 \quad (4.3)$$

We will later compute t_t to verify that our data satisfy $t > t_t$.

First, we perform an MCMC fit varying the CSM parameters: D and s from $\rho_{\text{CSM}} = Dr^{-s}$, and the explosion parameters M_{ej} and E_{ej} . We impose minimal physical constraints: $M_{\text{ej}}, E_{\text{ej}}, D > 0$, and the explosion velocity $v_{\text{ej}} = (2E_{\text{ej}}/M_{\text{ej}})^{0.5} < c$. The analytic model is only valid for $0 \leq s < 3$. We also try removing the degeneracy between M_{ej} and E_{ej} by imposing the observed photospheric velocity $v_{\text{phot}} = (10E_{\text{ej}}/3M_{\text{ej}})^{0.5} = 13000 \text{ km s}^{-1}$ (Margutti et al., 2017; Milisavljevic et al.,

2015). In both cases, MCMC fits do not converge as the explosion parameters mainly affect the shape of the light curve at early times. The fitted explosion energy can grow arbitrarily large with a steep CSM density profile that makes very dense CSM close to the star.

Instead, we use the explosion parameters inferred from early-time observations: $M_{\text{ej}} \sim 1.7 M_{\odot}$ and $E_{\text{ej}} \sim 1.8 \times 10^{51}$ erg (Margutti et al., 2017), and only fit for the CSM parameters. The results we obtain, with 1σ uncertainty, are $D = 10^{14.9 \pm 0.2}$ (cgs) and $s = 2.01 \pm 0.01$, which indicate that the CSM profile is wind driven. Recall that the parameter D sets the absolute density scale of the CSM. In the wind-driven scenario ($s = 2$), $D = \dot{M}/(4\pi v_w)$ where \dot{M} and v_w are the mass-loss rate and the wind velocity, respectively, and \dot{M}/v_w is dependent on the explosion parameters. To derive the exact dependence, we solved eq. (35) and (36) in Moriya et al. (2013) to eliminate ϵ and obtained $D \propto \dot{M}/v_w \propto M_{\text{ej}}^{3/2} E_{\text{ej}}^{-1/2}$. From our fitted distribution for D and this relation, we can write the mass-loss rate as a function of v_w and the explosion parameters as

$$\dot{M} = (1.7_{-0.6}^{+0.9}) \times 10^{-3} M_{\odot} \text{yr}^{-1} \left(\frac{v_w}{100 \text{ km s}^{-1}} \right) \left(\frac{M_{\text{ej}}}{1.7 M_{\odot}} \right)^{1.5} \left(\frac{E_{\text{ej}}}{1.8 \times 10^{51} \text{ erg}} \right)^{-0.5} \quad (4.4)$$

To check that we are in the $t > t_t$ limit, we compute the transition time using eq. (34) in Moriya et al. (2013), and found that $t_t = 345 \pm 12$ days. Hence, our observations from $t > 600$ days are well beyond this limit.

The density profile derived above allows us to estimate the total mass contained in the CSM. With the wind-driven density profile $\rho \propto r^{-2}$, the gas mass contained up to radius r is linearly proportional to r . The total (gas) mass of the wind-driven component of the CSM contained up to radius r is simply $M_{\text{CSM}} = 4\pi D r$. Because $D = 10^{14.9 \pm 0.2} \text{ g cm}^{-1}$, the wind-driven portion of the CSM contains $M_{\text{CSM}} = 5_{-2}^{+3} \times 10^{-18} \Delta r M_{\odot}/\text{cm}$. As such, even if the outer CSM extends out to 10 times the current shock location, 10^{18} cm, the total wind-driven CSM mass is only about $5_{-2}^{+3} M_{\odot}$. More likely, the region of the CSM containing the dust we observe only extends out the order of its current size ($\sim 2 \times 10^{17}$ cm), with the total mass of about $1 M_{\odot}$. Along with $\approx 1 M_{\odot}$ in the dense CSM shell (Margutti et al., 2017), the total CSM mass around SN 2014C is about $2_{-0.4}^{+0.6} M_{\odot}$. This total CSM mass constraint presents a further issue for the pure carbonaceous dust scenario, which needs $0.22 M_{\odot}$ of carbonaceous dust to explain the $9.7 \mu\text{m}$ flux observed at 1620 d. Recall that this dust mass is a lower limit, assuming that dust is optically thin and not clumpy, of

the total mass of dust emitting in the IR at that epoch. That quantity is itself a lower limit of the total mass of dust in the CSM because not all dust is illuminated by the shock interaction at that epoch. The very conservative upper limit of gas-to-dust ratio is then $9_{-2}^{+3}:1$, which is at odds with dusty media observed around Galactic massive stars (e.g., $38 \pm 15:1$ in LBV WRAY 15-751; Vamvatira-Nakou et al., 2013) and SN remnants (e.g., the Crab Nebula has gas-to-dust ratio of 26–39:1; Owen and Barlow, 2015).

Evolution of the He 1.083 μm Line Profile

Fig. 4.8 (left) shows the evolution of the line profile of the broad He I 1.083 μm line. The 2.058 μm line has a similar profile at all epochs, but the S/N is low as it is a much weaker line. We analyze spectra from days 1354 and 1693 because they have the highest S/N, and the other epochs that cover the *Y* band (1305 and 1621 days) are close in time to these two epochs. We model the profile of the 1.083 μm line with a combination of Gaussian components and find that both epochs are well fit by four Gaussian components. Fig. 4.8 (middle and right) shows the fitting results. There is a broad component approximately at rest, marked as “a”, with a FWHM velocity of $\approx 2000 \text{ km s}^{-1}$. This component is likely from the He-rich ejecta of the SN. Second, there are two intermediate components, marked “b” and “c”, at the central velocities of -4000 and about 0 km s^{-1} . They are both with a common FWHM of 500 km s^{-1} , suggesting that these intermediate lines are from the shocked CSM. Lastly, one narrow component (n1) with FWHM $< 100 \text{ km s}^{-1}$ is present. The n2 component is the hydrogen 1.094 μm line. The FWHM of all resolved lines (not n1 and n2) decreases by about 10% between the two epochs. For comparison, the CSM interaction model used in §4.3 also tracks the shock velocity. In the wind-driven case, we can differentiate eq. (19) in Moriya et al. (2013) with respect to t and get the shock velocity

$$v_{\text{sh}}(t) = \sqrt{\frac{2E_{\text{ej}}/M_{\text{ej}}}{1 + 2at}} \quad \text{where} \quad a = \sqrt{\frac{2E_{\text{ej}}}{M_{\text{ej}}^3}} \frac{\dot{M}}{v_w} \quad (4.5)$$

According to this equation, the shock velocity would decrease by 5% between 1354 and 1693 days, given the assumed ejecta mass, energy, and the fitted mass-loss rate and wind velocity inferred from the light curve. This is roughly consistent with the deceleration observed in the ejecta. The “b” component of the spectral profile may arise from the same hot spot found in the VLBI imaging (Bietenholz et al., 2018).

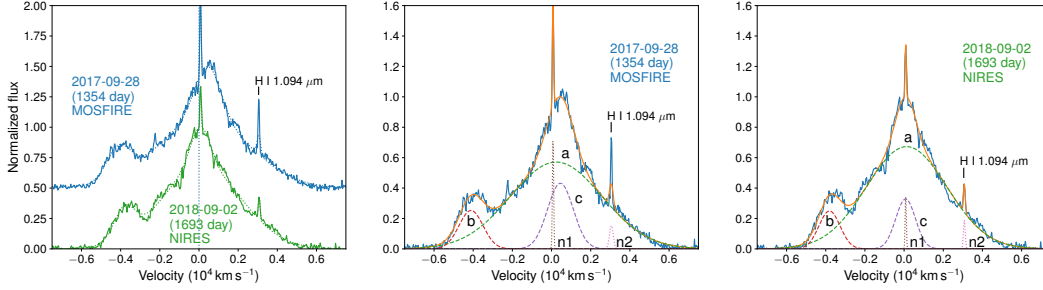


Figure 4.8: Left: the He I 1.083 μm line profile from our high-S/N spectra. Middle and right: line profiles from days 1354 and 1693, respectively. Spectra are normalized so the peak of the broad component is 1. For each epoch, we showed different Gaussian components used to fit the profile. For both epochs, the He 1.083 μm line can be fit with one broad component (a, 2000 km s^{-1}), two intermediate-width (b and c, 500 km s^{-1}) components centering at 0 and 4000 km s^{-1} , and lastly one narrow component (n1, $< 100 \text{km s}^{-1}$) at rest velocity. The n2 component is a narrow hydrogen 1.094 μm line.

4.4 Discussion and Conclusions

Multi-Component CSM and Potential Binary Origin

The CSM observed in SN 2014C clearly has several distinct components, both in density and composition. As shown already in the literature (Anderson et al., 2017; Margutti et al., 2017; Milisavljevic et al., 2015), the CSM has at least two density components: a low-density bubble up to $\sim 10^{16}$ cm, and a dense, hydrogen-rich shell starting at $\sim 5 \times 10^{16}$ cm. Continued IR observations, presented in this work, show that the CSM extends out to at least 1.4×10^{17} cm based on the current shock location at the latest *Spitzer* epoch at 1920 days. The light-curve shape, fitted with a CSM interaction model, further shows that the density profile of the outer part of the CSM differs from the constant-density shell observed at early times. The outer CSM density profile is well explained by a steady wind-driven scenario ($\rho_{\text{CSM}} \propto r^{-2}$) with a high mass-loss rate of $\dot{M} \approx 10^{-3} M_{\odot} \text{yr}^{-1}$. The evolution of the observed dust mass also shows two distinct density profiles in the CSM. Before 750 days post-explosion, the observed dust mass is growing as $M_{\text{dust}} \propto t^2$, indicating a CSM shell with constant density. After 750 days, the observed dust mass remains constant, indicating the CSM with a wind-driven ($\rho_{\text{CSM}} \propto r^{-2}$) density profile. In addition to the distinct density components, we infer from the SED fitting that the CSM likely contains both carbonaceous and silicate grains, which form in different environments (C/O ratio > 1 and < 1 , respectively), suggesting that the CSM was formed by stellar outflows with different compositions.

One possible explanation for the density and chemical inhomogeneity is that the CSM is created by a progenitor that is transitioning from the oxygen-rich phase (e.g., RSG or LBV) to the carbon-rich (e.g., WC) phase, similar to what has been suggested by Milisavljevic et al. (2015). In this scenario, the dense shell is formed by the fast WR wind sweeping up the slower RSG (or LBV) wind, which can mix in carbonaceous dust. There are three caveats of this scenario. (i) The WR phase would only last for ~ 10 yr because the wind velocity is $\sim 1000 \text{ km s}^{-1}$ and the CSM shell is at $\sim 10^{16} \text{ cm}$. This is much shorter than the expected life time of a WR. Furthermore, the LBV (or RSG phase) are not expected to transition directly into the WC phase, but have to go through the WN phase first, making this scenario even less likely. This caveat was mentioned in Milisavljevic et al. (2015). (ii) A single WR progenitor is incompatible with the low ejecta mass of $\sim 1.7 M_{\odot}$ inferred by Margutti et al. (2017). (iii) The wind parameter of $\dot{M}/v_w = 1.7 \pm 0.1 \times 10^{-3} M_{\odot} \text{ yr}^{-1} / 100 \text{ km s}^{-1}$, inferred from our light-curve fitting is inconsistent with the LBV quiescent wind phase. It is more consistent with either the high end of extreme RSG mass loss or the binary Roche-lobe overflow (RLOF) scenario (Smith, 2017).

These caveats can be resolved by considering a binary progenitor system to SN 2014C. In this scenario, the H-rich envelope of the progenitor star is stripped by binary interaction, not by its line-driven stellar wind (e.g., Podsiadlowski et al., 1992). As a result, the progenitor star need not be massive to be able to shed its hydrogen envelope, which is consistent with the ejected mass inferred from observations. Margutti et al. (2017) discussed this scenario in details as one of the possible origins of the dense CSM shell around SN 2014C (another scenario being late-stage nuclear-burning instability). They found from binary population modeling that 3–10% of SNe Ib/c progenitor went through a common-envelope mass-loss scenario in which the stripped H-rich envelope can remain around the progenitor system long enough to interact with the SN. Such a binary progenitor system can also explain the chemical inhomogeneity and the density profile in the outer CSM. The density profile created by a binary system, assuming no interactions between two winds, is $\rho_{\text{CSM}}(r) = (\dot{M}_1/v_1 + \dot{M}_2/v_2)/(4\pi r^2)$, where \dot{M}_i and v_i are the mass-loss rate and wind velocity of the two components, and r is much larger than the binary separation. This is consistent with the observed density profile presented in this work. This scenario is also in line with the growing consensus that most stripped-envelope SNe are created via binary interaction, as opposed to single star mass loss (e.g., De Marco and Izzard, 2017; Smith, 2014). SN 2014C stands out from the rest of SNe Ib/c perhaps due to the progenitor’s binary parameter that caused the mass-ejection

event to occur right before core collapse of one of the components.

RY Scuti as a Galactic Analog to the Progenitor System of SN 2014C

There is a potential Galactic analog to the progenitor system of SN 2014C: the massive binary system RY Scuti (Gehrz et al., 1995; Gehrz et al., 2001; Hjellming et al., 1973; Smith et al., 1999, 2002, 2011a). RY Scuti is an interacting binary caught shortly after major mass transfer events. It consists of a primary, mass-donor, O9/B0 supergiant star with a current mass of $8 M_{\odot}$ and a secondary, mass-gainer, O5 star with the current mass of $30 M_{\odot}$. The initial masses for the primary and secondary stars were estimated to be about 20–25 and 15–20 M_{\odot} . The He core mass of the primary star would have been roughly 6–8 M_{\odot} (Woosley and Weaver, 1986), indicating that it had lost most of its hydrogen envelope and would soon become a WR star. High-resolution imaging in the optical with *Hubble Space Telescope* (*HST*) and in the infrared using adaptive optics (AO) revealed detached, expanding tori of CSM ejected in separate eruptive mass-loss events (Smith et al., 1999, 2002, 2011a). The inner gas-rich torus was 3.4×10^{16} cm from the star, and was detected primarily in the optical. The outer dusty torus was 5.4×10^{16} cm from the star, and was detected primarily in the IR. Proper motion measurements from multi-epoch observations 6 (12) years apart in the infrared (optical) showed that the radial expansion velocity of the gas and dust tori was 40–50 km s^{-1} . The two tori had different velocities and were ejected separately, about 100 yr apart (Smith et al., 2011a).

The SN from the primary star of RY Scuti may resemble SN 2014C in the following aspects. First, the SN will initially be either of Type IIb or Ib/c, depending on how much hydrogen envelope is left. The SN will transition into a SN 2014C-like event once the SN shock reaches the location of the dusty tori. The strength of the interaction, however, may be much lower depending on the mass in the CSM. The outer dusty torus around RY Scuti was 5.4×10^{16} cm away from the star (measured from imaging), which is comparable to the location of the dense CSM shell around SN 2014C (Margutti et al., 2017). Hence, the timescale at which the shock interaction commences would be similar to that observed in SN 2014C (about 100 days post-explosion). Second, the toroidal geometry of the CSM will allow the SN shock to propagate unimpeded, explaining the constant shock velocity despite CSM interaction (Bietenholz et al., 2018). Third, the IR SED of the outer dusty torus observed by the Keck Long Wave Spectrometer (LWS) showed a strong silicate dust feature at $10 \mu\text{m}$, similar to what we inferred in SN 2014C (Gehrz et al., 2001).

Moreover, Gehrz et al. (2001) invoked a dust model with a mix of carbonaceous and astronomical silicate dust grains to explain the SED shape of RY Scuti, similar to what we did for SN 2014C. The temperature of the dust grains were slightly lower to what was observed in SN 2014C (300–400 K as opposed to 500 K), which is not unexpected given the lower luminosity from RY Scuti ($\approx 2 \times 10^6 L_\odot$) as opposed to what would be expected in a SN explosion. While RY Scuti and SN 2014C’s progenitor may be similar in many aspects, they differ sharply in the CSM mass. SN 2014C has of order $1 M_\odot$ in the CSM with about $5 \times 10^{-3} M_\odot$ of dust; meanwhile, RY Scuti has only $1.4 \times 10^{-6} M_\odot$ of dust (Gehrz et al., 2001). This led Smith et al. (2011a) to conclude that the SN from RY Scuti’s primary star will be an ordinary SN Ib/c and not an interacting SN IIn. They noted, however, that RY Scuti’s mass transfer was very conservative, because about $15 M_\odot$ has been transferred to the secondary star with only about $0.003 M_\odot$ lost into the CSM (gas mass of the inner torus; Smith et al., 2002). The progenitor system to SN 2014C may be a binary system much like RY Scuti, but with mass ratio and separation such that the mass transfer was much less conservative, resulting in much more mass being lost into the CSM.

Conclusion

SN 2014C’s prolonged IR emission reveals two important characteristics of the CSM. First, it likely contains a mixture of carbonaceous and silicate dust inferred from the SED including $9.7 \mu\text{m}$ photometry. If confirmed, this is the first identification of silicate dust in an interacting SN. Alternatively, the SED could also be fitted with purely carbonaceous dust with a cold, 300 K, component containing $0.22 M_\odot$ of dust grains. That scenario would be unprecedented as well. Second, the light-curve fitting shows that the CSM extends out to at least 1.4×10^{17} cm, with the wind-driven density profile in the outer part. This component is in addition to the inner low-density bubble and the dense shell with a constant density identified earlier in the literature. The chemical inhomogeneity of the CSM suggests that the progenitor system of SN 2014C is likely a binary with one component producing an oxygen-rich outflow and another component carbon-rich outflow. While most SNe Ib/c are not observed to interact with their lost hydrogen envelope, SN 2014C may present the extreme end of the population, where the binary-driven mass-ejection event that strips the progenitor’s envelope happens just before the core collapse, leaving a dense, detached H-rich CSM to interact with the SN shock. The progenitor system that produced SN 2014C may look very similar to RY Scuti, but with much

more mass ejected from the binary system into the CSM. This work underscores the importance of late-time IR observations to constrain CSM properties of interacting SNe, as the outer part of the CSM can only be probed by late-time interactions, which emit mostly in the IR. Assuming that this CSM does not abruptly end at this radius, the interaction will still be ongoing by the time that *JWST* becomes operational. It will enable IR spectroscopic observations of this SN and of other interacting SNe, which will help us understand SN 2014C's place in the continuum of SN types from Ib/c to IIn, and to construct a complete picture of how mass loss operates at the end of the life of a massive star.

Acknowledgement

We thank Takashi Moriya, Itsuki Sakon, and Takashi Onaka for helpful discussions. We thank Takuya Fujiyoshi for conducting the COMICS observations. This work was supported by the GROWTH (Global Relay of Observatories Watching Transients Happen) project funded by the National Science Foundation under PIRE grant No. 1545949. GROWTH is a collaborative project among California Institute of Technology (USA), University of Maryland College Park (USA), University of Wisconsin Milwaukee (USA), Texas Tech University (USA), San Diego State University (USA), University of Washington (USA), Los Alamos National Laboratory (USA), Tokyo Institute of Technology (Japan), National Central University (Taiwan), Indian Institute of Astrophysics (India), Indian Institute of Technology Bombay (India), Weizmann Institute of Science (Israel), The Oskar Klein Centre at Stockholm University (Sweden), Humboldt University (Germany), Liverpool John Moores University (UK), and University of Sydney (Australia). KM acknowledges support by JSPS KAKENHI Grant (18H04585, 18H05223, 17H02864). RDG is supported by NASA and the United States Air Force. Some of the data presented herein were obtained at the W. M. Keck Observatory, which is operated as a scientific partnership among the California Institute of Technology, the University of California and the National Aeronautics and Space Administration. The Observatory was made possible by the generous financial support of the W. M. Keck Foundation. This work is based in part on observations obtained at the Gemini Observatory, which is operated by the Association of Universities for Research in Astronomy, Inc., under a cooperative agreement with the NSF on behalf of the Gemini partnership: the National Science Foundation (United States), National Research Council (Canada), CONICYT (Chile), Ministerio de Ciencia, Tecnología e Innovación Productiva (Argentina), Ministério da Ciência, Tecnologia e Inovação (Brazil), and

Korea Astronomy and Space Science Institute (Republic of Korea). This work is based in part on data collected at Subaru Telescope, which is operated by the National Astronomical Observatory of Japan. The three aforementioned observatories are on the summit of Maunakea and the authors wish to recognize and acknowledge the very significant cultural role and reverence that the summit of Maunakea has always had within the indigenous Hawaiian community. We are most fortunate to have the opportunity to conduct observations from this mountain. Some of the data presented herein were obtained at Palomar Observatory, which is operated by a collaboration between California Institute of Technology, Jet Propulsion Laboratory, Yale University, and National Astronomical Observatories of China. This work is based in part on observations made with the *Spitzer Space Telescope*, which is operated by the Jet Propulsion Laboratory, California Institute of Technology under a contract with NASA. Support for this work was provided by NASA through an award issued by JPL/Caltech. This research has made use of the NASA/IPAC Extragalactic Database (NED), which is operated by the Jet Propulsion Laboratory, California Institute of Technology, under contract with the National Aeronautics and Space Administration. This research made use of Astropy, a community-developed core Python package for Astronomy (Astropy Collaboration et al., 2018).

Chapter 5

**WIRC+Pol: A LOW-RESOLUTION NEAR-INFRARED
SPECTROPOLARIMETER**

Tinyanont, S. et al. (Feb. 2019). “WIRC+Pol: A Low-resolution Near-infrared Spectropolarimeter”. In: *PASP* 131.996. DOI: 10.1088/1538-3873/aaef0f. arXiv: 1811.03138 [astro-ph.IM].

Samaporn Tinyanont¹ Maxwell A. Millar-Blanchaer^{2,3} Ricky Nilsson¹ Dimitri Mawet^{1,2} Heather Knutson⁴ Tiffany Kataria² Gautam Vasisht² Charles Henderson⁵
Keith Matthews¹ Eugene Serabyn² Jennifer W. Milburn¹ David Hale¹ Roger Smith¹ Shreyas Vissapragada¹ Louis D. Santos Jr.¹ Jason Kekas⁶ Michael J. Escuti^{6,7}

¹Department of Astronomy, California Institute of Technology, 1200 E. California Blvd, MC 249-17, Pasadena, CA 91125, USA

²Jet Propulsion Laboratory, California Institute of Technology, 4800 Oak Grove Dr, Pasadena, CA 91109, USA

³NASA Hubble Fellow

⁴Division of Geological and Planetary Sciences, California Institute of Technology, 1200 E. California Blvd, Pasadena, CA 91125, USA

⁵Department of Astronomy, Cornell University, 616A Space Science Building, Ithaca, NY 14853, USA

⁶ImagineOptix, Cary, NC 27519, USA

⁷Department of Electrical & Computer Engineering, North Carolina State University, Raleigh, NC, USA

Abstract

WIRC+Pol is a newly commissioned low-resolution ($R \sim 100$), near-infrared (J and H bands) spectropolarimetry mode of the Wide-field InfraRed Camera (WIRC) on the 200-inch Hale Telescope at Palomar Observatory. The instrument utilizes a novel polarimeter design based on a quarter-wave plate and a polarization grating (PG), which provides full linear polarization measurements (Stokes I , Q , and U) in one exposure. The PG also has high transmission across the J and H bands. The instrument is situated at the prime focus of an equatorially mounted telescope. As a result, the system only has one reflection in the light path providing minimal telescope-induced polarization. A data reduction pipeline has been developed for WIRC+Pol to produce linear polarization measurements from observations. WIRC+Pol has been on-sky since February 2017. Results from the first year commissioning data show that the instrument has a high dispersion efficiency as expected from the polariza-

tion grating. We demonstrate the polarimetric stability of the instrument with RMS variation at 0.2% level over 30 minutes for a bright standard star ($J = 8.7$). While the spectral extraction is photon noise limited, polarization calibration between sources remain limited by systematics, likely related to gravity dependent pointing effects. We discuss instrumental systematics we have uncovered in the data, their potential causes, along with calibrations that are necessary to eliminate them. We describe a modulator upgrade that will eliminate the slowly varying systematics and provide polarimetric accuracy better than 0.1%.

5.1 Introduction

The vast majority of astronomical observations are conducted using electromagnetic waves, which have three fundamental properties: intensity, frequency, and polarization. Photometry and spectroscopy, which account for most observations in the optical and near-infrared (NIR), are only sensitive to the first two properties of light. Polarimetry contains information unobtainable just by observing the broadband flux or spectrum of an object. Scattering processes, the Zeeman effect near a magnetized source, and synchrotron radiation are among the major astronomical sources of polarized light. In particular, scattering-induced polarization can be uniquely used to constrain the geometry of an unresolved scattering region. Polarization can reveal asymmetries because in a symmetric scattering region, assuming single scattering, the polarization vector will cancel out when viewed as a point source, leaving no net polarization.

WIRC+Pol is a spectropolarimetric upgrade to the Wide-field InfraRed Camera (WIRC; Wilson et al., 2003), the $8'7 \times 8'7$ NIR (1.1–2.3 μm) imaging camera at the prime focus ($f/3.3$) of the 200-inch Hale telescope at Palomar Observatory, the largest equatorially mounted telescope in the world. WIRC is an opto-mechanically simple, prime-focus, transmissive, in-line centro-symmetrical camera, which has demonstrated an exceptional photometric stability of 100 ppm/30 min, among the best ever recorded from the ground (Stefansson et al., 2017). Because it is at the prime focus of an equatorially mounted telescope, the light has to reflect only once off of the primary mirror, and the sky does not rotate with respect to the instrument. As a result, the instrumental polarization is expected to be low and stable, making WIRC ideal for a polarimetric upgrade. The instrument upgrade was motivated by the BD science case summarized below and it has become a part of the observatory's range of facility instruments for other observers in Palomar community. The upgrade was enabled by a novel optical device called a polarization

grating (PG), that makes a compact and simple low-resolution spectropolarimeter possible. In §5.2, we describe the WIRC+Pol instrument including the suite of upgrades we made to the original WIRC instrument. We compare a typical Wollaston prism-based polarimeter to our PG-based polarimeter. The data reduction pipeline is described in §5.3, and preliminary results exhibiting the instrument’s sensitivity are presented in §5.4. We discuss possible future instrument upgrades in §5.5. Conclusions are presented in §5.6.

Science Cases

A representative science case for WIRC+Pol and the usefulness of polarimetry is scattering in the atmosphere of brown dwarfs (BDs). BDs are substellar objects that cannot sustain hydrogen fusion in their core; hence, they are born hot with heat from gravitational collapse, then radiatively cool as they age. Therefore, their atmospheres progress through a range of temperatures with different chemical processes at play (see a review by Kirkpatrick, 2005). At a narrow temperature range of 1000–1200 K, the atmospheres undergo a sharp photometric and spectroscopic transition. The J band brightness increases and the NIR color ($J - K_s$) turns blue even though the temperature is dropping. As brown dwarfs transition from L-type to T-type, spectra start to show broad methane absorption. This L/T transition is often explained by a scenario in which clouds of condensates in the L dwarf’s atmosphere start to sink below the photosphere, giving way to a clear T-dwarf atmosphere. While models suggest that observations of T-dwarf atmospheres should be unpolarized, L dwarf atmospheres could be highly polarized due to the scattering of haze and cloud particles (Sengupta and Marley, 2009, 2010). L dwarfs can only be polarized if those scatterers are distributed asymmetrically on the surface, otherwise polarization from different parts of the disk will cancel out. Therefore, a detection of net polarization implies an asymmetry, which can be caused by oblateness of the BD disk due to rotation (Marley and Sengupta, 2011) and/or by patchiness or banding in the cloud distribution (de Kok et al., 2011; Stolker et al., 2017). While photometry and spectroscopy can provide some constraints on the cloud distribution by observing variability or using the Doppler imaging technique, respectively, they are only sensitive to rotationally asymmetric features. Longitudinally symmetric cloud bands like the ones we observe on Jupiter and predicted for brown dwarfs given their fast rotation rates (Showman and Kaspi, 2013), for example, would go unnoticed from photometric and spectroscopic monitoring. Polarimetric observations, therefore, provide a complementary approach: they can further prove the existence of

clouds on BDs, cementing their roles in the L/T transition, but then can also reveal the spatial and temporal evolution of these cloud structures. In doing so, polarimetric observations provide important constraints for understanding the atmospheric circulation of brown dwarfs (via general circulation models, GCMs; Showman and Kaspi, 2013; Tan and Showman, 2017; Zhang and Showman, 2014). Because BD atmospheres bear strong similarities with those of giant gas planets, they provide easily observable proxies to study planetary atmospheres in the high-mass regime.

This science case is only one of many examples where polarimetry is the only method to retrieve spatial information from an unresolved source. Other potential sciences cases of WIRC+Pol include scenarios where scattering occurs in unresolved asymmetric geometries. For example, the study of young stellar objects embedded in their primordial gas and dust cloud, magnetospheric accretion of dust around young “dipper” stars, and the ejecta of a core-collapse supernova (CCSN). For the CCSN science case, polarimetry is the only way to confirm asymmetry in the explosion mechanism inferred by theoretical models. However, all previous measurements have been conducted in the optical, where light echo from dust in the circumstellar medium (CSM) may mimic the signature of asymmetric ejecta (Nagao et al., 2017). Multi-wavelength observations, especially in the IR will help distinguishing the source of polarization since CSM dust scattering is inefficient in the IR while electron scattering in the SN ejecta is wavelength independent (Nagao et al., 2018).

Despite polarimeters’ unique capabilities, they are not nearly as available and utilized as imagers or spectrographs. This could be partially attributed to the additional complexity of polarimetric instruments, and the fact that most astronomical polarization signals are of an order $< 1\%$, making them difficult to observe. Furthermore, polarization is not as straightforward to interpret as photometry or spectroscopy. For instance, a 1% polarization detection from a BD can be caused by inhomogeneity in the cloud coverage, its oblate geometry, a disk around the object, or likely a combination of those sources. Careful radiative transfer modeling is required to meaningfully interpret polarimetric observations.

5.2 The Instrument

A Typical Polarimeter

A polarimeter relies on an optical device that differentiates light based on polarization, called an analyzer. Most designs utilize either a polarizer that transmits

only one polarization angle, or a beam-splitting analyzer that splits two orthogonal polarization angles into two outgoing beams. The polarizer-based polarimeters determine the full linear polarization (i.e., Stokes parameters I , Q , and U) by sampling the incoming beam at three, or more, position angles. This is typically done either by adding a rotating half-wave plate modulator in front of the analyzer, rotating the whole instrument, or using different polarizers to sample different angles. An example of an instrument that employs this technique is the polarimetry mode of the Advanced Camera for Surveys on board *Hubble Space Telescope*, which has three polarizers rotated at 60° from each other (Debes et al., 2016). While polarizers can fit inside a filter wheel of an existing instrument, the polarizer-based design is inefficient because the polarizer blocks about half of the incoming flux and each polarization angle has to be sampled separately. Alternatively, a polarimeter may use a beam-splitting analyzer, such as a Wollaston prism, that transmits most of the incoming flux into two outgoing beams with minimal loss. This allows two polarization angles to be sampled simultaneously with one Wollaston prism, and a full linear polarization measurement can be done with only two position angles (though more position angles are typically used to make redundant measurements in order to remove systematics). This is achieved either with a rotating modulator like in a polarizer-based instrument, or with a split-pupil design with two sets of Wollaston prisms at some angle from each other (double-wedged Wollaston Oliva, 1997). While being more optically complex, the Wollaston-based design is more efficient than the polarizer-based design because most of the incoming flux gets transmitted to the detector, even though more detector space is needed to image both beams. As a result, it is more widely used in ground-based instruments, where its higher optical complexity can be accommodated. There are many polarimeters of this type in use, e.g., the polarimetry and spectropolarimetry modes of the Long-slit Intermediate Resolution Infrared Spectrograph (LIRIS; Machado et al., 2004) on the 4.2-m William Herschel Telescope. Both of these polarimeter designs provide only broadband polarimetry and they have to be coupled with a traditional grating- or grism-based spectrograph to make a spectropolarimeter. The end result is an instrument that is large and optically complex.

Polarization Grating

WIRC+Pol is a uniquely designed low-resolution spectropolarimeter that can measure linear polarization as a function of wavelength in one exposure, while remaining physically small and optically simple. The key to this capability is a compact, liquid

crystal polymer-based device called a PG, which acts as a beam-splitting polarimetric analyzer and a spectroscopic grating at the same time (Escuti et al., 2006; Millar-Blanchaer et al., 2014; Packham et al., 2010). A PG uses a thin polymer film of elongated uniaxially birefringent liquid crystals arranged in a rotating pattern to split an incoming beam based on its polarization into the $m = \pm 1$ diffraction orders while simultaneously dispersing each outgoing beam into spectra (see Figs. 1 and 2 of Packham et al., 2010). A quarter-wave plate (QWP) can be placed before the PG to make a device that splits light based on linear polarization. To make this device capable of capturing the full linear polarization in one shot, two halves of the QWP have their fast axis rotated by 45° and two halves of the PG have the liquid crystals pattern 90° from each other (see Fig. 5.1 *center*). This effectively splits incoming light into four beams with polarization angle 0, 45, 90, and 135° . In addition, a PG also disperses each beam into a spectrum, with $> 99\%$ of the incident light into $m = \pm 1$ orders, $\sim 1\%$ into the 0th order and virtually no flux leaking into higher orders. Moreover, the PG's efficiency is nearly wavelength independent, unlike dispersion gratings which are normally blazed to enhance the efficiency around one specific wavelength. We demonstrate this property in our transmission measurements in §5.4. These properties make the PG a uniquely efficient disperser and a natural choice for a spectropolarimetric instrument. Furthermore, a QWP/PG device is thin enough to fit inside an instrument's filter wheel, simplifying its installation in an existing imaging camera. This is as opposed to a Wollaston prism whose thickness is governed by the required splitting angle.

WIRC Upgrade

For the original WIRC, the converging beam from the telescope primary mirror comes into focus inside of the instrument, then passes through the collimating optics, two filter wheels with a Lyot stop in the middle, and gets refocused onto the detector. To turn WIRC into a spectropolarimeter, three major components have been installed.

(i) A split-pupil QWP/PG device, manufactured by ImagineOptix (Escuti et al., 2006), was installed in the first filter wheel of WIRC, allowing it to be used with the broadband filters J and H , which are in the second filter wheel downstream from the PG in WIRC's optical path. The initial laboratory testings performed on the Infrared Coronagraphic Testbed (Serabyn et al., 2016) at the Jet Propulsion Laboratory demonstrated that it responds to a polarized light source as expected. The device was installed in WIRC in February 2017. The filter mount was modified

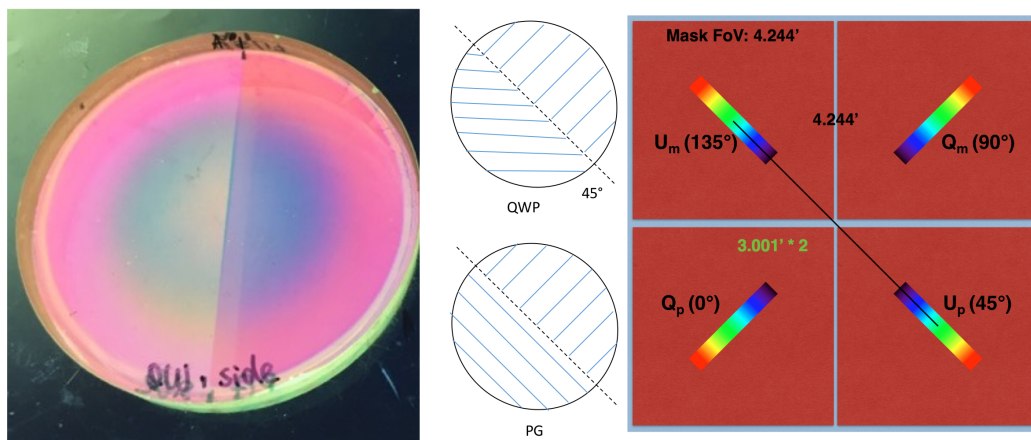


Figure 5.1: *Left:* Photograph of the actual QWP/PG device installed in WIRC's filter wheel. The line down the middle of the PG is where the pupil is split. *Center:* Schematics showing the split-pupil design for the QWP and PG. The top figure shows that the QWP's fast axes (notated by the blue lines) are rotated by 45° between the two halves and the bottom shows that the PG's grating axes (also notated by the blue lines) are rotated by 90° . As a result, the lower left (upper right) half of the device samples linear polarization angles 0 and 90° (45 and 135°). *Right:* Schematic of WIRC+Pol's focal plane image for a single point source. The split-pupil QWP/PG device splits and disperses light into four spectral traces in four quadrants of the detector. Each quadrant is labeled with the corresponding angles of linear polarization. The full field of view (FoV) here is $8'.7 \times 8'.7$ while the FoV limited by the mask is $4'.3 \times 4'.3$. The center of each of the four traces in the J band is $3'$ away from the location of the source in the FoV.

to accommodate the PG, which was installed at 7° angle with respect to the pupil plane to mitigate ghost reflections. This filter placement caused some non-common path systematic error since outgoing beams from the PG enter the broadband filter (also installed at 7°) at different angles, thus seeing different transmission profiles. We will discuss this issue in more detail in §5.3 and 5.4. The device is optimized for the J and H bands and can potentially be used over the J – H range simultaneously if an additional filter is installed to block the K -band thermal emission and limit the sky background. Laboratory testing confirmed the device's high efficiency, with $<1\%$ of total light in the zeroth order image, and over 99% in the four first order traces, with no leaks into higher orders. On-sky tests, to be discussed in §5.4, confirmed this measurement. The PG is designed with a grating period such that spectral traces on the detector have $1''$ seeing-limited resolution elements of $0.013 \mu\text{m}$. This is $R = \lambda/\Delta\lambda \sim 100$ in the J and H bands. The QWP/PG is oriented such that the four polarization spectral traces lie on the diagonal of the detector, in order to

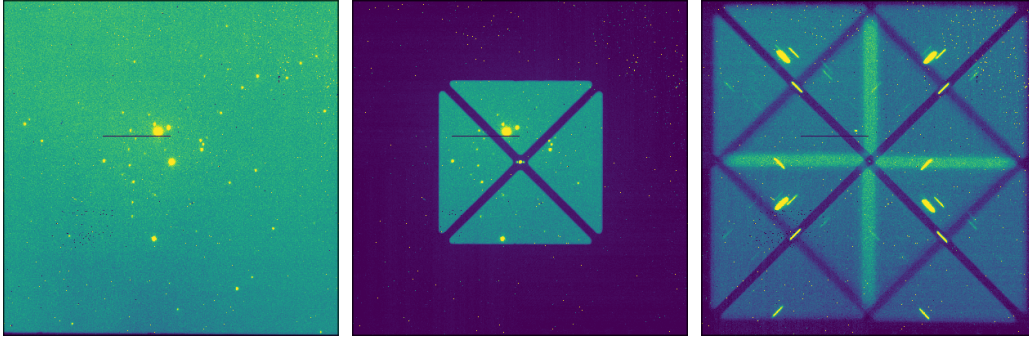


Figure 5.2: Raw images from WIRC+Pol of the crowded field around HD 38563, one of the known polarized stars used for calibration, which is the brightest star in this image. Note a bad column running through the star. *Left:* an image from the normal imaging mode with only the J -band filter in place. The full field of view (FoV) here is $8'.7 \times 8'.7$. *Center:* the focal plane mask is put into the optical path at the telescope's focal plane inside WIRC, restricting the field of view to $4'.3 \times 4'.3$. The metal bars in the center of the field of view hold the three circular holes, each $3''$ in diameter. *Right:* After the PG is put in place, the field is split into four based on linear polarization, and each of them is dispersed into four quadrants of the detector. The vertical and horizontal bright bars are where the fields overlap. Each point source is dispersed into $R \sim 100$ spectra. Note that the source in the slit has reduced background level. Only the zeroth order (undispersed) image of the brightest star in the field remains easily visible after the PG was inserted.

maximally fill the array, to achieve the largest field of view possible (see Fig. 5.1 for the schematic and Fig. 5.2 for an actual image). The large field of view allows for field stars to be used as polarimetric reference to monitor the polarimetric stability. Fig. 5.1 *center* shows the QWP's fast axes along with the PG's grating axes. The incident light on the lower left (upper right) half of the PG gets sampled at linear polarization angles 0 and 90° (45 and 135°) and sent to the lower left and upper right (lower right and upper left) quadrants of the detector (Fig. 5.1, (right)). In §5.4, we confirmed the orientation of the PG in the instrument by observing the polarized twilight. We determined that lower left, upper right, lower right, and upper left quadrants correspond to the polarization components with the electric vector at 0 , 90 , 45 , 135° with respect to North, increasing to East, respectively. Because the 200-inch is on an equatorial mount, these angles remained constant. Along with the QWP/PG device, a grism was also installed for a low-resolution spectroscopic mode, WIRC+Spec, for exoplanet transit spectroscopy. This observing mode is the topic of an upcoming publication.

(ii) A focal plane mask (Fig. 5.2 Center) was installed at the telescope's focal plane

inside the instrument at the same time as the PG was installed. The mask restricts the field of view to 4.3×4.3 so that the field can be split into four quadrants by the PG and still fit into the detector with minimal overlap (see Fig. 5.2 *center* and *right*). The mask can be inserted and removed from the focal plane using a cryogenic motor mechanism. The mask has opaque metal bars blocking its two diagonals with three circular holes in the center. The bars serve to block the sky background emission for a source inside one of the slit holes, providing higher sensitivity. The holes are $3''$ on-sky in diameter (0.25 mm at the telescope prime focus), to accommodate the median seeing of $1''.2$ at Palomar along with the typical guiding error of $1''/15$ min. The mask is made of aluminum and the slit holes have knife-blade edge with a typical thickness of $100 \mu\text{m}$, in order to reduce slit-induced polarization, which is proportional to the thickness, and inversely proportional to the width of the slit and the conductivity of the material (Keller, 2001). The holes are circular so that any slit-induced polarization is symmetric, and cancel out when the source is centered. Due to various instrumental systematics uncovered over the course of commissioning, in-slit observations are not yet fully characterized.

(iii) A science-grade HAWAII-2 detector, previously in Keck/OSIRIS (Larkin et al., 2003), was installed to replace the engineering-grade detector that had been in place since the failure of the original science-grade detector in 2012. The engineering-grade device had a defective quadrant that would prevent us from observing four spectra at the same time, and also had many cosmetic defects. The existing 4-channel read-out electronics were also upgraded to 32 channels, allowing for a faster read-out time and minimum exposure time of 0.92 s as opposed to 3.23 s. This shorter minimum exposure time enables observations of brighter sources, and proves necessary to access several bright unpolarized and polarized standard stars. The detector along with the 32-channel read-out electronics were installed and characterized in January 2017. We further discuss these tests in §5.4.

Along with the hardware upgrades, the instrument's control software received modifications. A new control panel was developed to insert and remove the polarimetric mask. An additional guiding mode based on 2D cross correlation was added to the WIRC guiding script, which previously used to rely on fitting 2D Gaussian profile to stars in the field.¹ With this update, the instrument can now guide on the elongated traces, which is useful both for WIRC+Pol and the spectroscopic mode,

¹The 2D cross correlation code was by A. Ginsburg, accessed from https://github.com/keflavich/image_registration

WIRC+Spec², especially for faint sources where the zeroth order image of the star is too dim to guide on. We note here that guiding is done on science images as WIRC has no separate guiding camera.

By adding the focal plane mask, and the beam-splitting and dispersing PG in the optical path, the raw image on the focal plane becomes quite complex. Fig. 5.2 shows raw images with (i) just the broadband J filter, (ii) with the focal plane mask inserted, and (iii) with both the mask and the PG inserted. From (ii) to (iii), one sees the masked focal plane image split and dispersed into four diagonal directions by the PG. Table 5.1 summarizes key specifications of WIRC imaging, spectroscopic (WIRC+Spec), and spectropolarimetric (WIRC+Pol) modes. Next we describe the data reduction process that turns these complicated images into polarization measurements.

5.3 Data Reduction Pipeline

WIRC+Pol is designed for a large survey of hundreds of BDs. It requires a robust and autonomous data reduction pipeline (DRP) to turn raw observations into polarimetric spectra with minimal user intervention. We have developed and tested a Python-based object-oriented DRP that satisfies those requirements. It is designed with flexibility to be used with future instruments that share WIRC+Pol's optical recipe, i.e., split-pupil QWP/PG with four traces imaged at once. The pipeline is designed to work with the spectroscopy mode, WIRC+Spec, as well. The schematic of the DRP is shown in Fig. 5.3. Briefly, the DRP first applies standard dark subtraction and flat-field correction to raw images. It then locates sources in each image, extracts the four spectra for each source, and then computes the polarized spectra. To correct for the instrument-induced effects, we normally observe an unpolarized star, chosen from Heiles (2000) immediately before or after a science observation. The DRP is still in constant development, but a working version can be obtained from https://github.com/WIRC-Pol/wirc_drp.

Dark Subtraction and Flat Fielding

The detector has a measured dark current of approximately $1 \text{ e}^-/\text{s}$, so dark subtraction is required for long exposures. There are a non-negligible number of pixels with high dark current, such that dark subtraction is required even for short exposure

²WIRC+Spec is the slitless spectroscopy mode of WIRC installed alongside WIRC+Pol. It involves a low-resolution grism in the filter wheel that work in J , H , and Ks bands with a resolving power of $R \sim 100$.

Table 5.1: Specifications of WIRC in different modes.

Instrument	WIRC
Telescope	Palomar 200-inch Hale
Focus	Prime
Detector	2048 × 2048 Hawaii 2
Spectropolarimetric mode	WIRC+Pol
Bandpass	<i>J, H</i>
Stokes Parameters	I, Q, U (simultaneous)
Spectral resolution	≈ 100 (seeing limited)
Slit size	3 arcsec & slitless
Field of View	4.35 × 4.35 arcmin
Sampling	0.25 arcsec per pixel
Angular resolution	≈ 1".2 (seeing limited)
Typical p accuracy	1%
Spectroscopic mode	WIRC+Spec
Bandpass	<i>J, H, K</i>
Spectral resolution	≈ 100 (seeing limited)
Slit size	slitless
Field of View	8.7 × 8.7 arcmin
Sampling	0.25 arcsec per pixel
Angular resolution	≈ 1".2 (seeing limited)
Imaging mode	
Wavelength range	1 to 2.5 microns
Bandpass	BB and NB filters
Field of View	8.7 × 8.7 arcmin
Sampling	0.25 arcsec per pixel
Angular resolution	≈ 1".2 (seeing limited)

time. The DRP automatically finds dark frames taken during the night, or nearby nights, and median combines frames with the same exposure times to create master dark frames for each exposure time. It then subtracts this master dark frame from science images with the same exposure time. In cases when the appropriate master dark with a proper exposure time is not available, the DRP can scale the exposure time of the given dark, although this is not ideal for hot pixel subtraction, and it is generally better to use dark frames with the same exposure time from a different night.

flat-field correction is crucial for our observations because we want to compare brightness in four spectral traces far apart on the detector. An uncorrected illumination variation can cause the four spectral traces to have different flux even when the source itself is unpolarized. Furthermore, the final polarimetric accuracy de-

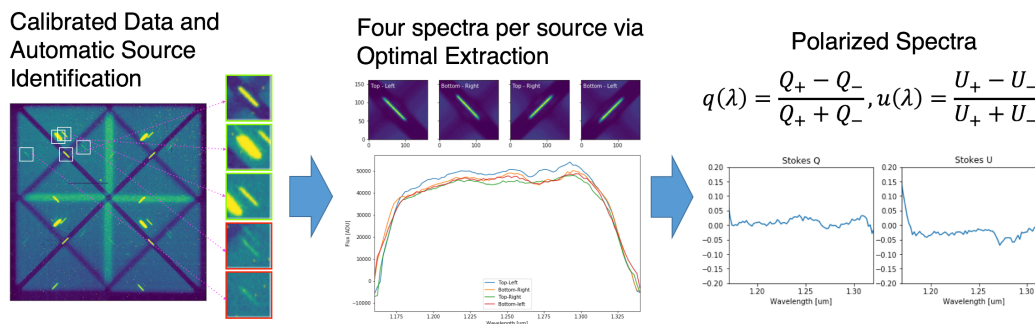


Figure 5.3: A schematic representing the work flow in the DRP starting with dark subtraction and flat fielding and source identification. Then the DRP extracts four spectra for four linear polarization angles 0, 90, 45, and 135° using optimal extraction. Finally the DRP computes normalized Stokes parameters q and u as functions of wavelengths using the flux spectra from the previous step.

depends on the accuracy of this flat-field correction. Flat fielding is generally difficult for polarimetric instruments due to the fact that one needs an evenly illuminated and unpolarized light source to obtain the calibration. As described by Patat and Romaniello (2006), the scenes typically used for flat-field correction, such as the twilight sky or a dome lamp, are polarized to some level. To circumvent this issue, one may take flat frames without the polarimetric optics in the optical path, which will be agnostic to the source's polarization. However, these flat frames will not capture the uneven illumination introduced by the polarization optics, which in our case we found to be significant at the sub-percent level. We therefore choose to take flat frames with all polarimetric optics in path (the focal plane mask, PG, and the broadband filter). We find that the dome flat lamp for the 200-inch telescope is sufficiently unpolarized to provide even illumination in the four quadrants of the detector. The spurious polarization introduced here can be subsequently removed by observing an unpolarized standard star. Fig. 5.4 compares the data corrected by flat fields taken with and without the polarimetric optics on the same scale. The image corrected by a flat field without the polarimetric optics shows no artifact near the edges of the field of view including the focal plane mask bars. However, the image corrected by the flat with the polarimetric optics in place shows a much more even background far away from edges. This is necessary since the uncorrected background variation is much stronger than the effect from polarization, of order 10%. Another set of dome flats with the PG removed but the mask in place is needed to subtract out the small, additive, zeroth order illumination in the flats with PG. This is so that the zeroth order subtracted PG flat represent the PG's efficiency

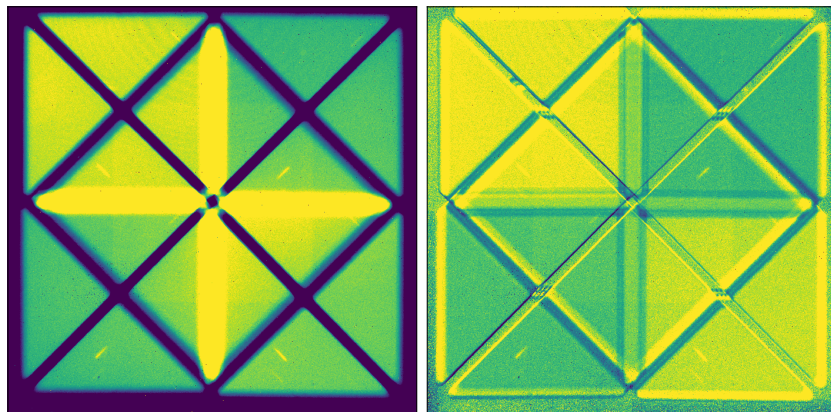


Figure 5.4: A comparison between the same science observation corrected using a flat field without (left) and with (right) the polarimetric optics (mask and PG) in place. While the correction using the flat without the polarimetric optics does not introduce more artifacts into the image, it fails to correct the uneven illumination due to the polarimetric optics. The leftover flat-field variation seen in the left figure is removed once we use a flat-field image with the polarimetric optics in place. After the flat fielding, one can notice a faint zeroth order background as a rectangle in the center of each image. This contribution is removed during background subtraction.

in the $m = \pm 1$ only. We note here that for the flat fielding to not affect the final signal-to-noise ratio (S/N) of the spectra to 0.1% level, the S/N needed is 1000. As a result, 10^6 photoelectrons are needed, and typically the total exposure time of 30 s without PG and 150 s with PG suffice.

Bad Pixel Determination

We identify bad pixels which have peculiar gain in a 3-step process. First we consider pixels with unusual dark currents. We use a series of dark exposures, taken during a standard calibration procedure, and compute median and median absolute deviation (MAD) of the count at each pixel. We choose to use MAD over standard deviation (SD) because the MAD's distribution is close to normal while SD's distribution is not, making it more difficult to make a cut based on the standard deviation of the distribution. Since the MAD's distribution is well described by the normal distribution near peak, we use `astropy` sigma-clipping algorithm to iteratively reject pixels that deviate more than 5σ from the mean. This creates the first bad pixel map which is particularly sensitive to hot pixels.

Next, we detect dead pixels in flat-field images by looking for pixels with spurious values in comparison to their neighboring pixel (local) and to the whole detector

(global). The local filtering can detect isolated bad pixels well, since their values will be significantly different from the norm established by pixels around them. The global filtering, on the other hand, is sensitive to patches of bad pixels where the local filtering fails since these pixels in the center are similar to surrounding, equally bad pixels. We note that computing local filtering iteratively can work as well, but may take up more computing time. For the local filtering, we use a master flat frame (dark subtracted, median combined, and normalized) obtained each night. We then create a map of standard deviation, where the value of each pixel is the standard deviation of a box of pixels around it (11×11 box works well). Pixels that deviate by more than 5σ from surrounding pixels are then rejected.

Finally, for the global filtering, we use the same master flat frame. We median filter the master flat to separate the large-scale variation component due to the uneven illumination of the focal plane from the pixel-to-pixel variation component. This step is necessary since the top part of the detector gets up to 20% more flux, which skews the distribution of pixel response if this large-scale variation is not removed. The master flat is divided by the large-scale variation map to get an image showing pixel-to-pixel variation. We find that the pixel-to-pixel map values follow the normal distribution well, so we again use sigma-clipping to reject extreme pixels. At the end of this process, we combine all 3 bad pixel maps: the hot pixels map using dark frames and local and global dead pixels maps from flat frames. In total, $\sim 20,000$ pixels are bad, 0.5% of the whole array. The time evolution of bad pixels is left for future work.

Automatic Source Detection

The spectropolarimetric images obtained by WIRC+Pol contain a composite of four moderately overlapping and spectrally dispersed images of the FOV. Further complexity is introduced by the cross-mask holding the slits/holes in the focal plane. Such an image (see Fig. 5.2 (right)) does not lend itself well to most of the standard source detection algorithms provided by, e.g., *Source Extractor* (Bertin and Arnouts, 1996), *DAOFIND* (Stetson, 1987), or IRAF's *starfind*.³ We developed a customized code for automatically detecting source spectra in WIRC+Pol images, which is incorporated into the current pipeline.

Flat-fielded science images are background subtracted, using a sky image taken $\sim 1'$ away from the science image to estimate the contribution from sky and mask. As

³<http://stdas.stsci.edu/cgi-bin/gethelp.cgi?starfind>

the relative positions of the quadruple of corresponding traces in the four quadrants are known, a single quadrant can be used for source detection. This assumes that the degree of linear polarization of all the sources in the field is small enough not to introduce large differences in brightness between corresponding traces, which is a reasonable assumption for most astrophysical objects. Since the four quadrants are just four copies of the same field, we use only the upper left quadrant for source finding. We convolve the quadrant with a white J or H (depending on the filter in which the science image was obtained) template spectrum that has a FWHM equal to the median seeing at Palomar, and that has the same orientation (assumed to be 45°) as the source spectra. This is essentially the traditional ‘matched filter’ method, which effectively enhances the S/N of any image features resembling the template spectrum in a background of white noise. The correlation image is then thresholded, typically at the median pixel value plus 5σ , where σ is calculated from background pixels only with sources masked out from the first round of sigma-clipping. Subsequent masking and labeling of non-zero features gives us a list of positions of detected spectra, ranked by source brightness, and saves user-specified size sub-frames around each spectrum. Any traces that cross into the regions with dark bars or bright overlapping regions (see Fig. 5.2 right) are rejected. The corresponding locations of all spectra in the remaining three quadrants are then calculated, and all sub-frames containing ‘good’ spectra are passed on to the spectral extraction part of the pipeline.

Spectral Extraction

The spectral extraction step employs a classical optimal extraction algorithm by Horne (1986). For each sub-frame of a spectral trace, we first have to estimate (i) the variance for each pixel and (ii) the sky background. For the dark-subtracted, flat-field-corrected, data D in the data number (ADU) unit, we obtain the variance image estimate by

$$V = \sigma_{RN}^2/Q^2 + D/Q \quad (5.1)$$

where σ_{RN} is the read-out noise RMS in the electron unit and Q is the gain in e^-/ADU ($12 e^-$ and $1.2 e^-/\text{ADU}$, respectively for WIRC+Pol, see §5.4). To estimate sky background, S , we fit a 2D low-order polynomial (default to second order, but it is user adjustable) to the image which has the spectral trace masked out.

This optimal extraction algorithm requires the spectral trace to be aligned with the detector grid, which is not the case for WIRC+Pol data. Therefore, we first rotate D , V , and S images using the `warpAffine` function from `OpenCV` with a rotation matrix

given by the `getRotationMatrix2D` function. We measured the angle to rotate by fitting a line to the brightest pixel in each column of the thumbnail D and we rotate around the center of the thumbnail. Next we describe the extraction algorithm. In a standard, non-optimal, spectral extraction procedure, the flux and variance at each wavelength bin is determined by the sum of the background-subtracted data along the spatial direction in that wavelength bin. This can be written as

$$F_{\lambda,\text{std}} = \sum_x (D_{\lambda,x} - S_{\lambda,x}) \quad (5.2)$$

$$\sigma_{F_{\lambda,\text{std}}}^2 = \sum_x V_{\lambda,x} \quad (5.3)$$

The summation boundary in the spatial (x) direction is $\pm 9\sigma$ from the peak of the trace where σ is determined by fitting a Gaussian profile along the spatial direction of the brightest part of the trace. This extraction method is non-optimal because it gives equal weight to the noisy wings of the spectral trace as it does the peak. As a result, the extracted 1D spectra are noisier, especially for low S/N data.

The optimal extraction algorithm solves this issue by fitting an empirical spectral profile to the trace and assigning more weight to the less noisy region. The key to this optimization is the profile image, P , of the data, which represent the probability of finding photons in each wavelength column as a function of spatial row. The profile image can be constructed as follows: (i) For each wavelength column λ of $D - S$, divide each pixel by $F_{\lambda,\text{std}}$ from (5.2). This gives us a normalized flux in each column. (ii) We assume that the profile varies slowly as a function of λ . As such, we can smooth P by applying a median filter in the λ direction, with the default filter size of 10 pixels. (iii) Then for each column (λ), we set all pixels with negative P to 0, and normalize P such that $\sum_x P_{\lambda,x} = 1$

With the knowledge of the spectral profile, we can revise the variance estimate from (5.1) by

$$V_{\text{revised}} = \sigma_{\text{RN}}^2 / Q^2 + |FP + S| / Q \quad (5.4)$$

where we replace the noisy data D by a model based on the measured flux F and profile P . (Note that FP term is $F_{\lambda,\text{std}}$ from (5.2) multiplying the image P column-by-column). Bad pixels that are not captured earlier in the calibration process and cosmic ray hits can be rejected by comparing the data to the model:

$$M = (D - S - FP)^2 < \sigma_{\text{clip}}^2 V_{\text{revised}} \quad (5.5)$$

where M is 1 where the difference is within some σ_{clip} of the expected standard deviation. At this stage, we can optimize the flux and variance spectra by

$$F_{\lambda,\text{opt}} = \frac{\sum_x MP(D - S)/V}{\sum_x MP^2/V} \quad (5.6)$$

$$V_{\lambda,\text{opt}} = \frac{\sum_x MP}{\sum_x MP^2/V} \quad (5.7)$$

If needed, one can iterate this process by reconstructing the profile image using this new optimized flux, then repeat the following steps (eq. (5.4) to (5.6)) to arrive at a cleaner final optimized flux and variance. This spectral extraction process is to be run on four spectral traces for each source. Adopting the Stokes parameters formulation of polarization, we call the traces corresponding to 0, 90, 45, and 135°, respectively, Q_p , Q_m , U_p , and U_m . The detector locations of these traces are lower left, upper right, lower right, and upper left (see Fig. 5.1 right).

Wavelength Solution

For the polarimetric calculation in the next step, it is crucial to ensure that all spectra are well aligned in wavelength. A precise absolute wavelength solution is not necessary at this step, so we first compute a relative wavelength solution between the four spectral traces. Aligning four spectra in wavelength is complicated because WIRC+Pol's filters and PG are tilted at 7° away from being orthogonal to the optical axis. As a result, the filter transmission profile differs for the four traces since the outgoing beams from the PG hit the filter at different angles (Ghinassi et al., 2002). This effect is also field dependent, since a source observed at different positions on the detector enter the filter at different angles. As a result of this profile shift, we cannot rely on the filter cutoff wavelengths to compute the wavelength solution. The best practice is to first align all the high S/N spectra (S/N~1000 per spectral channel) of a standard star to each other, relying on atmospheric absorption features at 1.26–1.27 μm due to O_2 in the J band and multiple CO_2 lines in the H band. These features can be seen clearly in the absolute throughput plot shown in Fig. 5.5. We note that some standard stars also have the hydrogen Paschen- β line at 1.28 μm and multiple Brackett lines in the H band that we can use for alignment as well. Currently we align the trough of the absorption line manually. After the four spectra of the standard star are aligned in wavelength, we can align spectra of our source to the corresponding spectra of the standard star. It is important that the source and the standard are observed at a similar position on the detector, so that the filter transmission profile for the two are identical. We found that the guiding script (described at the end of §5.2) can reliably put a new source on top of a given

reference star to within a pixel. We then can rely on the filter transmission cutoffs to align each of four traces of the source to those of the standard. For the absolute wavelength solution, we assume that wavelength is a linear function of the pixel position, which is reasonable at this low spectral resolution. The spectral dispersion in μm per pixel is given by comparing the measured spectrum (in pixels) to the filter transmission profile. The wavelength zeropoint is calibrated to the atmospheric absorption features used for alignment.

Polarization Calibration and Computation

Linear polarization Stokes parameters (q and u) are the normalized flux differences between the two orthogonal pairs.

$$q = (Q_p - Q_m)/(Q_p + Q_m) \quad (5.8)$$

$$u = (U_p - U_m)/(U_p + U_m) \quad (5.9)$$

The degree and angle of linear polarization can be computed with following equations:

$$p = \sqrt{q^2 + u^2} \quad (5.10)$$

$$\Theta = 0.5 \tan^{-1}(u/q) \quad (5.11)$$

In practice, however, the calculation is complicated by non-common path effects in WIRC+Pol's optical path. Firstly, the camera has an uneven illumination across the field of view—typical of a wide field instrument. This can introduce a flux difference between, e.g., Q_p and Q_m when the source is unpolarized. This effect remains at some level even after a flat-field-correction. Secondly, as mentioned earlier, the PG and all filters in WIRC were installed at 7° with respect to perpendicular of the optical axis to mitigate ghost reflections. As a result, the upper and lower spectral traces enter the broadband filters (either J or H) downstream from the PG at different angles, and experience slightly different filter transmission profiles (Ghinassi et al., 2002). This shift can be seen in the transmission curves shown in Fig. 5.5 (to be discussed in more details in §5.4).

In order to remove these non-common path effects, we follow the calibration scheme described here. For brevity, we consider the Q pair, as the process for the U pair is identical. First, we observe an unpolarized standard star at the same detector position as our target. The intrinsic spectrum of this standard is $S(\lambda)$, which is the same for all four traces since the standard is not polarized. We have the observed

spectrum

$$S'_p = S(\lambda) A_1(\lambda) F_p(\lambda) \quad (5.12)$$

$$S'_m = S(\lambda) A_1(\lambda) F_m(\lambda) \quad (5.13)$$

where $F_{p,m}(\lambda)$ are the filter transmission functions seen by the plus (lower) and minus (upper) traces. Note here that the filter transmission function depends on the angle of incidence on the broadband filter, therefore it also changes across the field of view. $A_1(\lambda)$ is the other transmission function which is similar for both traces (e.g., atmosphere, telescope reflective coating, etc.) If our science target has intrinsic fluxes I_p and I_m due to some intrinsic polarization, we will observe

$$I'_p = I_p(\lambda) A_2(\lambda) F_p(\lambda) \quad (5.14)$$

$$I'_m = I_m(\lambda) A_2(\lambda) F_m(\lambda) \quad (5.15)$$

where A may change due to, e.g., changing atmosphere. Recall that if this source has an intrinsic normalized Stokes parameter q , then $q = (I_p - I_m)/(I_p + I_m)$. We remove the transmission functions by dividing the observed target spectrum by the observed standard spectrum which sees the same filter transmission profile F . The ratio A_1/A_2 will cancel out here as well. We can then recover this intrinsic polarization by computing

$$\frac{I'_p/S'_p - I'_m/S'_m}{I'_p/S'_p + I'_m/S'_m} = \frac{I_p - I_m}{I_p + I_m} = q \quad (5.16)$$

Note that the standard star intrinsic spectrum term $S(\lambda)$ cancel out because it is the same for all 4 traces. A similar process can be applied to the U pair to measure u as well.

For polarimetric uncertainties, we first obtain uncertainties of the measured spectrum by computing the standard deviations in each spectral bin for each source and standard spectrum from the series of exposures. Then we compute uncertainties of the flux ratios I/S by error propagation assuming normal distribution. Let's denote flux ratios in (5.16) by $Q_p = I'_{Qp}/S'_{Qp}$ and so on. The uncertainties to q and u are also calculated by error propagation, assuming Gaussian error, using the following

equations:

$$\sigma_q = \frac{2}{(Q_p + Q_m)^2} \sqrt{(Q_m \sigma_{Q_p})^2 + (Q_p \sigma_{Q_m})^2} \quad (5.17)$$

$$\sigma_u = \frac{2}{(U_p + U_m)^2} \sqrt{(U_m \sigma_{U_p})^2 + (U_p \sigma_{U_m})^2} \quad (5.18)$$

$$\sigma_p = \frac{1}{p} \sqrt{(q \sigma_q)^2 + (u \sigma_u)^2} \quad (5.19)$$

$$\sigma_\Theta = \frac{1}{2p^2} \sqrt{(u \sigma_q)^2 + (q \sigma_u)^2} \quad (5.20)$$

We have confirmed from the commissioning data that q and u follow normal distribution. However, p is a non-negative quantity following a Rice distribution with a long positive tail (Jensen-Clem et al., 2016). Its mean value is biased to the positive and has to be corrected, especially when the value is close to zero, using (Wardle and Kronberg, 1974)

$$p^* = \sqrt{p^2 - \sigma_p^2} \quad (5.21)$$

5.4 Instrument Commissioning

Detector Characterization

Linearity and Dark Current Measurement

Infrared detectors have a linear response to photon counts up to a certain amount. We measure this linearity limit by taking flat exposures at different exposure times and plot the mean count as a function of exposure time. To quantify the linearity, we fitted a line through the first few data points where the response is still unambiguously linear. The deviation from this fit is then the degree of non-linearity. We found that the new H2 detector is linear to 0.2% level up to 20,000 ADU and to 1% level at 33,000 ADU.

The dark current can be measured by taking dark exposures at various exposure times and fitting a linear relation to the median count. We measure the median dark current across the detector to be $1 \text{ e}^-/\text{s}$. We note here that WIRC does not have a shutter, and dark frames are obtained by combining two filters with no overlapping bandpass, typically Brackett- γ and J -band filters.

Gain and Read-Out Noise

We measure the gain and the read-out noise of the detector using the property of Poisson statistics where the variance equals the mean value. If N is the number of

photoelectrons detected and ADU is the measured count, we have that $N = g\text{ADU}$ where g is the gain factor in e^-/ADU . The variance of the count is a sum of the photon shot noise and the detector read-out noise: $g^2\sigma_{\text{ADU}}^2 = \sigma_N^2 + \sigma_{\text{read-out}}^2$. But since $\sigma_N^2 = N$, we get

$$\frac{1}{g}\text{ADU} + \left(\frac{\sigma_{\text{read-out}}^2}{g^2}\right) = \sigma_{\text{ADU}}^2 \quad (5.22)$$

Hence, we can compute g and $\sigma_{\text{read-out}}$ by measuring σ_{ADU}^2 as a function of ADU. To do so, we took flat exposures at multiple exposure times within the linearity limit. At each exposure time, we took two images, $\text{IM}_{1,2}$. $\text{ADU}(t)$ is the mean count of $(\text{IM}_1 + \text{IM}_2)/2$ in the pair of images. The associated variance ($\sigma_{\text{ADU}(t)}^2$) is the count variance of $(\text{IM}_1 - \text{IM}_2)/2$ in the image. By measuring this at different exposure times, we could fit for g and $\sigma_{\text{read-out}}$, and arrived at $g = 1.2 e^-/\text{ADU}$ and $\sigma_{\text{read-out}} = 12 e^-$.

Polarization Grating Orientation

Recall that the QWP/PG device with the split-pupil design splits and disperses the incoming beam into 4 outgoing beams according to the incoming linear polarization states. To measure exactly what polarization angle each quadrant on the detector corresponds to, we observed the highly polarized twilight sky at zenith, where the polarization angle is perpendicular to the Sun's azimuth. Aggregating multiple observations from different nights over the year, we found that the 0, 90, 45, and 135° linear polarization angle (Q_p , Q_m , U_p , and U_m) corresponds to the lower left, upper right, lower right, and upper left quadrants, respectively. A more precise measurement of the angle of polarization is presented in §5.4.

Instrument Transmission

We conducted two separate measurements in order to characterize both WIRC+Pol's absolute transmission from above the atmosphere to detector, and the transmission of just the PG. The absolute transmission can be measured by observing an unpolarized source for which we know the spectrum in physical units. Comparing the spectrum observed by WIRC+Pol to this known spectrum allows us to measure the efficiency of photon transfer from top of the atmosphere to our detector. For this measurement, we first need a flux-calibrated spectrum of an unpolarized source, observed and calibrated using a different instrument. We observed unpolarized, A0 standard star HD 14069 on 2017 October 12 using *TripleSpec*, which is a medium-resolution near-IR spectrograph at the Cassegrain focus of the 200-inch telescope that has

simultaneous wavelength coverage from 0.9 to 2.4 μm , i.e., y , J , H , and K bands (Herter et al., 2008). To flux calibrate the spectrum, we also observed an A0V standard star, HIP 13917, at a similar airmass. Raw spectra for both HD 14069 and HIP 13917 are reduced and extracted using a version of the Spextool data reduction pipeline, modified for Palomar TripleSpec (Cushing et al., 2004). Finally, to remove telluric absorption and to flux calibrate the spectrum of HD 14069, we use the `xtellcorr` tool (Vacca et al., 2003), which derives TripleSpec’s transmission by comparing the A0V model spectrum (derived from Vega) to the observed A0V spectrum. This derived transmission, shown in Fig. 5.5 for reference, is applied to HD 14069’s observed spectrum in the instrumental unit to get the spectrum in a physical flux unit.

Next, we observed the same star using WIRC+Pol in the J band on 2017 October 16. The data were calibrated and extracted using the reduction pipeline described above, and we have four spectra in WIRC+Pol’s instrumental unit (ADU s^{-1}). Multiplying this spectrum by the gain and dividing by the width of each wavelength bin, we get the spectrum in $\text{e}^{-} \text{s}^{-1} \mu\text{m}^{-1}$. To get the TripleSpec spectra from the physical unit ($\text{erg s}^{-1} \text{cm}^{-2} \mu\text{m}^{-1}$) into the same unit, we multiply it by the telescope collecting area and divide by the energy per photon. We then convolve this spectrum with a Gaussian kernel down to WIRC+Pol resolution. The ratio between these two spectra is the fraction of photons from this source from the top of the atmosphere reaching WIRC+Pol’s detector. For the H band measurement, we observe a different star with the same spectral type (HD 331891), and repeat the analysis with the TripleSpec spectrum scaled for the new source.

Fig. 5.5 shows the transmission of each of the four WIRC+Pol spectral traces (note that the total flux is divided into 4 traces). The average transmission is overplotted. TripleSpec’s transmission, measured by our observations described above, is given for reference. The number is about a factor of 2 lower than previous measurements by Herter et al. (2008), which may be due to the different atmospheric conditions. We note that WIRC+Pol has a very high transmission, peaking at 17.5% and 30% in J and H bands, respectively. The four spectral traces have different relative transmission, which mimics an effect of instrumental polarization. We will discuss this issue in the next section, but this effect necessitates observations of an unpolarized standard star. The O_2 and CO_2 atmospheric absorption features in the J and H bands that we used to align the four spectral traces, as mentioned in §5.3, are visible in both WIRC+Pol’s and TripleSpec’s transmission curves. Additional features in

WIRC+Pol’s transmittance curve are due to the broadband filters. Finally, we note that TripleSpec’s transmission has a strong wavelength dependence, intrinsic to a surface relief grating, while WIRC+Pol’s transmission is almost flat. (The J -band slope is due to the telescope mirror coating, see Fig. 2 in Herter et al. (2008).)

In addition to the absolute transmission of the instrument, we also measured the transmission of the PG itself by observing a bright star (HD 43384) with and without the PG. We dark subtract and flat divide the raw data, then median combine images with and without the PG. We performed aperture photometry using an Astropy (Astropy Collaboration et al., 2018) affiliate `photutils` package to compare flux in the direct image without PG to flux in the spectral traces with PG. In an ideal scenario, all four traces will get an equal amount of flux, which is the direct flux divided by four. However, the measurement shows that the Q_p (lower left), Q_m (upper right), U_p (lower right), and U_m (upper left) have the efficiency of 88.3, 84.4, 98.7, and 99.2%, in comparison to the ideal scenario. Note that these numbers are consistent to what we found in the absolute transmission measurement. The difference between the Q and U pair transmission is likely due to the misalignment between the pupil plane and the WIRC instrument. This misalignment is also responsible for $\sim 20\%$ gradient in the flat field taken without the PG. We then assume that this difference is not due to an intrinsic difference between the transmission of the two halves of the PG. Thus we report its mean transmission as 93%.

Observations of Unpolarized Standard Stars

In order to quantify the instrumental polarization due to telescope pointing, we observed 4 different unpolarized standard stars: HD 93521, HD 96131, HD 107473, and HD 109055 (Heiles, 2000) on 2018 April 21. All stars are polarized to less than 0.1% in the V band, which yield negligible polarization in the IR assuming Serkowski law, $p(\lambda)/p(\lambda_{\max}) = \exp(-1.15 \ln^2(\lambda/\lambda_{\max}))$ (Serkowski et al., 1975). We observed the four stars in the aforementioned order, then repeat the observations in the same order so each star was visited twice. Fig. 5.6 (right) shows the location of these 4 stars on the sky in altitude-azimuth coordinates (which reflect gravity vector on the instrument). Hour angles in 2 hour interval are plotted as well. The total exposure time per visit is 500–600 s, resulting in typical S/N for the spectra of order 3000 for HD 93521 and HD 107474 ($J \sim 7.5$) and 1,500 for HD 96131 and HD 109055 ($J \sim 8.8$). For each of the two visits to the stars, we used HD 93521 as the “standard” ($S'_{p,m}$ in (5.16)) and the remaining 3 stars as the “source” ($I'_{p,m}$ in (5.16)). The resulting measured q and u are the difference between instrumental

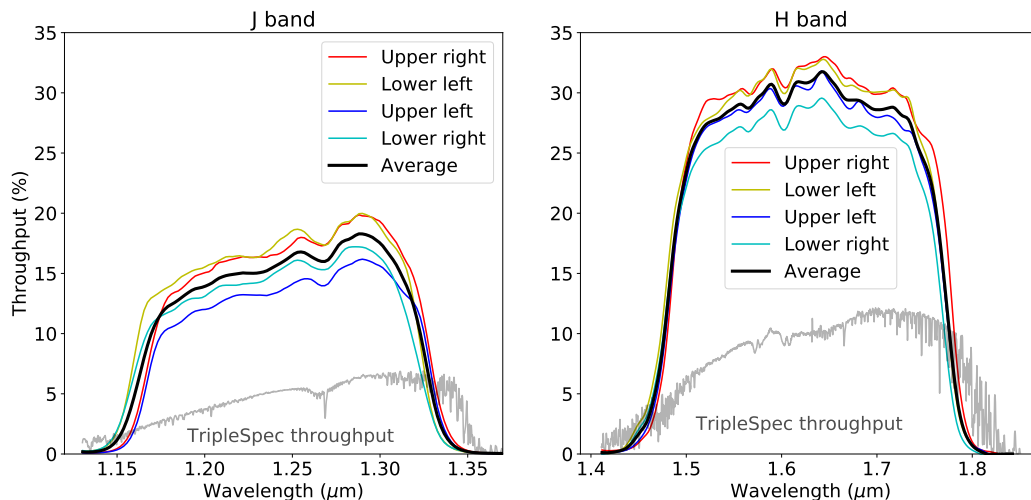


Figure 5.5: WIRC+Pol’s transmission in the *J* band and the *H* band. Individual trace’s transmission is computed from the ratio between 1/4 expected flux above the atmosphere to what is measured at the detector. The factor of 1/4 reflects the fact that we divide the incoming light into 4 beams for the 4 polarization angles. (Thus, if the transmission of the atmosphere and instrument were perfect, each trace would measure 100% throughput in these plots). The average transmission, which corresponds to the total instrumental transmission from top of the atmosphere to the 4 spectral traces, is overplotted. TripleSpec’s transmission is given for comparison, though TripleSpec has a higher spectral resolution and is much more optically complex. A few atmospheric absorption lines at 1.27, 1.57, and 1.61 μm visible in both TripleSpec and WIRC+Pol spectra in both *J* and *H* bands are used for confirming the wavelength solution. Other spectral features that are only present in WIRC+Pol’s efficiency come from the broadband *J* and *H* filters. The relative shift of the filter transmission profiles for upper traces and lower traces is evident, especially for the *J* band, due to different angles of incidence on the broadband filter.

polarization between the two standard stars. We then used HD 93521 observations from the two visits to calibrate each other. This provides us the first handle of the temporal stability of the instrumental polarization, which shall be discussed in greater details in §5.4. Fig. 5.6 (left) four panels show the measured degree and angle of polarization measured from these observations while the Fig. 5.6 (right) shows the locations of the 4 stars on-sky in the two sequences. The time delay between the first observation in each sequence and the beginning of the observation is annotated. Out of the 3 stars compared with HD 93521, only HD 109055 results in measured polarization consistent with zero to within 3σ . The other two stars show deviation up to 1%. We note that for both sequences, HD 96131 and HD 107473 were observed *closer* in time to HD 93521, however, they were *further* away on-sky.

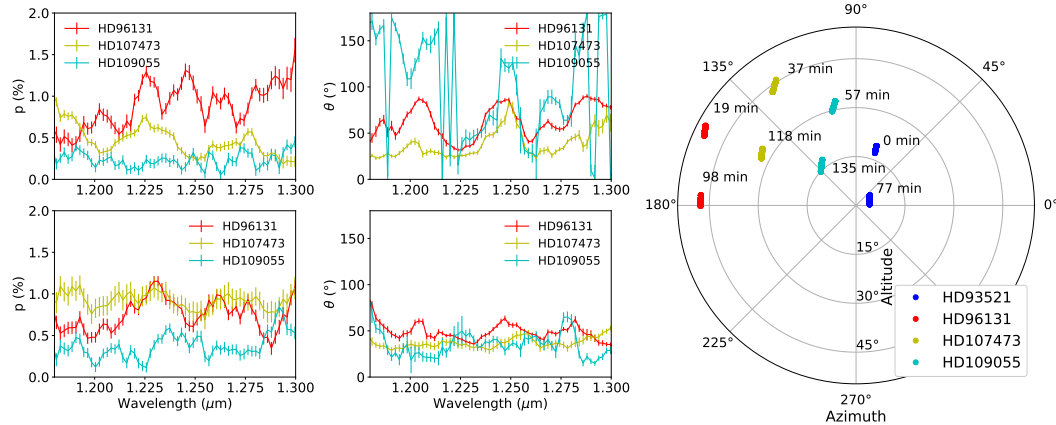


Figure 5.6: Left: four panels show measured degree and angle of polarization of 3 unpolarized standard stars HD 96131, HD 107473, and HD 109055 using HD 93521 as the standard (see text for reduction details). The top and bottom rows are from the first and second sets of observations. Right: the location of the stars on-sky during the observing sequence along with the time between the beginning of each sequence and the beginning of the first sequence is annotated. The black dots represent the 3-hour long sequence observation of HD 109055 on 2018 May 04. Lines of constant hour angle are plotted.

The intrinsic spectral type and brightness difference between these sources should not influence our reduction using the methods outlined above. Indeed, the deviation of measured polarization from zero did not seem to be a function of source’s intrinsic properties. HD 93521 and HD 109055, the pair that provided near-zero polarization differ in magnitude ($J = 7.5$ vs 8.7) and spectral type (O9.5III_{nn} vs A0V). This preliminary work led us to conclude that on-sky pointing may have a noticeable effect on the measured polarization, and has implications for our future observation strategy: to observe the unpolarized standard star closest to the source. This may be results of differential atmospheric effects from observations at different airmass, or stress induced birefringence from the changing gravity vector on the instrument at different telescope pointing.

Polarization Spatial Stability

As discussed earlier, we expect the polarization measurement of an unpolarized source to be non-zero due to instrumental systematics. This may be due to an intrinsic telescope or instrument-induced polarization or simply uncorrected flat-field variation. To quantify this effect, we mapped the polarization variability across the field of view by observing an A0 unpolarized standard star (HD 14069) in a grid across the full field of view on 2017 Nov 28. However, the observations were taken

at a relatively low S/N and over a long period of time where other factors may affect the measured polarization. While the fidelity of the measurements was not enough to construct a precise model of the polarization zero-point as a function of location on the field of view, we found enough evidence that the polarization zero-point can vary more than 1% across the field of view. This finding informed our decision to observe sources at one specific location on the detector to reduce this effect. (Each quadrant of the detector is split into four triangular regions by the focal plane mask (see Fig. 5.2), we pick the bottom triangle because of the general lack of bad pixels there.)

In order to better quantify the spatial dependence of the instrumental effect, on 2018 July 24 we observed an F8V unpolarized standard star HD 154892 at two dither positions on the detector (“A” and “B”). We first took a sequence of 18 exposures, 100 s each, switching between A and B positions with an offset of 25" after every image. Three hours later, we conducted a similar observation of HD 154892 at the same location on the detector with 20 exposures, 100 s each, switching between A and B positions. In this sequence, the A position is the same as the A position in sequence 1, however, the offset size was 30". For each sequence of the observations, we median combine all spectra from positions A and B separately. Then we use position A as the standard (i.e., $S'_{p,m}$ in (5.16)) to calibrate observations from position B (i.e., $I'_{p,m}$ in (5.16)). The measured q and u are then the *difference* between instrumental q and u at positions A and B. Fig. 5.7 (left) shows q and u differences between positions A and B for sequence 1 (solid line) and 2 (transparent line). The difference in instrumental polarization between these two positions are 1.0% and 1.5% in q and u , respectively. Fig. 5.7 (right) shows the difference between the two sequences, which quantify the temporal stability of the spatial systematic difference. While the average over the J band of the difference is around 0, some wavelength dependence exists. This may be from the fact that the offset between positions A and B was slightly difference between sequence 1 and 2 (25" vs 30"), or it could be a real temporal change in instrumental polarization spatial dependence. In summary, this measurement shows that the spatial dependence of the instrumental polarization is of order 1–1.5% over 30" on the detector, and this difference is temporally stable to $\pm \sim 0.3\%$. This finding underlines the need to observe a standard star and a science source at the exact same position on the detector, which can be done using the guiding script discussed in §5.2.

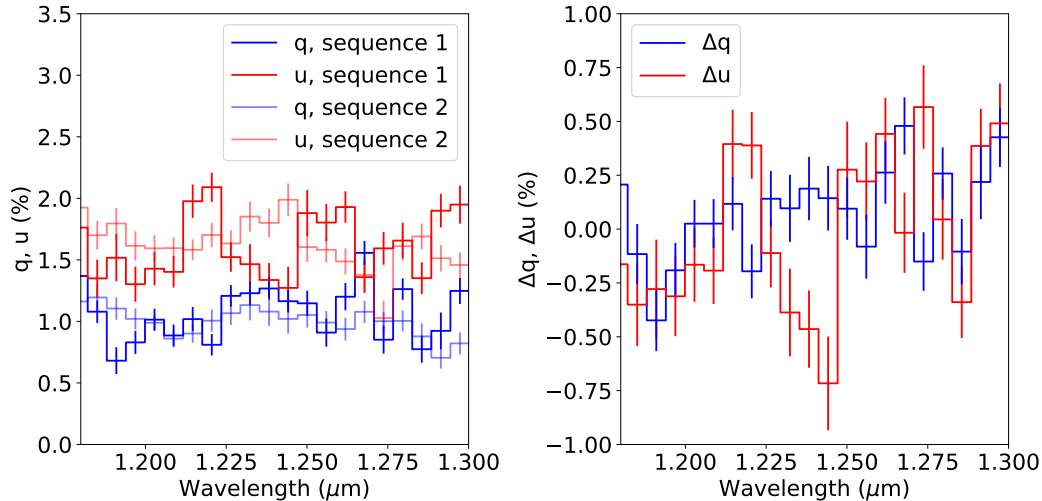


Figure 5.7: Left: q and u measured by using observations at position A to calibrate observations at position B. Solid lines are the results from the first sequence of observations while the transparent lines are the second sequence. These measured q and u reflect the difference between instrumental effects at the two positions. Right: The difference between measured q and u from the two sequences.

Polarization Temporal Stability

In this section we quantify the temporal stability of the systematic polarization. For instance, if we know that the 1% instrumental polarization can be well measured and is stable at 0.1% level over some period of time, then we can use observations of unpolarized standard stars to remove this systematic error and recover the source’s true polarization down to $\sim 0.1\%$ level. Hence, we need to quantify the timescale over which our instrumental polarization zero-point changes.

To conduct this measurement, we observed an A0V unpolarized ($0.07 \pm 0.07\%$ in the V band, consistent to zero) standard star (HD 109055; Heiles, 2000) on 2018 May 04 UT for 3 hours as the star traces 45° of telescope pointing angle in hour angle across the meridian. The on-sky location of HD 109055 is shown as black dots in Fig. 5.6. Our guiding script kept the source on a single point on the detector with guiding RMS $\sim 0.25''$ (1 pixel) to reduce the field of view dependent effects. We refocused the telescope twice during the observing sequence to keep up with the changing temperature inside the dome since our observations happened at the beginning of the night, which show up as gaps in our time series in Fig. 5.8. The data were reduced by the DRP using the procedure described above (§5.3). We first median combined all the spectra of the source, from which we computed median q_{median} and u_{median} to provide a baseline. Next we compute q_i and u_i spectra from each

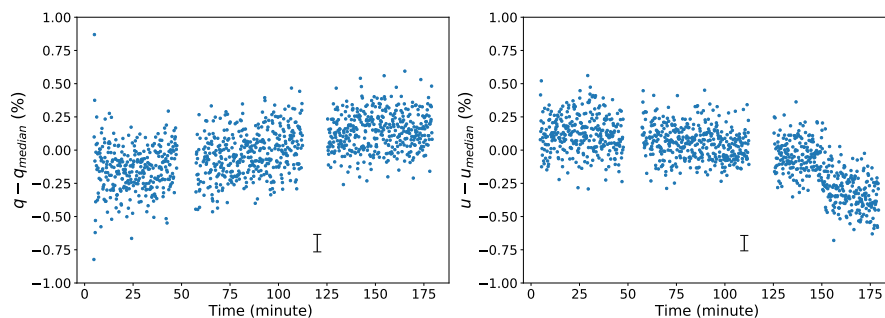


Figure 5.8: Temporal variation of the measured broadband normalized Stokes parameters q (left) and u (right) as functions of time since the first image. The broadband value is simply the median of q and u spectra within the J -band bandpass. Each data point plotted here comes from an individual image taken in the sequence, and is subtracted by the median broadband q and u across the whole observing sequence. Uncertainty in q and u remains constant, and a 1σ representative errorbar is shown in each plot. The two gaps in the data at 50 and 120 minutes are when we refocused the telescope.

of the single observations, and $q_i - q_{\text{median}}$, $u_i - u_{\text{median}}$ shows the variation in the polarimetric zero-point throughout our 3-hour long observing sequence. We found that the seeing conditions remain very stable and the polarimetric deviation in both q and u show no wavelength dependence, which may happen if the spectral resolution of the trace is changing due to seeing variations. Hence, for each observation, we use the median of $q_i - q_{\text{median}}$ and $u_i - u_{\text{median}}$ within the filter's bandpass as broadband values, shown in Fig. 5.8. The two gaps in the data indicate where we refocused the telescope. The RMS of the variation is 0.2% for both q and u over 30 minutes, corresponding to 0.13 range in airmass. Note that there are some long-term variations, whose origin remain uncertain. We note that the change in systematic polarization due to telescope pointing (discussed in §5.4) is quantitatively consistent with what we observed in this long sequence. While the telescope pointing effect contributes to the long-term variation in the systematic presented here, there might also be other components that are still unknown.

Observations of Known Polarized Stars

Once the polarimetric zero-point is well characterized, observations of stars with known polarization are required to measure the instrument's polarimetric efficiency and polarization angle zeropoint. The first star used was Elia 2-25, which is a polarized standard in Whittet et al. (1992) with $p = 6.46 \pm 0.02\%$ and $\theta = 24 \pm 1^\circ$ in the J band. It has near-IR polarization spectrum published by Miles-Páez et al.

(2014). We observed Elia 2-25 (Miles-Páez et al., 2014; Whittet et al., 1992) on 2018 May 06 for 17 min (10 min), followed immediately by an unpolarized standard HD 154892 (Heiles, 2000) for 8 min (2 min), both wall clock time (total integrated time). Both stars were put to within a pixel from each other on the detector to minimize the spatially dependent polarization effect discussed above. The total time of 25 min is short enough for the calibration to not be affected by the varying systematic shown in the previous section. Fig. 5.9 shows the degree of polarization (p in percent) and the angle of polarization (θ in degrees), in comparison from the literature result. The degree of polarization agrees to the literature value to within 0.5% across the whole spectrum, but the angle of polarization is greater than the literature value by 15° . We know that the instrument is aligned with North up to within 1° by observations of star trails, so this offset must be from the instrument itself. The second polarized standard observed was Schlute 14 with $p = 1.54 \pm 0.02\%$ and $\theta = 88 \pm 1^\circ$ in the J band (Whittet et al., 1992). Fig. 5.9 *bottom* shows the measured polarization compared to the literature. The results agree to those from Elia 2-25, with p accurate to within 0.5%. We note that the agreement between WIRC+Pol observations and literature values to within 0.5% is consistent to the systematic polarization due to telescope pointing as discussed in §5.4, since the unpolarized standards used here were not spatially close to the polarized standards on-sky. The angle of polarization, however, is offset from the literature value by 15° . We know from observing star trails on WIRC, with the telescope tracking off, that the orientation of instrument, since the PG/QWP, is offset from the North (0° angle of polarization) by $\sim 1^\circ$. The most likely culprit of the offset is the angle of polarization zero-point intrinsic to the PG/QWP device. In another word, the PG/QWP device was manufactured to sample 15° , 60° , 105° , and 150° , instead of the anticipated 0° , 45° , 90° , and 135° . As a result, it simply rotates the angle of polarization measurement by 15° and did not affect the degree of polarization. As a result, we can measure and subtract this offset during the course of an observation.

5.5 Future Instrument Upgrades

Informed by these commissioning results, we have identified a few potential upgrades that would improve the instrument's performance.

- An addition of a polarimetric modulator—a device that can rotate the incoming beam's polarization angle—will allow us to measure linear polarization from each of the four spectral traces using four different modulation angles. The

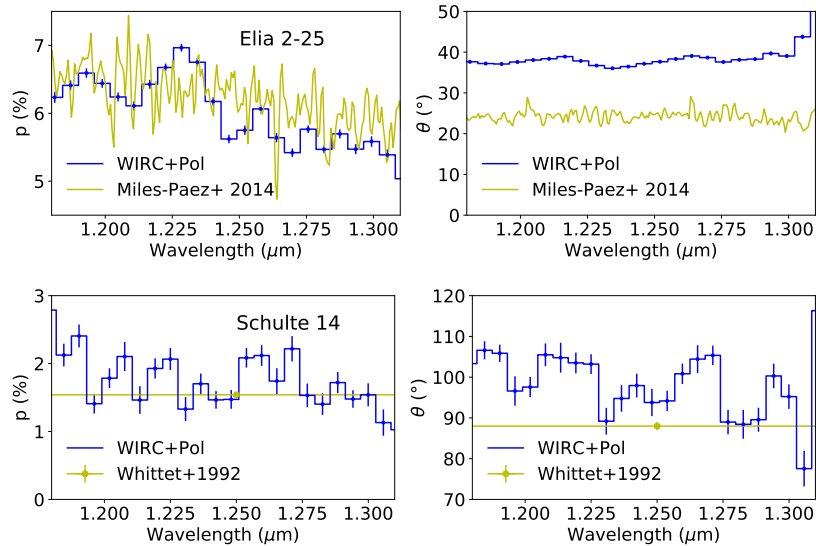


Figure 5.9: Degree (p) and angle (θ) of polarization for Elia 2-25 (*top*) and Schulte 14 (*bottom*) from WIRC+Pol in comparison to the results from Miles-Páez et al. (2014) or Whittet et al. (1992). The y-axes range for the two stars are the same. The degree of polarization agrees to within 0.5%, but the angle of polarization is $\sim 15^\circ$ off. Error bars only account for random errors, which appear to be smaller than typical scattering in p and θ values. This is likely due to systematic error in aligning spectra to compute polarization.

modulator will allow us to swap the incident polarization between different pairs of spectral traces, while the instrumental systematics stay constant. Thus allowing us to distinguish between true astrophysical polarization and instrumental systematics. This upgrade would remove the observed field dependent polarimetric zero-point and other slowly varying effects (§5.4, Fig. 5.8). The upgrade has been funded and will be implemented by the end of 2018.

- To minimize non-common path errors between the four spectral traces, the PG has to be the last optic in the optical train before the reimaging optics. This can be done by swapping the PG and broadband filters, which is a complicated process since the two filter wheels are not interchangeable, and the PG requires a special mounting on the filter wheel. Another solution to this problem is to place a $J+H$ band filter permanently in front of the PG. This way, the instrument will be able to observe in the J and H bands simultaneously with the caveat of a brighter sky background in the slitless mode. We note that this change may not be needed with the presence of a modulator.

5.6 Conclusion

We described a R \sim 100 near-IR spectropolarimeter, WIRC+Pol, on the 200-inch telescope at Palomar Observatory. The existing IR imaging camera, WIRC, was upgraded by an installation of a compact, liquid crystal polymer-based polarimetric device called a PG. The PG acts both as a polarimetric beamsplitter and a spectral disperser, and is small enough to fit inside the filter wheel of the instrument, simplifying the upgrade in comparison to using a Wollaston prism and another grating. We developed a data reduction pipeline that extracts spectra from the images and computes polarization of the observed source.

We have established the following key characteristics of the instrument. Firstly, the liquid-crystal-based QWP/PG device performs as expected, delivering a high dispersion efficiency of 93% into the first order spectra. This is an on-sky demonstration that a PG, apart from its polarimetric capabilities, is a very efficient disperser in comparison to a surface relief grating. Secondly, the commissioning data showed that the instrument can measure linear polarization reliably to 1% level for bright sources with known polarization given an appropriate observation strategy. The measured polarization angle is greater than literature values by $\sim 15^\circ$, which is constant and can be removed. The polarimetric uncertainty is currently limited by time-varying systematics, which may originate from telescope pointing, likely due to stress induced instrumental polarization or atmospheric effects. Thirdly, we documented difficulties of computing polarization from single-shot observations without a rotating modulator. Relying on comparing fluxes in four spectral traces in four quadrants of the detector to compute polarization risks confusing source's intrinsic polarization with instrument's flat-field and non-common path errors. We mitigated this effect by correcting our observations with deep flat-field images taken with all polarimetric optics in place, and also by keeping the source in all observations on a single location on the detector to within 1 pixel (0.25"). Another requirement to compute polarization from comparing fluxes in four spectra is that they must be well aligned in the wavelength direction. This was complicated by the fact that the broadband filters used are downstream from the PG, imprinting different transmission profiles on the four traces. This was mitigated by using atmospheric absorption features to align the spectra instead of using the filter cutoffs. The presented characterization of WIRC+Pol was crucial to inform the funded half-wave plate instrument upgrade in the near future. The discovered characteristics should inform the design of a future spectropolarimetric instrument using a PG. The lack of a rotating modulator in WIRC+Pol may have caused a number of systematics, but this design can

provide a very efficient spectropolarimeter with minimal moving parts, which may prove essential in incorporating such system in a future space-based instrument.

Acknowledgements

This work is supported by the National Science Foundation under Grant No. AAG-1816341. The WIRC+Pol upgrade was in part supported by a grant from the Mt. Cuba Astronomical Foundation. We thank Paulo Miles-Páez for providing us polarized spectra of Elia 2-25 polarized standard star for comparison with our observations and for discussions on best practices in reducing near-IR spectropolarimetric data. We thank staff of Palomar Observatory for assisting our observations. Palomar Observatory is operated by a collaboration between California Institute of Technology, Jet Propulsion Laboratory, Yale University, and National Astronomical Observatories of China.

Chapter 6

ACHIEVING A SPECTROPOLARIMETRIC PRECISION
BETTER THAN 0.1% IN THE NEAR-INFRARED WITH
WIRC+Pol

Tinyanont, S. et al. (Sept. 2019). “Achieving a spectropolarimetric precision better than 0.1% in the near-infrared with WIRC+Pol”. In: *Proc. SPIE*. Vol. 11132. Society of Photo-Optical Instrumentation Engineers (SPIE) Conference Series. DOI: 10.1117/12.2529863. arXiv: 1908.10409 [astro-ph.IM].

Samaporn Tinyanont¹ Maxwell Millar-Blanchaer^{1,2,5} Nemanja Jovanovic¹ Dimitri Mawet^{1,2} Gautam Vasisht² Jennifer W. Milburn¹ Eugene Serabyn² Michael Porter¹
Skyler Palatnick³ Connor Hopkins⁴

¹Department of Astronomy, California Institute of Technology, 1200 E California Blvd, MC 249-17, Pasadena, CA 91125, USA ²Department of Physics and Astronomy, University of Pennsylvania, 209 S 33rd St, Philadelphia, PA 19104 ⁴Pasadena High School, 2925 E Sierra Madre Blvd Pasadena, CA 91107 ⁵NASA Hubble Fellow

Abstract

WIRC+Pol is a near-infrared low-resolution spectropolarimeter on the 200-inch Telescope at Palomar Observatory. The instrument utilizes a polarization grating to perform polarimetric beam splitting and spectral dispersion simultaneously. It can operate either with a focal plane slit to reduce sky background or in a slitless mode. Four different spectra sampling four linear polarization angles are recorded in the focal plane, allowing the instrument to measure all linear polarization states in one exposure. The instrument has been on-sky since February 2017 and we found that the systematic errors, likely arising from flat fielding and gravity effects on the instrument, limit our accuracy to $\sim 1\%$. These systematic effects were slowly varying, and hence could be removed with a polarimetric modulator. A half-wave plate modulator and a linear polarizer were installed in front of WIRC+Pol in March 2019. The modulator worked as expected, allowing us to measure and remove all instrumental polarization we previously observed. The deepest integration on a bright point source ($J = 7.689$, unpolarized star HD 65970) demonstrated uncertainties in q and u of 0.03% per spectral channel, consistent with the photon noise limit. Observations of fainter sources showed that the instrument could reach the

photon noise limit for observations in the slitless mode. For observations in slit, the uncertainties were still a factor of few above the photon noise limit, likely due to slit loss.

6.1 Introduction

Polarization is a fundamental property of light that is often left unmeasured by astronomical observations largely due to its difficulties and the lack of dedicated instrumentation. The greatest challenge for measuring polarization for astronomical sources is that, in many cases, the polarization signal of interest is much smaller than 1%, requiring a large number of photons to establish a significant detection: 10^6 photons for 0.1% precision. The problem is exacerbated in the infrared (IR) where the bright sky background further limits the sensitivity. Current IR polarimeters offer either no spectral information but good sensitivity for faint sources or medium resolving power ($R \approx 1000$) but only sensitive to bright sources. The examples of these instruments are the Long-slit Intermediate Resolution Infrared Spectrograph (LIRIS) on the William Herschel Telescope (Manchado et al., 2004) and the Infrared Camera and Spectrograph (IRCS) on Subaru Telescope (Tokunaga et al., 1998; Watanabe et al., 2018). Another IR spectropolarimeter available is SPectropolarimètre InfraROUge (SPIROU) (Donati et al., 2018) on Canada-France-Hawaii Telescope (CFHT) on Maunakea, which operates at high spectral resolution ($R \approx 75000$). The high resolution combined with the smaller telescope limits SPIROU to observe bright stellar targets.

In February 2017, we installed a polarization grating (PG; Escuti et al., 2006; Millar-Blanchaer et al., 2014; Packham et al., 2010) into the Wide-field InfraRed Camera (WIRC; Wilson et al., 2003) at the prime focus of the 200-inch Hale Telescope at Palomar Observatory (P200). The resulting low-resolution ($R \approx 100$) near-IR (1.1–1.8 μm , *JH* bands) spectropolarimeter was named WIRC+Pol, and its design, data reduction pipeline, and instrumental characteristics were discussed in details in Tinyanont et al. (2019d). The original instrument was designed such that there were four spectral traces on the detector for one source; each of the traces correspond to 0° , 90° , 45° , and 135° angles of linear polarization. As such, linear polarization could be measured in one shot by comparing fluxes in these four spectral traces in the different quadrants of the detector. Fig. 6.1 shows WIRC+Pol data with one source in the field of view.

During the commissioning of the instrument, we uncovered that the instrumental

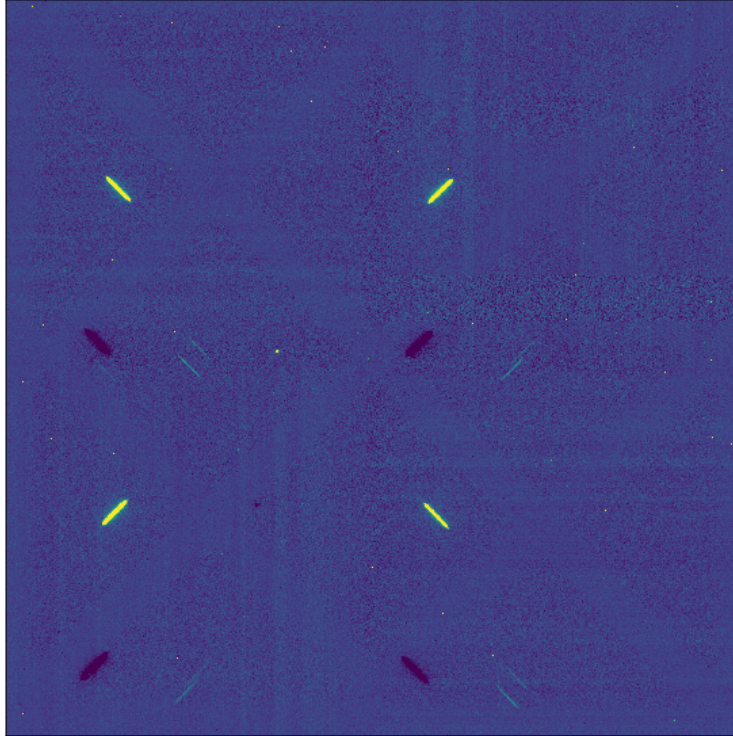


Figure 6.1: WIRC+Pol background-subtracted data with a bright standard star in the field of view. The four spectral traces probe four orthogonal angles of linear polarization. At the center of the four traces is the undispersed, zeroth order light of the star. Faint traces of a few background stars in the field of view could be seen.

systematics were strong, on the order of a few percent, and was highly dependent on the telescope pointing, as shown in Fig. 6 and 8 in Tinyanont et al. (2019d). The Hale telescope's polarization had been measured to be below 10 ppm (Wiktorowicz, 2009), so the systematics observed were from the instrument. This limited the instrument's accuracy, as it required an unpolarized standard star to be observed at a telescope pointing no further than about 10° from the source to obtain a systematic correction better than $\sim 1\%$. Moreover, the filter transmission profiles seen by the four traces were not the same. This was because the PG was installed upstream from the tilted broadband interference filter, resulting in the spectral traces entering the filter at different incident angles. The shifted transmission profile made wavelength alignment between the four traces difficult, and we had to rely on precisely aligning an atmospheric absorption feature in the spectra. Even then, the resulting polarization measurements still had significant spurious wavelength-dependent systematic in them (e.g., Fig. 6 left in Tinyanont et al., 2019d). It is crucial to note that these systematics only vary slowly with time (Fig. 8 in Tinyanont et al., 2019d), and could be removed using a polarimetric modulator. Lastly, the

focal plane mask of the instrument was designed to have an open area for slitless spectropolarimetry of bright sources, and three 3" circular holes to act as slits to limit sky background for faint sources. The circular design was chosen for two considerations: to reduce potential slit-induced polarization and to make it easier to manufacture on a traditional stainless steel substrate. We learned during commissioning that the circular slits required pointing and guiding precision beyond the telescope and instrument's capabilities, owing largely to the fact that P200 does not have a separate guider for prime-focus instruments, including WIRC.

In this work, we briefly describe the installation of a half-wave plate (HWP) modulator and a linear polarizer in front of WIRC+Pol, done in early 2019, and we will focus on the instrumental characterization post-upgrade. We will also discuss the novel slit design used to make a physically small rectangular slit required for the prime-focus instrument. §6.2 describes the upgrade and how the HWP allows us to measure and remove the systematics and §6.3 focuses on the new slit design. We explain our current observation technique with the HWP in §6.4. We show the instrumental characterization result, illustrating that the systematics have been removed for sources bright and faint in §6.5. We discuss the future characterization of the polarimetric efficiency and crosstalk, i.e., constructing the instrumental Mueller matrix for WIRC+Pol, using observations of polarized stars and observations of unpolarized stars with the linear polarizer in §6.6. Finally, we present our conclusions in §6.7.

6.2 Half-Wave Plate and Linear Polarizer Upgrades

The key hardware upgrade used to address the instrumental systematics from WIRC+Pol was the installation of a HWP and a LP in front of WIRC+Pol. WIRC+Pol only operated in the J and H bands and not in the thermal IR, which allowed the optics to be installed outside of the cryogenic dewar to reduce cost. Otherwise (in the K band and beyond), the IR emission from warm optics would contribute significantly to the background. The location of the optics in the $f/3.3$ converging beam presented strict requirements on the optics. The details of the optomechanical design of this upgrade will be presented in a future publication. Briefly, we installed a HWP and a LP on linear and rotation stages in front of WIRC, so that they could be inserted and removed from the beam, and rotated to an arbitrary angles independently. The optics sizes and placement were such that the 4.3' polarimetric field of view was not vignetted. The positions and rotation angles of the HWP and LP are stored in the header of images taken. The LP converts light from any source into

100% polarized light, which can be used to measure the polarimetric efficiency and crosstalk terms in the Mueller matrix of WIRC+Pol. This characterization work is deferred also for a future publication.

Polarization Calculation: Flux Ratio Method

We now demonstrate that calculating the normalized Stokes parameters using the observations at two different HWP angles effectively removes the systematic errors old WIRC+Pol suffered. We first note that a rotation of the HWP by θ rotates the incoming linear polarization angle by 2θ . As a result, by rotating the HWP to 0° , 45° , 22.5° , and 67.5° , we can cycle all four spectral traces through four different linear polarization angles, as visualized in Fig. 6.2. For simplicity, we consider q computed from the lower left (LL) and upper right (UR) traces, which, without the HWP, sample 0° and 45° , respectively. For a source with intrinsic polarization q and the total flux I , the observed fluxes at the HWP angle of 0° are

$$S_{LL,0}(\lambda) = (1 + q)I(\lambda)F_{LL}(\lambda)A_{t_1}(\lambda) \quad S_{UR,0}(\lambda) = (1 - q)I(\lambda)F_{UR}(\lambda)A_{t_1}(\lambda) \quad (6.1)$$

where F_i is the filter transmission profile seen by the i trace and A_{t_1} is the atmospheric transmissions at time t_1 . At the orthogonal HWP angle of 45° observed at a later time t_2 , the angle of polarization probed by the two traces flips:

$$S_{LL,45}(\lambda) = (1 - q)I(\lambda)F_{LL}(\lambda)A_{t_2}(\lambda) \quad S_{UR,45}(\lambda) = (1 + q)I(\lambda)F_{UR}(\lambda)A_{t_2}(\lambda) \quad (6.2)$$

In order to recover the intrinsic polarization q from these observations, we employ the flux ratio method presented in Zapatero Osorio et al. (2011), eq. (3) and (4). Following that formulation, we define a quantity

$$R_q^2 = \frac{S_{LL,0}/S_{UR,0}}{S_{LL,45}/S_{UR,45}} \quad (6.3)$$

$$= \frac{(1 + q)F_{LL}/(1 - q)F_{UR}}{(1 - q)F_{LL}/(1 + q)F_{UR}} \quad (6.4)$$

$$= \frac{(1 + q)^2}{(1 - q)^2} \quad (6.5)$$

The uncertainties of this quantity is simply a quadrature sum:

$$dR_q^2 = R_q^2 \sqrt{\left(\frac{dS_{LL,0}}{S_{LL,0}}\right)^2 + \left(\frac{dS_{LL,45}}{S_{LL,45}}\right)^2 + \left(\frac{dS_{UR,0}}{S_{UR,0}}\right)^2 + \left(\frac{dS_{UR,45}}{S_{UR,45}}\right)^2} \quad (6.6)$$

Then, q could be recovered by computing

$$\frac{R_q - 1}{R_q + 1} = q \quad (6.7)$$

The polarimetric uncertainty is

$$dq = \frac{dR_q^2}{(R_q + 1)^2 R_q^2} \quad (6.8)$$

Similar calculation can be done to obtain u .

Limitations of the Double Difference Method

Another primary method of computing polarization with a dual-beam polarimeter is to perform double difference. This is done by computing, for instance, q before and after modulating the HWP, then averaging the two. For WIRC+Pol, this would be

$$q_1 = \frac{S_{LL,0} - S_{UR,0}}{S_{LL,0} + S_{UR,0}} \quad (6.9)$$

$$q_2 = \frac{S_{UR,45} - S_{LL,45}}{S_{UR,45} + S_{LL,45}} \quad (6.10)$$

and the double differenced polarization is $q_{DD} = (q_1 + q_2)/2$. Writing down the full expressions for $S_{i,j}$, the previous quantity becomes

$$2q_{DD} = q_1 + q_2 \quad (6.11)$$

$$= \frac{(1+q)F_{LL} - (1-q)F_{UR}}{(1+q)F_{LL} + (1-q)F_{UR}} + \frac{(1+q)F_{UR} - (1-q)F_{LL}}{(1+q)F_{UR} + (1-q)F_{LL}} \quad (6.12)$$

This does not generally simplify to $q_{DD} = q$ due to the filter transmission difference between the four traces. This is also true for non-common path effects between the ordinary and extraordinary beams in a dual-beam polarimeter in general, and not just the filter transmission issue in our instrument.

One can alleviate this by computing the differencing first using the same trace at two HWP angles:

$$q_1 = \frac{S_{LL,0} - S_{LL,45}}{S_{LL,0} + S_{LL,45}} \quad (6.13)$$

$$q_2 = \frac{S_{UR,45} - S_{UR,0}}{S_{UR,45} + S_{UR,0}} \quad (6.14)$$

and the double differenced polarization is, instead, $q_{DD} = (q_1 + q_2)/2$. Writing down the full expressions for $S_{i,j}$, the previous quantity becomes

$$2q_{DD} = q_1 + q_2 \quad (6.15)$$

$$= \frac{(1+q)A_{t_1} - (1-q)A_{t_2}}{(1+q)A_{t_1} + (1-q)A_{t_2}} + \frac{(1+q)A_{t_2} - (1-q)A_{t_1}}{(1+q)A_{t_2} + (1-q)A_{t_1}} \quad (6.16)$$

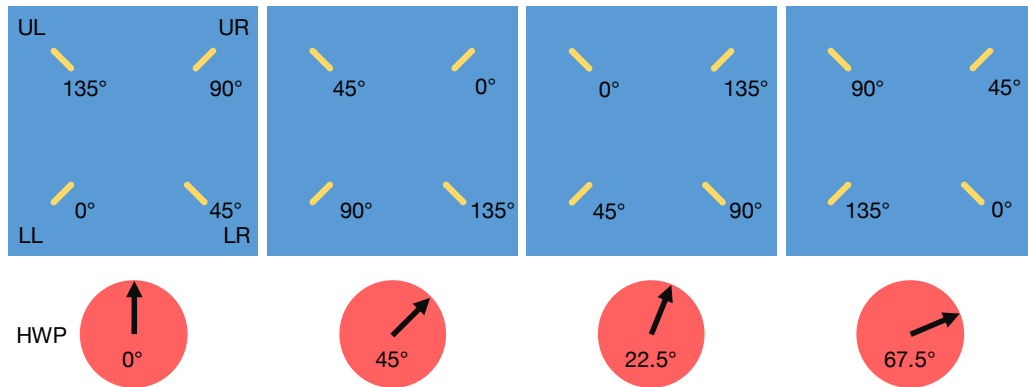


Figure 6.2: A schematic showing the four HWP angles used in a typical observing sequence: 0° , 45° , 22.5° , and 67.5° , and the corresponding linear polarization angle probed by the four spectral traces. At 0° , the linear polarization angle sampled by each of the four traces (Upper Left, Lower Right, Upper Right, and Lower Left) are as indicated on the figure. These angles were determined by observing twilight polarization (§4.2 in Tinyanont et al., 2019d).

This formulation works better. It could simplify to $q_{DD} = q$ if the atmospheric effects did not change between the two observations, i.e., $A_{t_1} = A_{t_2}$. Furthermore, both double differencing methods work for an unpolarized source $q = 0$. In summary, the flux ratio is more robust against non-common path effects and atmospheric changes during observations.

6.3 New Focal Plane Mask with Slit

Issues with Old Circular Slits

The focal plane mask of WIRC+Pol was also replaced in the 2019 upgrade. The first version of the mask was fabricated using the wire EDM process on stainless steel substrate. The shape of the slit mask could be seen in Fig. 2 (center) in Tinyanont et al. (2019d). In the center of the mask, there were three holes, $245 \mu\text{m}$ in diameter, corresponding to 3" on-sky at the $f/3.3$ focal plane of a 5.1-meter primary mirror. The decision to incorporate circular slits instead of a traditional rectangular slit was two-fold. First, circular slits in principle would reduce the amount of slit-induced polarization, as the symmetric shape of the slit would make the polarization created by the metal edge of the slit cancel out. Second, at the focal length at the prime focus, the physical size of the slit would be minute, making the fabrication difficult on aluminum or stainless steel.

From the first two years of operation with WIRC+Pol, we learned that the slit holes

presented challenges for telescope control, largely due to WIRC's lack of a separate guider camera to assist with pointing and guiding. First, the target acquisition was time consuming, and a slight offset from the center of the hole would result in large slit loss, which diminished the benefit gained from reduced sky background. Further, once the target was acquired, it was difficult to guide the telescope to keep the target inside the slit. This challenge was alleviated in cases where there were nearby sources in the slitless area of the focal plane, as we could guide on them instead. Lastly, it was difficult to dither the telescope to shuffle the source between three holes in order to perform sky subtraction, as there were no guider images to confirm the pointing. As a result, the slit holes remained largely unused, limiting WIRC+Pol's observations to relatively bright sources in the higher background slitless area.

New Slit Design

For the instrument upgrade, we also planned to install a new mask with a rectangular slit, in order to ease the operational requirements. The rectangular slit would retain the width of 3" to minimize slit loss provided the median seeing at Palomar of 1.5". The length of the slit was designed such that we would be able to observe a source in 2" seeing condition, in two dither positions in the slit that were 10σ apart, where σ is the standard deviation of the Gaussian (seeing limited) PSF of the source. This was to ensure that the source could be put into two different positions inside the slit so that an image observed with source at position A could use another image with source at position B as a background image for subtraction without the source self-subtracting. The slit length required to do this was 17". Thus, the physical size of the slit would be $245 \times 1388 \mu\text{m}$. The small physical size of the slit was difficult to archive precisely with the wire EDM fabrication used for the old slit mask. Instead, the new slit was manufactured on a silicon substrate using the electron-beam lithography (EBL) technique, which allowed for the slit to be cut into the substrate with high precision. The small rectangular piece of silicon with slit was then held in place by an aluminum mask (Fig. 6.3 top right).

Slit-Induced Polarization

The new rectangular slit would lack the symmetry of the old circular slit holes, and might induce polarization in the observed source. Calculation showed, however, that the expected slit-induced polarization should be very low. The slit-induced polarization is a function of slit width, depth (thickness of the slit in the direction

of light propagation), and the conductivity of the slit material. We estimated the slit-induced polarization using the relations derived by Slater (1959).

$$a_s = \frac{2}{b} \sqrt{\frac{\omega \epsilon_0}{2\sigma}} \left(1 - \left(\frac{n\lambda}{2b} \right)^2 \right)^{-1/2} \quad (6.17)$$

$$a_p = a_s \left(\frac{n\lambda}{2b} \right)^2 \quad (6.18)$$

$$P_{\text{slit}} = \frac{e^{-2a_p z} - e^{-2a_s z}}{e^{-2a_p z} + e^{-2a_s z}} \quad (6.19)$$

where b is the slit width, z is thickness, σ is the conductivity of the material, ω is the angular frequency of light, and λ is the wavelength. Parameters are in SI units, and ϵ_0 is the permittivity of free space. With the wire-EDM aluminum mask, the minimum thickness was $100 \mu\text{m}$, resulting in the expected slit polarization of order 1%. In the original design, this high potential of slit-induced polarization informed the decision to have circular holes to try to mitigate it. However, for the EBL silicon slit, the edge of the slit could be made to be only $9 \mu\text{m}$ thick. While the surface of the silicon slit was coated with metal to make it opaque, the bulk of the material was not a conductor, further reducing the expected slit-induced polarization. The upper limit of the slit-induced polarization from this design was 0.1%, calculated for aluminum's conductivity. (Equations above are only valid for conductors. For dielectric materials like silicon, Ismail (1986) showed that slit-induced polarization is lower.) Therefore, we concluded that the rectangular shape of the new slit would not create appreciable slit-induced polarization. We will show with data in §6.5 that this is the case.

Slit Dimensions Measurement

After the fabrication, we measured the dimensions of the slit using microscope images, and found that they were within a few microns of the specifications at $241.5 \times 1380 \mu\text{m}$. Fig. 6.3 (left) shows the image of the full slit that was installed in WIRC+Pol, along with (bottom right) a comparison between it and a reference aluminum slit of the same designed dimension. Note the vast improvement in the roughness of the edges, and how sharp the corners were on the silicon slit in comparison to the aluminum slit. The slit width is uniform, with $0.1 \mu\text{m}$ variation, across the length of the slit. Fig. 6.3 (top right) shows the silicon slit piece held in place in the new aluminum focal plane mask, which was installed in the focal mask mechanism inside WIRC.

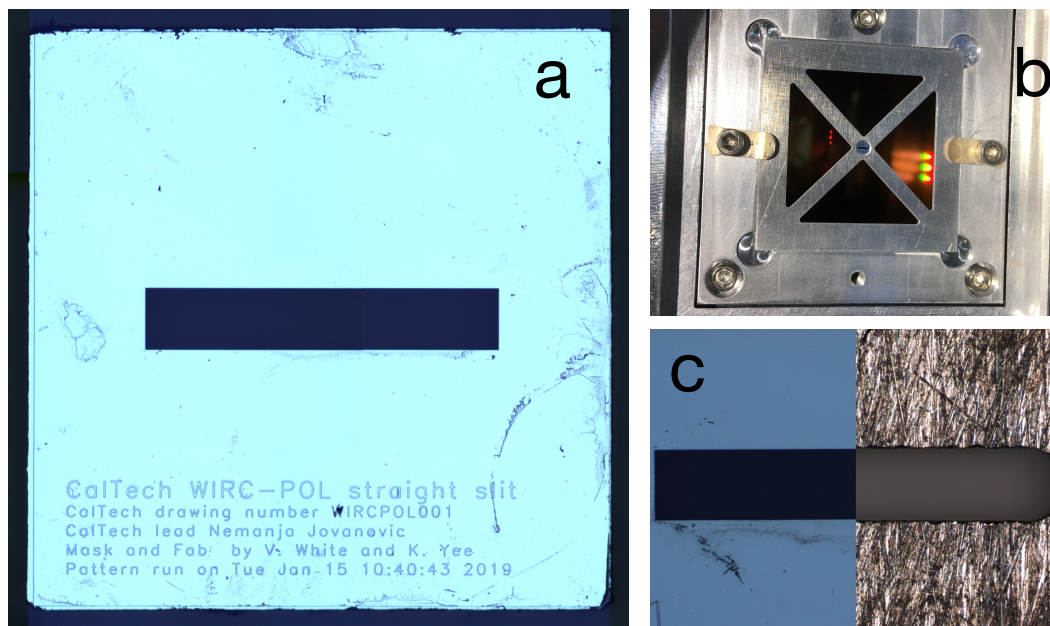


Figure 6.3: Left (a): image of the full silicon piece with the slit in the center. The dimensions were measured 241 by 1380 μm , within a few microns from designed dimensions. Top Right (b): the aluminum coated side of the slit installed in the new aluminum focal plane mask, both held in place in the focal plane mask mechanism inside WIRC. Bottom Right (c): the comparison between the silicon slit and the aluminum slit manufactured to the same specifications.

6.4 Observational Technique

Modulation Sequence

Along with the upgrade, the instrument control software was updated to take simple command scripts in order to automatize observing sequences. In order to remove the slowly varying systematics, we observed a source for up to 2 min in one HWP angle (this may include several individual frames or coadds), then we rotated the HWP such that the angle of polarization is rotated to an orthogonal angle (0° to 90° , and 45° to 135°). The 1–2 min limit were informed by the timescale at which the systematics changed. The overhead from the HWP rotation was minimal by design, approximately a second, which could be timed to coincide with detector readout in a future software upgrade. The systematics in WIRC+Pol prior to the HWP upgrade were not only a function of time, but also a strong function of the detector position of the source, with deviations of only $30''$ resulting in a 1% change in the systematics (Fig. 7 and §4.5 in Tinyanont et al., 2019d). With the HWP, we were able to remove the systematics for any given detector location. As a result, the strict guiding requirements for the old WIRC+Pol in order to assure that

sources and standard stars were observed at the same detector position no longer applied. As we will show in §6.5, the HWP modulator eliminated the need to observe an unpolarized standard star immediately before or after a science target to measure the instrumental polarization systematics, since the modulator allowed us to measure and remove those systematics for any source. Data also showed that the telescope polarization, and other instrumental polarization upstream of the waveplate was minimal. Observations have shown, however, that one might still need to observe either a polarized standard or an unpolarized standard with a linear polarizer to measure the angle of polarization zero point, and other Mueller matrix terms (polarization efficiency and crosstalk).

In-Slit Observation

For faint objects ($J \gtrsim 13$), objects in crowded fields, and extended sources, the observations are best performed with the source inside the slit to minimize sky background. The trade-off is that the sky background, while lower, is no longer spatially smooth as sky lines and focal plane mask features can be seen around the source trace. This requires image subtraction in order to remove the structured background. In order to do this, we observe a source in slit at a position “A” on one side of the slit at four HWP angles, then dither the telescope to move the source to the “B” position where the source is observed also at four HWP angles in the same rotation sequence. Due to the lack of a guiding camera, it is occasionally necessary to remove the PG and take a direct image of the slit to ensure that the source is still well centered. The images at the “B” position are then used as background images to be subtracted from images at the “A” positions at the same HWP angle. The WIRC+Pol data reduction pipeline (DRP), described in Tinyanont et al. (2019d) and publicly accessible at https://github.com/WIRC-Pol/wirc_drp, has been updated to reduce the new data with HWP. The pipeline applies the calculation described in §6.2 to compute double differencing q and u for each of the sets of four images with four HWP angles.

6.5 Calibrating Instrumental Polarization

In this section, we will demonstrate the instrument’s performance post-HWP upgrade, to show that the instrumental systematics have been effectively removed from WIRC+Pol. On the first night after the HWP installation, 2019 March 17 UT, we observed several unpolarized standard stars using the observation techniques described above. The list of unpolarized stars was obtained from Heiles (2000).

For these bright stars, the observations were obtained outside of the slit. The data were processed using the WIRC+Pol DRP, which applied dark subtraction and flat fielding, spectral extraction, and polarization calculation.

Bright Unpolarized Standard Star

Fig. 6.4 compares the measured q and u of an unpolarized star HD 65970 ($J = 7.689$) observed for 200 s using the HWP to that of an unpolarized star HD 109055 ($J = 8.731$) observed for 605 s without the HWP. The latter is the same observation presented in Fig. 6 top left in Tinyanont et al. (2019d) as the best zero polarization measurement with the old WIRC+Pol. The dashed lines mark zero polarization, expected for these stars, and the band around them indicate uncertainties expected from photon noise. The measurements are plotted with error bars computed from several sets of observations obtained for each source. It is evident that the strong, wavelength-dependent instrumental systematics, clearly visible in old WIRC+Pol data without the HWP, have been eliminated. The measurements for HD 65970 with the HWP are zero to within 1σ , and the uncertainties derived from the data are the same as what expected from photon noise.

Faint Source, Slitless

In addition to a bright unpolarized standard stars, we also observed several brown dwarfs (BD) and placed strict polarization upper limits on some of them. These observations were part of the BD and supernovae (SNe) spectropolarimetric surveys being conducted with WIRC+Pol. Fig. 6.5 (top) shows the normalized Stokes parameters q and u for a BD, 2MASS J18071593+5015316. The BD's magnitude was $J = 12.934$, and it was observed outside the slit for 80 min on 2019 July 16. The measured polarization was consistent with zero, and we noted that the uncertainties derived from the data (plotted as error bars) were 0.1%, consistent with the photon noise, which is marked by the red band on the plots. This result demonstrated that the background subtraction in the slitless mode was not biasing the measurement, even when the observations were background dominated.

Faint Source, In Slit

Lastly, Fig. 6.5 (bottom) shows the same plot for SN 2019ein, a Type Ia SN, observed at 14 days post-discovery (Burke et al., 2019; Tonry et al., 2019). The source was at $J \approx 14.5$ and the total exposure time was 84 min. At this phase, a typical SN Ia is not expected to be polarized (Wang and Wheeler, 2008), and our observations

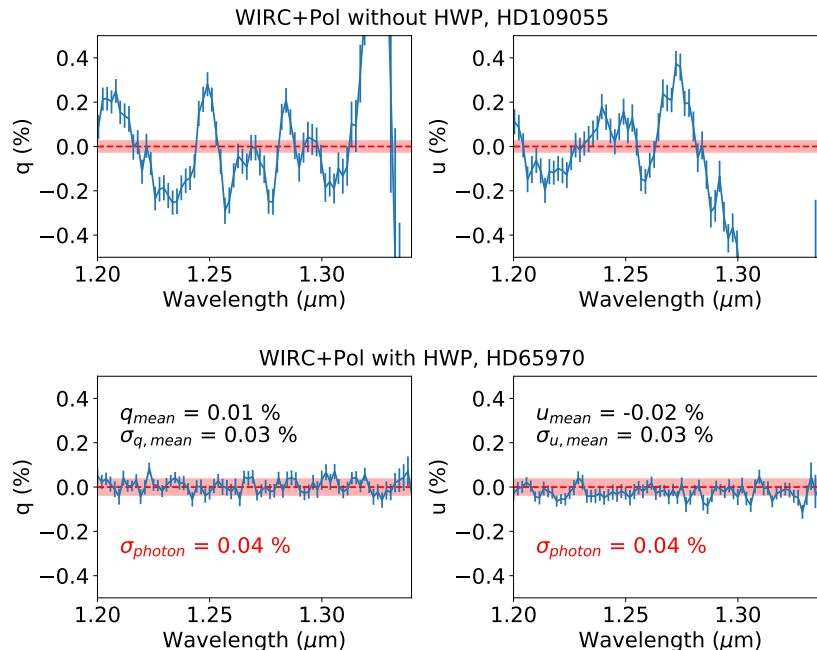


Figure 6.4: Top: normalized Stokes parameters q and u in percent of an unpolarized standard star HD 109055 observed with WIRC+Pol without the HWP. The dashed line at 0% indicates the expectation value, while the shaded region shows the expected uncertainties from photon noise. Bottom: the same of HD 65970 observed with WIRC+Pol with the HWP. The mean q and u and the associated uncertainties in the wavelength band shown are annotated on the plots. In this case, the measured q and u are within 1σ from zero, and the uncertainties are consistent with the photon noise, shown as the shaded region.

did not show significant departure from null polarization. We note that, unlike for the slitless observations, the uncertainties, which are the standard error of the mean derived from the series of exposures, are about a factor of four larger than what expected from photon noise. The cause of this was most likely the variable slit loss, resulting from the source moving slightly inside the slit between HWP rotations. This also demonstrates that the slit-induced polarization discussed in the prior section does not affect our measurements.

6.6 Future Characterizations

Angle of polarization zero point

The HWP installed in WIRC+Pol provides half-wave retardation over a large wavelength range but the fast axis is not wavelength independent. The angle of polarization zero point as a function of wavelength needs to be determined by observing both stars with known polarization and unpolarized standard stars with the LP. This

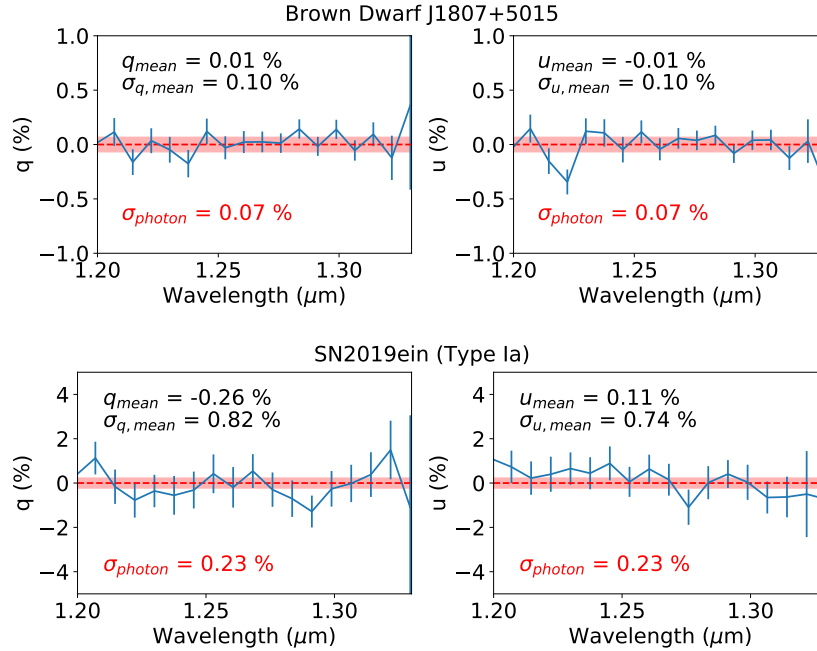


Figure 6.5: Top: Normalized Stokes parameters q (left) and u (right) of a brown dwarf J1807+5015, $J = 12.934$, observed for 80 min. The dashed lines mark zero polarization and the red bands are the expected photon noise. The brown dwarf was observed outside the slit. Bottom: Same for SN 2019ein, a thermonuclear Type Ia SN, which typically has zero polarization at this phase. The SN was at $J \approx 14.5$, and it was observed in the slit for 84 min.

measurement could be done with existing data.

The Mueller Matrix

The instrument's Mueller matrix, with circular polarization terms omitted, is the matrix in this following equation

$$\begin{bmatrix} 1 \\ q_{\text{obs}} \\ u_{\text{obs}} \end{bmatrix} = \begin{bmatrix} 1 & 0 & 0 \\ q_{\text{IP}} & \eta_q & \chi_{uq} \\ u_{\text{IP}} & \chi_{qu} & \eta_u \end{bmatrix} \begin{bmatrix} 1 \\ q \\ u \end{bmatrix} \quad (6.20)$$

It relates the intrinsic normalized Stokes vector to the observed one.

With the observations of unpolarized sources shown in the last section, we have already demonstrated that if $q = u = 0$, then the observed polarizations are also $q_{\text{obs}} = u_{\text{obs}} = 0$ to within the measured uncertainties. Hence, the upper limits of the instrumental polarization terms are $q_{\text{IP}}, u_{\text{IP}} < 0.03\%$. To measure the other terms in the Mueller matrix, namely the polarization efficiencies (η) and crosstalks (χ), we need observations of polarized standard stars with known, non-zero q and u ,

as functions of wavelength in the literature. The issue is that spectropolarimetric measurements of standard stars in the near-IR, unlike the broadband measurements, are rare. Therefore, we plan to use the combination of (i) Serkowski’s law fitted to broadband measurements presented in Whittet et al. (1992) and (ii) unpolarized standard stars observed with the LP in the beam. These observations have been obtained and we are reducing the data to measure the remaining terms in the Mueller matrix of WIRC+Pol and determine whether they are constant or are functions of telescope pointing.

6.7 Conclusion

WIRC+Pol is a low-resolution ($R \approx 100$), near-infrared (1.1–1.8 μm , *JH* bands) spectropolarimeter. The instrument employs a liquid-crystal-polymer-based PG to perform polarimetric beam splitting and spectral dispersion simultaneously. The instrument produces four spectral traces on the detector, probing 0° , 90° , 45° , and 135° angles of polarization at the same time, allowing it to measure Stokes parameters q and u in one shot. We found from commissioning data from the instrument in 2017–2018 that the polarimetric systematics from comparing fluxes in different traces across the detector were significant (few %) and were slowly changing with time. Thus, they were difficult to remove. In March 2019, a HWP and a LP were installed in front of the instrument, allowing us to modulate the angle of polarization probed by each of the four spectral traces. As a result, the Stokes parameters could be computed using the flux ratio method described earlier, which could measure and remove systematics due to non-common path and atmospheric effects. We verified the performance of the HWP by showing that the systematics were indeed removed, both for bright standard stars and faint sources. The polarimetric uncertainties for slitless observations now seem to be only photon noise limited. In addition to the HWP/LP, a new focal plane mask with a slit manufactured with EBL was also installed, allowing WIRC+Pol to more easily observe faint targets with reduced background. We are developing efficient observational guidelines for slit observations to reduce overhead from target acquisition and dithering. For observations in slit, the polarimetric uncertainties are a factor of a few larger than the photon noise, likely from variable slit loss. Future instrumental calibrations include (i) measuring the angle of polarization zero point as a function of wavelength and (ii) measuring the polarimetric efficiency and crosstalk, the remaining possibly non-zero terms of the Mueller matrix of WIRC+Pol. Scientific observations with WIRC+Pol has commenced with a large brown dwarf spectropolarimetric survey and a nearby

supernovae survey ongoing. First results from these surveys are expected later this year.

Chapter 7

**THE FIRST INFRARED SPECTROPOLARIMETRIC
DETECTION OF INTRINSIC POLARIZATION FROM A
CORE-COLLAPSE SUPERNOVA**

Tinyanont, S. et al. (2020). “The First Infrared Spectropolarimetric Detection of Intrinsic Polarization from a Core-Collapse Supernova”. Submitted.

Samaporn Tinyanont¹ Maxwell Millar-Blanchaer¹ Mansi M Kasliwal¹ Dimitri
Mawet^{1,2} Douglas C Leonard³ Mattia Bulla⁴ Kishalay De¹ Nemanja Jovanovic¹
Matthew Hankins¹ Gautam Vasisht² Eugene Serabyn²

¹Division of Physics, Mathematics and Astronomy, California Institute of Technology, 1200 E. California Blvd., Pasadena, CA 91125, USA ²Jet Propulsion Laboratory, California Institute of Technology, 4800 Oak Grove Dr, Pasadena, CA 91109, USA ³Department of Astronomy, San Diego State University, San Diego, CA 92182, USA ⁴Nordita, KTH Royal Institute of Technology and Stockholm University, Roslagstullsbacken 23, 106 91 Stockholm, Sweden

Abstract

We present the first infrared (IR) spectropolarimetric detection of a core-collapse supernova (CCSN). The measurement is enabled by the new highly sensitive WIRC+Pol instrument at Palomar Observatory, that can observe CCSNe ($M = -17$ mags) out to 20 Mpc to $\sim 0.1\%$ precision. IR spectropolarimetry is less affected than optical by dust scattering in the circumstellar and interstellar media, thereby providing a more unbiased probe of the intrinsic geometry of the SN ejecta. SN 2018hna, a blue supergiant explosion (SN 1987A-like), shows $2.0 \pm 0.3\%$ continuum polarization in the J band oriented at $\sim 160^\circ$ on-sky at 180 d after the explosion. Assuming prolate geometry like in SN 1987A, we infer an ejecta axis ratio of < 0.33 with the axis of symmetry pointing at 70° position angle. The axis ratio is similar to that of SN 1987A if it were observed edge-on, suggesting that they may share similar intrinsic geometry. We also observe other one core-collapse and two thermonuclear SNe in the J band. SN 2020oi, a stripped-envelope Type Ic SN in Messier 100 has $p = 0.37 \pm 0.09\%$ at peak light, indicative of either a 10% asymmetry or host interstellar polarization. The SNe Ia, 2019ein and 2020ue have $p < 0.33\%$ and $< 1.08\%$ near peak light, indicative of asymmetries of less than 10% and 20%, respectively.

7.1 Introduction

The shape of an astronomical explosion embeds crucial information about the underlying mechanism and the surrounding environment. A massive star ($\gtrsim 8 M_{\odot}$) dies in a core-collapse supernova (CCSN) when its nuclear fusion fuel is exhausted and its core collapses. The physical processes that launch a shock from the collapsed core, disrupting the star, remains an open question (Langer, 2012; Smartt, 2009; Woosley and Heger, 2015). Hydrodynamical simulations have only begun to readily produce explosions in the past few years when asymmetric three-dimensional processes are included (Burrows et al., 2019; Janka, 2012). The measurements of CCSN ejecta’s shape allow us to test these models. For Type Ia SNe, which are thermonuclear explosions of white dwarfs, the progenitor systems and detonation mechanisms also remain debated (Branch and Wheeler, 2017; Maoz et al., 2014), despite their use as standardizable candles to detect the accelerated expansion of the universe (Perlmutter et al., 1999; Riess et al., 1998). The ejecta shape can also distinguish among competing models (Cikota et al., 2019; Yang et al., 2019). Until the next SN in the Galaxy or Magellanic Clouds with spatially resolved observations, spectropolarimetry remains a unique tool to directly measure the SN ejecta shape in the plane of the sky. We present the first spectropolarimetric measurements of SNe in the near-infrared (near-IR), with data obtained on four SNe: 2018hna (87A-like), 2019ein (Ia), 2020oi (Ic), and 2020ue (Ia).

Optical and near-IR light from a SN gets polarized primarily by electron scattering. The shape of the ionized ejecta determines the amount and orientation of the polarization signal; more asymmetric ejecta generally yield more polarization. A review by Wang and Wheeler (2008) of optical polarimetry of SNe found that CCSNe are significantly polarized at the $\sim 1\%$ level at the epoch when the inner ejecta becomes visible, indicating a global asymmetry in the core-collapse mechanism. SNe Ia, on the other hand, have small continuum polarization with significant metal-line (silicon and calcium) polarization, indicating globally symmetric ejecta with metal-rich clumps. These measurements need to account for the polarization induced by dust scattering along the line of sight, both from the circumstellar medium around the SN (Nagao et al., 2017, 2018) and in the interstellar medium in the host galaxy and the Milky Way (Voshchinnikov, 2012). Measuring these intervening effects is difficult and often leads to inaccurate measurements of the polarization intrinsic to the SN. Near-IR spectropolarimetry is less susceptible than optical to dust-induced polarization contamination by a factor of 2–4 (J and H bands compared to V band; Whittet et al., 1992) Furthermore, the near-IR is more free of atomic lines (Pinto and Eastman,

2000), allowing for more accurate measurements of continuum polarization, and thus the global geometry of the SN ejecta. Until now, Near-IR spectropolarimetry has not been possible for most SNe because of the lack of sensitivity.

WIRC+Pol is a near-IR spectropolarimeter on the 200-inch Hale Telescope at Palomar Observatory, starting science operation in March 2019. It offers low spectral resolution ($R \sim 100$) with high throughput ($> 90\%$) as it leverages a novel liquid crystal based polarization grating (PG; Escuti et al., 2006; Millar-Blanchaer et al., 2014). WIRC+Pol can observe sources as faint as $J \sim 14.5$ to a polarimetric accuracy (1σ) of $\sim 0.1\%$ per spectral channel in less than two hours; much fainter than possible with IR spectropolarimeters previously available (Manchado et al., 2004; Watanabe et al., 2018). WIRC+Pol operates in the J and H bands, which cover the strong hydrogen Paschen- β ($1.282 \mu\text{m}$) line for Type II SNe and a continuum region for all SNe. Details of the instrument and the data reduction pipeline can be found in Tinyanont et al. (2019a) and Tinyanont et al. (2019c). Since the beginning of science operation, we have obtained IR spectropolarimetric data of all SNe with $J < 14.5$ visible from Palomar. Four SNe satisfied this criterion between March 2019 and March 2020, and we report their IR spectropolarimetric measurements here. In §7.2 we provide details of the observations, data reduction, and polarimetric calibrations. We analyze and discuss our spectropolarimetric results in §7.3. We provide a summary and conclusion in §7.4.

7.2 Observations and Data Reduction

Infrared Spectropolarimetry Observations

All observations are conducted with the WIRC+Pol instrument at Palomar Observatory. The instrument has all transmissive optics with a half-wave plate (HWP) in front of the cryostat, a focal plane mask at the telescope focal point inside the cryostat, and the PG in one of the filter wheels situated in the collimated beam inside the instrument. The detector on the focal plane is a HAWAII-2 detector. See Tinyanont et al. (2019a) and Tinyanont et al. (2019c) for more information about the instrument. We observe all SNe in two positions (“AB”) inside the slit for background subtraction; each position at HWP angles of 0° , 45° , 22.5° , and 67.5° . The exposure time is chosen to minimize sky background change between “A” and “B” observations, typically 60 s. We repeat the sequence for one hour of total exposure time to achieve $\sigma_{q,u} \sim 0.1\%$ for a $J = 14$ source; our observations yield a factor of few worse uncertainties. We observed four nearby SNe with WIRC+Pol: SNe 2018hna (87A-like), 2019ein (Ia), 2020oi (Ic), and 2020ue (Ia). Each target was accompanied

Table 7.1: Supernovae observed with WIRC+Pol

Name	Type	Host	d^*	A_J^\dagger	Obs. Date	Epoch from Discovery	Epoch from Peak	Exp. Time
SN			(Mpc)	(mag)	(UT)	(day)	(day)	(min)
2018hna	II-pec	UGC 7534	13 ± 3	0.009	2019-04-20	+180	+95	96
2019ein	Ia	NGC 5353	28 ± 6	0.009	2019-05-14	+13	-2	84
2020oi	Ic	M100	16 ± 3	0.019	2020-01-19	+12	0	72
2020ue	Ia	NGC 4636	16 ± 3	0.020	2020-02-04	+23	+9	56

*NED Average † Schlafly and Finkbeiner (2011)

by at least one polarized standard observation. Table 7.1 summarizes the sample, including their host, distance, Galactic extinction, observed epoch, exposure times, observing conditions, and references. Fig. 7.2 shows optical photometry of our four SNe from the public data stream of the Zwicky Transient Facility (ZTF; Bellm et al., 2019) in the r and g bands, and near-IR J -band photometry from the Gattini-IR telescope (De et al., 2020). These light curves are used to determine the phase of our spectropolarimetric observations.

SN 2018hna, Type II (SN 1987A-like), was discovered on 2018 Oct 22 (UT used throughout; Itagaki, 2018) and classified as SN II Leadbeater, 2018. The slow photometric evolution revealed that SN 2018hna is a rare SN 1987A-like SN. The Galactic extinction for this SN was $A_J = 0.009$ and the reddening was $E(B - V)_{MW} = 0.01$ mags (Schlafly and Finkbeiner, 2011). Singh et al. (2019) reported optical photometry and spectroscopy and constrained the explosion date and the V -band maximum light to 2018 Oct 19.8 and 2019 Jan 15.3, respectively. They detected shock-cooling emission from the early light curve, directly constraining the progenitor to be a $R \sim 50 R_\odot$ BSG. They also reported optical spectroscopy showing no Na I D absorption, confirming the minimal host/Galactic extinction. From their Fig. 1, SN 2018hna became optically thin in the J band at ~ 125 d post-explosion, while our observation was at 182 d post-explosion. This allows us to estimate the continuum optical depth at the epoch of our observations. Optical depth in the nebular phase varies as $\tau(t) = (t_0/t)^2$, where t_0 is the epoch where the ejecta has $\tau = 1$. Hence, the optical depth at our WIRC+Pol observation is $(125/182)^2 = 0.47$. We use this number to convert the observed polarization of this SN to its ejecta geometry. The axis ratio is highly dependent on the optical depth at this epoch, and we incorporate an uncertainty of ± 0.1 into our error calculation.

SN 1987A remains one of the best polarimetrically observed SNe to date. Jeffery (1991) summarized all spectropolarimetric data on SN 1987A with a homogeneous ISP subtraction. It was also the only SN with near-IR polarimetry, albeit broadband

(Allen et al., 1987; Bailey, 1988; West et al., 1987). These measurements provide a direct comparison to our data.

We observed SN 2018hna on 2019 Apr 20, 95 days from the maximum brightness, in median seeing conditions. Unlike other SNe, the individual exposure time was 120 s, and the A and B frames in the dither were taken almost 10 min apart. As a result, this data set required additional background-subtraction step as simple AB subtractions left significant background residual. We will discuss this in §7.2 and B.1. In addition to the WIRC+Pol observation, we also obtained IR spectrum of SN 2018hna using the Near-InfraRed Echellette Spectrograph (NIREs) on the 10-m Keck telescope on 2019 May 24.

SN 2019ein, Type Ia, was discovered on 2019 May 01 by the Asteroid Terrestrial-impact Last Alert System (ATLAS) SN survey (Tonry et al., 2019). Early spectroscopy taken on 2019 May 03 showed a high-velocity silicon feature at ~ 30000 km s $^{-1}$ (Burke et al., 2019). Such a feature was suggestive of an asymmetric metal-rich outflow, triggering our spectropolarimetric follow-up. The Galactic extinction for this SN was $A_J = 0.009$ and the reddening was $E(B - V)_{\text{MW}} = 0.011$ mags (Schlafly and Finkbeiner, 2011). The SN was observed with WIRC+Pol on 2019 May 14, 13 days after the first detection. We also obtained near-IR spectrum of SN 2019ein with Keck/NIREs on 2019 May 24. The polarized standard stars observed were Schulte 10 and 14. The high-velocity metal features had disappeared by that epoch, indicating that the photosphere might have overrun the metal-rich clump responsible for the feature (Pellegrino et al., 2020).

SN 2020oi, Type Ic, was discovered by ZTF through the event broker Automatic Learning for the Rapid Classification of Events (ALeRCE; <http://alerce.science/>) on 2020 Jan 07 (Forster et al., 2020) using the public data stream of ZTF (<https://ztf.uw.edu/alerts/public/>). It was classified as SN Ic on 2020 Jan 09 (Siebert et al., 2020). The Galactic extinction for this SN was $A_J = 0.019$ and the reddening was $E(B - V)_{\text{MW}} = 0.023$ mags (Schlafly and Finkbeiner, 2011). Despite its low Galactic extinction, the SN was close to the core of the galaxy and may have significant host extinction. A study of this SN based on ZTF optical light curve and spectroscopy will be presented in Horesh (2020).

We determined the host extinction from measuring the equivalent width of the Na I D absorption from the optical spectrum of SN 2020oi (described below). The equivalent width was 0.3 and 0.55 Å in the two doublets, which gives $E(B - V)_{\text{host}} = 0.136$ mags. This gives an ISP upper limit, $p_{\text{ISP,max}} \lesssim 9 \times E(B - V)$ (Voshchinnikov,

2012) of 1.2% in the V band. The ISP upper limit in the J band is 0.5% using Serkowski law (Serkowski et al., 1975). We observed SN 2020oi with WIRC+Pol on 2020 Jan 19, 12 d post-discovery and at peak. The polarized standard star observed was HD 279652. The seeing was $\sim 1''$, above average at Palomar.

SN 2020ue, Type Ia, was discovered on 2020 Jan 12 (Itagaki, 2018) and classified as a normal SN Ia (Kawabata, 2020). We observed SN 2020ue with WIRC+Pol on 2020 Feb 4, 23 d post-discovery and approximately 9 d post-maximum. The Galactic extinction for this SN was $A_J = 0.020$ and the reddening was $E(B - V)_{MW} = 0.025$ mags (Schlafly and Finkbeiner, 2011). The observing conditions were poor with $\sim 3''$ seeing, rendering the SNR inadequate even after 56 min on a $J \sim 13.5$ source.

Data Reduction

Calibrations and Background Subtraction

We use the WIRC+Pol Data Reduction Pipeline (DRP; https://github.com/WIRC-Pol/wirc_drp) to reduce our data. The detailed data reduction steps for WIRC+Pol data with HWP are in Tinyanont et al. (2019b). We first perform dark subtraction and flat fielding using appropriate calibration images taken on the same night. We then perform background subtraction, which is crucial because imperfect subtraction can bias polarization measurements. We observe all SNe at two dither positions along the slit, allowing us to use the “B” position image to subtract background off of the corresponding “A” image. We scale the background frame to match its median to that of the science frame to account for the constantly changing IR sky background. Observations of SN 2018hna have the single frame exposure time of 120 s, instead of 60 s used in later observations. As a result, the “A” and “B” observations at the same HWP angle are more than 8 minutes apart and the sky line emissions evolve noticeably between the two frames. In this case, we remove the background by fitting the profile across the slit with a Gaussian-smoothed piece-wise function that describes the slit transmission. In Appendix B.1, we show measurements using synthetic images to verify that the two background-subtraction methods yield similar results and that they do not introduce polarimetric biases.

Spectral Extraction

There are four spectral traces per source in WIRC+Pol data, tracing the polarization angles of 0° , 45° , 90° , and 135° . A HWP rotation of θ introduces a 2θ rotation in the polarization angle probed by these traces; this modulation allows us to measure

and remove instrumental polarization. The DRP rotates the spectral traces to align with the pixel grid using OpenCV bicubic interpolation. The spectra are extracted using the optimal extraction algorithm (Horne, 1986). The extraction range is set to $\pm 3\sigma$ of the spatial profile of the spectrum. We bin the spectra using a 5-pixel window to match the seeing limit; this results in $0.01 \mu\text{m}$ spectral resolution and $R = \lambda/\Delta\lambda = 120$ resolving power in the J band.

Polarization Calculation and Calibration

From the extracted flux spectra, we compute the normalized Stokes parameters q and u . We use the flux ratio method as it is the most robust against the non-common path systematics and the atmospheric changes (see §2.1 in Tinyanont et al., 2019b). Consider two observations at the HWP angles 0° and 45° , the flux in the upper left, lower right, upper right, lower left traces are noted as $S_{UL,LR,UR,LL}$. We compute

$$R_q^2 = \frac{S_{LL,0}/S_{UR,0}}{S_{LL,45}/S_{UR,45}} \quad \text{and} \quad q = \frac{R_q - 1}{R_q + 1} \quad (7.1)$$

The uncertainties of this quantity is a quadrature sum:

$$dR_q^2 = R_q^2 \sqrt{\left(\frac{dS_{LL,0}}{S_{LL,0}}\right)^2 + \left(\frac{dS_{LL,45}}{S_{LL,45}}\right)^2 + \left(\frac{dS_{UR,0}}{S_{UR,0}}\right)^2 + \left(\frac{dS_{UR,45}}{S_{UR,45}}\right)^2} \quad (7.2)$$

Then,

$$(7.3)$$

The polarimetric uncertainty is

$$dq = \frac{dR_q^2}{(R_q + 1)^2 R_q^2} \quad (7.4)$$

Similar calculation can be done on the upper left and lower right traces to obtain u . For the HWP angles 22.5° and 67.5° , the upper left and lower right traces now measure q and lower left/upper right u . WIRC+Pol has wavelength-dependent polarimetric efficiency and angle of polarization zero point, which can be calibrated with observations of polarized standard stars (§ B.2). From the Stokes parameters, we compute the fractional polarization $p = \sqrt{q^2 + u^2}$ and the angle of polarization $\theta = 0.5 \tan^{-1}(u/q)$. Note that p is positively biased because uncertainties in q and u sum positively. In this paper, we use the ‘‘debiased’’ fractional polarization, $p^* = \sqrt{p^2 - \sigma_p^2}$. (See Jensen-Clem et al., 2016 for the distribution of p .) We did not attempt to estimate and subtract the ISP because the expected ISP was smaller

than $\sim 0.1\%$, below our uncertainties in most cases. For SN 2020oi, we discussed above that the 0.4% broadband polarization observed may arise from the ISP in the host galaxy. Fig. 7.1 shows (i) q and u spectra, (ii) the q - u plane with (wavelength color-coded), and (iii) p and θ spectra of SNe 2018hna, 2019ein, 2020oi, and 2020ue. Finally, broadband polarization can be computed from spectropolarimetry by computing a ratio

$$q_{\text{broadband}} = \frac{\sum_{\lambda} q(\lambda) I(\lambda)}{\sum_{\lambda} I(\lambda)} \quad (7.5)$$

where $q(\lambda)$ and $I(\lambda)$ are q and flux spectra, respectively. We perform the same calculation for u , then compute $p_{\text{broadband}} = \sqrt{q_{\text{broadband}}^2 + u_{\text{broadband}}^2}$ along with the associated uncertainty. If $p_{\text{broadband}} < 3\sigma_{p,\text{broadband}}$, then we report 3σ upper limits.

Optical and Near-Infrared Photometry and Spectroscopy

To constrain the phase of our IR spectropolarimetric observations, we obtained optical and near-IR light curves of the SNe in our sample from the public data stream of ZTF and the data from Gattini-IR, respectively. Fig. 7.2 shows the light curves of the four SNe. The public ZTF photometry can be obtained via ALerCE, and the details of the data acquisition and image differencing photometry for ZTF can be found in Bellm et al. (2019) and Masci et al. (2019). Gattini-IR is a wide-field ($5^{\circ} \times 5^{\circ}$) J -band imager on a 30-cm telescope at Palomar Observatory (De et al., 2020). Gattini-IR surveys the whole sky visible from Palomar to the 5σ depth of 15.7 AB mag (14.8 Vega mag) every two nights. SNe 2018hna and 2020ue were detected in the Gattini-IR data. For SN 2020ue, the only data that existed are from Gattini-IR because it falls into a gap between ZTF CCDs. The peak epoch of each SN is estimated from these light curves.

In addition, SNe 2018hna and 2019ein were observed spectroscopically in the near-IR with Keck/NIRES both on 2019 May 24 using a typical ABBA dither for background subtraction. The total exposure time for each SN was 300 sec per dither position (1200 sec total). Telluric standard stars of spectral type A0V (HIP 56147 for SN 2018hna and HIP 61534 for SN 2019ein) were observed either before or after the observations of the SN. The data were flat fielded and extracted using `spectool` (Cushing et al., 2004) and the telluric calibration was performed using `xtellcor` (Vacca et al., 2003). The optical spectrum of SN 2020oi was obtained on 2020 Mar 22 using the Low-Resolution Imaging Spectrometer (LRIS) instrument on Keck telescope (Oke et al., 1995), and calibrated using a standard IRAF pipeline.

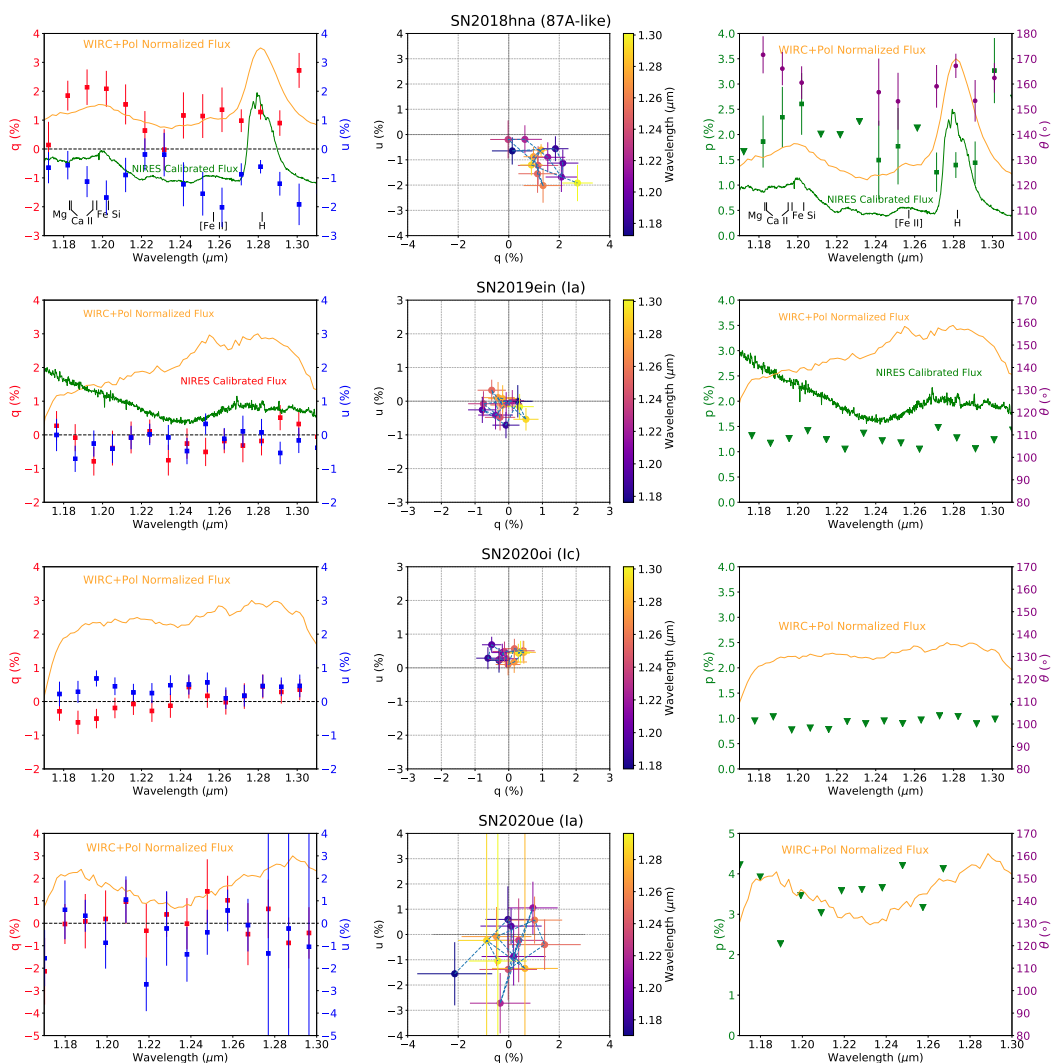


Figure 7.1: J -band IR spectropolarimetry of SNe 2018hna (87A-like), 2019ein (Ia), 2020oi (Ic), and 2020ue (Ia), from top to bottom. The left panels show q (red) and u (blue) spectra. The normalized, uncalibrated flux spectrum is plotted (yellow) to show spectral features. Calibrated NIRES spectrum is plotted for SNe 2018hna and 2019ein with line identifications. The middle panels are the q - u plane color-coded by wavelengths. The right panels show the debiased degree (p ; green square) and angle (θ ; purple circle) of polarization. For points with no significant detection (either $q < 3\sigma_q$ or $u < 3\sigma_u$), we plot $3\sigma_p$ upper limits (triangle), and we do not plot θ .

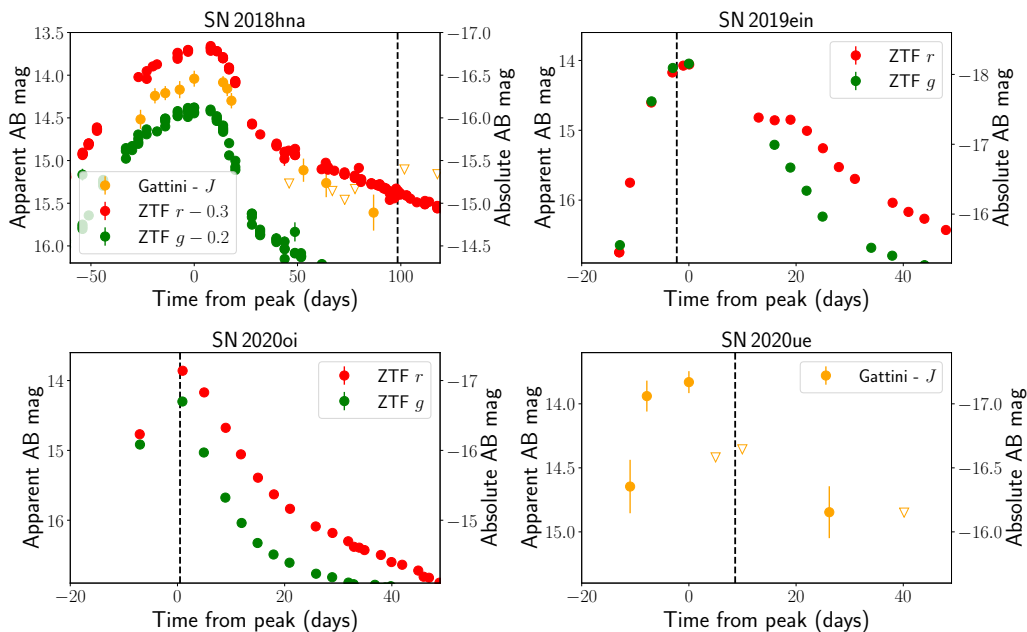


Figure 7.2: Optical (gr bands) and near-IR (J band) photometry of SNe 2018hna, 2019ein, 2020oi, and 2020ue. The optical photometry is from ZTF public data stream (Bellm et al., 2019; Masci et al., 2019) while near-IR photometry is from Gattini-IR (De et al., 2020). The epoch of spectropolarimetric observation of each SN is marked with a black dashed line. The x -axis indicates time from the peak of the light curve. The public ZTF photometry of SN 2018hna has been presented in Singh et al. (2019) and of SN 2020oi is presented in Horesh (2020).

7.3 Results and Discussions

SN 2018hna The IR spectropolarimetry of SN 2018hna is shown in Fig. 7.1 (top) along with flux measurements (§7.2). SN 2018hna shows significant ($> 4\sigma$) polarization of typically $2.0 \pm 0.7\%$ per spectral channel at $1.18\text{--}1.21\ \mu\text{m}$ and $1.24\text{--}1.27\ \mu\text{m}$ that cannot be attributed to ISP (§7.2). Spectral lines corresponding to these ranges are shown in Fig. 7.1 (top). The region between $1.21\text{--}1.24\ \mu\text{m}$ suffers most from sky emission, and is less than 2% polarized (3σ). Combining all these spectral channels together results in $2.0 \pm 0.3\%$ continuum polarization. The incomplete depolarization in the Paschen- β line ($1.28\ \mu\text{m}$) indicates that the ejecta are optically thin as a complete depolarization is caused by multiple scattering. This conclusion is supported by the absence of the P-Cygni absorption in the blue wing of the spectral line. The polarization is significantly enhanced to 3.5% redward of the Paschen- β line. This is likely because in a homologously expanding SN ejecta, Paschen- β photons are redshifted in the scatterer’s frame and are scattered redward in the observer’s frame, enhancing the degree of polarization in the red wing of

the line (Dessart and Hillier, 2011). If the polarization were caused by optically thick clumps, the angle of polarization would, in most cases, vary across spectral lines (Wang and Wheeler, 2008). However, the angle of polarization is consistently $150^\circ\text{--}170^\circ$, indicating that the observed polarization is created by the global geometry of the ejecta. Since the SN is in the optically thin phase, the polarization is probing the inner part of the ejecta most affected by the core collapse mechanism.

We compare the continuum polarization of SN 2018hna with models of (Hoflich, 1991) to constrain its ejecta shape. The electron scattering optical depth of SN 2018hna during our observation is $\tau \sim 0.5 \pm 0.1$ (§7.2), meaning that our observed polarization is 74% that of the maximum polarization (i.e., $\tau = 1$; Figs. 1 and 5 in (Hoflich, 1991)) Given a constant asymmetry with phase in a homologous expansion, SN 2018hna’s polarization would have peaked at $\sim 2.7 \pm 0.4\%$. If the ejecta are oblate, Fig. 4 in Hoflich (1991) shows that the axis ratio required to explain the observed polarization is 0.57 ± 0.11 where we account for both uncertainty in the polarization and optical depth. However, if the ejecta are prolate (like SN 1987A), the polarization is 40% smaller than that from the oblate ejecta of the same axis ratio (true for $\tau < 1$ according to Fig. 1 and 5 in Hoflich (1991)). Taking this into account, we get that the maximum axis ratio for the prolate ejecta is 0.33 ± 0.16 . We note that the model is valid for axis ratio > 0.2 . These numbers are the axis ratio of the ejecta projected on the plane of sky.

We now compare the geometry of SN 2018hna’s ejecta to that of SN 1987A. Fig. 7.3 (top) compares SN 2018hna’s IR spectropolarimetry to SN 1987A’s broadband IR polarimetry and optical spectropolarimetry. Optical spectropolarimetry of SN 1987A shows strong wavelength dependence over spectral lines. SN 1987A’s broadband polarization peaks at 1.5% and 1% in the *V* and *R* bands, corresponding to a projected axis ratio of 0.6–0.7 (prolate) The angle of polarization remains constant at around 110° , throughout its evolution (Jeffery, 1991). Images from the *Hubble Space Telescope* more than 10 years post-explosion (Fig. 7.4 right and Fig. 1 in Wang et al., 2002) reveal the ejecta geometry in broad agreement with what expected from polarization. The axis of symmetry is oriented at $\sim 14^\circ$ on-sky, in agreement with what expected from polarization for prolate ejecta (which produce angle of polarization perpendicular to the axis of symmetry) (Wang et al., 2002). The ejecta show more asymmetry with the projected axis ratio of ~ 0.5 , suggesting that the broadband polarimetry was diluted by unresolved line polarization, and provide lower limit for continuum polarization. The inclination angle of 45° , in-

ferred from the circumstellar ring, is also in agreement with the range derived by Hoflich (1991) from early-time polarimetry and light curve. Further, this angle is also within 10° from the inner circumstellar ring, indicating that the common symmetry extends to the circumstellar ring created before the explosion. The apparent common symmetry from the inner ejecta out to the CSM indicates a common origin, which is likely the binary merger that creates SN 1987A's blue supergiant (BSG) progenitor (Morris and Podsiadlowski, 2007). If SN 1987A were observed edge-on, the axis ratio of its prolate ejecta would have been 0.35, similar to what we inferred for SN 2018hna from our spectropolarimetric observation. Fig. 7.4 shows a schematic of SN 2018hna's ejecta informed by our observations, in comparison to the real image of SN 1987A. The underlying model is the same but observed at two different inclination angles. We show a 1987A-like circumstellar ring for scale (our observations do not probe the existence of such a ring.) The angular size of the ejecta at this epoch is $50 \mu\text{as}$, which is impossible to spatially resolve even by interferometry; polarimetry is the only way to constrain the geometry in the plane of the sky. We conclude from our polarimetric measurements that the apparent ejecta shape of SN 2018hna is a prolate spheroid with an axis ratio of ~ 0.33 oriented at $\sim 70^\circ$ on-sky. This shape looks similar to SN 1987A's ejecta observed edge-on, suggesting that they may share similar intrinsic geometry.

SN 2020oi is a CCSN that lacks both hydrogen and helium features (Type Ic), an explosion of a highly stripped progenitor star. Due to the lack of a hydrogen-rich envelope, the polarization of stripped-envelope SNe is typically at $\sim 1\%$ soon after peak light because the asymmetric inner ejecta are revealed right away. To demonstrate this, Fig. 7.3 (middle) shows optical spectropolarimetry of SNe 2005bf at +8 d (Ib; Tanaka et al., 2009), 2007gr at +21 d (Ic; Tanaka et al., 2008), and 2009mi at +26.5 d (Ic; Tanaka et al., 2012) post-maximum light; all exhibiting 0.5–1% polarization. For SN 2020oi, we do not detect significant near-IR polarization in the spectropolarimetry mode, with the typical upper limit (3σ) of 0.9% per spectral channel (Fig. 7.1 upper middle). Combining all the spectral channels together, the broadband polarization is significant: $0.37 \pm 0.09\%$. If this polarization is intrinsic, then SN 2020oi's visible ejecta at this epoch are only 10% asymmetric. However, the low level of polarization combined with the host galaxy reddening (§7.2) indicate that this polarization is more likely interstellar in origin.

SNe 2019ein and 2020ue (Ia) are both unpolarized at epochs close to the peak light with upper limits of 1.2% and 2.9% per spectral channel (3σ), respectively

(Fig. 7.1). The broadband upper limits are 0.33% and 1.08%, are indicative of a global asymmetry of less than 10% and 20%, respectively. In Fig. 7.3 (bottom), we show the highly polarized SN 2004dt (Leonard et al., 2005; Wang et al., 2006) and the normal SN 2005df (Cikota et al., 2019). The low continuum polarization of SNe Ia indicates spherically symmetric ejecta. Before and at peak luminosity, they show silicon and calcium line polarization originating from asymmetric metal-rich outflows at high velocities. The degree of line polarization is highly variable; e.g., SN 2004dt reaches $p > 2\%$ in the Si II and the Ca triplet lines while SN 2005df has $p = 0.3\%$ in the same lines. The line polarization typically weakens after peak as the symmetric ejecta become optically dominant. The polarimetric non-detections of SNe 2019ein and 2020ue at 2 d pre-maximum and 9 days post-maximum are consistent with the low continuum polarization expected for SNe Ia.

7.4 Conclusion

In summary, we present near-IR spectropolarimetry of four nearby SNe: SNe 2018hna (87-A like), 2019ein (Ia), 2020oi (Ic), and 2020ue (Ia). SN 2018hna shows $\sim 2\%$ polarization with $> 4\sigma$ significance per spectral channel (8σ broadband) across the J band with the angle of polarization around 160° at 180 d post-explosion, and enhanced polarization in the red wing of the hydrogen line. The result indicates that the ejecta of SN 2018hna have an axis ratio of $\lesssim 0.33$ and is oriented at about 70° on-sky. This inferred axis ratio is similar to that of SN 1987A if the latter were observed edge-on. Other SNe in the sample show no significant polarization, with upper limits (3σ per spectral channel) of $\sim 1\%$ for SNe 2019ein and 2020oi, and 2.8% for SN 2020ue.

These measurements are the first spectropolarimetry of SNe in the near-IR, enabled by the highly sensitive instrument WIRC+Pol on the historic 200-inch Hale telescope at Palomar Observatory. They will complement and build upon decades of effort in optical spectropolarimetric observations of SNe. IR spectropolarimetry of SNe will provide a new window to more accurately probe the shape of the SN ejecta imprinted by the explosion mechanism, in pursuit of answering decades-old questions on the progenitor system of SNe Ia and the explosion mechanism of CCSNe.

Acknowledgements

We thank Aleksandar Cikota and Jesper Sollerman for reading the manuscript and providing helpful comments and suggestions. We thank Luc Dessart for helpful discussions. We thank the following authors for providing machine-readable data

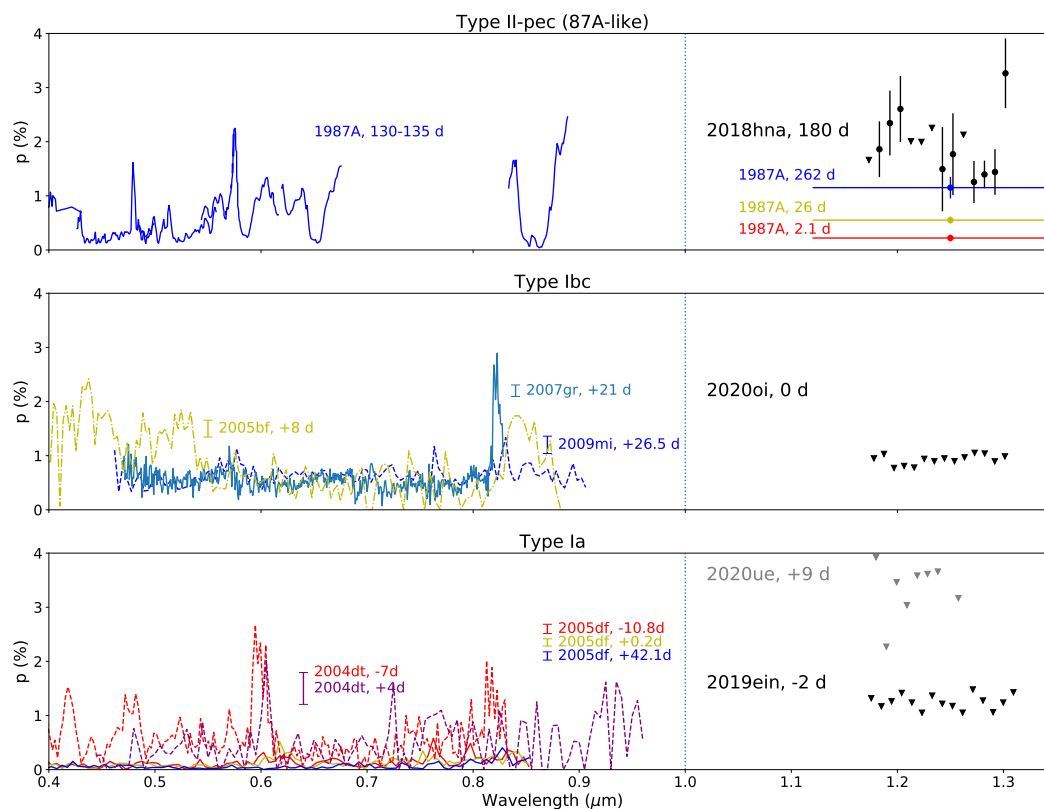


Figure 7.3: Spectropolarimetry of different types of SNe at different phases. From top to bottom, the fractional polarization as a function of wavelength of SNe of Types II-pec 87A-like, Ibc, and Ia are shown. Colors indicate the phase of the observation: red, yellow, and blue tones indicate pre-, near-, and post-peak, respectively. Epochs for SNe Ia and Ibc are relative to peak while those for 1987A-like are relative to explosion. Different line styles indicate different SNe. The median error bar size for each observation is indicated in front of the SN name/epoch label to avoid confusion in the plot. Data for SN 1987A and the -7 d epoch of SN 2004dt do not have uncertainties published. Our IR spectropolarimetry are plotted in black; other data points are from the literature. Filled circles are above 3σ in q or u ; triangles are 3σ upper limits. We caution that p is positively biased and does not follow Gaussian distribution. Literature data include SNe 1987A (Jeffery, 1991), 2004dt (Leonard et al., 2005; Wang et al., 2006), 2005bf (Tanaka et al., 2009), 2005df (Cikota et al., 2019), 2007gr (Tanaka et al., 2008), and 2009mi (Tanaka et al., 2012).

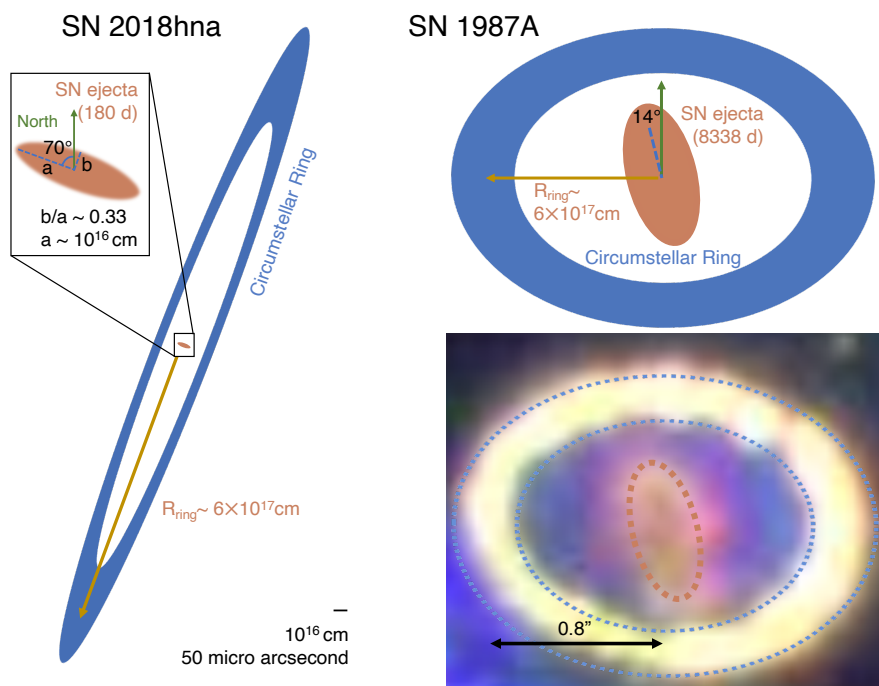


Figure 7.4: Left: schematic of SN 2018hna’s ejecta assuming prolate geometry. The circumstellar ring shown in the schematic is assuming that SN 2018hna has a ring with $6 \times 10^{17} \text{ cm}$ (0.2 pc) radius, similar to that observed around SN 1987A (Panagia, 1998). The provided inset shows that the ejecta are distributed in a prolate spheroid with an axis ratio of 0.33 inferred from our continuum polarization measurement ($2.0 \pm 0.3\%$). The symmetric angle of the ejecta is 70° from north based on our angle of polarization measurement of 160° . This is because a prolate spheroid produces polarization perpendicular to its symmetry axis. Assuming a typical expansion speed of $6,000 \text{ km s}^{-1}$, the size of the ejecta is about 10^{16} cm at 180 d post-explosion, as indicated in the figure. The angular size on-sky at the distance of SN 2018hna (13 Mpc) is $50 \mu\text{as}$, which is several orders of magnitude below the spatial resolution limit of optical-IR interferometers. Right: same schematic but for SN 1987A, showing prolate ejecta at 8338 d post-explosion. The physical size of the circumstellar ring is the same between the two figures. The spatially resolved, color composite image of SN 1987A at this epoch from *HST* is shown in the bottom right panel. Red, green, and blue in the image represent the F814W, F438W, and F225W filters, respectively. The image was obtained from the Hubble Legacy Archive and the data were from PID 11653, PI: Kirshner. The axis ratio of SN 1987A is roughly measured from the image to be about 0.5, and the SN is observed at 45° inclination angle. If SN 1987A were observed edge-on, the axis ratio would be similar to what we infer for SN 2018hna, suggesting that the two SNe have the same underlying geometry but observed from different inclination angles.

for the following SNe: A. Cikota for SN2005df; T. Nagao for SN2017gmr; M. Tanaka for SNe 2005bf, 2007gr, and 2009mi. The data presented herein were obtained at Palomar Observatory, which is operated by a collaboration between California Institute of Technology, Jet Propulsion Laboratory, Yale University, and National Astronomical Observatories of China. This research has made use of the NASA/IPAC Extragalactic Database (NED), which is operated by the Jet Propulsion Laboratory, California Institute of Technology, under contract with the National Aeronautics and Space Administration. This research made use of Astropy, a community-developed core Python package for Astronomy (Astropy Collaboration et al., 2018). The authors wish to recognize and acknowledge the very significant cultural role and reverence that the summit of Maunakea has always had within the indigenous Hawaiian community. We are most fortunate to have the opportunity to conduct observations from this mountain.

Chapter 8

THE FUTURE IS INFRARED BRIGHT

As we set out to demonstrate, IR observations of CCSNe provided crucial insights into stellar explosions. (Make these statements of finished works.) In Chapter 2, we completed the first systematic study of SN light curves at 3.6 and 4.5 μm using *Spitzer* as part of SPIRITS, doubling the number of SNe with *Spitzer* observations at the time. That work also inspired a follow-up study that compared all SN observations ever made with *Spitzer* (Szalai et al., 2019). In Chapter 3, we presented a detailed sequence of near-IR spectroscopy of a typical Type II-P SN well into the nebular phase. We showed the evolution of carbon monoxide emission feature at 2.3 μm , which traces the chemical evolution in its ejecta (87A here) In Chapter 4, we presented the first mid-IR detection of a SN from the ground (since SN 1987A), showing the first evidence of silicate dust in the CSM around an interacting SN. In Chapters 5 and 6, we presented the first astronomical instrument to employ a liquid-crystal-polymer-based polarization grating, which allowed for first spectropolarimetric observations in the IR for sources fainter than about 10 mags. Chapter 7 presented the first IR spectropolarimetric measurements of SNe, which are less contaminated by dust scattering compared to the optical. This included the first IR polarization detection of SN 2018hna, which revealed the geometry of a spatially unresolvable point source. These achievements underscore the fact that the dynamic IR sky is only now being explored.

In the last chapter of this thesis, I discuss how the landscape of time-domain astronomy in the IR is shifting in the past five years, and detail the bright prospects of dynamic IR astronomy.

8.1 Landscape of Science Cases Enabled by WIRC+Pol

Since its beginning of scientific operation in early 2019, WIRC+Pol has started to gain traction in the Palomar community due to its unique capability to provide precise near-IR spectropolarimetry of sources as faint as $J = 14.5$ in a reasonable observing time. The key science cases for WIRC+Pol are for sources that are IR bright, and not easily observable in the optical. The primary science case of WIRC+Pol is to conduct a spectropolarimetric survey of brown dwarfs (BDs), substellar objects whose atmosphere closely resembles that of gaseous giant planets.

Due to their intrinsically low temperature, BDs' SED peaks in the IR with most of them only discovered two decades ago by the first all-sky survey in the near-IR, 2MASS (Kirkpatrick et al., 1999). Prior to WIRC+Pol, only broadband polarimetry existed for BDs because they were too faint to observe spectropolarimetrically in the optical, and there were no sensitive spectropolarimetric instruments to observe them in the IR (e.g., Miles-Páez et al., 2014, 2017; Zapatero Osorio et al., 2011). With the HWP upgrade finished in March 2019, the BD survey is now going at full force with several interesting candidates identified and intensely monitored for rotationally modulated polarization.

In addition, there is a growing number of science cases to exploit WIRC+Pol's sensitivity. Another class of optically-faint IR-bright sources is young stellar objects (YSOs) embedded in their dusty natal cloud or circumstellar disk. There are two currently ongoing programs with WIRC+Pol to study these objects: one focusing on YSOs with spatially resolved nebulae to constrain the geometry of the dust cloud on the small, unresolvable scales, and another focusing on constraining the geometry of protoplanetary disks around these objects. Findings from these programs will have implications on star and planet formation. WIRC+Pol is also being used to observe active galactic nuclei (AGN) that show dust obscuration only in the X-ray and not in the optical. Spectropolarimetry can probe scattering in the inner part of their dusty torus, elucidating the origin of this classification mismatch. In many line of sights in the Milky Way, the dust properties deviate from the average, shifting the peak polarization closer to the IR. WIRC+Pol is currently being used to measure J and H bands polarization to a few tens of stars in the Milky Way to measure properties of dust grains in the ISM. Lastly, WIRC+Pol is also used to observe minor bodies in the solar system to measure their scattering phase function and to probe their composition.

8.2 Future of Supernova Spectropolarimetry

For SN spectropolarimetry, the future lies in multi-epoch, contemporaneous observations in the optical and near-IR to get a full picture of the evolving contribution from different polarizing mechanisms in the SN ejecta: continuum polarization from electron scattering (best probed in the IR), line polarization (optical and IR), and possibly CSM dust polarization (best probed in the optical). The study needs to include not just a handful of SNe, but a statistically significant number of them. Until recently, all SN spectropolarimetric studies focused on a small sample (mostly one) of SNe, with each study using different instruments and treating interstellar

polarization differently, making it difficult to make general statements on the explosion physics of SNe Ia and CCSNe. The limited sample size is simply due to the small number of SNe per year that are bright enough for spectropolarimetry even in the optical. Such an effort has been accomplished for SNe Ia by Cikota et al. (2019) using a large sample collected over a decade at the VLT, providing constraints to the explosion mechanisms of SNe Ia, possibly revealing two populations arising from sub-Chandrasekhar and Chandrasekhar mass WDs. A similar concerted effort to construct a homogeneous sample of a statistically significant number of CCSNe coupled with modern radiative transfer modeling (e.g., Dessart and Hillier, 2011) will start to allow spectropolarimetry to test core-collapse models and answer the decades-old problem of how massive stars explode.

8.3 Large-Sample Survey of Supernovae in the Infrared

While spectropolarimetry provides insights into the explosion mechanism of massive stars and how it shapes the ejecta of the SN, other aspects of a massive star's life and death can be probed by IR photometry and spectroscopy, which are available for a larger number of SNe in a shorter amount of time. Works on SN 2014C presented in this thesis demonstrate the power of IR observations in probing properties of the CSM, thereby constraining mass-loss history of the progenitor star up to the explosion. However, the fact remains IR observations that can probe CSM interactions remain scarce even for nearby SNe, leaving much of the parameter space unexplored.

As we partially uncovered with CCSNe observed by SPIRITS, CSM interactions happen in all subtypes of CCSNe, not just around the strongly interacting Type II_n SNe. In fact, there are several instances of Type II-P SNe from RSG progenitor, commonly thought to be results of single star evolution, showing moderate amount of interactions at many phases after the explosion. These evidence can be either in the high-velocity absorption feature of hydrogen and helium lines seen in SN 2017eaw, sustained excess IR flux seen in SN 2011ja, or peculiar boxy spectral profile seen in other SNe. In addition to their presence in all CCSN subtypes, CSM interactions do not necessarily commence right after the explosion, making long-term monitoring important. In some SNe II-P, the signs of interaction do not emerge until years post-explosion, most notably in the case of SN 2004et (Fabbri et al., 2011; Kotak et al., 2009), which would not have been caught if the SN were not observed three years after the explosion. The frequency and delay time distribution of CSM interaction across all subtypes of CCSNe is presently unknown. To measure them, a complete

survey of nearby CCSNe out to some time post-explosion is required.

There have been other efforts to produce large-sample observations of SNe in the IR, most notably the Carnegie Supernova Project-II, largely employing the Folded-port InfraRed Echellette (FIRE) spectrograph on the Magellan Telescope (Hsiao et al., 2019). They have observed 30 CCSNe, many at several epochs up to 150 d post-explosion (Davis et al., 2019), recovering that spectroscopic features we observed in SN2017eaw like the high-velocity He I $1.083 \mu\text{m}$ and the CO first overtone emission at $2.3 \mu\text{m}$. However, due to their incompleteness and the lack of coverage after ~ 150 d post-explosion, interactions with CSM further away than $\sim 10^{16}$ cm are not well constrained. A new survey designed specifically to probe late-time CSM interactions is in need.

This effort will be much assisted by wide-field IR time-domain surveys like those ubiquitous in the optical. While there are many technological challenges, great progress in surveying the IR sky has been made in the past few years with Palomar Gattini-IR (De et al., 2020; Moore and Kasliwal, 2019), which uses a small telescope with fast focal ratio to achieve large field of view on a single IR detector. Another approach taken to solve the detector cost issue in the IR is the employment of an alternative detector technology based on indium gallium arsenide (InGaAs) semiconductor (Simcoe et al., 2019). A new 1-meter telescope equipped with an InGaAs camera, the Wide-field Infrared Transient Explorer (WINTER), is coming online at Palomar Observatory in the near future. Among the wide range of science these surveys will enable, they will provide regular photometric monitoring of nearby SNe, allowing us to identify candidate SNe for detailed follow-up observations.

8.4 Next Decades with a Sensitive Mid-Infrared Observatory

Lastly, *Spitzer* concluded its mission in January 2020, a few months prior to my thesis defense, leaving the sky beyond $2.5 \mu\text{m}$ without a highly sensitive instrument. *James Webb Space Telescope (JWST)* is poised to take and far surpass *Spitzer's* position as our sensitive IR observatory, enabling high sensitivity photometry and spectroscopy between $0.6\text{--}28.5 \mu\text{m}$. Its primary mirror has more than 40 times larger light collecting area compared to *Spitzer*, allowing it to observe much fainter sources. Its spectroscopic sensitivity and coverage are novel, allowing us to probe important spectral features from molecules and dust, especially the $4.6 \mu\text{m}$ fundamental CO emission, and the $10 \mu\text{m}$ silicate dust features. *JWST* will present a vast leap in near- to mid-IR sensitivity, which will open up IR observations of CCSNe,

like those presented in this thesis, to a much larger volume than possible before. Many questions will be answered with *JWST* observations, ranging from the CSM composition to the chemical evolution and dust formation in CCSNe. We may be able to finally answer a decade-old question of whether or not CCSNe are net producer of dust grains observed in the universe.

As was the case with past decades of advancement in observational astronomy, we are likely to solve some problems, but more likely to uncover new ones. With new tools becoming available, both in space with *JWST* and *WFIRST*; and on the ground with new wide-field IR surveys like Palomar Gattini-IR and novel instrumentation like WIRC+Pol, the force of astronomical exploration will undoubtedly expand rapidly redward.

BIBLIOGRAPHY

- Abbott, T. M. et al. (Aug. 2000). “SWIR at the Nordic Optical Telescope: NOTCam”. In: *Optical and IR Telescope Instrumentation and Detectors*. Ed. by M. Iye and A. F. Moorwood. Vol. 4008. Society of Photo-Optical Instrumentation Engineers (SPIE) Conference Series.
- Abellán, F. J. et al. (June 2017). “Very Deep inside the SN 1987A Core Ejecta: Molecular Structures Seen in 3D”. In: *ApJL* 842, L24. DOI: 10.3847/2041-8213/aa784c. arXiv: 1706.04675 [astro-ph.SR].
- Adams, S. M. and C. S. Kochanek (Sept. 2015). “LOSS’s first supernova? New limits on the ‘impostor’ SN 1997bs”. In: *MNRAS* 452. DOI: 10.1093/mnras/stv1409. arXiv: 1502.00001 [astro-ph.SR].
- Allen, D. A. et al. (Mar. 1987). “Supernova 1987A in the Large Magellanic Cloud”. In: *IAU Circ.* 4351. URL: <https://ui.adsabs.harvard.edu/abs/1987IAUC.4351....1A>.
- Anand, G. S., L. Rizzi, and R. B. Tully (Sept. 2018). “A Robust Tip of the Red Giant Branch Distance to the Fireworks Galaxy (NGC 6946)”. In: *AJ* 156, 105. DOI: 10.3847/1538-3881/aad3b2. arXiv: 1807.05229.
- Anderson, G. E. et al. (Apr. 2017). “The peculiar mass-loss history of SN 2014C as revealed through AMI radio observations”. In: *MNRAS* 466. DOI: 10.1093/mnras/stw3310. arXiv: 1612.06059 [astro-ph.HE].
- Anderson, J. P. et al. (May 2014). “Characterizing the V-band Light-curves of Hydrogen-rich Type II Supernovae”. In: *ApJ* 786.1, 67, p. 67. DOI: 10.1088/0004-637X/786/1/67. arXiv: 1403.7091 [astro-ph.HE].
- Andrews, J. E. et al. (May 2010). “SN 2007od: A Type IIP Supernova with Circumstellar Interaction”. In: *ApJ* 715. DOI: 10.1088/0004-637X/715/1/541. arXiv: 1004.1209 [astro-ph.SR].
- Andrews, J. E. et al. (Apr. 2011). “Photometric and Spectroscopic Evolution of the IIP SN 2007it to Day 944”. In: *ApJ* 731, 47. DOI: 10.1088/0004-637X/731/1/47. arXiv: 1102.2431.
- Andrews, J. E. et al. (Apr. 2016). “Early dust formation and a massive progenitor for SN 2011ja?” In: *MNRAS* 457. DOI: 10.1093/mnras/stw164. arXiv: 1509.06379 [astro-ph.SR].
- Antonucci, R. R. J. and J. S. Miller (Oct. 1985). “Spectropolarimetry and the nature of NGC 1068.” In: *ApJ* 297. DOI: 10.1086/163559.
- Arcavi, I. et al. (Sept. 2012). “Caltech Core-Collapse Project (CCCP) Observations of Type II Supernovae: Evidence for Three Distinct Photometric Subtypes”. In: *ApJL* 756.2, L30, p. L30. DOI: 10.1088/2041-8205/756/2/L30. arXiv: 1206.2029 [astro-ph.CO].

- Argo, M. et al. (May 2017a). “e-MERLIN 5GHz observations of SN2017eaw in NGC6946”. In: *ATel*, No. 10421 10421.
- Argo, M. et al. (June 2017b). “e-MERLIN detection of SN2017eaw in NGC6946”. In: *ATel*, No. 10472 10472.
- Arkharov, A. A. et al. (May 2017). “NIR follow-up of SN 2017eaw”. In: *ATel*, No. 10407 10407.
- Arnett, D., B. Fryxell, and E. Mueller (June 1989). “Instabilities and Nonradial Motion in SN 1987A”. In: *ApJL* 341. doi: 10.1086/185458.
- Astropy Collaboration et al. (Oct. 2013). “Astropy: A community Python package for astronomy”. In: *A&A* 558, A33. doi: 10.1051/0004-6361/201322068. arXiv: 1307.6212 [astro-ph.IM].
- Astropy Collaboration et al. (Sept. 2018). “The Astropy Project: Building an Open-science Project and Status of the v2.0 Core Package”. In: *AJ* 156, 123. doi: 10.3847/1538-3881/aabc4f. arXiv: 1801.02634 [astro-ph.IM].
- Ayani, K., T. Hashimoto, and H. Yamaoka (Jan. 2003). “Supernovae 2003J, 2003K, 2003L, 2003M”. In: *IAU Circ.* 8048. URL: <http://adsabs.harvard.edu/abs/2003IAUC.8048....2A>.
- Baade, W. and F. Zwicky (May 1934). “Cosmic Rays from Super-novae”. In: *Proceedings of the National Academy of Science* 20.5. doi: 10.1073/pnas.20.5.259.
- Bailey, J. (Jan. 1988). “Spectropolarimetry of SN 1987A with the AAT.” In: *Proceedings of the Astronomical Society of Australia* 7.
- Barlow, M. J. et al. (July 2010). “A Herschel PACS and SPIRE study of the dust content of the Cassiopeia A supernova remnant”. In: *A&A* 518, L138. doi: 10.1051/0004-6361/201014585. arXiv: 1005.2688.
- Bellm, E. C. et al. (Jan. 2019). “The Zwicky Transient Facility: System Overview, Performance, and First Results”. In: *PASP* 131.995. doi: 10.1088/1538-3873/aaecbe. arXiv: 1902.01932 [astro-ph.IM].
- Bertin, E. and S. Arnouts (June 1996). “SExtractor: Software for source extraction.” In: *A&AS* 117. doi: 10.1051/aas:1996164.
- Bianco, F. B. et al. (Aug. 2014). “Multi-color Optical and Near-infrared Light Curves of 64 Stripped-envelope Core-Collapse Supernovae”. In: *ApJS* 213, 19. doi: 10.1088/0067-0049/213/2/19. arXiv: 1405.1428 [astro-ph.SR].
- Bietenholz, M. F. et al. (Apr. 2018). “SN 2014C: VLBI images of a supernova interacting with a circumstellar shell”. In: *MNRAS* 475. doi: 10.1093/mnras/stx3194. arXiv: 1707.09935 [astro-ph.HE].
- Bilinski, C. et al. (Mar. 2018). “SN2012ab: a peculiar Type II_n supernova with aspherical circumstellar material”. In: *MNRAS* 475.1. doi: 10.1093/mnras/stx3214. arXiv: 1712.03370 [astro-ph.SR].

- Bock, D. C.-J. et al. (June 2006). “First results from CARMA: the combined array for research in millimeter-wave astronomy”. In: *Society of Photo-Optical Instrumentation Engineers (SPIE) Conference Series*. Vol. 6267. Proc. SPIE. doi: 10.1117/12.674051.
- Borish, H. J. et al. (Mar. 2015). “Near-infrared Spectroscopy of the Type II_n SN 2010jl: Evidence for High Velocity Ejecta”. In: *ApJ* 801.1, 7. doi: 10.1088/0004-637X/801/1/7. arXiv: 1406.5531 [astro-ph.SR].
- Bose, S. et al. (June 2015). “SN 2013ej: A Type III_L Supernova with Weak Signs of Interaction”. In: *ApJ* 806, 160. doi: 10.1088/0004-637X/806/2/160. arXiv: 1504.06207 [astro-ph.HE].
- Botticella, M. T. et al. (July 2010). “Supernova 2009kf: An Ultraviolet Bright Type IIP Supernova Discovered with Pan-STARRS 1 and GALEX”. In: *ApJL* 717. doi: 10.1088/2041-8205/717/1/L52. arXiv: 1001.5427.
- Bouchet, P. and J. Danziger (Jan. 2014). “9500 Nights of Mid-Infrared Observations of SN 1987A: the birth of the remnant”. In: *IAU Symposium*. Ed. by A. Ray and R. A. McCray. Vol. 296. IAU Symposium. doi: 10.1017/S1743921313009162.
- Bradley, L. et al. (Jan. 2019). *astropy/photutils: v0.6*. doi: 10.5281/zenodo.2533376. URL: <https://doi.org/10.5281/zenodo.2533376>.
- Branch, D. and J. C. Wheeler (2017). *Supernova Explosions*. doi: 10.1007/978-3-662-55054-0.
- Bright, J. et al. (May 2017). “AMI-LA 15 GHz Observation of the Type IIP Supernova SN 2017eaw”. In: *ATel, No. 10394* 10394.
- Brown, R. L., W. Wild, and C. Cunningham (Jan. 2004). “ALMA - the Atacama large millimeter array”. In: *Advances in Space Research* 34. doi: 10.1016/j.asr.2003.03.028.
- Burke, J. et al. (May 2019). “Classification of AT 2019ein as a young SN Ia-peculiar”. In: *Transient Name Server AstroNote* 8.
- Burrows, A., D. Radice, and D. Vartanyan (May 2019). “Three-dimensional supernova explosion simulations of 9-, 10-, 11-, 12-, and 13- M_{\odot} stars”. In: *MNRAS* 485.3. doi: 10.1093/mnras/stz543. arXiv: 1902.00547 [astro-ph.SR].
- Cameron, E. (June 2011). “On the Estimation of Confidence Intervals for Binomial Population Proportions in Astronomy: The Simplicity and Superiority of the Bayesian Approach”. In: *PASA* 28. doi: 10.1071/AS10046. arXiv: 1012.0566 [astro-ph.IM].
- Cao, Y. et al. (Sept. 2013). “Discovery, Progenitor and Early Evolution of a Stripped Envelope Supernova iPTF13bvn”. In: *ApJL* 775.1, L7. doi: 10.1088/2041-8205/775/1/L7. arXiv: 1307.1470 [astro-ph.SR].

- Cappellaro, E. and M. Turatto (Oct. 1986). “Supernova 1986J in NGC 891”. In: *IAU Circ.* 4262. URL: <http://adsabs.harvard.edu/abs/1986IAUC.4262...3C>.
- Chakraborti, S. et al. (Sept. 2013). “The Progenitor of SN 2011ja: Clues from Circumstellar Interaction”. In: *ApJ* 774, 30. DOI: 10.1088/0004-637X/774/1/30. arXiv: 1302.7067 [astro-ph.HE].
- Chakraborti, S. et al. (Jan. 2016). “Probing Final Stages of Stellar Evolution with X-Ray Observations of SN 2013ej”. In: *ApJ* 817, 22. DOI: 10.3847/0004-637X/817/1/22. arXiv: 1510.06025 [astro-ph.HE].
- Chambers, K. C. et al. (Dec. 2016). “The Pan-STARRS1 Surveys”. In: *arXiv e-prints*, arXiv:1612.05560. arXiv: 1612.05560 [astro-ph.IM].
- Cherchneff, I. (May 2014). “Dust production in Supernovae”. In: *ArXiv e-prints*. arXiv: 1405.1216 [astro-ph.SR].
- Chevalier, R. A. (July 1982). “Self-similar solutions for the interaction of stellar ejecta with an external medium.” In: *ApJ* 258. DOI: 10.1086/160126.
- Chevalier, R. A. and E. P. Liang (Sept. 1989). “The Interaction of Supernovae with Circumstellar Bubbles”. In: *ApJ* 344. DOI: 10.1086/167802.
- Chugai, N. N. and R. A. Chevalier (Apr. 2006). “Late Emission from the Type Ib/c SN 2001em: Overtaking the Hydrogen Envelope”. In: *ApJ* 641. DOI: 10.1086/500539. eprint: astro-ph/0510362.
- Chugai, N. N., R. A. Chevalier, and V. P. Utrobin (June 2007). “Optical Signatures of Circumstellar Interaction in Type IIP Supernovae”. In: *ApJ* 662. DOI: 10.1086/518160. eprint: astro-ph/0703468.
- Cikota, A. et al. (Nov. 2019). “Linear spectropolarimetry of 35 Type Ia supernovae with VLT/FORS: an analysis of the Si II line polarization”. In: *MNRAS* 490.1. DOI: 10.1093/mnras/stz2322. arXiv: 1908.07526 [astro-ph.HE].
- Clark, J. S. et al. (Dec. 2003). “Dusty ring nebulae around new candidate Luminous Blue Variables”. In: *A&A* 412. DOI: 10.1051/0004-6361:20031372.
- Cohen, M., W. A. Wheaton, and S. T. Megeath (Aug. 2003). “Spectral Irradiance Calibration in the Infrared. XIV. The Absolute Calibration of 2MASS”. In: *AJ* 126. DOI: 10.1086/376474. eprint: astro-ph/0304350.
- Cohen, M. et al. (Apr. 1999). “Spectral Irradiance Calibration in the Infrared. X. A Self-Consistent Radiometric All-Sky Network of Absolutely Calibrated Stellar Spectra”. In: *AJ* 117.4. DOI: 10.1086/300813.
- Conseil, E. et al. (Mar. 2013). “Supernova 2013ai in NGC 2207 = Psn J06161835-2122329”. In: *Central Bureau Electronic Telegrams* 3431. URL: <http://adsabs.harvard.edu/abs/2013CBET.3431...1C>.

- Cortini, G. et al. (July 2013). “Supernova 2013ee in NGC 3079 = Psn J10015683 +5541440”. In: *Central Bureau Electronic Telegrams* 3597. URL: <http://adsabs.harvard.edu/abs/2013CBET.3597....1C>.
- Crowther, P. A. and L. J. Smith (Sept. 1999). “NaSt1: a Wolf-Rayet star cloaked by an eta Car-like nebula?” In: *MNRAS* 308. DOI: 10.1046/j.1365-8711.1999.02707.x. eprint: astro-ph/9903410.
- Cushing, M. C., W. D. Vacca, and J. T. Rayner (Apr. 2004). “Spextool: A Spectral Extraction Package for SpeX, a 0.8-5.5 Micron Cross-Dispersed Spectrograph”. In: *PASP* 116. DOI: 10.1086/382907.
- Dall’Ora, M. et al. (June 2014). “The Type IIP Supernova 2012aw in M95: Hydrodynamical Modeling of the Photospheric Phase from Accurate Spectrophotometric Monitoring”. In: *ApJ* 787.2, 139. DOI: 10.1088/0004-637X/787/2/139. arXiv: 1404.1294 [astro-ph.SR].
- Davis, S. et al. (Dec. 2019). “Carnegie Supernova Project-II: Near-infrared Spectroscopic Diversity of Type II Supernovae”. In: *ApJ* 887.1, 4. DOI: 10.3847/1538-4357/ab4c40. arXiv: 1910.03410 [astro-ph.HE].
- de Kok, R. J., D. M. Stam, and T. Karalidi (Nov. 2011). “Characterizing Exoplanetary Atmospheres through Infrared Polarimetry”. In: *ApJ* 741, 59. DOI: 10.1088/0004-637X/741/1/59. arXiv: 1108.1290 [astro-ph.EP].
- De Marco, O. and R. G. Izzard (Jan. 2017). “Dawes Review 6: The Impact of Companions on Stellar Evolution”. In: *PASA* 34, e001. DOI: 10.1017/pasa.2016.52. arXiv: 1611.03542 [astro-ph.SR].
- De, K. et al. (Feb. 2020). “Palomar Gattini-IR: Survey Overview, Data Processing System, On-sky Performance and First Results”. In: *PASP* 132.1008. DOI: 10.1088/1538-3873/ab6069. arXiv: 1910.13319 [astro-ph.IM].
- Debes, J. H. et al. (Jan. 2016). “Wide-Field Infrared Survey Telescope-Astrophysics Focused Telescope Assets coronagraphic operations: lessons learned from the Hubble Space Telescope and the James Webb Space Telescope”. In: *Journal of Astronomical Telescopes, Instruments, and Systems* 2.1, 011010. DOI: 10.1117/1.JATIS.2.1.011010. arXiv: 1511.06277 [astro-ph.IM].
- Dessart, L. and D. J. Hillier (Jan. 2008). “Time-dependent effects in photospheric-phase Type II supernova spectra”. In: *MNRAS* 383. DOI: 10.1111/j.1365-2966.2007.12538.x. arXiv: 0710.0784.
- Dessart, L. and D. J. Hillier (Aug. 2011). “Synthetic line and continuum linear-polarization signatures of axisymmetric Type II supernova ejecta”. In: *MNRAS* 415.4. DOI: 10.1111/j.1365-2966.2011.18967.x. arXiv: 1104.5346 [astro-ph.SR].
- Diamond, T. R., P. Hoefflich, and C. L. Gerardy (June 2015). “Late-time Near-infrared Observations of SN 2005df”. In: *ApJ* 806, 107. DOI: 10.1088/0004-637X/806/1/107. arXiv: 1410.6759 [astro-ph.SR].

- Donati, J.-F. et al. (2018). “SPIRou: A NIR Spectropolarimeter/High-Precision Velocimeter for the CFHT”. In: *Handbook of Exoplanets, ISBN 978-3-319-55332-0. Springer International Publishing AG, part of Springer Nature, 2018, id.107.* DOI: 10.1007/978-3-319-55333-7_107.
- Draine, B. T. and H. M. Lee (Oct. 1984). “Optical properties of interstellar graphite and silicate grains”. In: *ApJ* 285. DOI: 10.1086/162480.
- Drout, M. R. et al. (Nov. 2011). “The First Systematic Study of Type Ibc Supernova Multi-band Light Curves”. In: *ApJ* 741.2, 97. DOI: 10.1088/0004-637X/741/2/97. arXiv: 1011.4959 [astro-ph.CO].
- Duszanowicz, G. et al. (Nov. 2006). “Supernovae 2006lu-2006mx”. In: *IAU Circ.* 8771. URL: <http://adsabs.harvard.edu/abs/2006IAUC.8771....1D>.
- Dwek, E. (Nov. 1983). “The infrared echo of a type II supernova with a circumstellar dust shell - Applications to SN 1979c and SN 1980k”. In: *ApJ* 274. DOI: 10.1086/161435.
- Dwek, E. and R. G. Arendt (Sept. 2015). “The Evolution of Dust Mass in the Ejecta of SN1987A”. In: *ApJ* 810, 75. DOI: 10.1088/0004-637X/810/1/75. arXiv: 1507.07019 [astro-ph.SR].
- Dwek, E. et al. (Nov. 1983). “The evolution of the infrared emission from the Type II supernova 1980k in NGC 6946 - The dust formation model”. In: *ApJ* 274. DOI: 10.1086/161434.
- Dwek, E., A. Sarangi, and R. G. Arendt (Feb. 2019). “The Evolution of Dust Opacity in Core Collapse Supernovae and the Rapid Formation of Dust in Their Ejecta”. In: *ApJL* 871.2, L33. DOI: 10.3847/2041-8213/aaf9a8. arXiv: 1812.08234 [astro-ph.SR].
- Eldridge, J. J. et al. (Nov. 2017). “Binary Population and Spectral Synthesis Version 2.1: Construction, Observational Verification, and New Results”. In: *PASA* 34, e058. DOI: 10.1017/pasa.2017.51. arXiv: 1710.02154 [astro-ph.SR].
- Eldridge, J. J. et al. (Dec. 2018). “Supernova lightCURVE POPulation Synthesis I: Including interacting binaries is key to understanding the diversity of type II supernova lightcurves”. In: *PASA* 35. DOI: 10.1017/pasa.2018.47. arXiv: 1811.00282 [astro-ph.SR].
- Elias-Rosa, N. et al. (Nov. 2011). “The Massive Progenitor of the Possible Type II-Linear Supernova 2009hd in Messier 66”. In: *ApJ* 742, 6. DOI: 10.1088/0004-637X/742/1/6. arXiv: 1108.2645 [astro-ph.SR].
- Elias-Rosa, N. et al. (Nov. 2013). “On the progenitor of the Type Ic SN 2013dk in the Antennae galaxies”. In: *MNRAS* 436. DOI: 10.1093/mnrasl/slt124. arXiv: 1307.7755 [astro-ph.SR].
- Epinat, B. et al. (Aug. 2008). “GHASP: an H α kinematic survey of spiral and irregular galaxies - VI. New H α data cubes for 108 galaxies”. In: *MNRAS* 388. DOI: 10.1111/j.1365-2966.2008.13422.x. arXiv: 0805.0976 [astro-ph].

- Ercolano, B., M. J. Barlow, and P. J. Storey (Sept. 2005). “The dusty MOCASSIN: fully self-consistent 3D photoionization and dust radiative transfer models”. In: *MNRAS* 362. DOI: 10.1111/j.1365-2966.2005.09381.x. eprint: astro-ph/0507050.
- Ercolano, B. et al. (Apr. 2003). “MOCASSIN: a fully three-dimensional Monte Carlo photoionization code”. In: *MNRAS* 340. DOI: 10.1046/j.1365-8711.2003.06371.x. eprint: astro-ph/0209378.
- Ercolano, B. et al. (Apr. 2008). “X-Ray Enabled MOCASSIN: A Three-dimensional Code for Photoionized Media”. In: *ApJS* 175. DOI: 10.1086/524378. arXiv: 0710.2103.
- Ergon, M. et al. (Aug. 2015). “The Type IIb SN 2011dh: Two years of observations and modelling of the lightcurves”. In: *A&A* 580, A142. DOI: 10.1051/0004-6361/201424592. arXiv: 1408.0731 [astro-ph.SR].
- Escuti, M. J. et al. (2006). “Simplified spectropolarimetry using reactive mesogen polarization gratings”. In: vol. 6302. DOI: 10.1117/12.681447. URL: <https://doi.org/10.1117/12.681447>.
- Fabbri, J. et al. (Dec. 2011). “The effects of dust on the optical and infrared evolution of SN 2004et”. In: *MNRAS* 418.2. DOI: 10.1111/j.1365-2966.2011.19577.x. arXiv: 1110.3166 [astro-ph.GA].
- Fazio, G. G. et al. (Sept. 2004). “The Infrared Array Camera (IRAC) for the Spitzer Space Telescope”. In: *ApJS* 154. DOI: 10.1086/422843. eprint: astro-ph/0405616.
- Filippenko, A. V. (1997). “Optical Spectra of Supernovae”. In: *ARA&A* 35. DOI: 10.1146/annurev.astro.35.1.309.
- Filippenko, A. V. and R. J. Foley (Feb. 2005). “Supernovae 2004gw, 2005T, and 2005ae”. In: *IAU Circ.* 8486. URL: <http://adsabs.harvard.edu/abs/2005IAUC.8486....3F>.
- Filippenko, A. V., W. D. Li, and M. Modjaz (Apr. 1999). “Supernova 1999bw in NGC 3198”. In: *IAU Circ.* 7152. URL: <http://adsabs.harvard.edu/abs/1999IAUC.7152....2F>.
- Filippenko, A. V., T. Matheson, and L. C. Ho (Oct. 1993). “The “Type IIb” Supernova 1993J in M81: A Close Relative of Type Ib Supernovae”. In: *ApJL* 415. DOI: 10.1086/187043.
- Filippenko, A. V. et al. (2001). “The Lick Observatory Supernova Search with the Katzman Automatic Imaging Telescope”. In: *IAU Colloq. 183: Small Telescope Astronomy on Global Scales*. Ed. by B. Paczynski, W.-P. Chen, and C. Lemme. Vol. 246. Astronomical Society of the Pacific Conference Series.
- Folatelli, G. et al. (Oct. 2014). “A Blue Point Source at the Location of Supernova 2011dh”. In: *ApJL* 793.2, L22. DOI: 10.1088/2041-8205/793/2/L22. arXiv: 1409.0700 [astro-ph.SR].

- Folatelli, G. et al. (Oct. 2015). “The Progenitor of the Type IIb SN 2008ax Revisited”. In: *ApJ* 811.2, 147. DOI: 10.1088/0004-637X/811/2/147. arXiv: 1509.01588 [astro-ph.SR].
- Foley, R. J. et al. (June 2004). “Supernovae 2004bu, 2004bw, 2004bz, 2004cb, and 2004cc”. In: *IAU Circ.* 8353. URL: <http://adsabs.harvard.edu/abs/2004IAUC.8353....3F>.
- Foley, R. J. et al. (Mar. 2007). “SN 2006jc: A Wolf-Rayet Star Exploding in a Dense He-rich Circumstellar Medium”. In: *ApJL* 657. DOI: 10.1086/513145. eprint: astro-ph/0612711.
- Foreman-Mackey, D. et al. (Mar. 2013). “emcee: The MCMC Hammer”. In: *PASP* 125. DOI: 10.1086/670067. arXiv: 1202.3665 [astro-ph.IM].
- Forster, F. et al. (Jan. 2020). “ALeRCE/ZTF Transient Discovery Report for 2020-01-07”. In: *Transient Name Server Discovery Report 2020-67*.
- Fox, O. D. and A. V. Filippenko (July 2013). “The Late-time Rebrightening of Type Ia SN 2005gj in the Mid-infrared”. In: *ApJL* 772, L6. DOI: 10.1088/2041-8205/772/1/L6. arXiv: 1304.4934 [astro-ph.HE].
- Fox, O. D. et al. (Jan. 2016). “An Excess of Mid-infrared Emission from the Type Iax SN 2014dt”. In: *ApJL* 816, L13. DOI: 10.3847/2041-8205/816/1/L13. arXiv: 1510.08070 [astro-ph.HE].
- Fox, O. D. et al. (Dec. 2010). “Disentangling the Origin and Heating Mechanism of Supernova Dust: Late-time Spitzer Spectroscopy of the Type IIIn SN 2005ip”. In: *ApJ* 725. DOI: 10.1088/0004-637X/725/2/1768. arXiv: 1005.4682 [astro-ph.HE].
- Fox, O. D. et al. (Nov. 2011). “A Spitzer Survey for Dust in Type IIIn Supernovae”. In: *ApJ* 741, 7. DOI: 10.1088/0004-637X/741/1/7. arXiv: 1104.5012 [astro-ph.SR].
- Fox, O. D. et al. (July 2013). “Late-time Circumstellar Interaction in a Spitzer Selected Sample of Type IIIn Supernovae”. In: *AJ* 146, 2. DOI: 10.1088/0004-6256/146/1/2. arXiv: 1304.0248 [astro-ph.SR].
- Fox, O. D. et al. (July 2014). “Uncovering the Putative B-star Binary Companion of the SN 1993J Progenitor”. In: *ApJ* 790.1, 17. DOI: 10.1088/0004-637X/790/1/17. arXiv: 1405.4863 [astro-ph.HE].
- Fox, O. et al. (Jan. 2009). “Near-Infrared Photometry of the Type IIIn SN 2005ip: The Case for Dust Condensation”. In: *ApJ* 691. DOI: 10.1088/0004-637X/691/1/650. arXiv: 0807.3555 [astro-ph].
- Fransson, C., P. Lundqvist, and R. A. Chevalier (Apr. 1996). “Circumstellar Interaction in SN 1993J”. In: *ApJ* 461. DOI: 10.1086/177119.

- Freedman, W. L. et al. (May 2001). “Final Results from the Hubble Space Telescope Key Project to Measure the Hubble Constant”. In: *ApJ* 553. DOI: 10.1086/320638. eprint: astro-ph/0012376.
- Fuller, J. (Sept. 2017). “Pre-supernova outbursts via wave heating in massive stars - I. Red supergiants”. In: *MNRAS* 470. DOI: 10.1093/mnras/stx1314. arXiv: 1704.08696 [astro-ph.SR].
- Fuller, J. and S. Ro (May 2018). “Pre-supernova outbursts via wave heating in massive stars - II. Hydrogen-poor stars”. In: *MNRAS* 476. DOI: 10.1093/mnras/sty369. arXiv: 1710.04251 [astro-ph.SR].
- Gall, C., J. Hjorth, and A. C. Andersen (Sept. 2011). “Production of dust by massive stars at high redshift”. In: *A&A Rev.* 19, 43. DOI: 10.1007/s00159-011-0043-7. arXiv: 1108.0403 [astro-ph.CO].
- Gall, C. et al. (July 2014). “Rapid formation of large dust grains in the luminous supernova 2010jl”. In: *Nature* 511. DOI: 10.1038/nature13558. arXiv: 1407.4447 [astro-ph.SR].
- Gehrz, R. D. and J. A. Hackwell (Dec. 1974). “Circumstellar dust emission from WC9 stars.” In: *ApJ* 194. DOI: 10.1086/153281.
- Gehrz, R. D. and E. P. Ney (June 1990). “Confirmation of Dust Condensation in the Ejecta of Supernova 1987a”. In: *Proceedings of the National Academy of Science* 87. DOI: 10.1073/pnas.87.11.4354.
- Gehrz, R. D. et al. (Jan. 1995). “RY Scuti: Infrared and Radio Observations of the Mass-Loss Wind of a Massive Binary Star System”. In: *ApJ* 439. DOI: 10.1086/175184.
- Gehrz, R. D. et al. (Jan. 2007). “The NASA Spitzer Space Telescope”. In: *Review of Scientific Instruments* 78.1. DOI: 10.1063/1.2431313.
- Gehrz, R. D. et al. (Sept. 2001). “Keck LWS Images of the Compact Nebula around RY Scuti in the Thermal Infrared”. In: *ApJ* 559.1. DOI: 10.1086/322325.
- Gerardy, C. L. et al. (Dec. 2002). “Carbon Monoxide in the Type Ic Supernova 2000ew”. In: *PASJ* 54. DOI: 10.1093/pasj/54.6.905. eprint: astro-ph/0207480.
- Ghinassi, F. et al. (May 2002). “Transmission curves and effective refraction indices of MKO near infrared consortium filters at cryogenic temperatures”. In: *A&A* 386. DOI: 10.1051/0004-6361:20020266. eprint: astro-ph/0202483.
- Gomez, H. L. et al. (Nov. 2012). “A Cool Dust Factory in the Crab Nebula: A Herschel Study of the Filaments”. In: *ApJ* 760, 96. DOI: 10.1088/0004-637X/760/1/96. arXiv: 1209.5677.
- Grefenstette, B., F. Harrison, and M. Brightman (May 2017). “NuSTAR Observation of SN2017eaw”. In: *ATel, No. 10427* 10427.

- Hamuy, M. et al. (Jan. 2006). “The Carnegie Supernova Project: The Low-Redshift Survey”. In: *PASP* 118.839. DOI: 10.1086/500228. arXiv: astro-ph/0512039 [astro-ph].
- Hanner, M. (Sept. 1988). *Grain optical properties*. Tech. rep.
- Hansen, J. E. and J. W. Hovenier (May 1974). “Interpretation of the polarization of Venus.” In: *Journal of Atmospheric Sciences* 31. DOI: 10.1175/1520-0469(1974)031<1137:IOTPOV>2.0.CO;2.
- Harrison, F. A. et al. (June 2013). “The Nuclear Spectroscopic Telescope Array (NuSTAR) High-energy X-Ray Mission”. In: *ApJ* 770, 103. DOI: 10.1088/0004-637X/770/2/103. arXiv: 1301.7307 [astro-ph.IM].
- Heiles, C. (Feb. 2000). “9286 Stars: An Agglomeration of Stellar Polarization Catalogs”. In: *AJ* 119. DOI: 10.1086/301236. eprint: astro-ph/9910303.
- Helou, G. et al. (Nov. 2013). “The Mid-infrared Light Curve of Nearby Core-collapse Supernova SN 2011dh (PTF 11eon)”. In: *ApJL* 778, L19. DOI: 10.1088/2041-8205/778/1/L19. arXiv: 1309.4891 [astro-ph.SR].
- Herter, T. L. et al. (July 2008). “The performance of TripleSpec at Palomar”. In: *Ground-based and Airborne Instrumentation for Astronomy II*. Vol. 7014. Proc. SPIE. DOI: 10.1117/12.789660.
- Herter, T. L. et al. (2018). “FORCAST: A Mid-Infrared Camera for SOFIA”. In: *Journal of Astronomical Instrumentation* 7, 1840005-451. DOI: 10.1142/S2251171718400056.
- Hjellming, R. M., L. C. Blankenship, and B. Balick (Apr. 1973). “Radio Emission Nebulae Surrounding MWC 349 and RY Scuti”. In: *Nature Physical Science* 242.119. DOI: 10.1038/physci242084a0.
- Hodapp, K. W. et al. (Dec. 2003). “The Gemini Near-Infrared Imager (NIRI)”. In: *PASP* 115. DOI: 10.1086/379669.
- Hoflich, P. (June 1991). “Asphericity effects in scattering dominated photospheres.” In: *A&A* 246.
- Horesh, A. (2020). Submitted.
- Horne, K. (June 1986). “An optimal extraction algorithm for CCD spectroscopy”. In: *PASP* 98. DOI: 10.1086/131801.
- Hosseinzadeh, G. et al. (July 2018). “Short-lived Circumstellar Interaction in the Low-luminosity Type IIP SN 2016bkv”. In: *ApJ* 861, 63. DOI: 10.3847/1538-4357/aac5f6. arXiv: 1801.00015 [astro-ph.HE].
- Houck, J. R. et al. (Sept. 2004). “The Infrared Spectrograph (IRS) on the Spitzer Space Telescope”. In: *ApJS* 154. DOI: 10.1086/423134. eprint: astro-ph/0406167.

- Hsiao, E. Y. et al. (Apr. 2013). “The Earliest Near-infrared Time-series Spectroscopy of a Type Ia Supernova”. In: *ApJ* 766.2, 72. DOI: 10.1088/0004-637X/766/2/72. arXiv: 1301.6287 [astro-ph.CO].
- Hsiao, E. Y. et al. (Jan. 2019). “Carnegie Supernova Project-II: The Near-infrared Spectroscopy Program”. In: *PASP* 131.995. DOI: 10.1088/1538-3873/aae961. arXiv: 1810.08213 [astro-ph.SR].
- Indebetouw, R. et al. (Feb. 2014). “Dust Production and Particle Acceleration in Supernova 1987A Revealed with ALMA”. In: *ApJL* 782, L2. DOI: 10.1088/2041-8205/782/1/L2. arXiv: 1312.4086 [astro-ph.SR].
- Ismail, M. A. (May 1986). “Transmission of Light by Slit Designed for Astronomical Spectrograph”. In: *Ap&SS* 122.1. DOI: 10.1007/BF00654377.
- Itagaki, K. (Oct. 2018). “Transient Discovery Report for 2018-10-22”. In: *Transient Name Server Discovery Report* 2018-1614.
- Itagaki, K. et al. (Apr. 2013). “Supernova 2013bu in NGC 7331 = Psn J22370217 +3424052”. In: *Central Bureau Electronic Telegrams* 3498. URL: <http://adsabs.harvard.edu/abs/2013CBET.3498...1I>.
- Janka, H.-T. (Nov. 2012). “Explosion Mechanisms of Core-Collapse Supernovae”. In: *Annual Review of Nuclear and Particle Science* 62.1. DOI: 10.1146/annurev-nucl-102711-094901. arXiv: 1206.2503 [astro-ph.SR].
- Janka, H.-T. (2017). “Neutrino-Driven Explosions”. In: *Handbook of Supernovae*. Ed. by A. W. Alsabti and P. Murdin. DOI: 10.1007/978-3-319-21846-5_109.
- Jeffery, D. J. (Nov. 1991). “Catalog of SN 1987A Polarimetry Corrected for Interstellar Polarization”. In: *ApJS* 77. DOI: 10.1086/191610.
- Jencson, J. E. et al. (Mar. 2017). “SPIRITS 15c and SPIRITS 14buu: Two Obscured Supernovae in the Nearby Star-forming Galaxy IC 2163”. In: *ApJ* 837.2, 167. DOI: 10.3847/1538-4357/aa618f. arXiv: 1609.04444 [astro-ph.HE].
- Jencson, J. E. et al. (Nov. 2019). “The SPIRITS Sample of Luminous Infrared Transients: Uncovering Hidden Supernovae and Dusty Stellar Outbursts in Nearby Galaxies”. In: *ApJ* 886.1, 40. DOI: 10.3847/1538-4357/ab4a01. arXiv: 1901.00871 [astro-ph.HE].
- Jensen-Clem, R. et al. (Apr. 2016). “Point Source Polarimetry with the Gemini Planet Imager: Sensitivity Characterization with T5.5 Dwarf Companion HD 19467 B”. In: *ApJ* 820, 111. DOI: 10.3847/0004-637X/820/2/111. arXiv: 1601.01353 [astro-ph.EP].
- Johansson, J. et al. (Apr. 2017). “Spitzer observations of SN 2014J and properties of mid-IR emission in Type Ia supernovae”. In: *MNRAS* 466.3. DOI: 10.1093/mnras/stw3350. arXiv: 1411.3332 [astro-ph.HE].

- Johnson, S. A., C. S. Kochanek, and S. M. Adams (Oct. 2018). “The quiescent progenitors of four Type II-P/L supernovae”. In: *MNRAS* 480. DOI: 10.1093/mnras/sty1966. arXiv: 1712.03957 [astro-ph.SR].
- Jones, E., T. Oliphant, P. Peterson, et al. (2001). *SciPy: Open source scientific tools for Python*. [Online; accessed 2015-05-01]. URL: <http://www.scipy.org/>.
- Kamble, A. et al. (Jan. 2014). “VLA observations of type Ib supernova SN 2014C (PSN J22370560+3424319)”. In: *The Astronomer’s Telegram* 5763. URL: <http://adsabs.harvard.edu/abs/2014ATel.5763....1K>.
- Kamenetzky, J. et al. (Aug. 2013). “Carbon Monoxide in the Cold Debris of Supernova 1987A”. In: *ApJL* 773, L34. DOI: 10.1088/2041-8205/773/2/L34. arXiv: 1307.6561 [astro-ph.SR].
- Kankare, E. et al. (Dec. 2014). “SN 2005at - A neglected type Ic supernova at 10 Mpc”. In: *A&A* 572, A75. DOI: 10.1051/0004-6361/201424563. arXiv: 1409.1758 [astro-ph.SR].
- Kasliwal, M. M. et al. (Apr. 2017). “SPIRITS: Uncovering Unusual Infrared Transients with Spitzer”. In: *ApJ* 839.2, 88. DOI: 10.3847/1538-4357/aa6978. arXiv: 1701.01151 [astro-ph.HE].
- Kataza, H. et al. (Aug. 2000). “COMICS: the cooled mid-infrared camera and spectrometer for the Subaru telescope”. In: *Optical and IR Telescope Instrumentation and Detectors*. Ed. by M. Iye and A. F. Moorwood. Vol. 4008. Society of Photo-Optical Instrumentation Engineers (SPIE) Conference Series. DOI: 10.1117/12.395433.
- Kawabata, M. (Jan. 2020). “Transient Classification Report for 2020-01-12”. In: *Transient Name Server Classification Report* 2020-114.
- Keller, C. U. (Dec. 2001). “Instrumentation for Astrophysical Spectropolarimetry”. In: *Astrophysical Spectropolarimetry*: ed. by J. Trujillo-Bueno, F. Moreno-Insertis, and F. Sanchez. Cambridge: Cambridge University Press. DOI: 10.1017/CB09780511564802.012.
- Kervella, P. et al. (Jan. 2016). “The close circumstellar environment of Betelgeuse. III. SPHERE/ZIMPOL imaging polarimetry in the visible”. In: *A&A* 585, A28. DOI: 10.1051/0004-6361/201527134. arXiv: 1511.04451 [astro-ph.SR].
- Khan, R. (May 2017). “Mid-IR progenitor of AT 2017eaw in NGC 6946”. In: *The Astronomer’s Telegram* 10373. URL: <http://adsabs.harvard.edu/abs/2017ATel10373....1K>.
- Kilpatrick, C. D. and R. J. Foley (Dec. 2018). “The dusty progenitor star of the Type II supernova 2017eaw”. In: *MNRAS* 481. DOI: 10.1093/mnras/sty2435.
- Kilpatrick, C. D. et al. (Oct. 2018). “A potential progenitor for the Type Ic supernova 2017ein”. In: *MNRAS* 480.2. DOI: 10.1093/mnras/sty2022. arXiv: 1808.02989 [astro-ph.SR].

- Kim, M. et al. (Jan. 2014). “Supernova 2014C in NGC 7331 = Psn J22370560 +3424319”. In: *Central Bureau Electronic Telegrams* 3777. URL: <http://adsabs.harvard.edu/abs/2014CBET.3777....1K>.
- Kirkpatrick, J. D. (2005). “NEW SPECTRAL TYPES L AND T”. In: *Annu. Rev. Astron. Astrophys* 43. DOI: 10.1146/annurev.astro.42.053102.134017. URL: <http://www.annualreviews.org/doi/pdf/10.1146/annurev.astro.42.053102.134017>.
- Kirkpatrick, J. D. et al. (July 1999). “Dwarfs Cooler than “M”: The Definition of Spectral Type “L” Using Discoveries from the 2 Micron All-Sky Survey (2MASS)”. In: *ApJ* 519.2. DOI: 10.1086/307414.
- Kochanek, C. S. (Dec. 2011). “The Astrophysical Implications of Dust Formation during the Eruptions of Hot, Massive Stars”. In: *ApJ* 743, 73. DOI: 10.1088/0004-637X/743/1/73. arXiv: 1109.2596 [astro-ph.SR].
- Kochanek, C. S. (Mar. 2019). “The physics of flash (supernova) spectroscopy”. In: *MNRAS* 483. DOI: 10.1093/mnras/sty3363. arXiv: 1807.09778.
- Kochanek, C. S., D. M. Szczygiel, and K. Z. Stanek (Oct. 2012). “Unmasking the Supernova Impostors”. In: *ApJ* 758, 142. DOI: 10.1088/0004-637X/758/2/142. arXiv: 1202.0281 [astro-ph.SR].
- Kong, A. K. H. and K. L. Li (May 2017). “X-ray emission of SN 2017eaw and its progenitor”. In: *ATel, No. 10380* 10380.
- Kotak, R. et al. (Aug. 2005). “Early-Time Spitzer Observations of the Type II Plateau Supernova SN 2004dj”. In: *ApJL* 628. DOI: 10.1086/432719. eprint: astro-ph/0506407.
- Kotak, R. et al. (Nov. 2006). “Spitzer Measurements of Atomic and Molecular Abundances in the Type IIP SN 2005af”. In: *ApJL* 651. DOI: 10.1086/509655. eprint: astro-ph/0609706.
- Kotak, R. et al. (Oct. 2009). “Dust and The Type II-Plateau Supernova 2004et”. In: *ApJ* 704. DOI: 10.1088/0004-637X/704/1/306. arXiv: 0904.3737 [astro-ph.SR].
- Kumar, B. et al. (July 2014). “Broad-band polarimetric follow-up of Type IIP SN 2012aw”. In: *MNRAS* 442. DOI: 10.1093/mnras/stu811. arXiv: 1404.6060 [astro-ph.HE].
- Langer, N. (Sept. 2012). “Presupernova Evolution of Massive Single and Binary Stars”. In: *ARA&A* 50. DOI: 10.1146/annurev-astro-081811-125534. arXiv: 1206.5443 [astro-ph.SR].
- Laor, A. and B. T. Draine (Jan. 1993). “Spectroscopic constraints on the properties of dust in active galactic nuclei”. In: *ApJ* 402. DOI: 10.1086/172149.

- Larkin, J. E. et al. (Mar. 2003). “OSIRIS: infrared integral field spectrograph for the Keck adaptive optics system”. In: *Instrument Design and Performance for Optical/Infrared Ground-based Telescopes*. Ed. by M. Iye and A. F. M. Moorwood. Vol. 4841. Proc. SPIE. doi: 10.1117/12.461775.
- Lau, R. M. et al. (Apr. 2015). “Old supernova dust factory revealed at the Galactic center”. In: *Science* 348. doi: 10.1126/science.aaa2208. arXiv: 1503.07173 [astro-ph.SR].
- Lauroesch, J. T. et al. (Mar. 2006). “Supernova 2006X in NGC 4321”. In: *Central Bureau Electronic Telegrams* 421. URL: <http://adsabs.harvard.edu/abs/2006CBET...421....1L>.
- Law, N. M. et al. (Dec. 2009). “The Palomar Transient Factory: System Overview, Performance, and First Results”. In: *PASP* 121. doi: 10.1086/648598. arXiv: 0906.5350 [astro-ph.IM].
- Le Bertre, T. et al. (June 2012). “Discovery of a detached H I gas shell surrounding α Orionis”. In: *MNRAS* 422. doi: 10.1111/j.1365-2966.2012.20853.x. arXiv: 1203.0255 [astro-ph.SR].
- Leadbeater, R. (Oct. 2018). “Transient Classification Report for 2018-10-26”. In: *Transient Name Server Classification Report* 2018-1638.
- Leggett, S. K. et al. (Oct. 2003). “L’ and M’ standard stars for the Mauna Kea Observatories Near-Infrared system”. In: *MNRAS* 345.1. doi: 10.1046/j.1365-8711.2003.06943.x. arXiv: astro-ph/0307032 [astro-ph].
- Leonard, D. C. et al. (Mar. 2006). “A non-spherical core in the explosion of supernova SN 2004dj”. In: *Nature* 440. doi: 10.1038/nature04558. eprint: astro-ph/0603297.
- Leonard, D. C. et al. (Oct. 2005). “Evidence for Spectropolarimetric Diversity in Type Ia Supernovae”. In: *ApJ* 632.1. doi: 10.1086/432866. arXiv: astro-ph/0506470 [astro-ph].
- Liu, W., A. Dalgarno, and S. Lepp (Sept. 1992). “Carbon Monoxide in SN 1987A”. In: *ApJ* 396. doi: 10.1086/171749.
- Low, F. J., G. H. Rieke, and R. D. Gehrz (Sept. 2007). “The Beginning of Modern Infrared Astronomy”. In: *ARA&A* 45. doi: 10.1146/annurev.astro.44.051905.092505.
- Lyman, J. D. et al. (Mar. 2016). “Bolometric light curves and explosion parameters of 38 stripped-envelope core-collapse supernovae”. In: *MNRAS* 457.1. doi: 10.1093/mnras/stv2983. arXiv: 1406.3667 [astro-ph.SR].
- Mackey, J. et al. (Aug. 2014). “Interacting supernovae from photoionization-confined shells around red supergiant stars”. In: *Nature* 512. doi: 10.1038/nature13522. arXiv: 1408.2522 [astro-ph.SR].

- Maguire, K. et al. (May 2010). “Optical and near-infrared coverage of SN 2004et: physical parameters and comparison with other Type IIP supernovae”. In: *MNRAS* 404. DOI: 10.1111/j.1365-2966.2010.16332.x. arXiv: 0912.3111 [astro-ph.SR].
- Manchado, A. et al. (Sept. 2004). “First light for LIRIS (long-slit intermediate-resolution infrared spectrograph)”. In: *Ground-based Instrumentation for Astronomy*. Ed. by A. F. M. Moorwood and M. Iye. Vol. 5492. Proc. SPIE. DOI: 10.1117/12.549188.
- Maoz, D., F. Mannucci, and G. Nelemans (Aug. 2014). “Observational Clues to the Progenitors of Type Ia Supernovae”. In: *ARA&A* 52. DOI: 10.1146/annurev-astro-082812-141031. arXiv: 1312.0628 [astro-ph.CO].
- Marchenko, S. V. and A. F. J. Moffat (June 2017). “Search for polycyclic aromatic hydrocarbons in the outflows from dust-producing Wolf-Rayet stars”. In: *MNRAS* 468.2. DOI: 10.1093/mnras/stx563. arXiv: 1703.01236 [astro-ph.SR].
- Margutti, R. et al. (Feb. 2017). “Ejection of the Massive Hydrogen-rich Envelope Timed with the Collapse of the Stripped SN 2014C”. In: *ApJ* 835, 140. DOI: 10.3847/1538-4357/835/2/140. arXiv: 1601.06806 [astro-ph.HE].
- Marion, G. H., D. Milisavljevic, and J. Irwin (May 2012a). “Supernova 2012cc in NGC 4419 = PSN J12265681+1502455.” In: *Central Bureau Electronic Telegrams* 3105. URL: <http://adsabs.harvard.edu/abs/2012CBET.3105...2M>.
- Marion, G. H. et al. (May 2012b). “Supernova 2012cg in NGC 4424 = PSN J12271283+0925132.” In: *Central Bureau Electronic Telegrams* 3111. URL: <http://adsabs.harvard.edu/abs/2012CBET.3111...3M>.
- Marley, M. S. and S. Sengupta (Nov. 2011). “Probing the physical properties of directly imaged gas giant exoplanets through polarization”. In: *MNRAS* 417. DOI: 10.1111/j.1365-2966.2011.19448.x. arXiv: 1106.0492 [astro-ph.EP].
- Martínez-González, S. et al. (Dec. 2019). “Supernovae within Pre-existing Wind-blown Bubbles: Dust Injection versus Ambient Dust Destruction”. In: *ApJ* 887.2, 198. DOI: 10.3847/1538-4357/ab571b. arXiv: 1911.05079 [astro-ph.GA].
- Masci, F. J. et al. (Jan. 2019). “The Zwicky Transient Facility: Data Processing, Products, and Archive”. In: *PASP* 131.995. DOI: 10.1088/1538-3873/aae8ac. arXiv: 1902.01872 [astro-ph.IM].
- Mathis, J. S., W. Ruml, and K. H. Nordsieck (Oct. 1977). “The size distribution of interstellar grains.” In: *ApJ* 217. DOI: 10.1086/155591.
- Matsuura, M. et al. (Feb. 2015). “A Stubbornly Large Mass of Cold Dust in the Ejecta of Supernova 1987A”. In: *ApJ* 800, 50. DOI: 10.1088/0004-637X/800/1/50. arXiv: 1411.7381 [astro-ph.SR].

- Mattila, S. et al. (Sept. 2008). “Massive stars exploding in a He-rich circumstellar medium - III. SN 2006jc: infrared echoes from new and old dust in the progenitor CSM”. In: *MNRAS* 389. DOI: 10.1111/j.1365-2966.2008.13516.x. arXiv: 0803.2145.
- Mauerhan, J. C. et al. (Apr. 2013). “The unprecedented 2012 outburst of SN 2009ip: a luminous blue variable star becomes a true supernova”. In: *MNRAS* 430. DOI: 10.1093/mnras/stt009. arXiv: 1209.6320 [astro-ph.SR].
- Mauerhan, J. C. et al. (Jan. 2017). “Asphericity, Interaction, and Dust in the Type II-P/II-L Supernova 2013EJ in Messier 74”. In: *ApJ* 834, 118. DOI: 10.3847/1538-4357/834/2/118. arXiv: 1611.07930 [astro-ph.SR].
- Mauerhan, J. et al. (Aug. 2014). “Multi-epoch spectropolarimetry of SN 2009ip: direct evidence for aspherical circumstellar material”. In: *MNRAS* 442. DOI: 10.1093/mnras/stu730. arXiv: 1403.4240 [astro-ph.SR].
- Mauerhan, J. C. et al. (Nov. 2015). “Spectropolarimetry of SN 2011dh in M51: geometric insights on a Type IIb supernova progenitor and explosion”. In: *MNRAS* 453.4. DOI: 10.1093/mnras/stv1944. arXiv: 1506.08844 [astro-ph.SR].
- Mauerhan, J. C. et al. (Aug. 2018). “Stripped-envelope supernova SN 2004dk is now interacting with hydrogen-rich circumstellar material”. In: *MNRAS* 478.4. DOI: 10.1093/mnras/sty1307. arXiv: 1803.07051 [astro-ph.SR].
- Maud, J. R. et al. (Oct. 2011). “The Yellow Supergiant Progenitor of the Type II Supernova 2011dh in M51”. In: *ApJL* 739.2, L37. DOI: 10.1088/2041-8205/739/2/L37. arXiv: 1106.2565 [astro-ph.SR].
- Maxwell, A. J. et al. (Apr. 2010). “Supernova 2010br in NGC 4051”. In: *Central Bureau Electronic Telegrams* 2245. URL: <http://adsabs.harvard.edu/abs/2010CBET.2245....2M>.
- Mazzali, P. A. et al. (Apr. 2014). “Hubble Space Telescope spectra of the Type Ia supernova SN 2011fe: a tail of low-density, high-velocity material with Z & Z_{\odot} ”. In: *MNRAS* 439.2. DOI: 10.1093/mnras/stu077. arXiv: 1305.2356 [astro-ph.CO].
- McClelland, C. M. et al. (Apr. 2013). “The Mid-infrared and Optical Decay of SN 2011fe”. In: *ApJ* 767, 119. DOI: 10.1088/0004-637X/767/2/119. arXiv: 1302.5421.
- McCray, R. (Apr. 1997). “SN1987A enters its second decade”. In: *Nature* 386.6624. DOI: 10.1038/386438a0.
- McLean, I. S. et al. (Sept. 2012). “MOSFIRE, the multi-object spectrometer for infra-red exploration at the Keck Observatory”. In: *Ground-based and Airborne Instrumentation for Astronomy IV*. Vol. 8446. Proc. SPIE. DOI: 10.1117/12.924794.
- Meikle, W. P. S. et al. (May 1989). “Spectroscopy of supernova 1987A at 1-5 microns. I - The first year”. In: *MNRAS* 238. DOI: 10.1093/mnras/238.1.193.

- Meikle, W. P. S. et al. (Apr. 1993). “Spectroscopy of supernova 1987A at 1-4 microns. II - Days 377 to 1114”. In: *MNRAS* 261. DOI: 10.1093/mnras/261.3.535.
- Meikle, W. P. S. et al. (Aug. 2007). “A Spitzer Space Telescope Study of SN 2003gd: Still No Direct Evidence that Core-Collapse Supernovae are Major Dust Factories”. In: *ApJ* 665. DOI: 10.1086/519733. arXiv: 0705.1439.
- Meikle, W. P. S. et al. (May 2011). “Dust and the Type II-plateau Supernova 2004dj”. In: *ApJ* 732, 109. DOI: 10.1088/0004-637X/732/2/109. arXiv: 1103.2885 [astro-ph.SR].
- Miles-Páez, P. A., E. Pallé, and M. R. Zapatero Osorio (Feb. 2014). “Simultaneous optical and near-infrared linear spectropolarimetry of the earthshine”. In: *A&A* 562, L5. DOI: 10.1051/0004-6361/201323009. arXiv: 1401.6029 [astro-ph.EP].
- Miles-Páez, P. A. et al. (Apr. 2017). “Optical and near-infrared linear polarization of low and intermediate-gravity ultracool dwarfs”. In: *MNRAS* 466.3. DOI: 10.1093/mnras/stw3278. arXiv: 1612.08054 [astro-ph.SR].
- Milisavljevic, D. et al. (Sept. 2008). “The Evolution of Late-Time Optical Emission from SN 1986J”. In: *ApJ* 684. DOI: 10.1086/590426. arXiv: 0804.1545.
- Milisavljevic, D. et al. (Dec. 2011). “Supernova 2011ja in NGC 4945 = PSN J13051112-4931270.” In: *Central Bureau Electronic Telegrams* 2946. URL: <http://adsabs.harvard.edu/abs/2011CBET.2946...2M>.
- Milisavljevic, D. et al. (Dec. 2015). “Metamorphosis of SN 2014C: Delayed Interaction between a Hydrogen Poor Core-collapse Supernova and a Nearby Circumstellar Shell”. In: *ApJ* 815, 120. DOI: 10.1088/0004-637X/815/2/120. arXiv: 1511.01907 [astro-ph.HE].
- Millar-Blanchaer, M. et al. (July 2014). “Polarization gratings for visible and near-infrared astronomy”. In: *Advances in Optical and Mechanical Technologies for Telescopes and Instrumentation*. Vol. 9151. Proc. SPIE. DOI: 10.1117/12.2056998.
- Milligan, S., B. W. Cranton, and M. F. Skrutskie (Nov. 1996). “Development of a three-channel SWIR camera, for ground-based astronomical imaging. (Two micron all sky survey, 2MASS)”. In: *Current Developments in Optical Design and Engineering VI*. Ed. by R. E. Fischer and W. J. Smith. Vol. 2863. Proc. SPIE. DOI: 10.1117/12.256209.
- Monard, L. A. G. et al. (Dec. 2011). “Supernova 2011ja in NGC 4945 = Psn J13051112-4931270”. In: *Central Bureau Electronic Telegrams* 2946. URL: <http://adsabs.harvard.edu/abs/2011CBET.2946...1M>.
- Monard, L. A. G. et al. (Sept. 2014). “Supernova 2014df in NGC 1448 = Psn J03442399-4440081”. In: *Central Bureau Electronic Telegrams* 3977. URL: <http://adsabs.harvard.edu/abs/2014CBET.3977...1M>.

- Mooley, K. P. et al. (May 2017). “Further AMI-LA observations of SN2017eaw at 15 GHz”. In: *ATel*, No. 10413 10413.
- Moore, A. M. and M. M. Kasliwal (Jan. 2019). “Unveiling the dynamic infrared sky”. In: *Nature Astronomy* 3. doi: 10.1038/s41550-018-0675-x.
- Morales-Garoffolo, A. et al. (Dec. 2014). “SN 2013df, a double-peaked IIb supernova from a compact progenitor and an extended H envelope”. In: *MNRAS* 445. doi: 10.1093/mnras/stu1837. arXiv: 1409.2784 [astro-ph.SR].
- Moriya, T. et al. (July 2011). “Supernovae from red supergiants with extensive mass loss”. In: *MNRAS* 415. doi: 10.1111/j.1365-2966.2011.18689.x. arXiv: 1009.5799 [astro-ph.SR].
- Moriya, T. J. et al. (Oct. 2013). “An analytic bolometric light curve model of interaction-powered supernovae and its application to Type II_n supernovae”. In: *MNRAS* 435.2. doi: 10.1093/mnras/stt1392. arXiv: 1307.2644.
- Moriya, T. J. et al. (Jan. 2016). “On the nature of rapidly fading Type II supernovae”. In: *MNRAS* 455.1, pp. 423–430. doi: 10.1093/mnras/stv2336. arXiv: 1510.01656 [astro-ph.HE].
- Morozova, V., A. L. Piro, and S. Valenti (Mar. 2017). “Unifying Type II Supernova Light Curves with Dense Circumstellar Material”. In: *ApJ* 838.1, 28, p. 28. doi: 10.3847/1538-4357/aa6251. arXiv: 1610.08054 [astro-ph.HE].
- Morozova, V., A. L. Piro, and S. Valenti (May 2018). “Measuring the Progenitor Masses and Dense Circumstellar Material of Type II Supernovae”. In: *ApJ* 858.1, 15, p. 15. doi: 10.3847/1538-4357/aab9a6. arXiv: 1709.04928 [astro-ph.HE].
- Morris, T. and P. Podsiadlowski (Feb. 2007). “The Triple-Ring Nebula Around SN 1987A: Fingerprint of a Binary Merger”. In: *Science* 315.5815. doi: 10.1126/science.1136351. arXiv: astro-ph/0703317 [astro-ph].
- Mould, J. and S. Sakai (Oct. 2008). “The Extragalactic Distance Scale without Cepheids”. In: *ApJL* 686. doi: 10.1086/592964.
- Nagao, T. et al. (Oct. 2019). “The aspherical explosion of the Type IIP SN 2017gmr”. In: *MNRAS* 489.1. doi: 10.1093/mnrasl/slz119. arXiv: 1907.10505 [astro-ph.HE].
- Nagao, T., K. Maeda, and M. Tanaka (Oct. 2017). “Circumstellar Light Echo as a Possible Origin of the Polarization of Type IIP Supernovae”. In: *ApJ* 847.2, 111. doi: 10.3847/1538-4357/aa8b0d. arXiv: 1709.02077 [astro-ph.HE].
- Nagao, T., K. Maeda, and M. Tanaka (July 2018). “Multi-band Polarization of Type IIP Supernovae Due to Light Echo from Circumstellar Dust”. In: *ApJ* 861.1, 1. doi: 10.3847/1538-4357/aac94e. arXiv: 1805.11865 [astro-ph.HE].

- Nakano, S. et al. (Oct. 2012). “Supernova 2012fh in NGC 3344 = Psn J10433405 +2453290”. In: *Central Bureau Electronic Telegrams* 3263. URL: <http://adsabs.harvard.edu/abs/2012CBET.3263....1N>.
- Nakano, S. et al. (Mar. 2013). “Supernova 2013am in M65 = Psn J11185695 +1303494”. In: *Central Bureau Electronic Telegrams* 3440. URL: <http://adsabs.harvard.edu/abs/2013CBET.3440....1N>.
- Nayana, A. J. and P. Chandra (June 2017a). “GMRT radio detection of a type II supernova SN 2017eaw”. In: *ATel, No. 10534* 10534.
- Nayana, A. J. and P. Chandra (May 2017b). “Low frequency GMRT observations of supernova SN 2017eaw”. In: *ATel, No. 10388* 10388.
- Nieuwenhuijzen, H. and C. de Jager (May 1990). “Parametrization of stellar rates of mass loss as functions of the fundamental stellar parameters M, L, and R.” In: *A&A* 231.
- Nozawa, T. et al. (Dec. 2003). “Dust in the Early Universe: Dust Formation in the Ejecta of Population III Supernovae”. In: *ApJ* 598. DOI: 10.1086/379011. eprint: [astro-ph/0307108](http://arxiv.org/abs/astro-ph/0307108).
- Nozawa, T. et al. (Sept. 2008). “Early Formation of Dust in the Ejecta of Type Ib SN 2006jc and Temperature and Mass of the Dust”. In: *ApJ* 684. DOI: 10.1086/589961. arXiv: 0801.2015.
- O’Hara, T. B. et al. (Dec. 2003). “The Dust Ring of Luminous Blue Variable Candidate HD 168625: Infrared Observations and Model Calculations”. In: *ApJ* 598. DOI: 10.1086/379058.
- Oh, C. and M. J. Escuti (Oct. 2008). “Achromatic diffraction from polarization gratings with high efficiency”. In: *Opt. Lett.* 33.20. DOI: 10.1364/OL.33.002287. URL: <http://ol.osa.org/abstract.cfm?URI=ol-33-20-2287>.
- Oke, J. B. et al. (Apr. 1995). “The Keck Low-Resolution Imaging Spectrometer”. In: *PASP* 107. DOI: 10.1086/133562.
- Oliva, E. (June 1997). “Wedged double Wollaston, a device for single shot polarimetric measurements”. In: *A&AS* 123. DOI: 10.1051/aas:1997175.
- Ossenkopf, V., T. Henning, and J. S. Mathis (Aug. 1992). “Constraints on cosmic silicates”. In: *A&A* 261.
- Owen, P. J. and M. J. Barlow (Mar. 2015). “The Dust and Gas Content of the Crab Nebula”. In: *The Astrophysical Journal* 801.2, 141. DOI: 10.1088/0004-637X/801/2/141. arXiv: 1501.01510 [astro-ph.GA].
- Packham, C. et al. (Dec. 2010). “Polarization Gratings: A Novel Polarimetric Component for Astronomical Instruments”. In: *PASP* 122. DOI: 10.1086/657904.
- Panagia, N. (Jan. 1998). “New distance determination to the LMC.” In: *Mem. Soc. Astron. Italiana* 69.

- Panagia, N. (2005). “A Geometric Determination of the Distance to SN 1987A and the LMC”. In: *IAU Colloq. 192: Cosmic Explosions, On the 10th Anniversary of SN1993J*. Ed. by J.-M. Marcaide and K. W. Weiler. DOI: 10.1007/3-540-26633-X_78.
- Pancharatnam, S. (1956). “Generalized theory of interference, and its applications”. In: *Proceedings of the Indian Academy of Sciences - Section A* 44.5. ISSN: 0370-0089. DOI: 10.1007/BF03046050. URL: <https://doi.org/10.1007/BF03046050>.
- Pastorello, A. et al. (Sept. 2008). “Massive stars exploding in a He-rich circumstellar medium - I. Type Ibn (SN 2006jc-like) events”. In: *MNRAS* 389. DOI: 10.1111/j.1365-2966.2008.13602.x. arXiv: 0801.2277.
- Patat, F. and M. Romaniello (Jan. 2006). “Error Analysis for Dual-Beam Optical Linear Polarimetry”. In: *PASP* 118. DOI: 10.1086/497581. eprint: astro-ph/0509153.
- Pellegrino, C. et al. (Mar. 2020). “Constraining the Source of the High Velocity Ejecta in the Type Ia SN 2019ein”. In: *arXiv e-prints*, arXiv:2003.05946. arXiv: 2003.05946 [astro-ph.HE].
- Perlmutter, S. et al. (June 1999). “Measurements of Ω and Λ from 42 High-Redshift Supernovae”. In: *ApJ* 517.2. DOI: 10.1086/307221. arXiv: astro-ph/9812133 [astro-ph].
- Pilbratt, G. L. (Mar. 2003). “Herschel Space Observatory mission overview”. In: *IR Space Telescopes and Instruments*. Ed. by J. C. Mather. Vol. 4850. Proc. SPIE.
- Pinto, P. A. and R. G. Eastman (Feb. 2000). “The Physics of Type IA Supernova Light Curves. II. Opacity and Diffusion”. In: *ApJ* 530.2. DOI: 10.1086/308380.
- Podsiadlowski, P., P. C. Joss, and J. J. L. Hsu (May 1992). “Presupernova Evolution in Massive Interacting Binaries”. In: *ApJ* 391. DOI: 10.1086/171341.
- Pojmanski, G. et al. (Jan. 2008). “Supernova 2007sr in NGC 4038”. In: *Central Bureau Electronic Telegrams* 1213. URL: <http://adsabs.harvard.edu/abs/2008CBET.1213....1P>.
- Pooley, D. et al. (June 2002). “X-Ray, Optical, and Radio Observations of the Type II Supernovae 1999em and 1998S”. In: *ApJ* 572. DOI: 10.1086/340346. eprint: astro-ph/0103196.
- Pozzo, M. et al. (May 2006). “Optical and infrared observations of the Type IIP SN2002hh from days 3 to 397”. In: *MNRAS* 368. DOI: 10.1111/j.1365-2966.2006.10204.x. eprint: astro-ph/0602372.
- Pugh, H. and W. Li (Dec. 2004). “Supernovae 2004gn and 2004go”. In: *IAU Circ.* 8448. URL: <http://adsabs.harvard.edu/abs/2004IAUC.8448....3P>.

- Reilly, E. et al. (Sept. 2017). “Spectropolarimetry of the 2012 outburst of SN 2009ip: a bi-polar explosion in a dense, disc-like CSM”. In: *MNRAS* 470. DOI: 10.1093/mnras/stx1228.
- Rho, J. et al. (Jan. 2008). “Freshly Formed Dust in the Cassiopeia A Supernova Remnant as Revealed by the Spitzer Space Telescope”. In: *ApJ* 673. DOI: 10.1086/523835. arXiv: 0709.2880.
- Rho, J. et al. (Sept. 2018). “Near-infrared Spectroscopy of Supernova 2017eaw in 2017: Carbon Monoxide and Dust Formation in a Type II-P Supernova”. In: *ApJL* 864, L20. DOI: 10.3847/2041-8213/aad77f. arXiv: 1808.00683.
- Rieke, G. H. et al. (Sept. 2004). “The Multiband Imaging Photometer for Spitzer (MIPS)”. In: *ApJS* 154. DOI: 10.1086/422717.
- Riess, A. G. et al. (Sept. 1998). “Observational Evidence from Supernovae for an Accelerating Universe and a Cosmological Constant”. In: *AJ* 116.3. DOI: 10.1086/300499. arXiv: astro-ph/9805201 [astro-ph].
- Ryder, S. D. et al. (Mar. 2018). “Ultraviolet Detection of the Binary Companion to the Type IIb SN 2001ig”. In: *ApJ* 856.1, 83. DOI: 10.3847/1538-4357/aaaf1e. arXiv: 1801.05125 [astro-ph.SR].
- Sakon, I. et al. (Feb. 2009). “Properties of Newly Formed Dust by SN 2006JC Based on Near- to Mid-Infrared Observation With AKARI”. In: *ApJ* 692.1. DOI: 10.1088/0004-637X/692/1/546. arXiv: 0711.4801 [astro-ph].
- Salvo, M., M. Bessell, and B. Schmidt (Aug. 2003). “Supernova 2003hn in NGC 1448”. In: *IAU Circ.* 8187. URL: <http://adsabs.harvard.edu/abs/2003IAUC.8187....1S>.
- Salvo, M., B. Schmidt, and M. Owers (Aug. 2005). “Supernova 2005df in NGC 1559”. In: *IAU Circ.* 8581. URL: <http://adsabs.harvard.edu/abs/2005IAUC.8581....2S>.
- Sana, H. et al. (July 2012). “Binary Interaction Dominates the Evolution of Massive Stars”. In: *Science* 337. DOI: 10.1126/science.1223344. arXiv: 1207.6397 [astro-ph.SR].
- Sarangi, A. and I. Cherchneff (Oct. 2013). “The Chemically Controlled Synthesis of Dust in Type II-P Supernovae”. In: *ApJ* 776, 107. DOI: 10.1088/0004-637X/776/2/107. arXiv: 1309.5887 [astro-ph.SR].
- Sarangi, A. and I. Cherchneff (Mar. 2015). “Condensation of dust in the ejecta of Type II-P supernovae”. In: *A&A* 575, A95. DOI: 10.1051/0004-6361/201424969. arXiv: 1412.5522 [astro-ph.SR].
- Sarangi, A., E. Dwek, and R. G. Arendt (May 2018a). “Delayed Shock-induced Dust Formation in the Dense Circumstellar Shell Surrounding the Type II_n Supernova SN 2010jl”. In: *ApJ* 859, 66. DOI: 10.3847/1538-4357/aabfc3. arXiv: 1804.06878 [astro-ph.SR].

- Sarangi, A., M. Matsuura, and E. R. Micelotta (Apr. 2018b). “Dust in Supernovae and Supernova Remnants I: Formation Scenarios”. In: *Space Sci. Rev.* 214, 63. DOI: 10.1007/s11214-018-0492-7.
- Schlafly, E. F. and D. P. Finkbeiner (Aug. 2011). “Measuring Reddening with Sloan Digital Sky Survey Stellar Spectra and Recalibrating SFD”. In: *ApJ* 737, 103. DOI: 10.1088/0004-637X/737/2/103. arXiv: 1012.4804 [astro-ph.GA].
- Schlegel, E. M. (May 1990). “A new subclass of Type II supernovae?” In: *MNRAS* 244.
- Sengupta, S. and M. S. Marley (Dec. 2009). “Multiple Scattering Polarization of Substellar-mass Objects: T Dwarfs”. In: *ApJ* 707. DOI: 10.1088/0004-637X/707/1/716. arXiv: 0910.4240 [astro-ph.SR].
- Sengupta, S. and M. S. Marley (Oct. 2010). “Observed Polarization of Brown Dwarfs Suggests Low Surface Gravity”. In: *ApJL* 722. DOI: 10.1088/2041-8205/722/2/L142. arXiv: 1009.2145 [astro-ph.SR].
- Serabyn, E., K. Liewer, and D. Mawet (Nov. 2016). “Laboratory demonstration of a dual-stage vortex coronagraph”. In: *Optics Communications* 379. ISSN: 0030-4018. DOI: 10.1016/j.optcom.2016.05.042. URL: <https://www.sciencedirect.com/science/article/pii/S0030401816304047?via%7B5C%7D3Dihub>.
- Serkowski, K., D. S. Mathewson, and V. L. Ford (Feb. 1975). “Wavelength dependence of interstellar polarization and ratio of total to selective extinction”. In: *ApJ* 196. DOI: 10.1086/153410.
- Shapiro, P. R. and P. G. Sutherland (Dec. 1982). “The polarization of supernova light - A measure of deviation from spherical symmetry”. In: *ApJ* 263. DOI: 10.1086/160559.
- Shappee, B. J. et al. (June 2014). “The Man behind the Curtain: X-Rays Drive the UV through NIR Variability in the 2013 Active Galactic Nucleus Outburst in NGC 2617”. In: *ApJ* 788.1, 48. DOI: 10.1088/0004-637X/788/1/48. arXiv: 1310.2241 [astro-ph.HE].
- Showman, A. P. and Y. Kaspi (Oct. 2013). “Atmospheric Dynamics of Brown Dwarfs and Directly Imaged Giant Planets”. In: *ApJ* 776, 85. DOI: 10.1088/0004-637X/776/2/85. arXiv: 1210.7573 [astro-ph.EP].
- Siebert, M. R. et al. (Jan. 2020). “UCSC Transient Classification Report for 2020-01-09”. In: *Transient Name Server Classification Report 2020-90*.
- Simcoe, R. A. et al. (Feb. 2019). “Background-limited Imaging in the Near Infrared with Warm InGaAs Sensors: Applications for Time-domain Astronomy”. In: *AJ* 157.2, 46. DOI: 10.3847/1538-3881/aae094. arXiv: 1805.08791 [astro-ph.IM].

- Singh, A. et al. (Sept. 2019). “SN 2018hna: 1987A-like Supernova with a Signature of Shock Breakout”. In: *ApJL* 882.2, L15. DOI: 10.3847/2041-8213/ab3d44. arXiv: 1908.07807 [astro-ph.HE].
- Siviero, A. et al. (Mar. 2012). “Supernova 2012aw in M95 = PSN J10435372 +1140177.” In: *Central Bureau Electronic Telegrams* 3054. URL: <http://adsabs.harvard.edu/abs/2012CBET.3054....4S>.
- Skrutskie, M. F. et al. (Feb. 2006). “The Two Micron All Sky Survey (2MASS)”. In: *AJ* 131. DOI: 10.1086/498708.
- Slater, J. (1959). *Microwave transmission*. Dover book ; S564. Dover Publications. URL: <https://books.google.com/books?id=PvZMAQAATIAAJ>.
- Sluder, A., M. Milosavljević, and M. H. Montgomery (Nov. 2018). “Molecular nucleation theory of dust formation in core-collapse supernovae applied to SN 1987A”. In: *MNRAS* 480. DOI: 10.1093/mnras/sty2060. arXiv: 1612.09013 [astro-ph.SR].
- Smartt, S. J. (Sept. 2009). “Progenitors of Core-Collapse Supernovae”. In: *ARA&A* 47.1. DOI: 10.1146/annurev-astro-082708-101737. arXiv: 0908.0700 [astro-ph.SR].
- Smith, L. J., P. A. Crowther, and R. K. Prinja (Jan. 1994). “A study of the luminous blue variable candidate He 3-519 and its surrounding nebula”. In: *A&A* 281.
- Smith, N. (Aug. 2014). “Mass Loss: Its Effect on the Evolution and Fate of High-Mass Stars”. In: *ARA&A* 52. DOI: 10.1146/annurev-astro-081913-040025. arXiv: 1402.1237 [astro-ph.SR].
- Smith, N. and W. D. Arnett (Apr. 2014). “Preparing for an Explosion: Hydrodynamic Instabilities and Turbulence in Presupernovae”. In: *ApJ* 785, 82. DOI: 10.1088/0004-637X/785/2/82. arXiv: 1307.5035 [astro-ph.SR].
- Smith, N., R. J. Foley, and A. V. Filippenko (June 2008). “Dust Formation and He II λ 4686 Emission in the Dense Shell of the Peculiar Type Ib Supernova 2006jc”. In: *ApJ* 680. DOI: 10.1086/587860. arXiv: 0704.2249.
- Smith, N. et al. (Apr. 2009a). “Coronal Lines and Dust Formation in SN 2005ip: Not the Brightest, but the Hottest Type IIn Supernova”. In: *ApJ* 695. DOI: 10.1088/0004-637X/695/2/1334. arXiv: 0809.5079.
- Smith, N. (June 2006). “The Structure of the Homunculus. I. Shape and Latitude Dependence from H₂ and [Fe II] Velocity Maps of η Carinae”. In: *ApJ* 644.2. DOI: 10.1086/503766. arXiv: astro-ph/0602464 [astro-ph].
- Smith, N. (2017). “Interacting Supernovae: Types IIn and Ibn”. In: *Handbook of Supernovae, ISBN 978-3-319-21845-8. Springer International Publishing AG, 2017, p. 403*. DOI: 10.1007/978-3-319-21846-5_38.

- Smith, N., K. H. Hinkle, and N. Ryde (Mar. 2009b). “Red Supergiants as Potential Type II_n Supernova Progenitors: Spatially Resolved 4.6 μm CO Emission Around VY CMa and Betelgeuse”. In: *AJ* 137.3. DOI: 10.1088/0004-6256/137/3/3558. arXiv: 0811.3037 [astro-ph].
- Smith, N. and S. P. Owocki (July 2006). “On the Role of Continuum-driven Eruptions in the Evolution of Very Massive Stars and Population III Stars”. In: *ApJL* 645.1. DOI: 10.1086/506523. arXiv: astro-ph/0606174 [astro-ph].
- Smith, N. et al. (Aug. 1999). “HUBBLE SPACE TELESCOPE Images of the Compact Nebula around RY Scuti”. In: *AJ* 118.2. DOI: 10.1086/300965.
- Smith, N. et al. (Oct. 2002). “The WR+OB Progenitor RY Scuti: Intensive Spectroscopy of Its Compact Double-Ring Nebula”. In: *ApJ* 578.1. DOI: 10.1086/342365.
- Smith, N. et al. (Dec. 2011a). “Episodic mass loss in binary evolution to the Wolf-Rayet phase: Keck and HST proper motions of RY Scuti’s nebula”. In: *MNRAS* 418.3. DOI: 10.1111/j.1365-2966.2011.19614.x. arXiv: 1105.2329 [astro-ph.SR].
- Smith, N. et al. (Apr. 2011b). “Observed fractions of core-collapse supernova types and initial masses of their single and binary progenitor stars”. In: *MNRAS* 412.3. DOI: 10.1111/j.1365-2966.2011.17229.x. arXiv: 1006.3899 [astro-ph.HE].
- Spromilio, J. et al. (July 1988). “Carbon monoxide in supernova 1987A”. In: *Nature* 334. DOI: 10.1038/334327a0.
- Stefansson, G. et al. (Oct. 2017). “Toward Space-like Photometric Precision from the Ground with Beam-shaping Diffusers”. In: *ApJ* 848, 9. DOI: 10.3847/1538-4357/aa88aa. arXiv: 1710.01790 [astro-ph.IM].
- Stetson, P. B. (Mar. 1987). “DAOPHOT - A computer program for crowded-field stellar photometry”. In: *PASP* 99. DOI: 10.1086/131977.
- Stolker, T. et al. (Nov. 2017). “Polarized scattered light from self-luminous exoplanets. Three-dimensional scattering radiative transfer with ARTES”. In: *A&A* 607, A42. DOI: 10.1051/0004-6361/201730780. arXiv: 1706.09427 [astro-ph.EP].
- Stritzinger, M. et al. (Sept. 2012). “Multi-wavelength Observations of the Enduring Type II_n Supernovae 2005ip and 2006jd”. In: *ApJ* 756, 173. DOI: 10.1088/0004-637X/756/2/173. arXiv: 1206.5575.
- Sugerman, B. E. K. et al. (July 2006). “Massive-Star Supernovae as Major Dust Factories”. In: *Science* 313. DOI: 10.1126/science.1128131. eprint: astro-ph/0606132.
- Sugerman, B. et al. (Nov. 2004). “Supernova 1999bw in NGC 3198”. In: *IAU Circ.* 8442. URL: <http://adsabs.harvard.edu/abs/2004IAUC.8442....2S>.

- Szalai, T. and J. Vinkó (Jan. 2013). “Twelve type II-P supernovae seen with the eyes of Spitzer”. In: *A&A* 549, A79. DOI: 10.1051/0004-6361/201220015. arXiv: 1211.0854 [astro-ph.SR].
- Szalai, T. et al. (Mar. 2011). “Dust formation in the ejecta of the type II-P supernova 2004dj”. In: *A&A* 527, A61. DOI: 10.1051/0004-6361/201015624. arXiv: 1012.2035 [astro-ph.SR].
- Szalai, T. et al. (Aug. 2016). “The continuing story of SN Iib 2013df: new optical and IR observations and analysis”. In: *MNRAS* 460. DOI: 10.1093/mnras/stw1031. arXiv: 1604.08046 [astro-ph.SR].
- Szalai, T. et al. (Apr. 2019). “A Comprehensive Analysis of Spitzer Supernovae”. In: *ApJS* 241.2, 38. DOI: 10.3847/1538-4365/ab10df. arXiv: 1803.02571 [astro-ph.HE].
- Tan, X. and A. P. Showman (Feb. 2017). “Effects of Latent Heating on Atmospheres of Brown Dwarfs and Directly Imaged Planets”. In: *ApJ* 835, 186. DOI: 10.3847/1538-4357/835/2/186. arXiv: 1701.02782 [astro-ph.EP].
- Tanaka, M. et al. (Dec. 2008). “Optical Spectropolarimetry and Asphericity of the Type Ic SN 2007gr”. In: *ApJ* 689.2. DOI: 10.1086/592325. arXiv: 0806.1589 [astro-ph].
- Tanaka, M. et al. (July 2009). “Spectropolarimetry of the Unique Type Ib Supernova 2005bf: Larger Asymmetry Revealed by Later-Phase Data”. In: *ApJ* 699.2. DOI: 10.1088/0004-637X/699/2/1119. arXiv: 0906.1062 [astro-ph.HE].
- Tanaka, M. et al. (July 2012). “Three-dimensional Explosion Geometry of Stripped-envelope Core-collapse Supernovae. I. Spectropolarimetric Observations”. In: *ApJ* 754.1, 63. DOI: 10.1088/0004-637X/754/1/63. arXiv: 1205.4111 [astro-ph.SR].
- Tervo, J. and J. Turunen (June 2000). “Paraxial-domain diffractive elements with 100% efficiency based on polarization gratings”. In: *Optics Letters* 25.11. DOI: 10.1364/OL.25.000785.
- Tinyanont, S. et al. (Dec. 2016). “A Systematic Study of Mid-infrared Emission from Core-collapse Supernovae with SPIRITS”. In: *ApJ* 833.2, 231. DOI: 10.3847/1538-4357/833/2/231. arXiv: 1601.03440 [astro-ph.SR].
- Tinyanont, S. et al. (Sept. 2019a). “Achieving a spectropolarimetric precision better than 0.1% in the near-infrared with WIRC+Pol”. In: *Proc. SPIE*. Vol. 11132. Society of Photo-Optical Instrumentation Engineers (SPIE) Conference Series. DOI: 10.1117/12.2529863. arXiv: 1908.10409 [astro-ph.IM].
- Tinyanont, S. et al. (Mar. 2019b). “Supernova 2017eaw: Molecule and Dust Formation from Infrared Observations”. In: *ApJ* 873.2, 127. DOI: 10.3847/1538-4357/ab0897. arXiv: 1901.01940 [astro-ph.HE].

- Tinyanont, S. et al. (Feb. 2019c). “WIRC+Pol: A Low-resolution Near-infrared Spectropolarimeter”. In: *PASP* 131.996. DOI: 10.1088/1538-3873/aaef0f. arXiv: 1811.03138 [astro-ph.IM].
- Tinyanont, S. et al. (Feb. 2019d). “WIRC+Pol: A Low-resolution Near-infrared Spectropolarimeter”. In: *PASP* 131.996. DOI: 10.1088/1538-3873/aaef0f. arXiv: 1811.03138 [astro-ph.IM].
- Todini, P. and A. Ferrara (Aug. 2001). “Dust formation in primordial Type II supernovae”. In: *MNRAS* 325. DOI: 10.1046/j.1365-8711.2001.04486.x. eprint: astro-ph/0009176.
- Tokunaga, A. T. et al. (Aug. 1998). “Infrared camera and spectrograph for the SUBARU Telescope”. In: *Proc. SPIE*. Ed. by A. M. Fowler. Vol. 3354. Society of Photo-Optical Instrumentation Engineers (SPIE) Conference Series. DOI: 10.1117/12.317277.
- Tomasella, L. et al. (May 2017). “Spectroscopic observation of SN 2017eaw by NUTS (NOT Un-biased Transient Survey)”. In: *The Astronomer’s Telegram* 10377. URL: <http://adsabs.harvard.edu/abs/2017ATel10377....1T>.
- Tonry, J. L. et al. (June 2018). “ATLAS: A High-cadence All-sky Survey System”. In: *PASP* 130.988. DOI: 10.1088/1538-3873/aabadf. arXiv: 1802.00879 [astro-ph.IM].
- Tonry, J. et al. (May 2019). “ATLAS Transient Discovery Report for 2019-05-01”. In: *Transient Name Server Discovery Report* 2019-678.
- Tsvetkov, D. Y. et al. (May 2018). “Light Curves of the Type II-P Supernova SN 2017eaw: The First 200 Days”. In: *Astronomy Letters* 44. DOI: 10.1134/S1063773718050043.
- Umana, G. et al. (Mar. 2009). “The Dusty Nebula Surrounding HR Car: A Spitzer View”. In: *ApJ* 694.1. DOI: 10.1088/0004-637X/694/1/697. arXiv: 0901.2447 [astro-ph.GA].
- Vacca, W. D., M. C. Cushing, and J. T. Rayner (Mar. 2003). “A Method of Correcting Near-Infrared Spectra for Telluric Absorption”. In: *PASP* 115. DOI: 10.1086/346193. eprint: astro-ph/0211255.
- Valenti, S. et al. (Feb. 2008). “The Carbon-rich Type Ic SN 2007gr: The Photospheric Phase”. In: *ApJL* 673.2. DOI: 10.1086/527672. arXiv: 0712.1899 [astro-ph].
- Vamvatira-Nakou, C. et al. (Sept. 2013). “Herschel imaging and spectroscopy of the nebula around the luminous blue variable star WRAY 15-751”. In: *Astronomy and Astrophysics* 557, A20. DOI: 10.1051/0004-6361/201321853. arXiv: 1307.0759 [astro-ph.SR].
- Van Dyk, S. D. (May 2013). “Late-time Dust Emission from the Type II_n Supernova 1995N”. In: *AJ* 145, 118. DOI: 10.1088/0004-6256/145/5/118. arXiv: 1305.0028 [astro-ph.SR].

- Van Dyk, S. D. et al. (May 2017). “The Probable Red Supergiant Progenitor of SN 2017eaw”. In: *The Astronomer’s Telegram* 10378. URL: <http://adsabs.harvard.edu/abs/2017ATel110378...1V>.
- Van Dyk, S. D. et al. (Nov. 2011). “The Progenitor of Supernova 2011dh/PTF11leon in Messier 51”. In: *ApJL* 741.2, L28. DOI: 10.1088/2041-8205/741/2/L28. arXiv: 1106.2897 [astro-ph.CO].
- Van Dyk, S. D. et al. (June 2018). “SN 2017ein and the Possible First Identification of a Type Ic Supernova Progenitor”. In: *ApJ* 860.2, 90. DOI: 10.3847/1538-4357/aac32c. arXiv: 1803.01050 [astro-ph.SR].
- Vanbeveren, D., C. De Loore, and W. Van Rensbergen (1998). “Massive stars”. In: *A&A Rev.* 9. DOI: 10.1007/s001590050015.
- Voshchinnikov, N. V. (Dec. 2012). “Interstellar extinction and interstellar polarization: Old and new models”. In: *JQSRT* 113.18. DOI: 10.1016/j.jqsrt.2012.06.013. arXiv: 1206.4090 [astro-ph.GA].
- Wang, L. and J. C. Wheeler (May 1996). “Polarization of SN 1987A Revisited”. In: *ApJL* 462. DOI: 10.1086/310026. eprint: astro-ph/9602156.
- Wang, L. and J. C. Wheeler (Sept. 2008). “Spectropolarimetry of Supernovae”. In: *ARA&A* 46. DOI: 10.1146/annurev.astro.46.060407.145139. arXiv: 0811.1054.
- Wang, L. et al. (Nov. 2002). “The Axisymmetric Ejecta of Supernova 1987A”. In: *ApJ* 579.2. DOI: 10.1086/342824. arXiv: astro-ph/0205337 [astro-ph].
- Wang, L. et al. (Dec. 2006). “Premaximum Spectropolarimetry of the Type Ia SN 2004dt”. In: *ApJ* 653.1. DOI: 10.1086/508250. arXiv: astro-ph/0409593 [astro-ph].
- Wardle, J. F. C. and P. P. Kronberg (Dec. 1974). “The linear polarization of quasi-stellar radio sources at 3.71 and 11.1 centimeters”. In: *ApJ* 194. DOI: 10.1086/153240.
- Watanabe, M. et al. (July 2018). “Near-infrared adaptive optics imaging- and spectropolarimetry with the infrared camera and spectrograph of the Subaru Telescope”. In: *Proc. SPIE*. Vol. 10702. Society of Photo-Optical Instrumentation Engineers (SPIE) Conference Series. DOI: 10.1117/12.2311969.
- Werner, M. W. et al. (Sept. 2004). “The Spitzer Space Telescope Mission”. In: *ApJS* 154. DOI: 10.1086/422992. eprint: astro-ph/0406223.
- West, R. M. et al. (Feb. 1987). “Supernova 1987A in the Large Magellanic Cloud”. In: *IAU Circ.* 4319. URL: <https://ui.adsabs.harvard.edu/abs/1987IAUC.4319...1W>.
- Wheeler, J. C., V. Johnson, and A. Clocchiatti (June 2015). “Analysis of late-time light curves of Type IIb, Ib and Ic supernovae”. In: *MNRAS* 450. DOI: 10.1093/mnras/stv650. arXiv: 1411.5975 [astro-ph.SR].

- Whittet, D. C. B. et al. (Feb. 1992). “Systematic variations in the wavelength dependence of interstellar linear polarization”. In: *ApJ* 386. DOI: 10.1086/171039.
- Wiggins, P. (May 2017). “Psn J20344424+6011359 = Supernova 2017eaw in NGC 6946”. In: *Central Bureau Electronic Telegrams* 4390. URL: <http://adsabs.harvard.edu/abs/2017CBET.4390....1W>.
- Wiktorowicz, S. J. et al. (Nov. 2015). “A Ground-based Albedo Upper Limit for HD 189733b from Polarimetry”. In: *ApJ* 813.1, 48. DOI: 10.1088/0004-637X/813/1/48. arXiv: 1507.03588 [astro-ph.EP].
- Wiktorowicz, S. J. (Jan. 2009). “Unambiguous black hole mass from polarimetry and application to hot Jupiters”. PhD thesis. California Institute of Technology.
- Williams, B. J. and O. D. Fox (July 2015). “SOFIA Observations of SN 2010jl: Another Non-Detection of the 9.7 μm Silicate Dust Feature”. In: *ApJ* 808, L22. DOI: 10.1088/2041-8205/808/1/L22. arXiv: 1507.00008 [astro-ph.HE].
- Wilson, J. C. et al. (Mar. 2003). “A Wide-Field Infrared Camera for the Palomar 200-inch Telescope”. In: *Instrument Design and Performance for Optical/Infrared Ground-based Telescopes*. Ed. by M. Iye and A. F. M. Moorwood. Vol. 4841. Proc. SPIE. DOI: 10.1117/12.460336.
- Wooden, D. H. et al. (Oct. 1993). “Airborne spectrophotometry of SN 1987A from 1.7 to 12.6 microns - Time history of the dust continuum and line emission”. In: *ApJS* 88. DOI: 10.1086/191830.
- Woods, P. M. et al. (Mar. 2011). “The SAGE-Spec Spitzer Legacy programme: the life-cycle of dust and gas in the Large Magellanic Cloud - Point source classification I”. In: *MNRAS* 411.3. DOI: 10.1111/j.1365-2966.2010.17794.x. arXiv: 1009.5929 [astro-ph.GA].
- Woosley, S. E. and A. Heger (Sept. 2015). “The Remarkable Deaths of 9-11 Solar Mass Stars”. In: *ApJ* 810, 34. DOI: 10.1088/0004-637X/810/1/34. arXiv: 1505.06712 [astro-ph.SR].
- Woosley, S. E., A. Heger, and T. A. Weaver (Nov. 2002). “The evolution and explosion of massive stars”. In: *Reviews of Modern Physics* 74.4. DOI: 10.1103/RevModPhys.74.1015.
- Woosley, S. E. and T. A. Weaver (1986). “The physics of supernova explosions”. In: *ARA&A* 24. DOI: 10.1146/annurev.aa.24.090186.001225.
- Yamaoka, H. et al. (Jan. 2014). “Supernova 2014L in M99 = Psn J12184868 +1424435”. In: *Central Bureau Electronic Telegrams* 3795. URL: <http://adsabs.harvard.edu/abs/2014CBET.3795....2Y>.
- Yang, Y. et al. (Mar. 2019). “The Young and Nearby Normal Type Ia Supernova 2018gv: UV-Optical Observations and the Earliest Spectropolarimetry”. In: *arXiv e-prints*, arXiv:1903.10820. arXiv: 1903.10820 [astro-ph.HE].

- Yaron, O. et al. (Feb. 2017). “Confined dense circumstellar material surrounding a regular type II supernova”. In: *Nature Physics* 13. DOI: 10.1038/nphys4025. arXiv: 1701.02596 [astro-ph.HE].
- Young, E. T. et al. (Apr. 2012). “Early Science with SOFIA, the Stratospheric Observatory For Infrared Astronomy”. In: *ApJL* 749.2, L17. DOI: 10.1088/2041-8205/749/2/L17. arXiv: 1205.0791 [astro-ph.IM].
- Zapartas, E. et al. (Nov. 2019). “The diverse lives of progenitors of hydrogen-rich core-collapse supernovae: the role of binary interaction”. In: *A&A* 631, A5. DOI: 10.1051/0004-6361/201935854. arXiv: 1907.06687 [astro-ph.HE].
- Zapatero Osorio, M. R. et al. (Oct. 2011). “Near-infrared Linear Polarization of Ultracool Dwarfs”. In: *ApJ* 740, 4. DOI: 10.1088/0004-637X/740/1/4. arXiv: 1107.2498 [astro-ph.SR].
- Zauderer, B. A. et al. (Jan. 2014). “CARMA Millimeter Detection of SN 2014C (PSN J22370560+3424319)”. In: *The Astronomer’s Telegram* 5764. URL: <http://adsabs.harvard.edu/abs/2014ATel.5764....1Z>.
- Zhang, X. and A. P. Showman (June 2014). “Atmospheric Circulation of Brown Dwarfs: Jets, Vortices, and Time Variability”. In: *ApJL* 788, L6. DOI: 10.1088/2041-8205/788/1/L6. arXiv: 1403.2143 [astro-ph.EP].

Appendix A

MCMC FITTING OF THE SED AND LIGHT CURVE OF SN 2014C

A.1 SED Fitting with Dust Models

To determine best-fit values for the dust parameters in the SED fittings in §4.3, and the CSM parameters in the light-curve fitting in §4.3, we used the `emcee` package to run MCMC on our data. For the first model with all carbonaceous dust, there were 6 parameters: $M_{\text{cold,warm,hot}}$ and $T_{\text{cold,warm,hot}}$. The dust composition was purely carbonaceous and the grain size was $0.1 \mu\text{m}$. The initial values of these parameters were obtained by running a more traditional least square fit on the data using the `curve_fit` routine in the `scipy.optimize` package. The prior distribution for all parameters are uniform, with only positive values allowed for mass and temperatures. We ran MCMC using 400 walkers for 1000 steps, and determined that the convergence happened after 200 steps. Fig. A.1 shows the resulting posterior distribution of the 6 parameters, along with the median and $\pm 1\sigma$ values.

For the second model with a mixture of carbonaceous and silicate dust, there were five free parameters: M_{warm} , T_{warm} , M_{hot} , T_{hot} , and f_{Si} . The prior distribution was also uniform with positive mass and temperatures. The silicate fraction f_{Si} could be between 0 and 1. The initial values were also obtained with a least square fit using `curve_fit`. We ran MCMC using 400 walkers for 2000 steps, and determined that the convergence happened after 1000 steps. We note that the temperature and mass of the hot component are not as well constrained because the near-IR SED deviates from the dust model, potentially due to poor background subtraction. Fig. A.2 shows the resulting posterior distribution of the 5 parameters, along with the median and $\pm 1\sigma$ values.

A.2 Light-Curve Fitting with CSM Models

As discussed in the main text, we found that the MCMC fit can only constrain CSM density parameters, namely D and s from $\rho_{\text{CSM}} = Dr^{-s}$, and not the explosion parameters (E_{ej} and M_{ej}). We considered a model with D and s as free parameters. Similarly to the SED fit, the initial values were determined using least square fitting. We also used a uniform prior distribution with physical parameters set to positive numbers, and $0 \leq s < 3$. Fig. A.3 shows the corner plots for the fit.

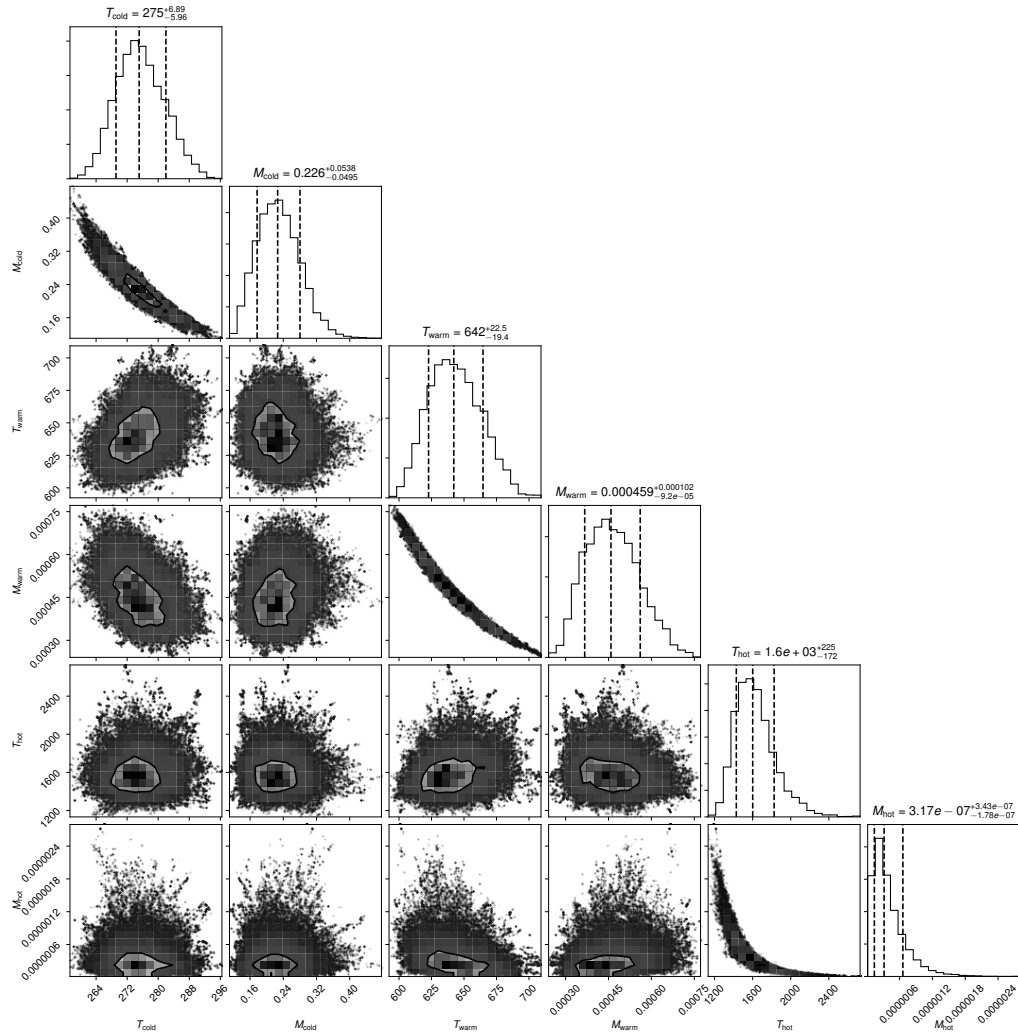


Figure A.1: The corner plot showing the results of MCMC fitting of the SED shown in Fig. 4.5 using a dust model with 3 temperature components. Each component has two parameters: temperature and mass. All components only have carbonaceous dust with the grain size of $0.1 \mu\text{m}$. Units of mass and temperatures are M_{\odot} and K, respectively.

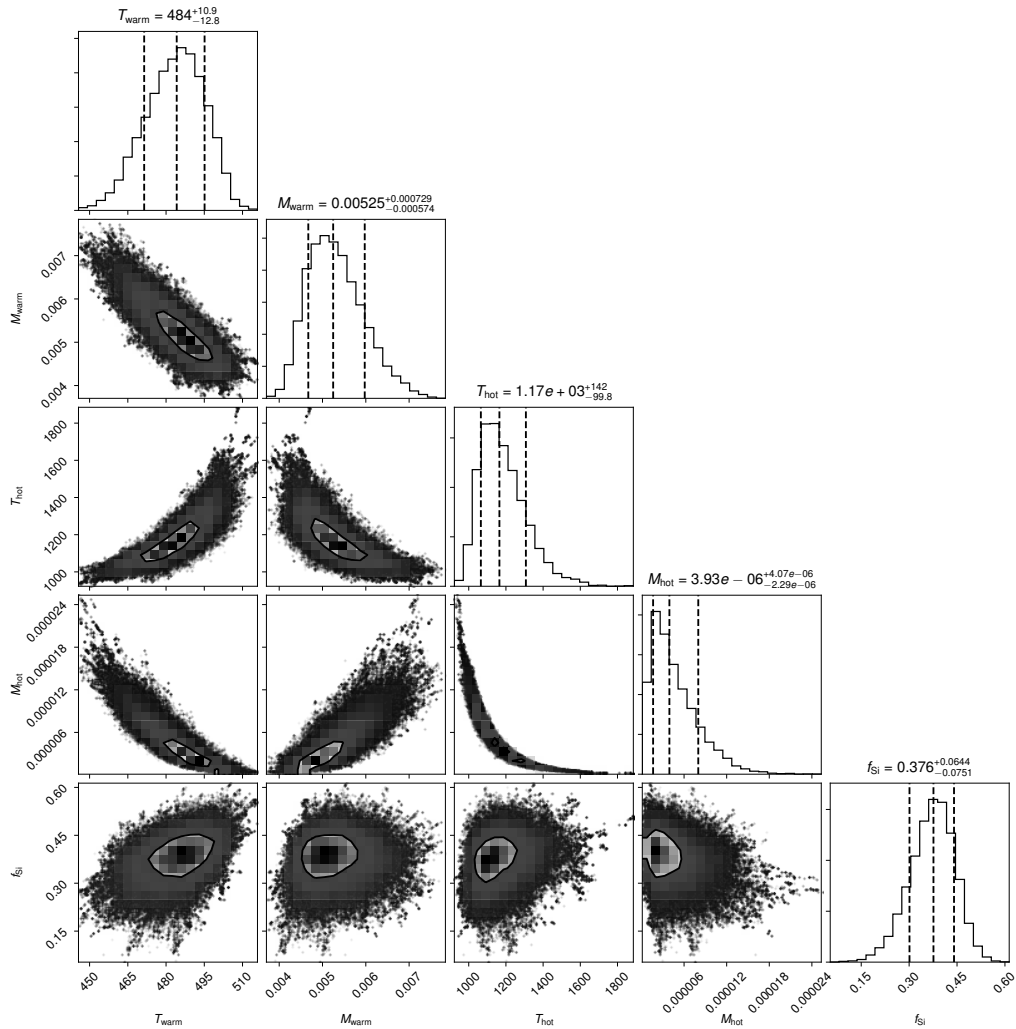


Figure A.2: The corner plot showing the results of MCMC fitting of the SED shown in Fig. 4.5 using a dust model with two temperature components. The warm component has a mixture of carbonaceous and silicate dust with the mass fraction of f_{Si} in silicate. The total mass and temperature of this component are M_{warm} and T_{warm} , respectively. The hot component only consists of carbonaceous dust, though both composition looks identical at this temperature. The total mass and temperature of this component are M_{hot} and T_{hot} , respectively. Units of mass and temperatures are M_{\odot} and K, respectively.

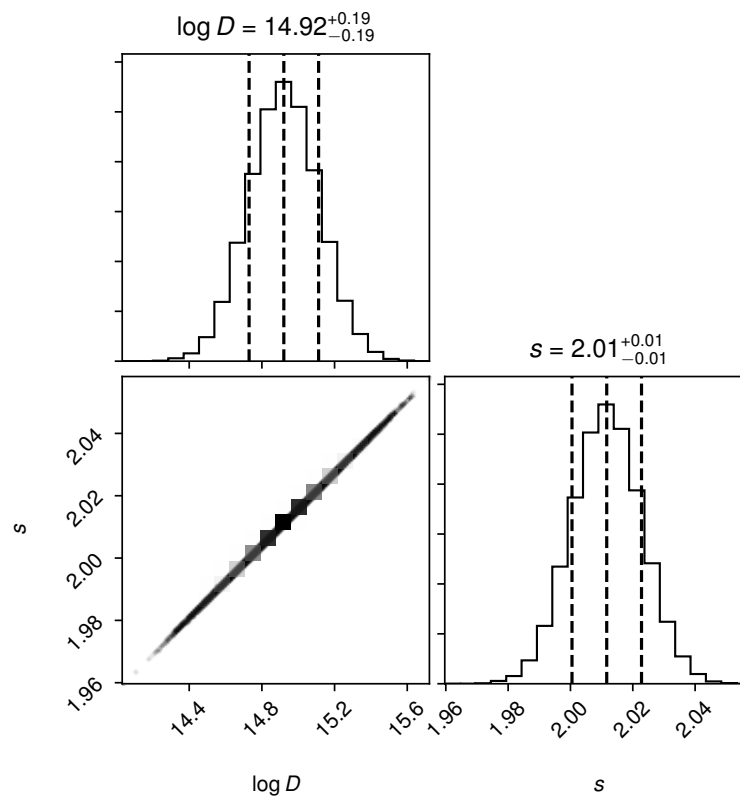


Figure A.3: The corner plot showing the results of MCMC fitting of the light curve from §4.3 where we fitted a light curve of the SN interacting with a CSM with the density profile $\rho_{\text{CSM}} = Dr^{-s}$ with D and s as the free parameters in the fit.

Appendix B

WIRC+POL CALIBRATION AND DATA VERIFICATION

B.1 Verification of WIRC+Pol Results against Background Subtraction

To demonstrate that our polarization measurements are not significantly affected by the background subtraction, we injected a synthetic source with the flux spectrum similar to the SNe considered here into a real data set from WIRC+Pol with the same exposure time. We used a sequence of 120 exposures of 60 s each. The HWP was cycled between 0° , 45° , 22.5° , and 67.5° with one exposure per HWP angle. For the simulation, we used the same seeing conditions to simulate the source and we check to ensure that the total counts in the synthetic data are similar to the real observations. We produced two synthetic data sets with the SN unpolarized to provide a control sample and polarized with $p = 2\%$ and $\theta = 0^\circ$ to replicate the real observation.

We extracted the synthetic source to determine whether the background-subtraction strategy we used for the SN data could reproduce the injected polarization. All extraction methods are the same as used for the real SN data. We used both the AB subtraction (used for SNe 2019ein, 2020oi, and 2020ue data) and the slit fitting subtraction (used for SN 2018hna). Fig. B.1 shows the q and u spectra of the synthetic source, with red showing results from the AB subtraction and blue from the slit fitting subtraction. The top row shows results for the unpolarized source, and the bottom row the 2% , $\theta = 0^\circ$ source. The left two columns are q and u in percent, while the right two columns are normalized by the standard deviation of the measurement.

The results show the following: (1) Our data reduction process does not introduce a systematic polarimetric offset to the data. The broadband measurement agrees with the injected value to within 1σ . (2) A wavelength-dependent scatter from the expectation value is present, but the measurements never deviate away more than 3σ from the expectation value. (3) We repeated the experiment using several spectral shapes, source brightness, and seeing conditions. We found that in all cases, the polarimetric measurements do not depart from the expected value for more than 3σ . (4) The AB background subtraction and slit fitting subtraction produce statistically equivalent results. From these results, we report a polarimetric detection when

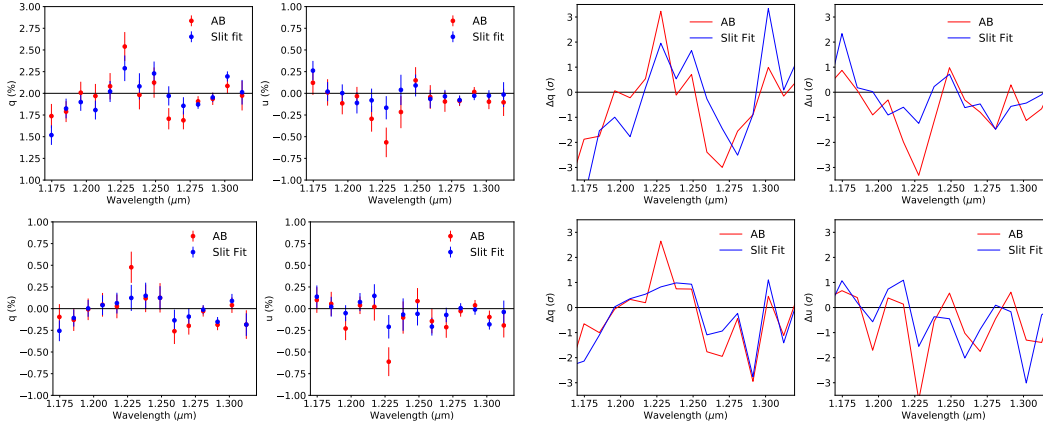


Figure B.1: Normalized Stokes parameters extracted from the synthetic data of a source with SN 2018hna flux spectrum and magnitude at the same seeing condition. The top row shows results for a synthetic source with $p = 2\%$ and $\theta = 0^\circ$, similar to what is observed in SN 2018hna. The bottom row shows results for observations assuming $p = 0\%$. The two left columns show q and u in percent as functions of wavelength along with 1σ error bars. The two right columns show the deviation of the observed q and u from the injected values in the unit of standard deviation. Red points are results from AB subtraction while blue are from using the slit fitting routine.

either q or u is more than 3σ away from zero.

B.2 Polarimetric Efficiency and Angle of Polarization Calibration from Observations of Polarized Standard Stars

A polarimeter can be characterized by a Mueller matrix that operates on the intrinsic Stokes vector yielding the measured Stokes vector. Because WIRC+Pol is not sensitive to circular polarization, we limit our analysis to the normalized Stokes parameters q and u , and write

$$\begin{bmatrix} 1 \\ q_{\text{obs}} \\ u_{\text{obs}} \end{bmatrix} = \begin{bmatrix} 1 & 0 & 0 \\ IP_q & \eta_q & \chi_{u \rightarrow q} \\ IP_u & \chi_{q \rightarrow u} & \eta_u \end{bmatrix} \begin{bmatrix} 1 \\ q \\ u \end{bmatrix} \quad (\text{B.1})$$

The terms in the Mueller matrix are the following: $IP_{q,u}$ are the instrumental polarization in q and u ; $\eta_{q,u}$ are the polarimetric efficiencies; and $\chi_{q \rightarrow u, u \rightarrow q}$ are the crosstalks, where all these terms are functions of wavelength. From observations of unpolarized standard stars, we showed that the instrumental polarization terms are both smaller than 0.03% (Tinyant et al., 2019b). Since these values are much smaller than the error bars on our data, for simplicity in our analysis we set $IP_q = IP_u = 0$.

For the remaining terms in Equation B.1, we split the 4 spectral traces created by the WIRC+Pol polarization grating into two pairs, equivalent to two independent dual-channel polarimeters, and find independent efficiency and crosstalk terms for each pair. To determine the efficiency and crosstalk terms, we took observations of three polarized standard stars (Elias 2-14, Elias 2-22, and Schulte 14) obtained on UT 2019 April 14 and 15 and compared our measurements against their expected polarization based on the Serkowski fits in Whittet et al. (1992). We expect the efficiency and crosstalk to vary slowly with wavelength across the J -band, and as a result we treated the η and χ terms as 3rd-degree polynomials as a function of wavelength, rather than fit for a value in each wavelength bin. Using the measured q and u values for all three standard stars, we simultaneously fit for the polynomial coefficients of each η and χ term between $1.18 \mu\text{m}$ and $1.30 \mu\text{m}$. The resultant polynomial fits can be seen in Fig. B.2.

In Fig. B.3 we show the corrected on-sky q and u measurements derived by inverting Equation B.1 for each wavelength bin (using the polynomials in Fig. B.2), as well as the expected Serkowski law values (Whittet et al., 1992). The excellent agreement between our corrected measurements and the on-sky data suggests that our Mueller matrix calibration well represents the system (at least within the $1.18 \mu\text{m}$ to $1.30 \mu\text{m}$ window.) Although the data used for this calibration were not obtained simultaneously with our supernova observations, we expect the crosstalks and efficiencies to only vary slowly in time and the results of this time-difference to be well below the statistical errors on our data. To obtain calibrated supernova data, we inverted Equation B.1 for each wavelength bin to obtain the on-sky values, q and u .

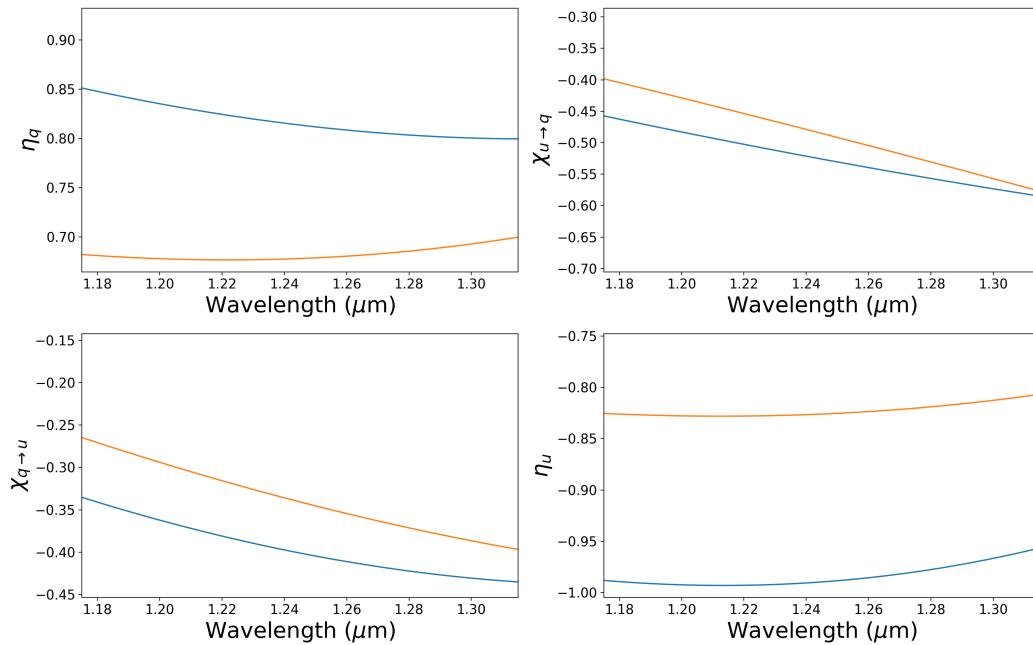


Figure B.2: The best-fit polynomials for the WIRC+Pol wavelength-dependent efficiencies and crosstalks, defined in Equation B.1. One curve is shown for each of the two spectral trace pairs (see Tinyanont et al., 2019c for the trace definitions): blue for the U_p and U_m pair, and orange for Q_p and Q_m .

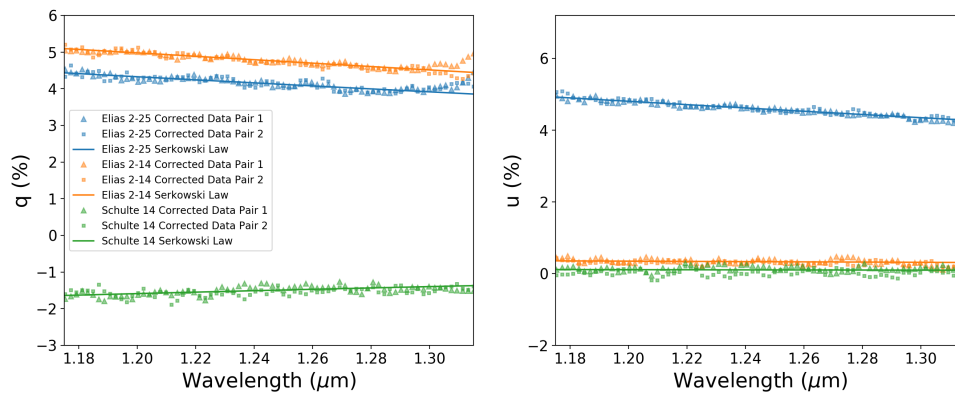


Figure B.3: The corrected q and u values for the three polarized standard stars for trace pair 1 (triangles) and trace pair 2 (squares). Also shown are the expected on-sky values from the Serkowski law fit by Whittet et al. (1992) (solid lines). The good agreement across most of wavelength range between the corrected data and the Serkowski laws for all three stars demonstrates that our model is accurate to well below the error bars on our SN data.